Title

COMBINED SURFACE SCIENCE AND CATALYTIC STUDIES OF HYDROCARBON REACTIONS OVER PLATINUM SINGLE CRYSTAL SURFACES

Author

Zaera, F.

Publication Date

1984-08-01

Lawrence Berkeley Laboratory
UNIVERSITY OF CALIFORNIA

Materials & Molecular Research Division

COMBINED SURFACE SCIENCE AND CATALYTIC STUDIES OF HYDROCARBON REACTIONS OVER PLATINUM SINGLE CRYSTAL SURFACES

F. Zaera
(Ph.D. Thesis)

August 1984

Prepared for the U.S. Department of Energy under Contract DE-AC03-76SF00098

DISCLAIMER

LBL-18311

COMBINED SURFACE SCIENCE AND CATALYTIC STUDIES OF HYDROCARBON REACTIONS OVER PLATINUM SINGLE CRYSTAL SURFACES

Francisco Zaera
Ph.D. Thesis

Lawrence Berkeley Laboratory
University of California
Berkeley, California 94720

August 1984

This work was supported by the Director, Office of Energy Research, Office of Basic Energy Sciences, Material Science Division of the U.S. Department of Energy under contract number DE-AC03-76SF00098.

Combined Surface Science and Catalytic Studies of Hydrocarbon Reactions over Platinum Single Crystal Surfaces.

By Francisco Zaera

Materials and Molecular Research Division
Lawrence Berkeley Laboratory,
and Department of Chemistry
University of California, Berkeley CA 94720.

ABSTRACT

Results from chemisorption studies under ultra-high vacuum (UHV) have been correlated with data from catalytic reactions at atmospheric pressures for some hydrocarbon reactions over platinum surfaces. Ethylidyne, which forms during room temperature chemisorption of ethylene over Pt (111), was shown to be stable towards rehydrogenation or deuterium exchange under atmospheric conditions by using high resolution electron energy loss spectroscopy (HREELS) and a radiotracer technique. Ethylene hydrogenation over Pt (111) surfaces at near room temperature displayed kinetic parameters that were in agreement with those reported for supported catalysts (e.g., the activation energy was 11 Kcal/mole). Low energy electron diffraction (LEED), thermal desorption spectroscopy (TDS), and HREELS, all indicate the presence of ethylidyne on the surface after reactions, and therefore it was concluded that ethylene hydrogenates on top of this chemisorbed layer. The exchange of ethane with D_2 over Pt (111) was also studied between 470 and 620 K, and gave an activation energy of 19 Kcal/mole. The product distribution peaked at one (d_1) and six (d_6) deuterium atoms per ethane molecule, indicating the existence of two competitive mechanisms. Again, a diffuse 2x2 LEED

pattern suggested the presence of ethylidyne on the platinum surface, which in this case can be easily hydrogenated to give d_6 ethane. At above 550 K some hydrogenolysis was also detected (E_a=34 Kcal/mole), with turnover frequencies about three orders of magnitude smaller than those for the exchange. Isobutane, neopentane, n-hexane and methylcyclopentane (MCP) conversion were also investigated over platinum surfaces of different crystallographic orientations. Surface defects proved to be important for the light alkanes but not for n-hexane or MCP reactions. The structure sensitivity for the various reactants was followed by measuring initial rates over six surfaces. Higher activities on stepped and kinked surfaces for the light alkanes correlated with the presence of patches of bare low coordination platinum atoms, as seen by using a CO titration technique. The opposite was true for the heavier alkanes. A correspondence between this behavior and the different bond-shift and cyclic mechanisms was also established. Finally, the effect of potassium as additive and of rhenium alloyed with platinum was studied for reforming reactions. Potassium poisoned all n-hexane reactions due to an electronic interaction of the potassium with the surface. Rhenium, which seems to be in the metallic state after reduced in the alloy, increased the selectivity for hydrogenolysis. Sulfur over the latter system reduces all activity, but particularly methane formation.

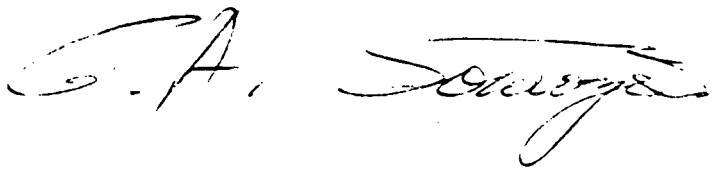

TABLE OF CONTENT

CHAPTER FIVE: THE ROLE OF ADDITIVES IN HYDROCARBON CATALYSIS OVER PLATINUM SINGLE CRYSTAL SURFACES.

ACKNOWLEDGMENTS

The culmination of this research effort was only possible thanks to the multiple help that I received during its realization. I wish to mention first of all professor Gabor Somorjai for the opportunity he gave me to work in his laboratory doing exciting research in a very estimulating environment. From his many attributes I am most grateful for his ability to offer almost unlimitted freedom while keeping in mind the research goals.

Along with professor Somorjai, the help offered by his many group members was very much appreciated. Special thanks to Wilfred Tysoe, who helped me in many ways, including the acquisition of the XPS data; Mark Davis, who introduced me to this field and taught me most of the basics over my first year in the group; Bruce Koel and Brian Bent, which obtained most of the vibrational spectra; David Godbey, for putting up with me for the last year and for obtaining some of the data reported throughout the thesis; Andrew Gellman, who was kind enough to perform some preliminary experiments in the Pt-Re-S system; and Mark Logan, willing to do some experiments in his chamber while mine was having serious contamination problems. This list should also include Tom Gentle, always ready to help, specially at night, when help was so hard to find.

I am also grateful to the support staff of LBL for keeping me going at all times. Thanks to Keith Franck for his patience (or lack of

it) in solving all sort of problems related to the vacuum chamber. Thanks to G. Baum, J. Severns, S. Stewart, C. Sterling, G. Pelatowski, and many others.

Thanks to my country, Venezuela, which through FONINVES (now CEPET), provided me with finantial support for the studies. I am grateful to the chemistry department of the University Simón Bolívar, and specially to professor Isak Rusinek, for the complete education they provided me with. Perhaps it took me these four years in Berkeley to look back and place the problems of Venezuela in perspective, and to learn to have just a little bit more hope in its future.

This work was supported by the Director, Office of Energy Research, Office of Basic Energy Sciences, Material Science Division of the U.S. Department of Energy under contract number DE-AC03-76SF00098.

CHAPTER ONE: INTRODUCTION AND OVERVIEW

Heterogeneous catalysis is of vital importance in virtually all industrial processes existing nowdays. Of all catalyst materials used, platinum is perhaps the most versatile. It can be used in ammonia oxidation to produce fertilizers, in carbon monoxide oxidation for car emission control, in almost any electrochemical cell, and in hydrocarbon processing [1].

Catalytic reforming, one of the most important industrial applications of catalysis, is also based on the use of platinum. Its objective is to improve the octane number of naphtas, or light distillates from petroleum, for burning in modern high compression ratio internal combustion engines. Coincidentally, it is also the major source of aromatics for chemicals [2-4]. In reforming, gasoline-range molecules, including those formed from larger hydrocarbons by cracking, are reconstructed, or reformed, without changing their carbon number. The reactions involved include isomerization, hydrogenation, dehydrocyclization and dehydrogenation, in order to produce branched paraffins or aromatic compounds, that have higher octane numbers, that is, better anti-knock ratings. This is illustrated in fig. 1.1, where the octane number of several hydrocarbons is plotted as a function of carbon number and compound families. The thermodynamics of some typical reactions involved in the process are summarized in table 1.1 [5].

The first catalytic reforming process using a noble metal catalyst, called platforming or platinum reforming, was introduced by Universal Oil Products in 1949 [6]. Typical industrial operation conditions are temperatures between 750 and 800 K, pressures of 10-35 atmospheres, liquid hourly space velocities of 1 to 5, and hydrogen to hydrocarbon ratios ranging from 3 to 10. The catalyst is a highly dispersed metallic phase, with between 0.3 and 0.6% wt. platinum, supported on an acidic oxide like γ-Al_2O_3, and promoted using small amounts of chlorine (close to 1%). In these catalysts the two components are believed to perform the major reactions independently: while platinum possesses high activity for hydrogenation and dehydrogenation processes, the acidic component is active for isomerization and hydrocracking [3,4]. In fact, the metal phase alone is able to perform all reactions mentioned [7]. An understanding of these systems is further complicated by the presence of strong metal-support interactions (SMSI) [8], the growth of carbonaceous deposits that poison the catalyst activity [7,9], and additional poisoning by metals, or by compounds containing oxygen, nitrogen or sulfur atoms [3]. Also, new improved catalysts include at least one second metal, like Re [10], Ir [11] or Sn [12].

Extensive research has been done on these systems, and many review articles have been published [2,4,7,13-17]. The level of understanding attained so far, however, has been limited due to the complexity of the problem. It is therefore useful to develop model systems in which components of the full process can be isolated and studied in detail. In

this respect, the present thesis is a contribution to the ongoing research in our group aimed at the use of surface science techniques in order to understand the details of the role of the metallic phase in the overall reforming process.

A large amount of work has been done on the adsorption of hydrocarbons over well characterized metallic surfaces under ultra-high vacuum (UHV) [18-23]. Unfortunately, the relationship between these chemisorbed species and the actual intermediates in catalytic reactions under atmospheric conditions is far from clear. In order to solve this "pressure gap" problem, an environmental cell was developed in our laboratory almost ten years ago [24], a device that allows the transfer of catalytic samples between UHV and atmospheric environments without exposing them to air. In this way, high pressure reactions can be performed over well characterized surfaces, and changes in the catalytic surface before and after exposures to high pressure gases can be correlated to kinetic parameters of the systems studied.

Previous model catalytic studies at low (10^{-7} Torr) and high (1 atm) reactant pressures by Blakely [25], Herz [26], Smith [27], Gillespie [28], Davis [29] and Sachtler [30] revealed the special importance of surface structure, chemical additives, and the carbonaceous deposits forming during gas exposures in controlling the activity and selectivity of platinum in several important types of catalyzed hydrocarbon reactions. Reaction rates over platinum single crystals were proven to be comparable to those over practical catalysts [31,32]. The pre-

sence of defects on the surfaces increased the activity for some reactions, like cyclohexane dehydrogenation and n-heptane aromatization [26, 28]. This effect was enhanced if, together with the introduction of kink sites, strongly bonded oxygen was added [27,28]. The crystallographic orientation was also important: (100) terraces were more active for light alkane convertion, but less active for aromatization reactions, as compared with the closed packed (111) surfaces (see, for instance, fig. 1.2) [29]. A methodology for characterizing the carbonaceous residues formed over the metallic surfaces during high pressure reactions was developed [29]. They grow in three dimensional islands and cover most of the surface, but leave small patches of bare platinum, those being the responsibles for most of the reforming activity.

The thesis research presented here was specifically designed to provide a detailed understanding of the surface intermediates involved in the mechanism for most hydrocarbon conversion reactions. The approach was to try to link the profuse amount of information on catalytic activity and selectivity of high surface area industrial materials with the chemisorption data reported in the literature over well characterized surfaces and under UHV conditions. The starting point chosen for this purpose was one of the simplest system, the hydrogenation of ethylene. In chapter three the chemisorption of ethylene at room temperature to form ethylidyne [33] is considered regarding its relevance for high pressure processes. By using high resolution electron energy loss spectroscopy (HREELS) and a radiotracer technique, it was concluded that ethylidyne, once formed, was stable towards room temperature rehydrogenation

with 1 atm. H_2. Deuterium exchange in the methyl group does occur, but it is a relativly slow process, with turnover frequencies on the order of 10^{-4}-10^{-5} exchanges/molec.•sec. Ethylidyne saturated surfaces were observed after high pressure ethylene hydrogenation experiments over Pt (111), as seen by using low energy electron diffraction (LEED), thermal desorption spectroscopy (TDS), and HREELS. The high activity of the surface for this reaction, where the turnover frequencies were on the order of 1-100 molec./Pt atom•sec., suggests that the hydrogenation takes place on a second layer, on top of an ethylidyne covered metallic surface. Ethane-deuterium exchange reactions were also studied, and the presence of ethylidyne after high pressure studies was inferred as well. In this case, however, the higher reaction temperatures imply that rehydrogenation of ethylidyne has now comparable rates to those for the exchange, so ethylidyne is proposed to be a direct intermediate in the mechanism that explains the formation of fully deuterated ethane, one of the two major products of the reaction.

Rearrangement reactions of heavier alkanes were also studied. Isobutane, neopentane, n-hexane and methylcyclopentane conversion over six different platinum single crystal surfaces were investigated in order to characterize the active sites responsible for the possible reaction mechanisms. The light alkanes isobutane and neopentane, that isomerize through the so called bond-shift mechanism [15-17], convert faster over low coordination platinum atoms. This was concluded from both an increase in reaction rates over stepped and kinked surfaces, and by CO titration of the active sites after reactions. n-Hexane skeletal rearrangement, by contrast, was concluded to go mainly through a five

membered ring intermediate, because of the similar behavior with methylcyclopentane hydrogenolysis reactions. This cyclic mechanism was proven to occur over flat close packed (111) terraces: both n-hexane and methylcyclopentane conversions were structure insensitive over the surfaces studied, and the carbonaceous deposits formed during reactions blocked all defect sites within few minutes of starting the reactions. It was also concluded that n-hexane aromatization does not go through the formation of a C_5-cycle intermediate.

Additionally, in chapter five some work on the effect of additives in the performance of the metal catalyst is reported. Potassium was a non-selective poison for all n-hexane reactions. The inhibition of the dehydrogenation of adsorbed hydrocarbon species due to the electronic modification of the surface induced by the alkali explained the changes in reactivity reported. Some preliminary work on the role of rhenium in reforming catalysts is also presented. Chemisorption of small molecules over rhenium films was studied in order to compare with the behavior of platinum, and to try to develop a chemical method of characterizing the surfaces resulting from alloying rhenium with platinum. The final oxidation state of Re in Pt-Re systems was studied after exposures to oxidizing and reducing environments using X-ray photoelectron spectroscopy (XPS). It was found that only low oxidation states of rhenium ($<+4$) could exist after standard pretreatment of reforming catalysts prepared by depositing rhenium over platinum, and full reduction to the metallic state was achieved if both metals were alloyed. Finally, some reaction rates were measured over Re and Pt-Re surfaces, but no unique results were obtained.

Table 1.1

Gibbs free energy for typical reforming reactions.

	T(K)	ΔG^{o}(Kcal/mole)
Hydrogenation		
$CH_2=CH_2 + H_2 \rightarrow CH_3CH_3$	300	-24.10
benzene + $3H_2$ → cyclohexane	300	-23.25
Dehydrogenation		
iso-C_4H_{10} → iso-$C_4H_8 + H_2$	500	12.39
cyclohexane → benzene + $3H_2$	500	5.17
Isomerization		
n-C_4H_{10} → iso-C_4H_{10}	500	-0.16
Dehydrocyclization		
n-C_6H_{14} → methylcyclopentane + H_2	500	4.69
Aromatization		
n-C_6H_{14} → benzene + $4H_2$	500	10.85
Hydrogenolysis		
$CH_3CH_3 + H_2 \rightarrow 2CH_4$	500	-16.86

FIGURE CAPTIONS

Fig. 1.1. Octane number for various low molecular weight hydrocarbons showing the effect of changes in the number of carbon atoms.

Fig. 1.2. Reaction rates for n-hexane and n-heptane aromatization catalyzed at 573 K and atmospheric pressures over the two flat (111) and (100) platinum single crystal faces.

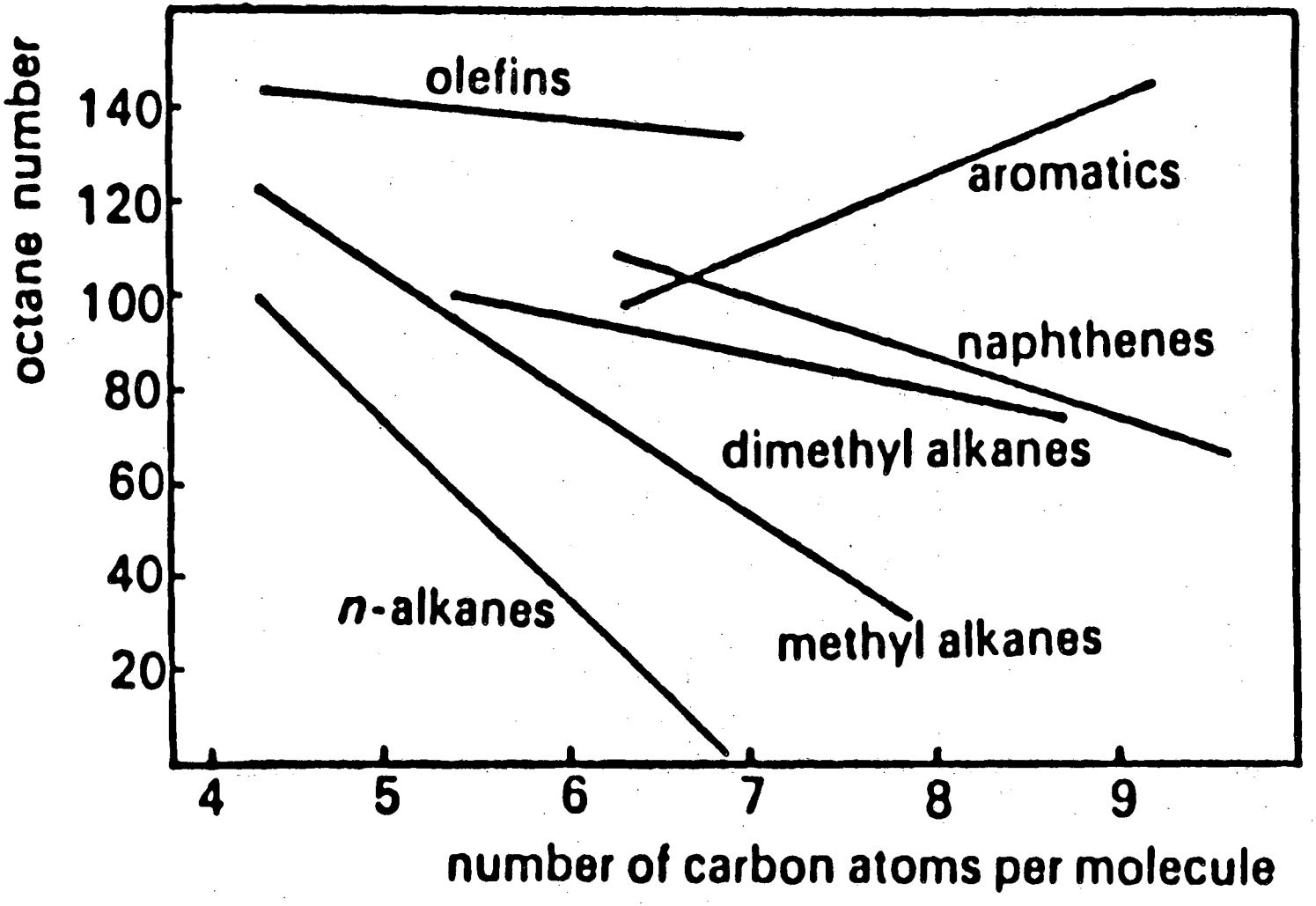

XBL 846-2627

fig. 1.1

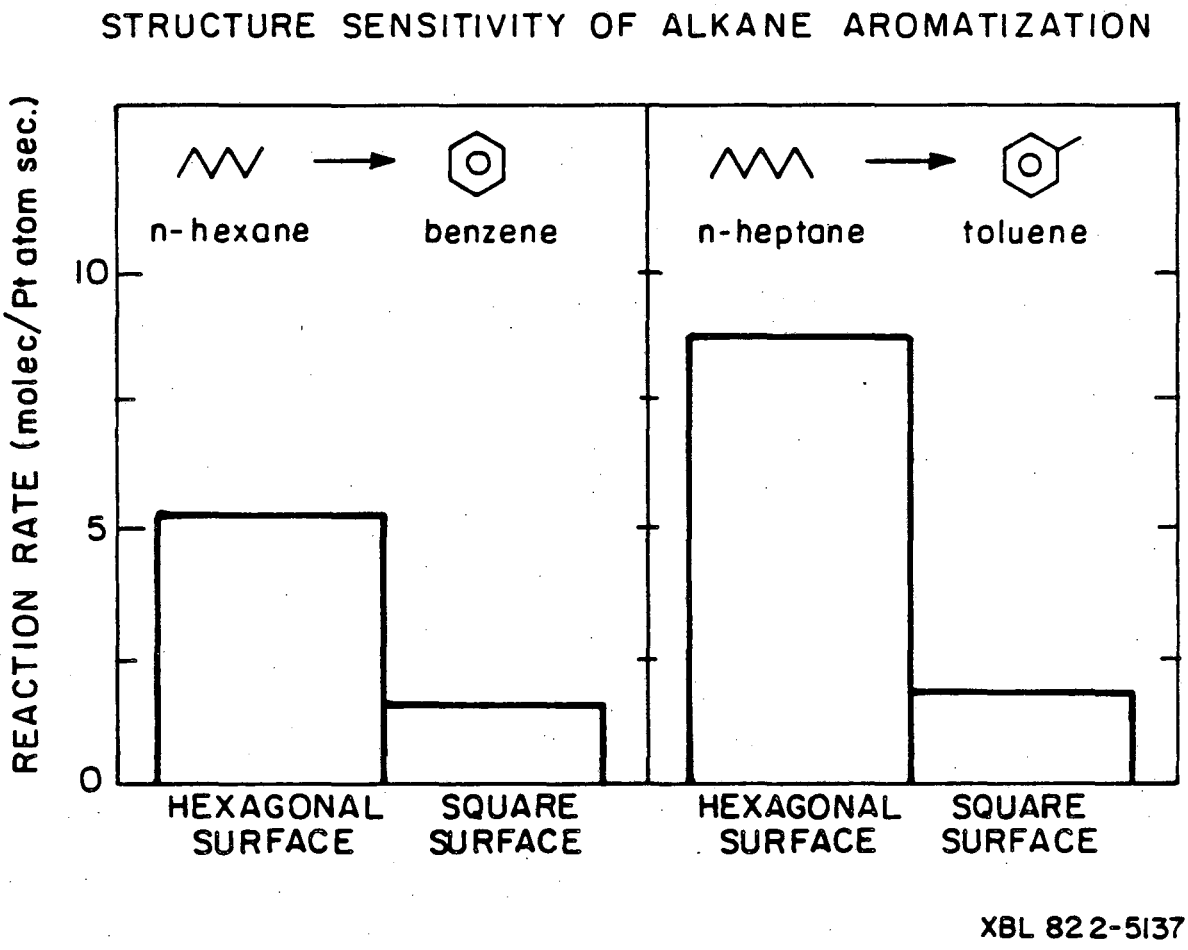
STRUCTURE SENSITIVITY OF ALKANE AROMATIZATION
REACTION RATE (molec/Pt atom sec.)
10
5
0
n-hexane
benzene
n-heptane
toluene
HEXAGONAL SURFACE
SQUARE SURFACE
HEXAGONAL SURFACE
SQUARE SURFACE
XBL 822-5137

fig. 1.2

References.

1) G.A. Somorjai, "Chemistry in Two Dimensions: Surfaces", Cornell University Press, Ithaca 1981.

2) J.H. Sinfelt, in "Catalysis: Science and Technology", Vol. 1, J.R. Anderson and M. Boudart, eds., Springer-Verlag, Berlin 1981.

3) T. Edmonds, in "Catalysis and Chemical Processes", R. Pearce and W.R. Patterson, eds., Leonard Hill, London 1981.

4) B.C. Gates, J.R. Katzer and G.C.A. Schuit, "Chemistry of Catalytic Processes", McGraw-Hill, New York 1979.

5) D.R. Stull, E.F. Wastrum, Jr., and G.C. Sinke, "The Chemical Thermodynamics of Organic Compounds", John Wiley & Sons, New York 1969.

6) V. Haensel, U.S. Patent 2,479,109 (1949).

7) S.M. Davis and G.A. Somorjai, in "The Chemical Physics of Solid Surfaces and Heterogeneous Catalysis", Vol. 4, D.A. King and D.P. Woodruff, eds., Elsevier, Amsterdam 1982.

8) R.T.K. Baker, E.B. Prestridge and R.L. Garten, J. Catal., 56, 304 (1979).

9) See, for instance, "Catalyst Deactivation", B. Delmon and G.F. Froment, eds., Elsevier, Amsterdam 1980.

10) H.E. Kluksdahl, U.S. Patent 3,415,737 (1968).

11) J.H. Sinfelt, U.S. Patent 3,953,368 (1976).

12) F.M. Dautzenberg, German Patent 2,121,765 (1971).

13) G.C. Bond and P.B. Wells, in "Advances in Catalysis", Vol. 15, D.D. Eley, H. Pines and P.B. Weisz, eds., Academic Press, New York 1964, pp. 91-226.

14) J.R. Anderson and B.G. Baker, in "Chemisorption and Reactions on Metallic Films", J.R. Anderson, ed., Academic Press, London 1971, pp. 1-62.

15) J.R. Anderson, in "Advances in Catalysis", Vol. 23, D.D. Eley, H. Pines and P.B. Weisz, eds., Academic Press, New York 1973, pp. 1-90.

16) J.K.A. Clarke and J.J. Rooney, in "Advances in Catalysis", Vol. 25, D.D. Eley, H. Pines and P.B. Weisz, eds., Academic Press, New York 1976, pp. 125-183.

17) F.G. Gault, in "Advances in Catalysis", Vol. 30, D.D. Eley, H. Pines and P.B. Weisz, eds., Academic Press, New York 1981, pp. 1-95.

18) J.J. McCarroll, Surf. Sci., 53, 297 (1975).

19) H. Ibach, H. Hopster and B. Sexton, Appl. Surf. Sci., 1, 1 (1977).

20) S.J. Thomson, in "Catalysis", Vol. 1, C. Kemball, ed., The Chemical Society Burlington House, London 1977, pp. 1-36.

21) S.J. Thomson, in "Catalysis", Vol. 3, C. Kemball and D.A. Dowden, eds., The Chemical Society Burlington House, London 1980, pp. 1-80.

22) R.W. Joyner, in "Catalysis", Vol. 5, G.C. Bond and G. Webb, eds., The Royal Society of Chemistry Burlington House, London 1982, pp. 1-47.

23) R.J. Koestner, M.A. Van Hove and G.A. Somorjai, J. Phys. Chem., 87, 203 (1983).

24) D.W. Blakely, E. Kozak, B.A. Sexton and G.A. Somorjai, J. Vac. Sci. Technol., 13, 1901 (1976).

25) D.W. Blakely, Ph.D. Thesis, University of California, Berkeley 1976.

26) R. Herz, Ph.D. Thesis, University of California, Berkeley 1977.

27) C.E. Smith, Ph.D. Thesis, University of California, Berkeley 1978.

28) W.D. Gillespie, Ph.D. Thesis, University of California, Berkeley 1980.

29) S.M. Davis, Ph.D. Thesis, University of California, Berkeley 1981.

30) J.W.A. Sachtler, Ph.D. Thesis, College Van Dekanem 1982.

31) D.R. Kahn, E.E. Petersen and G.A. Somorjai, J. Catal., 34, 294 (1974).

32) S.M. Davis and G.A. Somorjai, J. Catal., 64, 60 (1980).

33) L.L. Kesmodel, L.H. Dubois and G.A. Somorjai, Chem. Phys. Lett., 56, 267 (1978).

CHAPTER TWO: EXPERIMENTAL METHODS

2.1. Apparatus.

Most of the research described in this thesis was carried out in a low pressure-high pressure system designed for combined surface analysis and catalytic studies using small area samples [1,2]. A schematic diagram and a photograph of this apparatus are shown in figs. 2.1 and 2.2. Using this system, the metallic samples can be prepared and characterized under ultra-high vacuum (UHV) conditions, and then isolated from the main chamber by the use of an enviromental cell. The cell connects to a recirculation loop that can be used as a batch reactor for high pressure catalytic experiments. Subsequently to reaction, the cell can be evacuated and opened, in order to reexpose the catalyst to UHV for further surface characterization.

The main vacuum system consisted of a home made stainless steel belljar, about 50 liters in volume, that was pumped by both a high speed oil diffusion pump (Varian VHS-6) equipped with a liquid nitrogen cold trap (Varian 362-6), and a water cooled titanium sublimation pump (the filament holder was Ultex 214-0400, mounted in a home made water cooled jacket). A base pressure of $6\text{-}8\times10^{-10}$ torr was achieved after 24 hrs. bake out at 425 K, but during periods of continual experimentation it rose to $1\text{-}3\times10^{-9}$ torr. The residual gases were mostly H_2O, CO, H_2, and air (from a virtual leak in the sample manipulator). Pumping speeds, S, were estimated for H_2 and CO, by leaking these gases into the chamber to a given pressure and following the pressure drop as a function of time when the leak was stopped [3] (fig. 2.3). Values of about 850 l/s and 450 l/s

at $1x10^{-5}$ torr pressure were obtained for H_2 and CO respectively.

This chamber was equipped with the following:

1) an ion sputtering gun (PHI 4-161) for crystal cleaning;
2) a quadrupole mass spectrometer (UTI-100C) for residual gas analysis, thermal desorption studies, and analysis of products in deuterium exchange reactions;
3) a nude ion gauge (Varian 971-5008) for pressure measurements;
4) a glancing incident CRT electron gun for Auger excitations;
5) a four grid electron optics energy analyzer (Varian 981-0127) for low energy electron diffraction and Auger electron spectroscopy, with an off-axis electron gun (Varian 981-2125) in the middle for the LEED experiments;
6) Three variable leak valves (Varian 951-5106), one of them equipped with a 0.125" O.D. stainless steel doser pointing to the metallic sample, for introducing gases at low pressures;
7) depending on the experiments, a 6" flange could be used to support a surface barrier detector for ^{14}C-radiotracer analysis, a planar magnetron sputtering gun for rhenium deposition, or a SAES getter potassium source. Each of these additions will be described in their respective sections.

The single crystal or foil samples were mounted on a rotable manipulator as shown in fig. 2.1. As discussed by Gillespie [2,4], this mounting scheme permits the sample to be heated to above 1300 K without significantly heating any other part of the chamber, thus avoiding any

extraneous catalytic activity. The mounting was checked in air for uniformity of heating before inserting it into the chamber. A chromel-alumel thermocouple pair (0.005" diameter) was spotwelded to a side or to the edge of the sample. The accuracy of the temperature readings was checked first under UHV by measuring the minimum temperature at which the sample starts to glow. This temperature was 785±10 K when measured in complete darkness. A second check was developed for the thermocouple readings under high pressure gases, consisting in a comparison of the experimental and reported equilibrium constant between isobutane and isobutene. Both techniques are described in great detail elsewhere [5,6].

When closed, the enviromental cell could be connected to an external loop that could act as a reactor. A diagram of this loop and the manifold for gas handling is shown in fig. 2.4. A metal bellows (Metal Bellows Corp., MB-21) or a micropump (Micropump 120-000-100) provided continuous gas circulation, and two Wallace-Tiernan gauges (61A-1A-0500 and 61A-1A-0015) were used for measuring the pressure of reactant gases. The valve V_{15} was a right angle high conductance valve (Varian 951-5014, conductance of 5 l/s), and the line from it to the main vacuum manifold was made out of 0.75" tubing, so the isolation cell could be evacuated as rapidly as possible after the reaction studies. The pumping was carried out initially using a mechanical pump, followed by the use of one or two liquid nitrogen cooled sorption pumps.

Gas samples from the loop were taken periodically by the use of

an eight port sampling valve. Initially a Carle 8793 valve eqipped with two identical 0.5 ml sampling loops made out of 0.0625" O.D. stainless steel tubing was used. This reduced the circulation speed of the gases considerably, so a bypass valve (V_{12}) was installed. This way the flow rate could be increased from 50 ml/min. to 500 ml/min. Subsequently this eight port valve was replaced by a Valco one (Valco 2-2979) with sampling loops made out of 0.125" O.D. tubing, partially solving the conductance problem. In any case, total mixing of the reactant gases was checked by leaking them to the main chamber and analyzing them with the mass spectrometer. This way it could be ensured that complete mixing occurred in less than 1-2 minutes. Since the total volume of the reactor was about 200 ml (measured by expanding a known volume of gas and recording the presure drop), the gas flow was always greater than 100 ml/min.

The gas chromatograph (Hewlett-Packard 5830A) was equipped with a microprocessor which was used to determine peak areas. The signal was calibrated using a primary standard mixture consisting of 100 ppm (mole basis) of methane in nitrogen (Matheson). All other hydrocarbon products were calibrated against the methane value by using the published data for sensitivity factors of a flame ionization detector [7]. Various chromatographic columns were used for the different experiments. Two 80/100 Poropack N columns (6' and 12' long, 0.125" O.D.) were used to separate ethylene from ethane. Heavier hydrocarbons were separated by using 0.19% picric acid on 80/100 Carbopack columns (4' and 8' long, 0.125" O.D.). Benzene could not be separated from n-hexane by using the previous column, so either a 10% squalene on 60/80 Chromosorb W or a

5% TCEP on 60/80 Chromosorb G column were used for this purpose. To avoid running the same reaction twice in order to obtain separation of all products, a system was design to alternate between two columns in the gas chromatograph. The design, shown schematically in fig. 2.5, was driven by the microprocessor in a way that gas samples were analyzed by each column alternately.

The X-ray photoelectron and high resolution electron energy loss spectroscopies experiments were performed in two different apparatuses similar to the one just described. The XPS system was equipped with a Mg X-ray source (PHI 04-151) and a double pass cylindrical mirror analyzer for electron energy analysis (PHI 15-255G), both mounted on hydrolically driven bellows for optimizing the electron collection geometry. The HREELS apparatus was a two-tier chamber, with the HREELS spectrometer located in the lower level (homemade). The schematics of both systems are shown in figs. 2.6 and 2.7; they have been described in detail elsewhere [8-10].

FIGURE CAPTIONS

Fig 2.1. Schematic diagram of the ultra-high vacuum-high pressure apparatus used for combined surface analysis and catalytic studies.

Fig 2.2. Photograph of the apparatus shown schematically in fig. 2.1.

Fig 2.3. Pressure drop as a function of time for H_2 and CO, as measured with an ion gauge inside the UHV chamber. Characteristic time constants for pumping are estimated from the slope of these plots.

Fig 2.4. Schematic diagram of the microbatch reactor and external gas handling system. The dashed line represents the actual gas recirculation loop.

Fig. 2.5. Diagram of the sampling valves in the gas chromatograph, showing the sequence for taking two samples through two different separation columns.

Fig. 2.6. Schematic diagram of the apparatus used for X-ray photoelectron experiments.

Fig. 2.7. Schematic diagram of the apparatus used for high resolution electron energy loss spectroscopy.

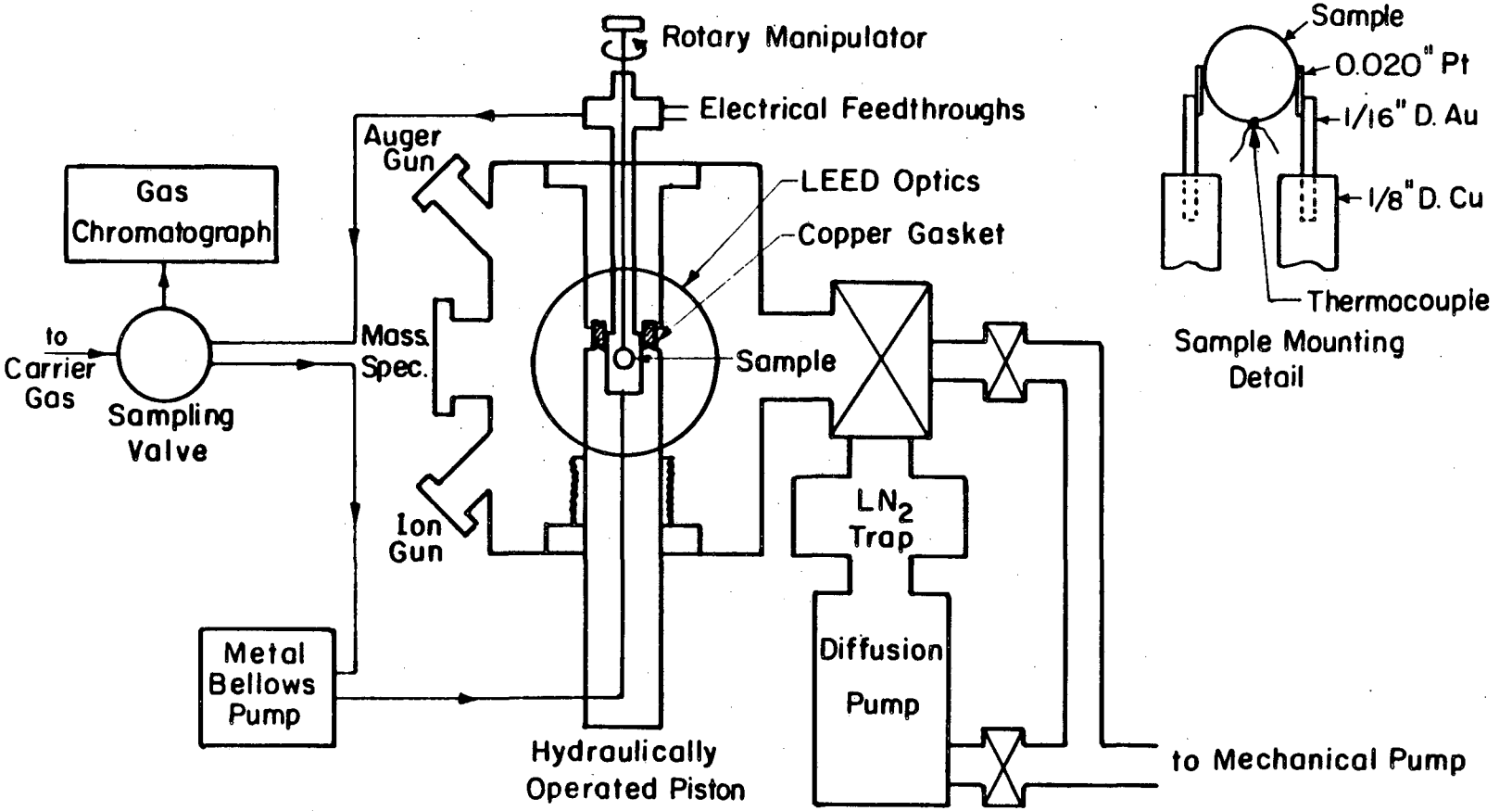

XBL 805-5117

fig. 2.1

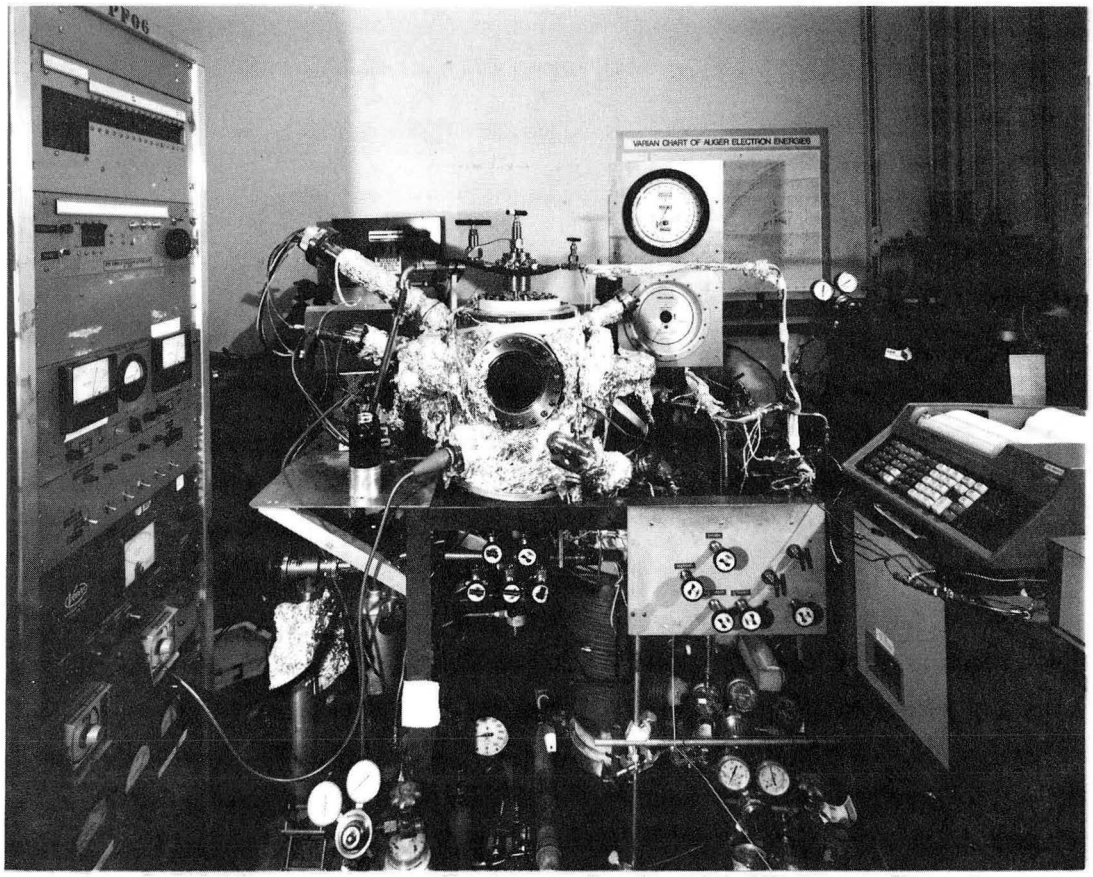

CBB 819-9188

Fig. 2.2

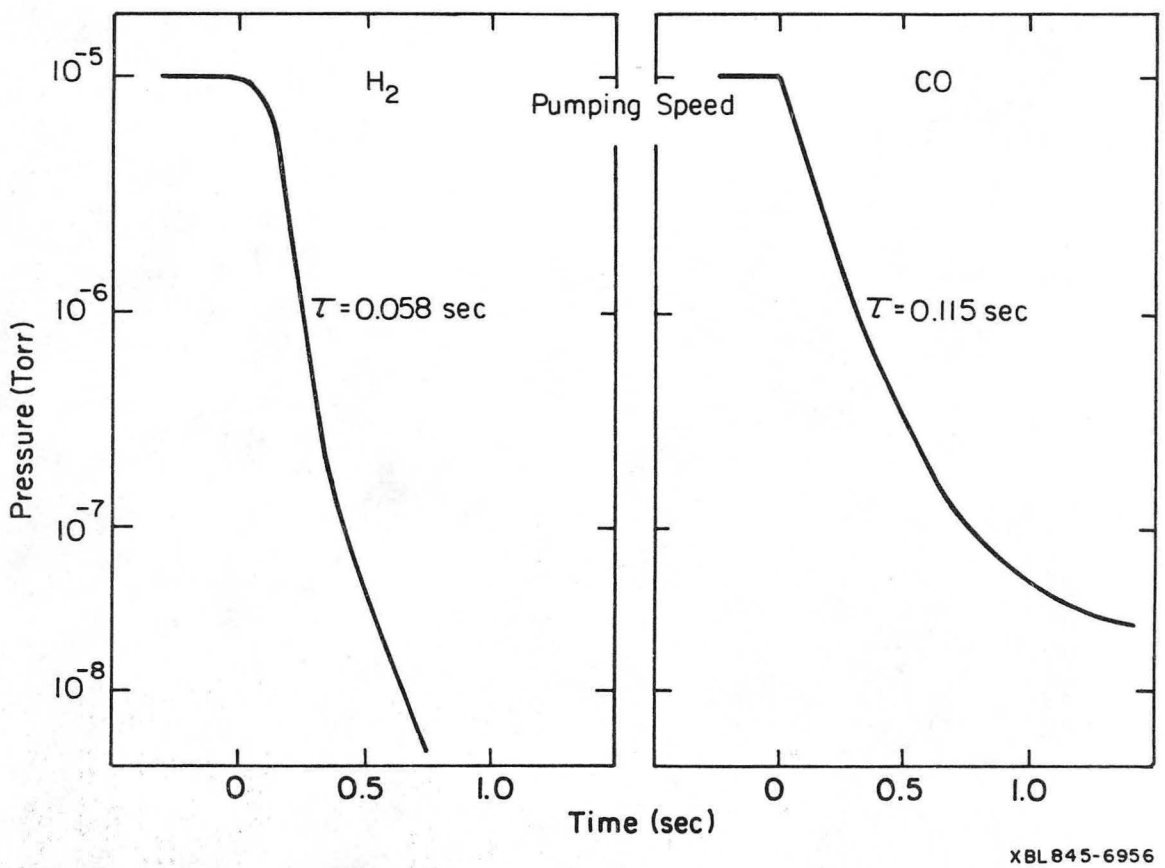
10^{-5}
10^{-6}
10^{-7}
10^{-8}
Pressure (Torr)
H_2
Pumping Speed
CO
τ = 0.058 sec
τ = 0.115 sec
0
0.5
1.0
0
0.5
1.0
Time (sec)
XBL845-6956

fig. 2.3

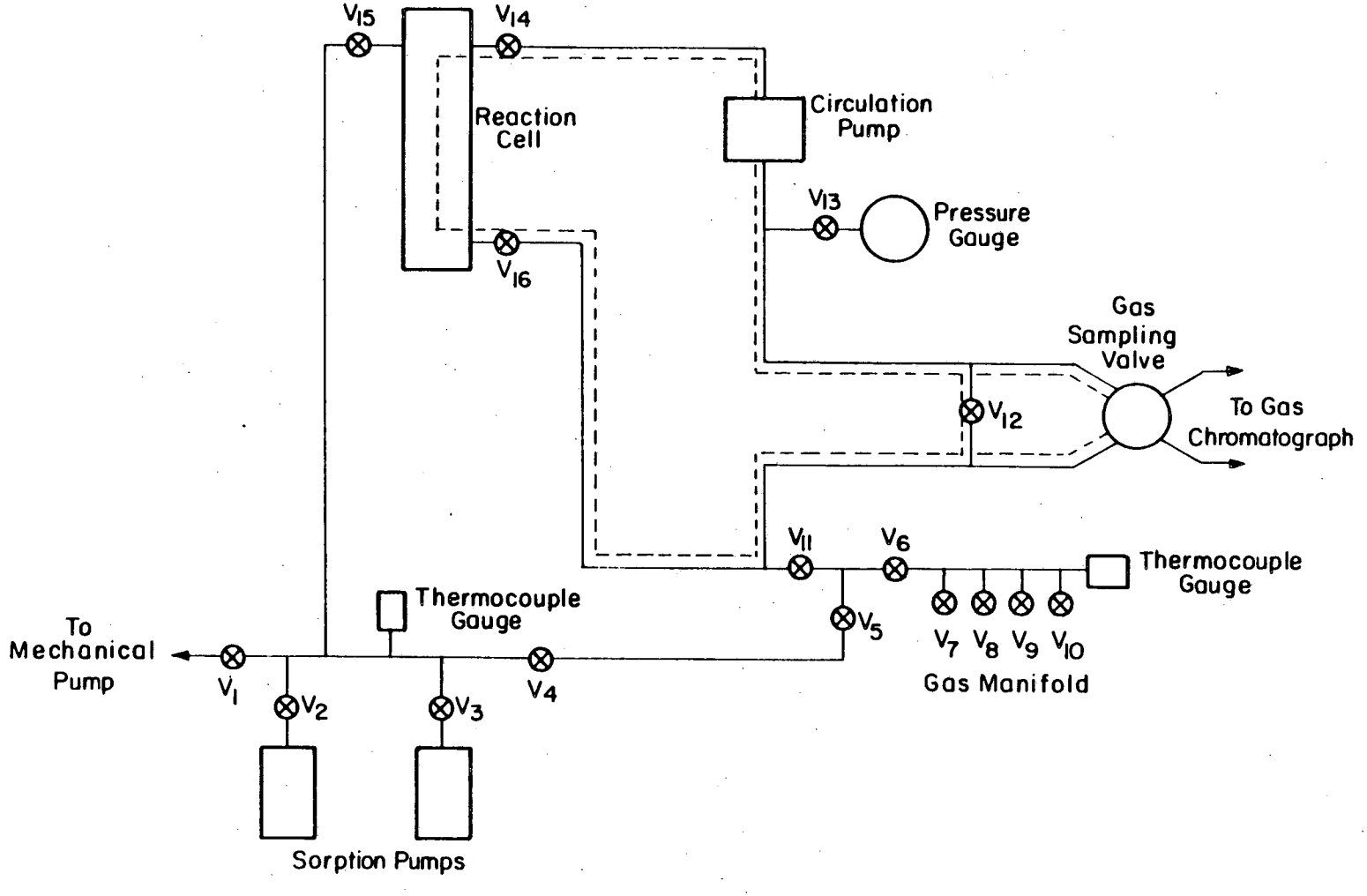

XBL 807-5523

fig. 2.4

Sequence for Gas Sampling in the Gas Chromatograph

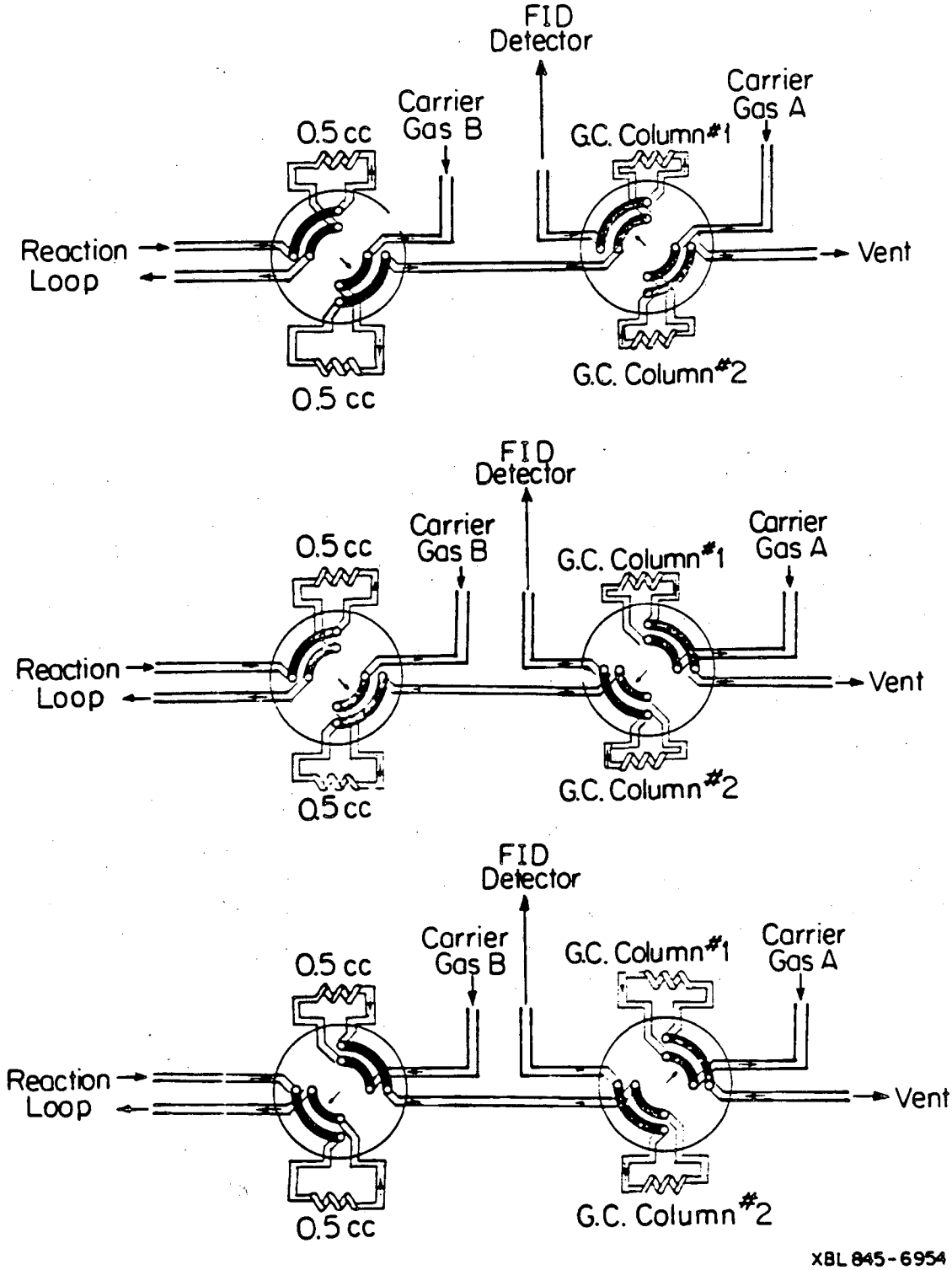

fig. 2.5

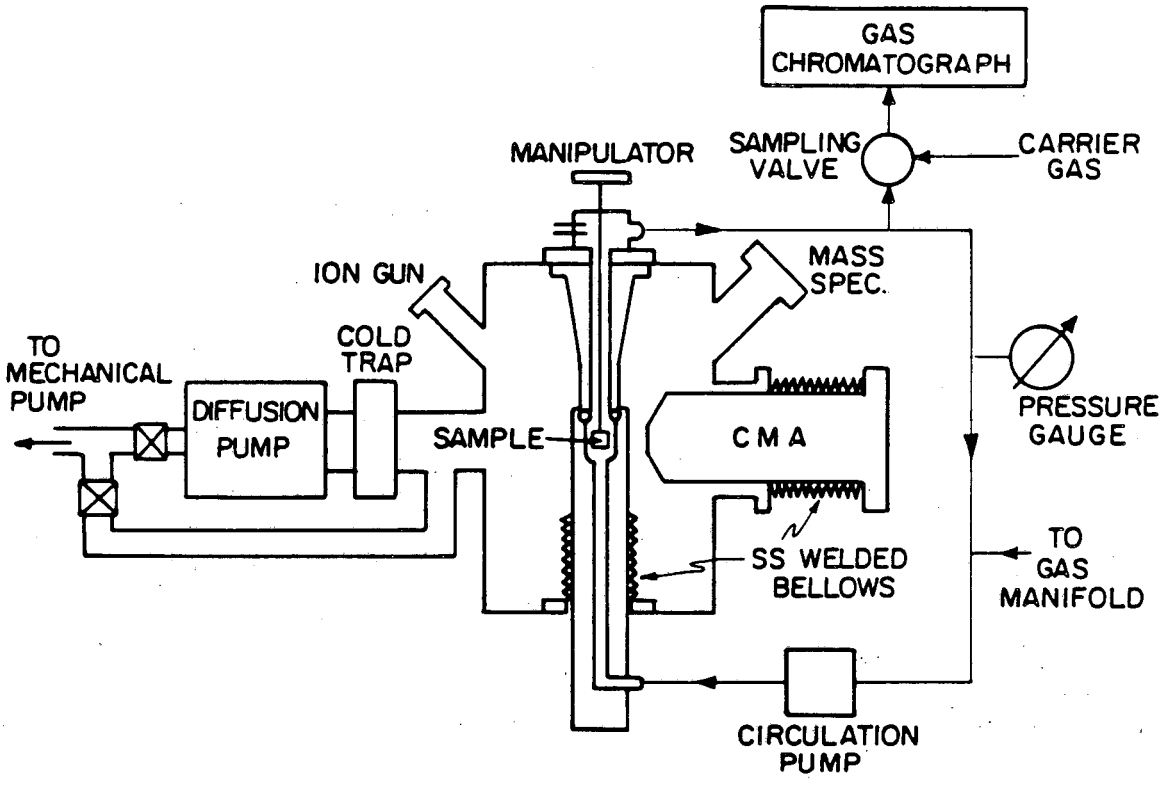
GAS
CHROMATOGRAPH
MANIPULATOR
SAMPLING
VALVE
CARRIER
GAS
ION GUN
MASS
SPEC.
TO
MECHANICAL
PUMP
COLD
TRAP
DIFFUSION
PUMP
SAMPLE
CMA
PRESSURE
GAUGE
SS WELDED
BELLOWS
TO
GAS
MANIFOLD
CIRCULATION
PUMP
(a)
SAMPLE
CMA
(b)
XBL814-5584

fig. 2.6

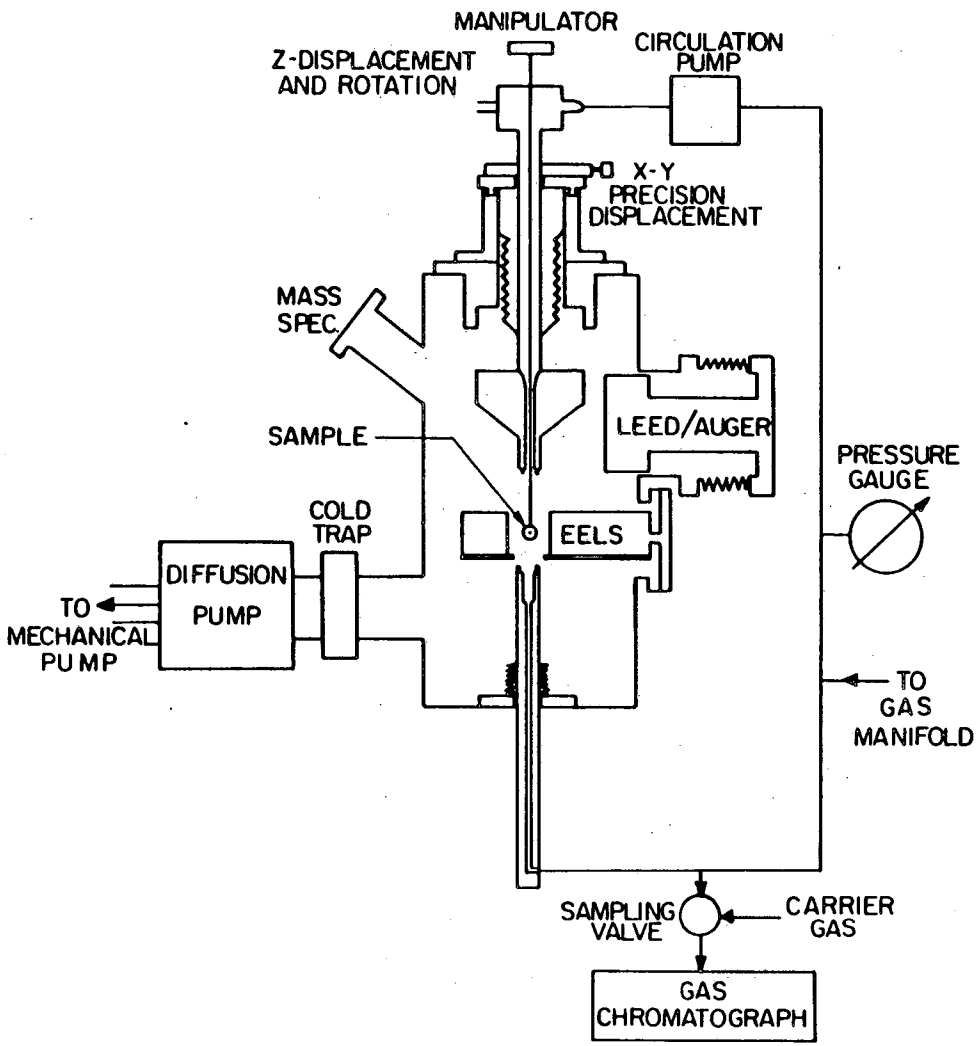

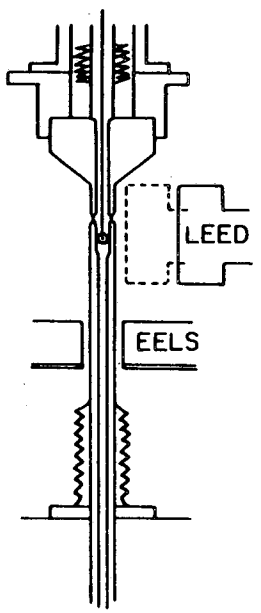

XBL 8111-6950

fig. 2.7

2.2 Surface analysis methods.

A combination of surface science techniques have been used through out this thesis to characterize the catalytic samples before and after high or low pressure treatment. Since our main concern is to understand what happens in the solid-gas interphase, spectroscopic techniques that sample only the topmost layers of the solid are needed. Slow electrons are ideally suited for this purpose, because their penetration through solids is of only few layers. Fig. 2.8 shows the dependence of the electrons inelastic mean free path as a function of their kinetic energy. A broad minimun of less than 10 occurs in the 10-400 eV energy range. This is the basis for most of the techniques used in this work: Auger electron spectroscopy (AES), low energy electron diffraction (LEED), X-ray photoelectron spectroscopy (XPS), and high resolution electron energy loss spectroscopy (HREELS).

When a collimated monoenergetic electron beam hits a solid surface, several processes take place. A plot of the number of scattered electrons, N(E), versus electron energy is shown in fig. 2.9 for such an experiment. At low energies a strong and broad peak is obtained, due to the emission of secondary electrons created from a cascade process involving inelastic collisions between primary electrons and electrons in the solid. At intermediate energies, Auger electrons are emitted. These can be detected over the secondary electron background by recording a derivative spectrum (fig 2.9, insert a). At the other extreme of energies, the elastically scattered electrons may be used to obtain structural information since they may diffract from surface atoms. Diffraction patterns obtained

constitute the basis for LEED (fig 2.9, insert c). Also, energy losses due to vibrational or electronic transitions, can be detected. An example of this is high resolution electron energy loss spectroscopy (HREEL). A typical spectrum, in this case for ethylidyne on Rh(111), is shown in fig. 2.9.

Besides electron based spectroscopic techniques, thermal desorption spectroscopy (TDS) and ^{14}C-radiotracer experiments were used extensively in the work here reported. Since most of the above techniques are well developed and have been reviewed many times, only a brief description of each will be included here.

2.2.1. Auger electron spectroscopy.

Auger electron spectroscopy (AES) was used throughout this research to monitor the elemental composition of the metallic samples before and after chemisorption and catalytic studies. It was also used to estimate absolute coverages of adsorbants. In principle, information about the electronic environment of the atoms can be obtained from the shape of the Auger peaks; this property was used here only qualitatively to differentiate between carbidic and graphitic carbon [11] (fig. 2.10).

Auger transitions are autoionization processes that arise from electrostatic interaction between two electrons in an atom after the creation of a core hole. These excited ionic states are formed when an inner shell electron is extracted by photoionization, ion impact or, as the case of these experiments, electron scattering. Once created, the

ions rapidly decay by either X-ray fluorescence or Auger electron emission. These processes are shown schematically in fig. 2.11. In the Auger process an outer shell electron relaxes to the inner shell vacancy, and the released energy is transferred to a second electron that is consequently ejected. This Auger electron will have a characteristic kinetic energy, that can be calculated from the expression [12]

$$E_{ijk}(z) = E_i(z) - E_j(z) - E_k(z-\Delta) - e\cdot\Phi_{sp} \qquad (2.1)$$

where the subscripts i, j and k represent the electronic energy levels involved in the process, z is the atomic number of the atom, Δ is the effective charge after the initial ionization, and Φ_{sp} is the work function of the spectrometer referred to vacuum. $E_k(z-\Delta)$ also includes a correction due to electronic relaxation of the environment surrounding the ionized atom. It is this characteristic kinetic energy of the Auger electron that permits the identification of the chemical composition of surfaces. As an example, Auger electron spectra of clean and contaminated platinum surfaces are shown in fig. 2.12.

The quantitative yield of Auger electrons depends on the efficiency of the three steps involved in the overall process [13]:

1) Excitation of the atom, in our case by the primary and backscattered electron current $I_o(1+r)$;

2) Auger electron emission yield as opposed to X-ray fluorescence (assuming isotropic distribution); and

3) electron transport to the surface. For an uniform depth concentration of N_A, the final Auger yield I_A becomes:

$$I_A = C \cdot I_O (1+r) \cdot \sigma_i \cdot P_{ijk} \cdot \lambda \cdot N_A \qquad (2.2)$$

where σ_i is the ionization cross section for the inner shell i, P_{ijk} is the Auger emission probability, and λ is the attenuation length of the electron. C is a proportionality constant that includes the detector efficiency. Although some of these parameters (e.g., σ_i, P_{ijk}) are atomic constants which are easy to determine, others (r and λ) are more difficult to obtain. Thus, for quantitative measurements, a calibration against another independent technique is preferred whenever possible. Some of the methods used for this purpose include the use of LEED, radioactive tracers, microbalances, evaporation of films of known thickness, and ellipsometry. Since the spectra is generally taken in the derivative mode, the calibration is usually made using the peak to peak height rather than the area under the N(E) trace, but, if a Gaussian peak shape is assumed, both quantities are proportional [14].

Another calibration method for AES is based on the shape of the plot of Auger signal against exposure of the substance under study (the so called uptake curves). Several useful models have been developed to predict the change in Auger peak intensities depending upon the nature of the adsorbate film growth mechanism. Examples are shown schematically in fig. 2.13. If it is assumed that the adsorbate attenuates the emitted electrons uniformly, the Auger emission current for substrate and adsorbate can be written as:

$$I_s = I_s^o \cdot \exp(-Z/\lambda) \qquad (2.3)$$

and

$$I_a = I_a^o[1 - \exp(-Z/\lambda)] \qquad (2.4)$$

where Z is the surface layer thickness and the ^{o} superscript refers to infinite thickness. An alternative model, proposed by Gallon [15], uses a layer by layer growth mechanism (the Frank-Van der Merwe model), leading to the following expression:

$$I_a^n = I_a^o[1 - (1 - I_a^1/I_a^o)^n] \qquad (2.5)$$

in which n represents the n^{th} layer. In this case, clear breaks are observed after the completion of each layer in the Auger signal vs. deposition time curves, facilitating the calibration. Coverages of deposited metals are generally determined this way.

A diagram of the experimental set up for AES in this thesis is shown in fig. 2.14. The sample is irradiated using a glancing incident electron beam (about 70^o from the surface normal) of kinetic energies of around 2 KeV. The Auger electrons are detected using a four grid retarding field analyzer, in which the first and fourth grids are grounded. A retarding field V_r, along with a small superimposed ac voltage ($V_m \cdot \sin\omega t$), is applied to the second and third grids in order to obtain the derivative spectrum. The electron current is collected on the screen by applying a 300-1000 V positive voltage. This current can be expanded as a Taylor series:

$$I(V_r+V_m\cdot\sin\omega t) = I(V_r) + I'(V_r)\cdot V_m\cdot\sin\omega t + [I''(V_r)/2!]V_m^2\cdot\sin^2\omega t + \ldots. \qquad (2.6)$$

and since

$$I(V_r) \propto \int_{E=eV_r}^{\infty} N(E')dE' \qquad \text{and}$$
$$\sin^2\omega t = [1 - \cos 2\omega t]/2 \qquad (2.7)$$

then

$$dN(E)/dE \propto I''(V_r) \qquad (2.8)$$

therefore, the signal at twice the frecuency of the original modulation is proportional to dN(E)/dE. This is recorded as a function of the retarding voltage V_r using a lock-in amplifier (PAR-HR-8) [12].

2.2.2. Low energy electron diffraction.

Low energy electron diffraction (LEED) yields information about the geometry of the topmost layers of solids. The technique is based on the wave nature of electrons. According to the de Broglie relationship, electrons have associated a wavelength λ with them, given by the expression:

$$\lambda = h/(m\cdot v) = \sqrt{150/V} \qquad (\lambda \text{ in Angstroms}) \qquad (2.9)$$

h being Planck's constant, m the rest mass of an electron, v its velocity, and eV its kinetic energy. Hence, when an electron beam impinges on a

crystal surface, a fraction of these electrons are elastically scattered by the atomic core potentials which may constructively or destructively interfere depending on the atomic positions, analogous to X-ray diffraction experiments [12]. Constructive scattering will occur at certain angles ϕ, which can be calculated using Bragg's equation. For normal electron beam incidence:

$$\sin\phi = (n \cdot \lambda)/d_{h,k} \approx (n/d_{h,k})\sqrt{150/V} \qquad (2.10)$$

where n is an integer denoting the order of diffraction and $d_{h,k}$ is the distance between parallel rows of scatterers in the [h,k] direction. Information about the shape and dimensions of the unit cell of adsorbates may thus easily be determined and compared with the substrate (if periodicity is present). For instance, a (2x2) adsorbate overlayer means that the chemisorbed species order on the solid surface in such way that its unit cell has the same shape of that of the substrate, but is twice as long in both directions.

Electron scattering is not a purely two dimensional process, since the electrons can penetrate 3 or 4 layers into the solid (see fig. 2.8). This means that the change in intensity of the diffraction spots as a function of incident energy contains structural information that can, in principle, be analyzed to yield bond angles and distances. Unfortunately, since electrons interact strongly with matter, the simple kinematic theory used in x-ray structure determinations is not accurate enough in this case, and multiple scattering has to be considered, making the data analysis a difficult task [16].

Only information about the unit cell of the adsorbates was derived from LEED in this thesis. Besides the shape and dimensions of the unit cell, the degree of ordering can be inferred from the sharpness of the overlayer diffraction spots. Since the coherence width of the electron beam is 50-100 Å, disorder within this distance will cause spot broadening [17].

A schematic representation of the experiment is shown in fig 2.15. A monochromatic electron beam impinges on the surface at close to normal incidence, and the elastically scattered electrons are filtered using the retarding field analyzer (fig 2.14), and accelerated into the phosphorescent screen. The patterns can then be photographed through the UHV chamber viewport. An example of these pictures is shown in fig. 2.9c.

2.2.3. Thermal desorption spectroscopy.

Thermal desorption spectroscopy (TDS), sometimes also called thermal programmed desorption (TPD), provides information on adsorption states, populations, energetics of bonding, chemical reactions on surfaces, and adsorbate-adsorbate interactions.

In the TDS experiments the solid sample is heated in a controlled way (generally in a linear fashion) and the desorption of the different species is followed using mass spectrometry. The desorption rate F(t) from a sample of area A, is related to the partial pressure obtained using a mass spectrometer by the expression:

$$F(t) = (k \cdot S)\Delta p \qquad (2.11)$$

where k is a constant, S is the pumping speed of the system (and is assumed to be much larger than the desorption rates), and Δp is the pressure change due to the desorption. This desorption rate can also be expressed as an Arrhenius expression:

$$F(t) = \nu_n \cdot f(\theta) \cdot \exp[-E_{des}/RT] \qquad (2.12)$$

where ν is the preexponential factor, n is the desorption order, $f(\theta)$ is an adsorbate coverage dependent function, and E_{des} is the activation energy for the desorption process.

If it is assumed that the temperature varies linearly with time ($T=T_o+\beta \cdot t$), and if ν_n and E_{des} are coverage independent, Redhead has shown that [20]:

$$E_{des}/(RT_p^2) = (\nu_1/\beta)\exp[-E_{des}/RT_p] \qquad 1^{st} \text{ order} \qquad (2.13)$$

and $$E_{des}/(RT_p^2) = (\nu_2/\beta)\theta_o \exp[-E_{des}/RT_p] \qquad 2^{nd} \text{ order} \qquad (2.14)$$

where T_p is the temperature of maximum desorption, β is the heating rate, and θ_o is the initial coverage. According to this model, T_p is independent of the initial coverage for first order desorption, but it decreases with incresing θ_o for the second order process. Therefore, the molecularity of the desorption can be inferred from a T_p vs. θ_o plot. The shape of TDS peaks also contains this information. To extract values for ν_n and E_{des}, on the other hand, θ_o and β should be varied independently. Sin-

ce this is experimentally difficult, E_{des} is most often calculated by assuming a value for ν_n, either obtained from an independent experiment or by estimation ($\nu_1 \approx 10^{13}$ sec^{-1}). Alternatively, expressions have been derived by Edwards [21] and Chan et. al. [22], where E_{des} can be calculated independently of the value of ν_n by using not only T_p, but also information from the desorption peak shape. From Chan work, for a first order desorption:

$$E_{des} = k \cdot T_p [-1+(Y_{1/2}^2+5.832)^{1/2}/Y_{1/2}]$$
$$Y_{1/2} = (\Delta w_{1/2}/T_p) 1K \qquad (2.15)$$

where k is Boltzman's constant and $\Delta w_{1/2}$ is the full width at half maximum. Either a value $\nu_1 = 10^{13}$ sec^{-1} or expression (2.15) was used in this thesis.

Experimentally, the sample was heated linearly (or nearly linearly) by passing a constant current through it. Heating rates of 30-50 K/s were obtained this way. The change in partial pressures was recorded versus time or sample temperature by using a X-Y chart recorder or a PET microcomputer. Details of the computer and the software are described elsewhere [23]. Activation energies for the sequential dehydrogenation of chemisorbed hydrocarbons and carbonaceous deposits were estimated by assuming first order decomposition reactions [24]. Also, relative coverages were calculated from the area under the TDS traces, as described in the procedure section.

2.2.4. X-ray photoelectron spectroscopy.

X-ray photoelectron spectroscopy is mainly used to obtain information about oxidation states from shifts in the binding energies of core electrons. When a material is exposed to electromagnetic radiation of high enough energy, emission of electrons is observed. This phenomenon is called photoionization, photoemission, or photoelectric effect. The kinetic energy of the outcoming electron, E_{kin}, is related to the ionization energy (or binding energy, E_i) by the Einstein relationship:

$$h \cdot \nu = E_{kin} + E_i + e \cdot \phi_{sp} \qquad (2.16)$$

where $h \cdot \nu$ is the energy of the monochromatic photons, and the third term in the right hand side is a correction due to the work function of the spectrometer ϕ_{sp}. A photoelectron spectrum is obtained by measuring the outcoming electron flux, $n(E_{kin})$, as a function of E_{kin} [25,26]. Beside the peaks due to electrons comming directly from the atomic orbitals, Auger electrons produced from the decay of ionized atoms are detected as well. Other features are also present in the spectra. Since Al Kα (1486.6 eV) or, as in our case, Mg Kα (1253.6 eV) soft X-ray are used as excitation sources, satellite transitions create additional peaks in the resulting spectra, since the incident radiation is not monochromatic. For Mg, for instance, the most important extra peaks are shifted by 8.4 eV (8% of main intensity) and 10.2 eV (4.1%) towards higher energies [27]. The photoelectric process may leave the ion in an excited state few electron volts above the ground level. Then the kinetic energy of the outgoing electron is reduced by this relaxation energy of the ion. These are called shake-up lines, and they are generally

most intense for paramagnetic elements. If the additional excitation is a second stage of ionization, so that two photoelectrons emerge, the term shake-off is used. Multiplet splitting, energy loss lines, and valence lines and bands are also commonly seen in these spectra. Finally, secondary electrons are emitted from cascade effects produced by the emitted electrons.

As mentioned earlier, the main interest in using XPS is to obtain information on changes in ionization energies of core electrons due to changes in the chemical enviroment, the so-called chemical shifts. The simplest model of chemical shifts is based on the idea that the ionization energy changes are a result of changes in the electronic potential at the valence shell as electrons are drawn away from or towards that shell. Thus, more oxidized atoms would bind the remaining electrons tighter, and the ionization energies would be higher than for neutral atoms. Unfortunately, other effects make this straightforward interpretation not entirely valid. Relaxation due to the interaction of the ionizing electron with all other electrons in the same and in neighboring atoms is important. These effects generally decrease the binding energy of the photoelectron as the oxidation increases, an opposite trend to the electrostatic effect previously discussed. In any case, an estimate of oxidation states can be obtained empirically by comparing binding energies with reported values for different compounds containing the element of interest.

Quantitative information about the amount of a certain element

present on the surface can be obtained using this technique. However, the high kinetic energies of the emitted electrons (10-1000 eV) make this technique less surface sensitive than AES, since the escape depth at these energies is of the order of 10-30 Å. Auger electrons may also be detected this way, but the yield is very small, since the ionization cross section of x-rays is low.

Experimentally, x-rays are generated by bombarding a Mg target with a electron beam of about 40 mAmps and 10 KeV. The radiation is filtered with an aluminum window to avoid contamination of the sample from desorption from the magnesium anode. The solid to be analyzed is placed about 1 cm from the x-ray source, and the outgoing photoelectrons analyzed using a double pass cylindrical mirror analyzer (fig. 2.16). The electrons are retarded by a variable potential applied to the grid at the front of the detector, allowing only electrons of a determined energy to be filtered and focussed into the electron multiplier (a channeltron) by applying a potential difference between the inner and outer cylinders. Using this retarding mode, the instrumental resolution ΔE_{sp} remains constant across the spectrum, and is given by

$$\Delta E_{sp}/eV_5 = K \qquad (2.17)$$

where eV_5 is the kinetic (or pass) energy of the electrons after passing the retarding field, and K is a constant. eV_5 can be written in terms of the spectrometer parameters

$$V_5 = V_4/[1.3Ln(R_{out}/R_{in})] \qquad (2.18)$$

where V_4 is the potential difference between the cylinders, and R the cylinder radii. Combining both equations and substituting the values for our spectrometer, we finally get the following expresion

$$\Delta E_{sp} = 0.007 e V_5 \qquad (2.19)$$

Therefore, for V_4=40 V, ΔE=0.28 eV, and for V_4=160 V. ΔE=1.12 eV. The diameter of the target area from which photoelectrons are detected by the analyzer is reduced proportionally to the square root of the ratio of the pass energy to the initial kinetic energy of the electron, reducing the counting rate accordingly (counting rate $\propto eV_5/E_i$). Selecting the appropiate pass energy is then a compromise between the desired resolution and the signal intensity that can be obtained. The ultimate resolution in the spectra however is limited by the width of the incident X-ray beam, that for Mg Kα_{12} line is 0.7 eV (full width at half maximum).

The data was acquired and processed using a PET microprocessor. The details of the software used are described elsewhere [23]. The energy scale was calibrated using a value of 70.9 eV for the binding energy of the $4f_{7/2}$ platinum electrons [27]. This resulted in a value for the spectrometer work function of 4.3 V.

2.2.5. High resolution electron energy loss spectroscopy.

High resolution electron energy loss spectroscopy (HREELS) gives information about vibrational energies of surface species. The characteristic vibrational frequencies of each bond permits the structure and

bonding of adsorbed species to be determined. Also, information regarding the identity of the chemisorbed moieties, their geometrical orientation, the characteristics of the adsorption site, the nature of the bonds involved, and even bond lengths, angles and energies can be obtained.

When an electron beam impinges on a sample surface, some electrons scatter elastically from the atomic centers, but others will interact with the adsorbed species, losing a certain amount of energy depending on the type of interaction considered. In the case of vibrations, then, energy losses equal to the vibrational energy of the surface species will be detected. The interaction of electrons with vibrational modes can be divided into two types: long and short range [28]. The long range scattering is due to interactions between dynamic dipole moments associated with each vibrational mode and the electrostatic potential of the incoming electron. Short range scattering involves interactions between the incoming electron and charge densities of adsorbates through polarization (impact scattering), or electron capture in the immediate vicinity of the adsorbate (resonance scattering). Long and short range interactions can be distinguished since the former have a strong angular dependence, with appreciable intensity only around the specular scattering. Short range interactions, on the other hand, are more isotropic. A dipole moment selection rule applies to the electrostatic-dipole interaction, so that only vibrations with dipole components perpendicular to the surface are detected this way. This selection rule is useful for assigning the vibrational modes, because only vibrations that belong to totally symetric reresentations (A_1, A' and A) are observable as fundamentals

in dipole scattering, and are almost absent in non specular directions. Additional information can be obtained by isotopically labelling the adsorbate, and by comparison with gas and liquid phase compounds and with organometallic analogues.

A diagram of the HREEL spectrometer is shown in fig. 2.17. It has been described in detail previously [10]. Briefly, it consists of two 127° cylindrical deflector analyzers, one for the generation of a monochromatic incident electron beam, and the second for scattered electron energy analysis. Electrons emitted from a filament are focused onto the entrance slit of the first monochromator, collimated, and accelerated and focussed on the sample. The backscattered electrons are then decelerated, energy analyzed and detected using a channeltron electron multiplier. The electrostatic properties of this analyzer are very similar to those of the cylindrical mirror analyzer described in the XPS section. The equations for the resolution of this spectrometer are:

$$\Delta E_{sp} = 0.006 E_{pass} \qquad (2.20)$$

and

$$E_{pass} = (e\Delta V/2)\mathrm{Ln}(R_{out}/R_{in}) = 1.81\Delta V \qquad (2.21)$$

where ΔE_{sp} is the resolution, E_{pass} is the kinetic or pass energy of the electrons through the spectrometer, ΔV is the potential difference between the inner and outer sections, and R_{in} and R_{out} their respective radii. Typical values for ΔV of 0.3-0.5 V were used, giving resolutions of 3-5.5 mV (25-50 cm^{-1}). Signals of the order of 10^4-10^6 counts per second (cps) for specular reflection and 1-10^4 cps for inelastic scatte-

ring were commonly obtained.

2.2.6. ^{14}C radiotracer detection technique.

Radiotracer methods are among the most powerful techniques for measuring very low concentrations of materials in a transient environment. They are of particular value when studying the residence time of a surface layer in the presence of the same molecule in the gas phase as often occurs in heterogeneous catalysis. While static radiotracer measurements directly determine the absolute adsorbate surface coverage on the catalyst, dynamic experiments can also be easily carried out to determine the kinetics of important surface phenomena such as isothermal adsorption and desorption, and rehydrogenation of adsorbed species.

While ^{14}C radiotracer techniques have been used by several groups to investigate the interaction of hydrocarbons with metal powders and supported metal catalysts [29-31], they have found only limited application in studies carried out under UHV conditions. A thin window Geiger-Müller (GM) counter has been developed for studies of ^{14}CO chemisorption over nickel single crystals under ultra-high vacuum [32], sensitive enough to detect down to 10^{12} adsorbed molecules. We have recently developed an alternative system in our laboratory that uses a surface barrier detector (Ortec TA-23-25-300) [5,33]. Schematic diagrams of this system is shown in figs. 2.18 and 2.19. The detector is a large area diode consisting of a partially depleted slice of ultrapure n-type silicon mounted in an insulating ring. The front and back surfaces are metallized. The entrance contact-surface barrier (gold window, 40 $\mu g \cdot cm^{-2}$)

and depth of the depletion region (300 μm) are chosen to optimize the detector efficency for low energy beta radiation (^{14}C E_{max}=158 KeV, its range in silicon is about 150 μm). The front surface of the insulating ring is grounded to the metal case and to the shield of a standard Microdot connector. The back surface of the ring contacts the center electrode of the connector which functions as a signal output and bias voltage connection. Free charge carriers created during operation by ionizing radiation are separated by an electric field that is produced by an externally applied reverse bias (50-100 V). Integration of the current induced on the detector contacts yields an output pulse that is proportional to the energy of the ionizing radiation [34]. Output pulses are amplified and shaped by a charge sensitive preamplifier (Ortec 142) and a linear amplifier (Ortec 575). For point-by-point measurements, N(E) beta spectra are collected and stored in a pulse height analyzer (Tracor TN 1705). The energy scale is calibrated using the signal from a tail pulse generator (BNC RP2) applied to the preamplifier test input. Integration of the timed spectra yields a count rate that is proportional to the radioactivity present in the source. Alternatively, a ratemeter or multichannel scaler can be used for continuous measurements using an appropiately wide window (about 35 to 158 KeV). A more detailed diagram of the detector mounting assembly, showing the electrical connections and provisions for cooling, is shown in fig. 2.19.

The detector was calibrated by using a standard solution of ^{14}C-polymethylmethacrylate disolved in ethyl acetate. Known volumes of

the solution (with known specific radioactivity) were deposited on the sample and the solvent was then evaporated. The signal was optimized in order to discriminate leakage currents and random fluctuations in the charge carrier density by setting the lower discrimination level of the β-particles kinetic energy [5,33]. The total efficiency of the detector, including geometrical factors, was about 3%. This was sufficient to detect few percent of a monolayer in a reasonable time. This technique was used in the present work to calibrate the absolute coverage of ethylene chemisorbed over Pt(111) surfaces, and to study the stability of carbonaceous deposits towards high pressure hydrogenation.

FIGURE CAPTIONS

Fig. 2.8. Universal curve for condensed phases showing the dependence of the inelastic electron mean free path (attenuation length) as a function of kinetic energy.

Fig. 2.9. A typical distribution of electrons, N(E), as a function of kinetic energy, observed after a solid sample is irradiated with a monoenergetic beam of electrons. The dashed line represents the contribution due to secondary electrons. The inserts show how the different energy ranges are used for surface analysis. AES (a), HREELS (b), and LEED (c) are shown for the case of ethylene adsorption over Rh(111) surfaces at 300 K.

Fig. 2.10. Auger electron spectra of carbidic and graphitic carbon.

Fig. 2.11. Energy level diagrams comparing the Auger emission and X-ray fluorescence mechanisms for deexcitation of an excited ion.

Fig. 2.12. Auger electron spectra of a clean platinum single crystal surface and of a platinum surface that was initially contaminated with several surface impurities.

Fig. 2.13. Growth mechanisms for thin films on metal substrates together with the expected variations in Auger signals of both substrate and adsorbate.

Fig. 2.14. Schematic of a retarding field analyzer for Auger electron spectroscopy and low energy electron diffraction.

Fig. 2.15. Scheme of the low energy electron diffraction experiment for an idealized crystal lattice.

Fig. 2.16. Schematic diagram of the double pass cylindrical mirror analyzer for x-ray photoelectron spectroscopy.

Fig. 2.17. Scheme of the high resolution electron energy loss spectrometer.

Fig. 2.18. Block diagram showing the experimental arrangement and counting electronics for radiotracer studies using a surface barrier detector in an ultra-high vacuum chamber. An expanded cross section of the surface barrier detector is also shown.

Fig. 2.19. Schematic diagram of the detector mounting assembly showing the detector offset along with the output/bias connection and provisions for cooling the detector with circulating water or liquid nitrogen.

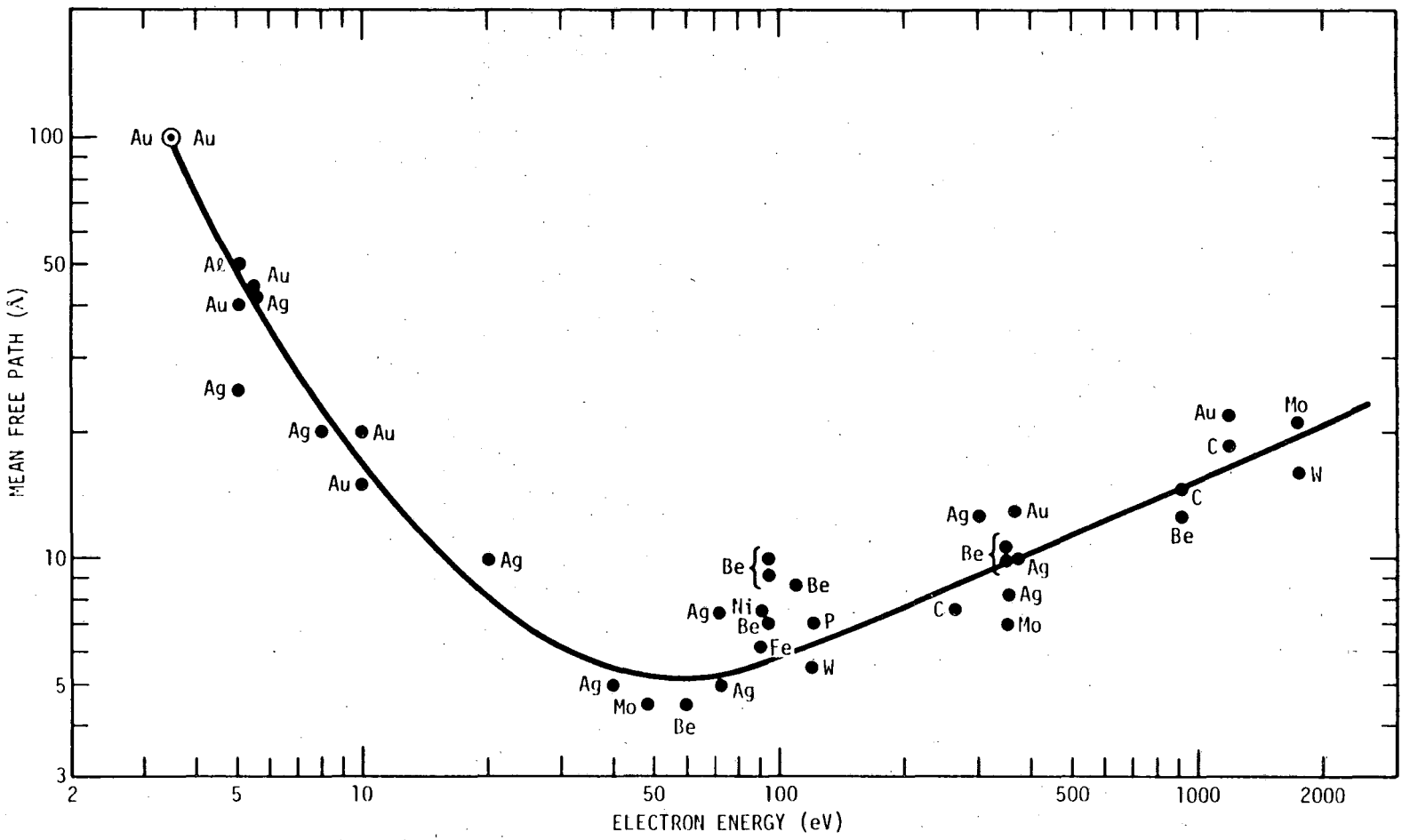
MEAN FREE PATH (Å)
100
50
10
5
3
2
5
10
50
100
500
1000
2000
ELECTRON ENERGY (eV)
Au Au
Au
Au
Ag
Ag
Ag
Au
Au
Ag
Be
Be
Ag
Ni
Be
P
Fe
W
Ag
Mo
Be
Ag
Ag
Au
Be
Ag
Ag
C
Mo
Au
Mo
C
W
C
Be
XBL 733-5917

fig. 2.8

ENERGY DISTRIBUTION OF SCATTERED ELECTRONS FROM A c(4×2) MONOLAYER OF C_2H_3 ON Rh(111) AT 300K

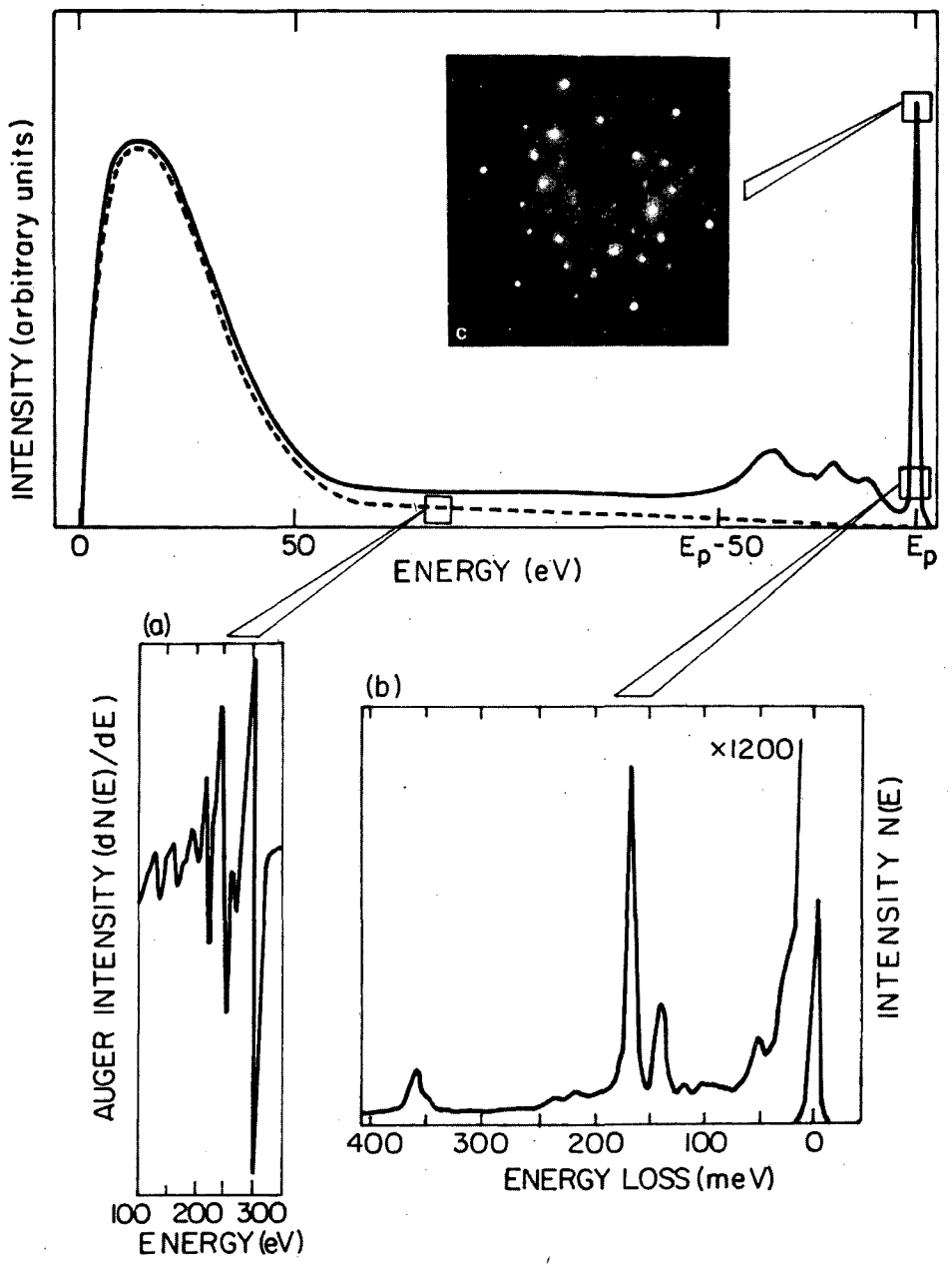

XBB 830-11012

Fig. 2.9

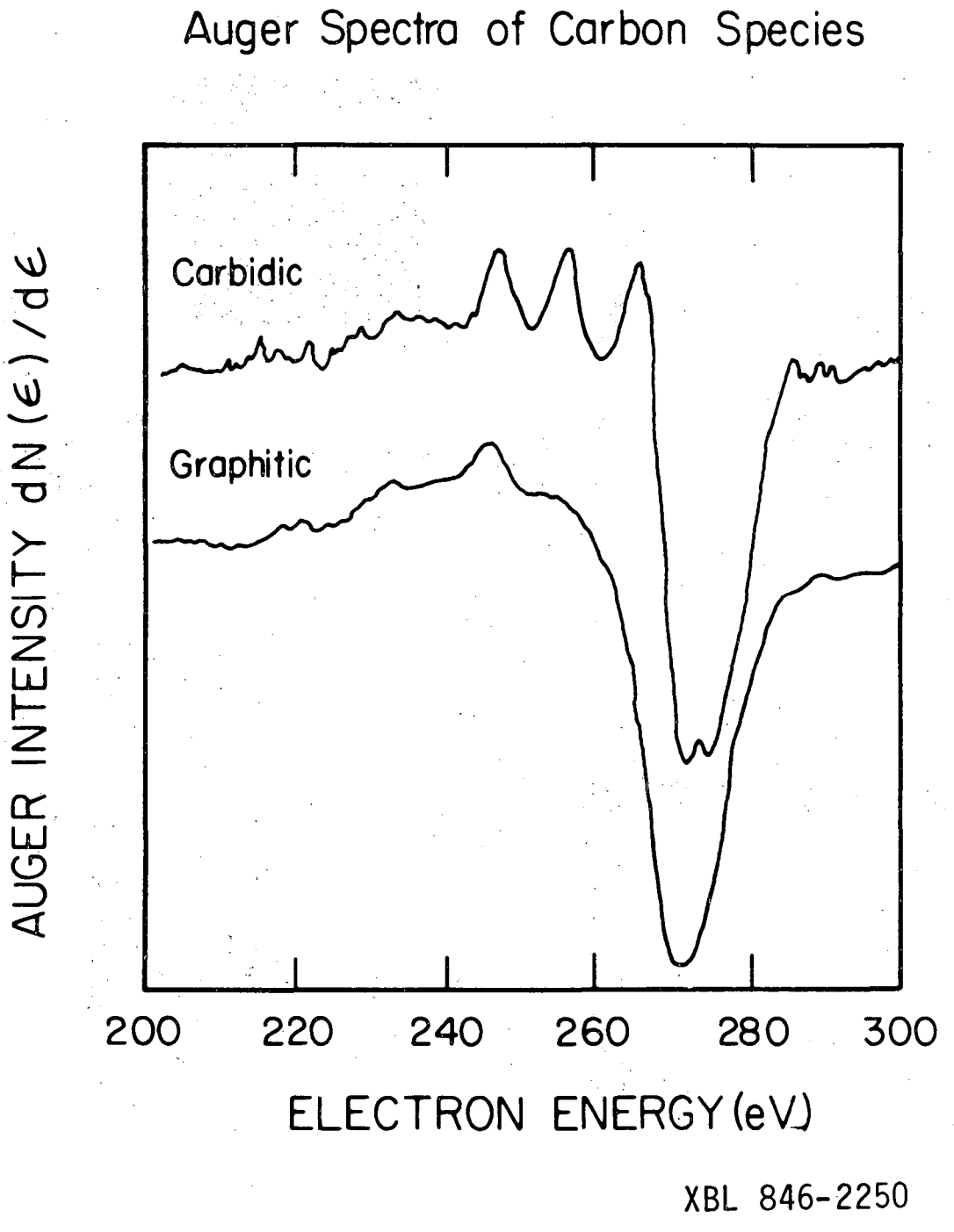
Auger Spectra of Carbon Species
Carbidic
Graphitic
AUGER INTENSITY dN(ε)/dε
200
220
240
260
280
300
ELECTRON ENERGY (eV)
XBL 846-2250

fig. 2.10

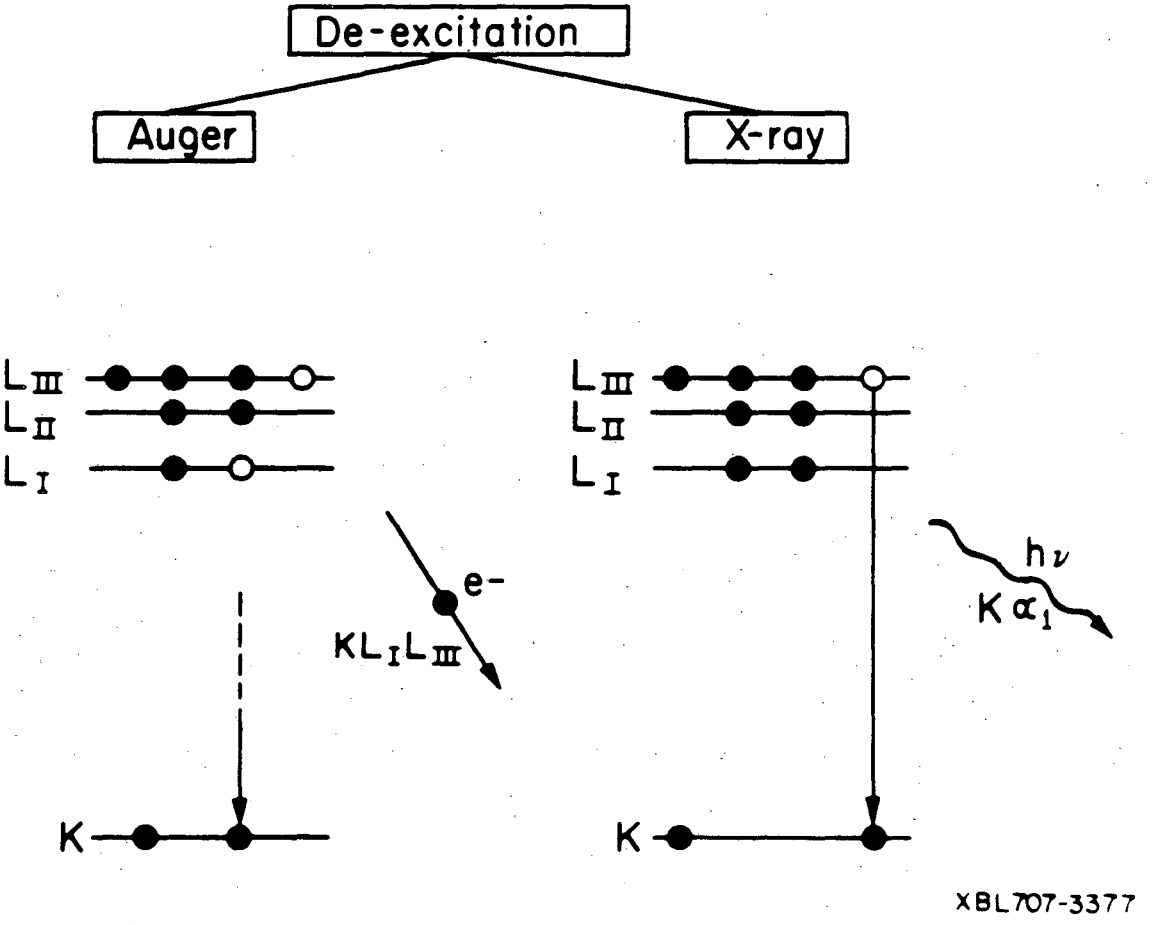
De-excitation
Auger
X-ray
L_{III}
L_{II}
L_I
e-
KL_IL_{III}
K
L_{III}
L_{II}
L_I
$h\nu$
$K\alpha_1$
K
XBL707-3377

fig. 2.11

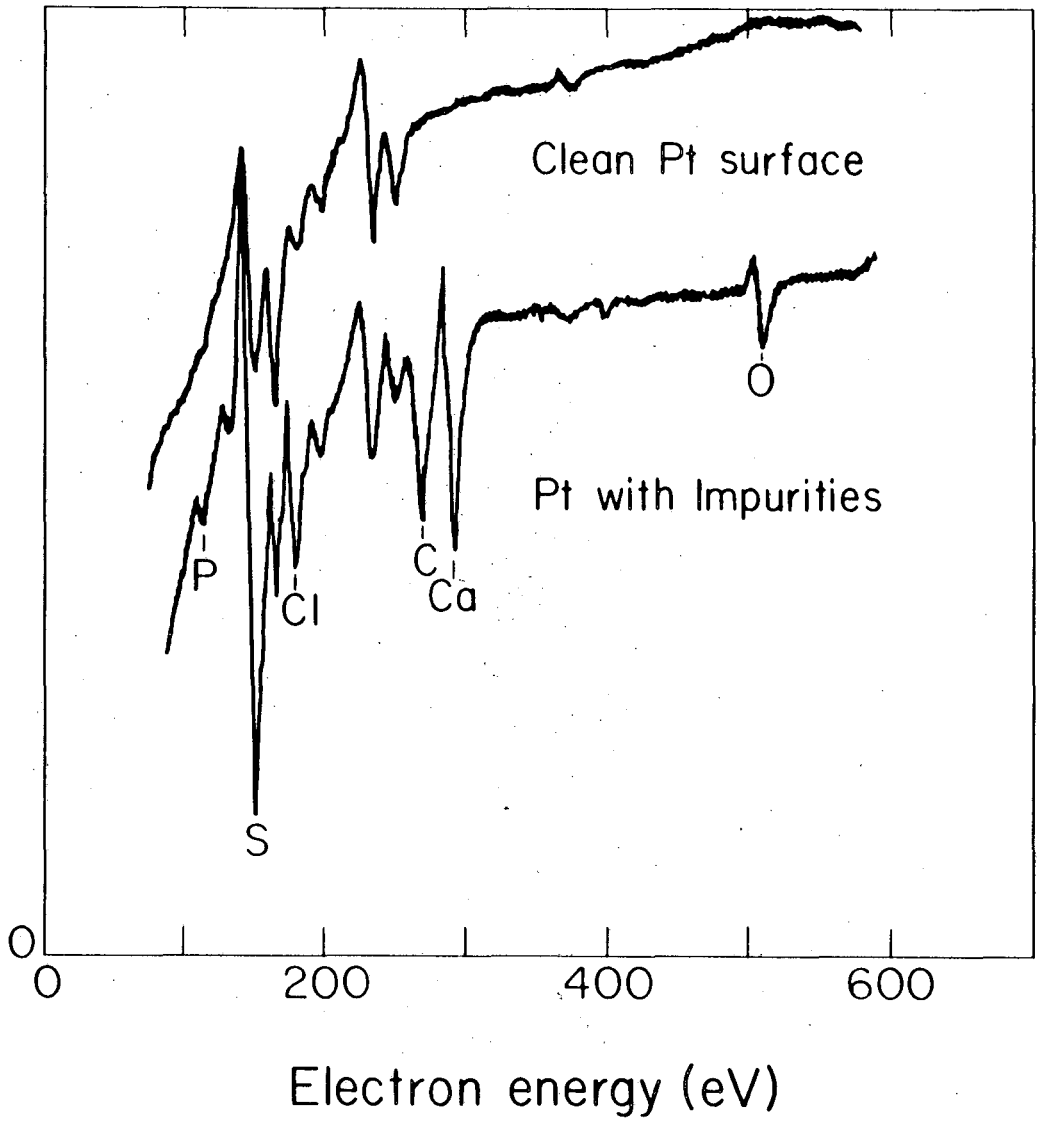
Clean Pt surface
Pt with Impurities
O
P
S
Cl
C
Ca
0
0
200
400
600
dN(E)
dE
(arb.
units)
Electron energy (eV)
XBL 818-1104

fig. 2.12

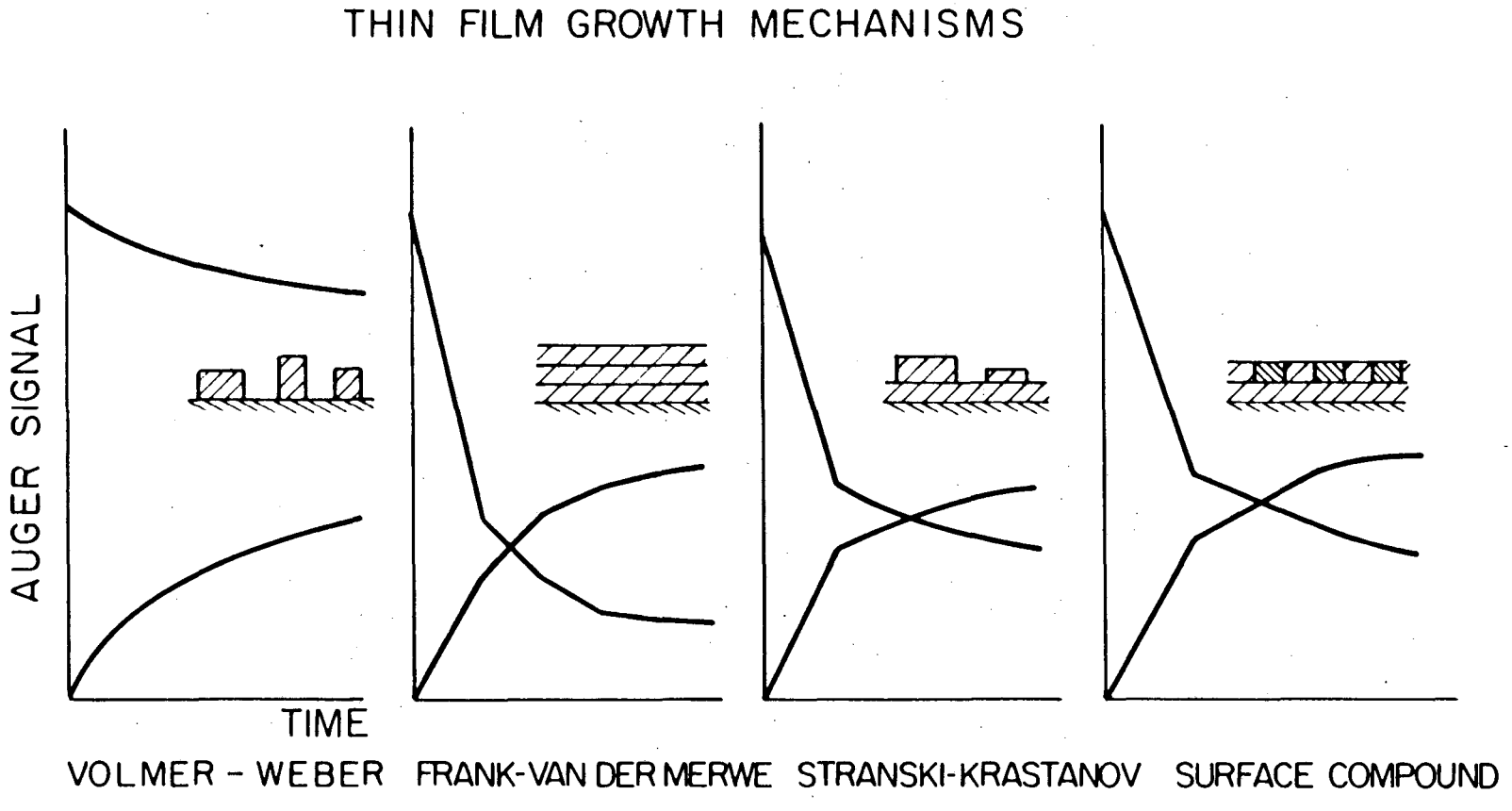
THIN FILM GROWTH MECHANISMS
AUGER SIGNAL
TIME
VOLMER - WEBER
FRANK-VAN DER MERWE
STRANSKI-KRASTANOV
SURFACE COMPOUND
XBL 814-5523

fig. 2.13

Retarding Field Analyzer for Auger Electron Spectroscopy

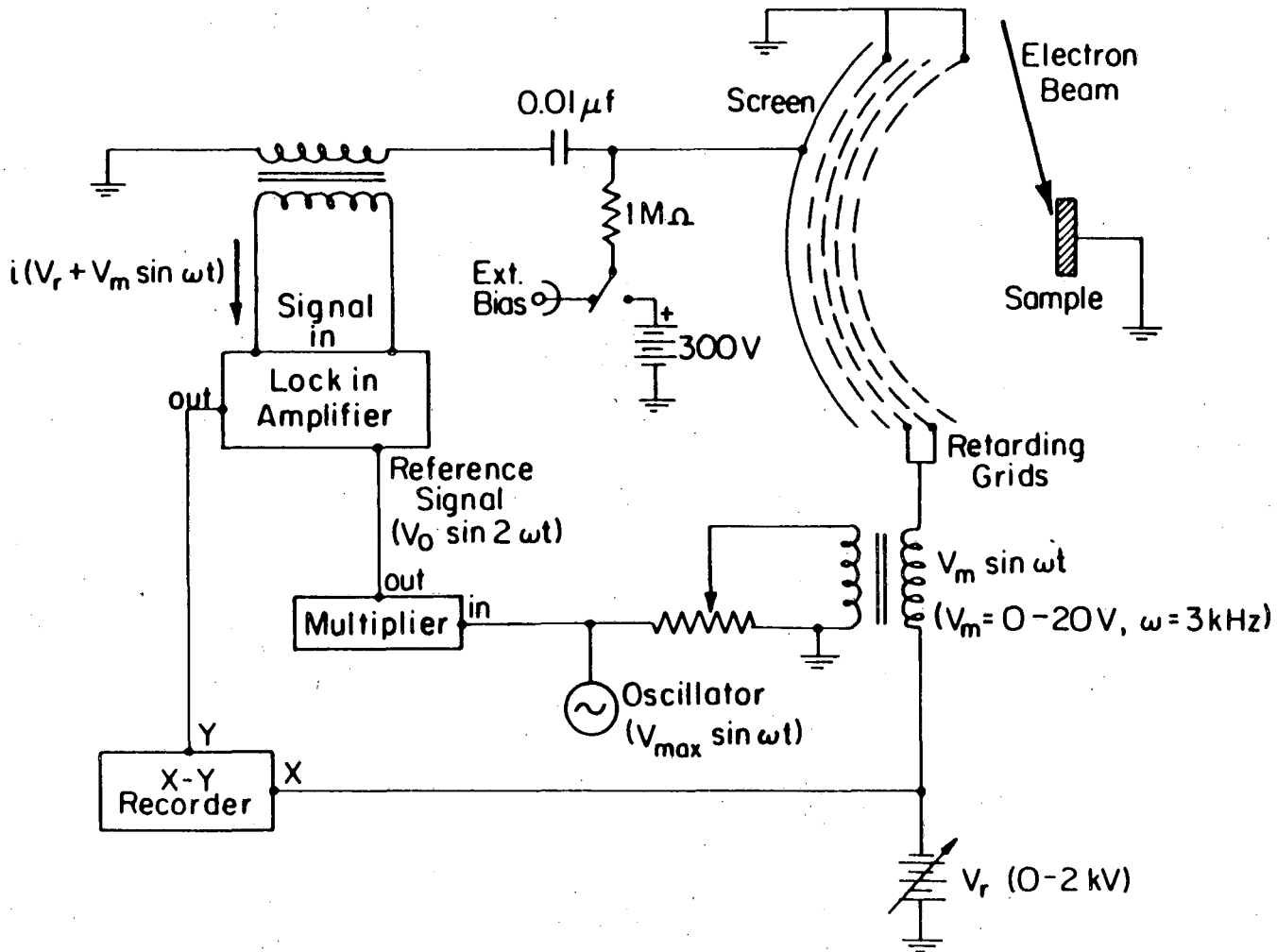

XBL 842-6631

fig. 2.14

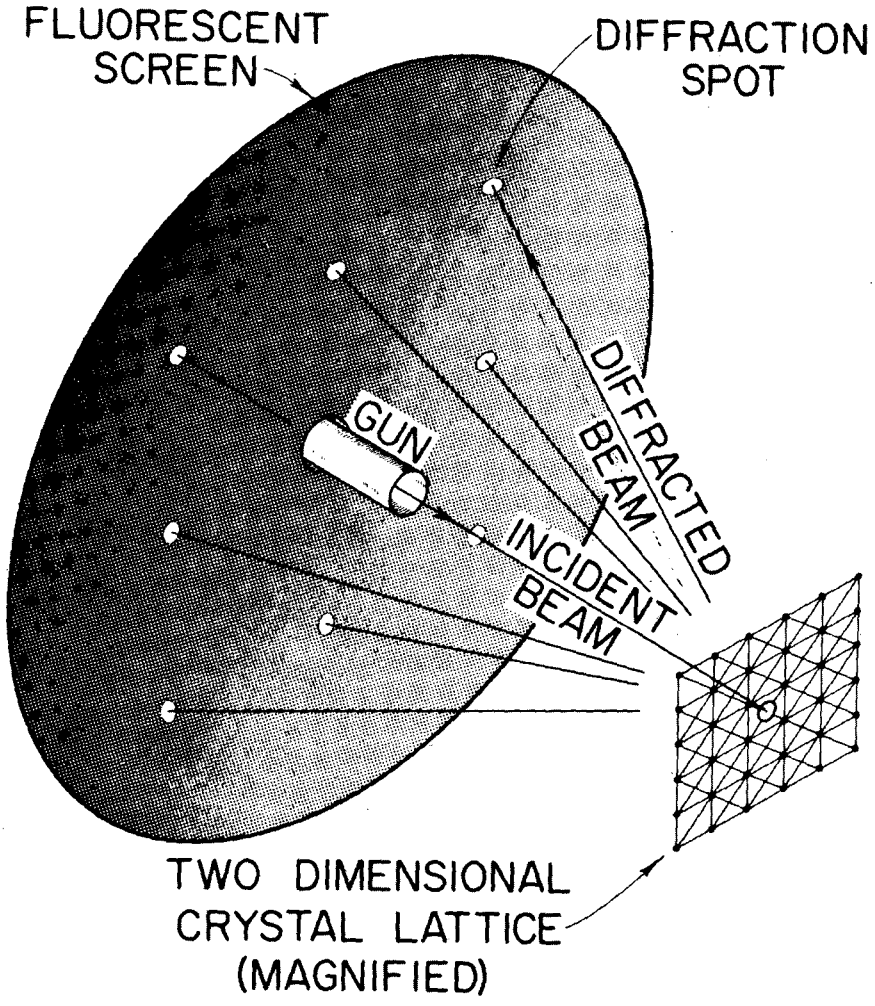

XBB 708-3583

Fig. 2.15

Double Pass Cylindrical Mirror Analyzer
Retarding Pulse Counting Mode

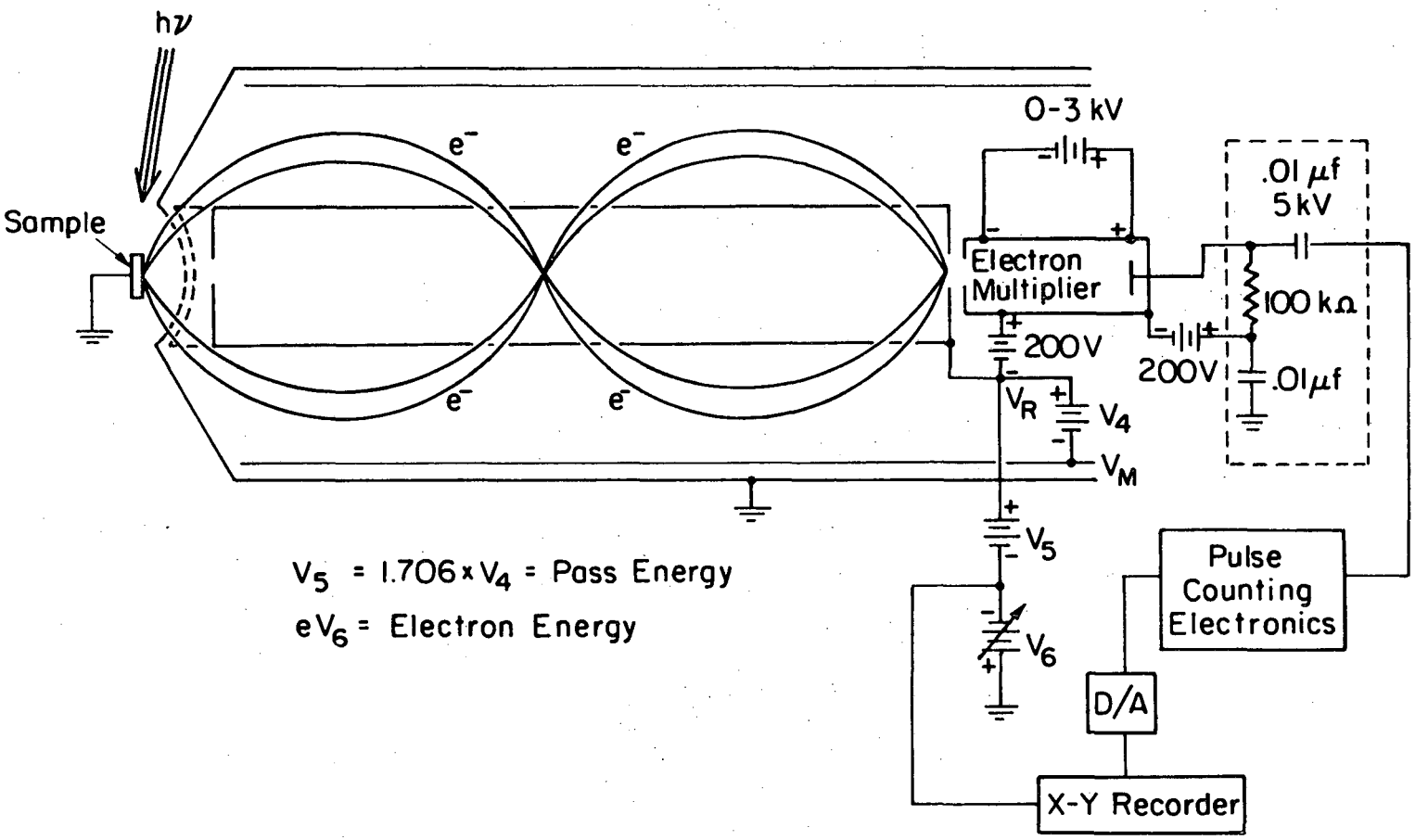

fig. 2.16

HREELS SPECTROMETER

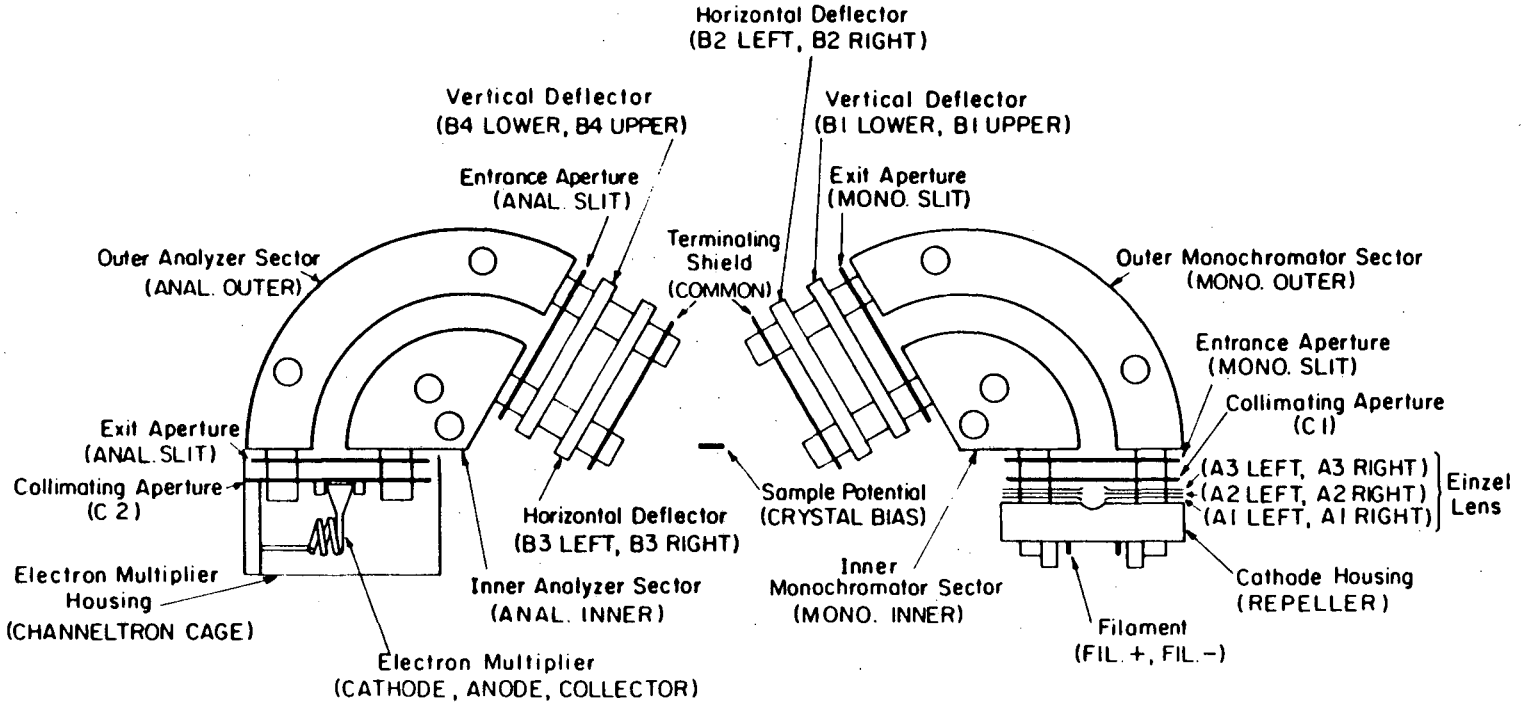

XBL 839-6319

fig. 2.17

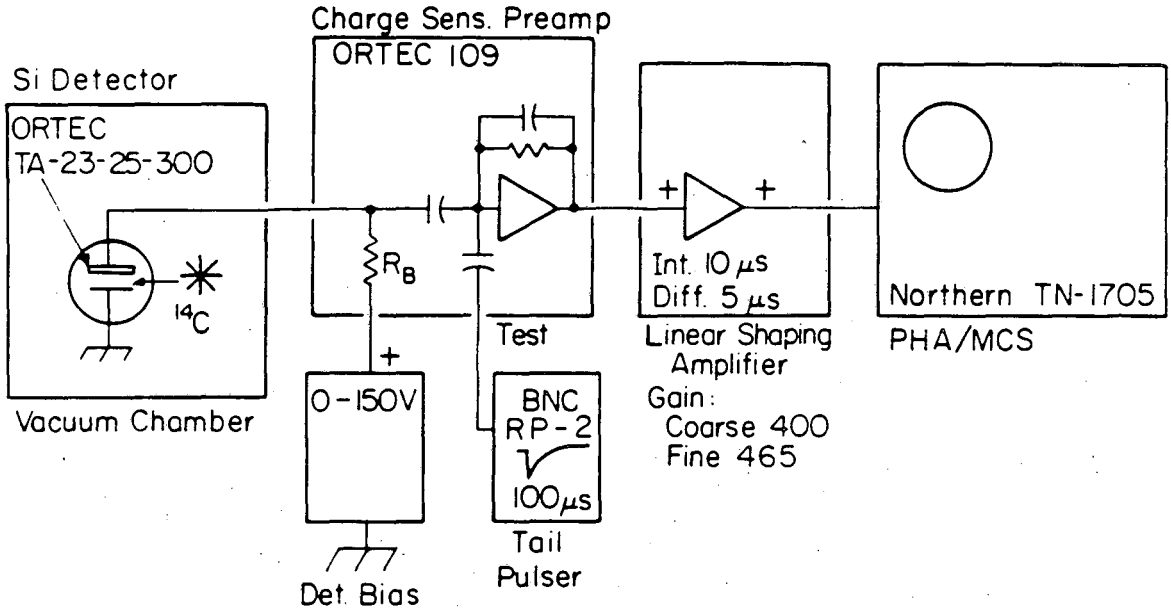

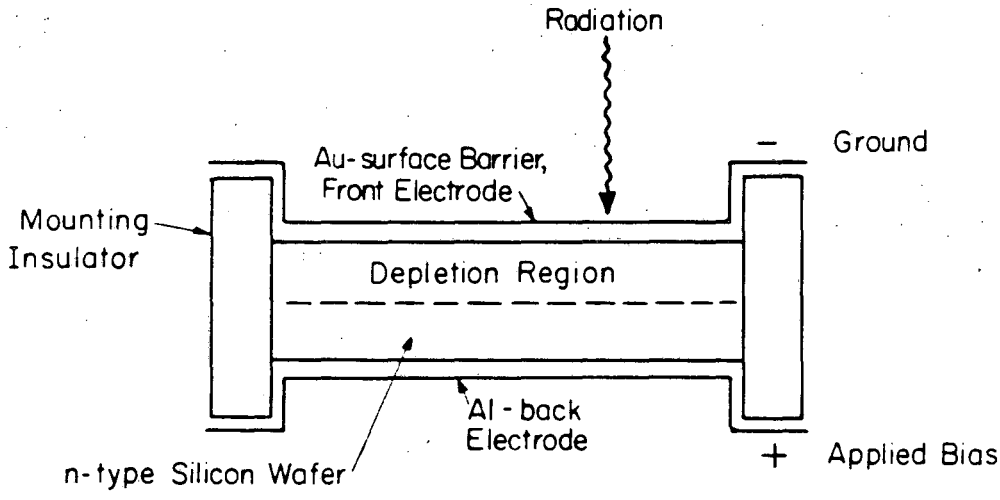

Detector Detail

XBL811-5007

fig. 2.18

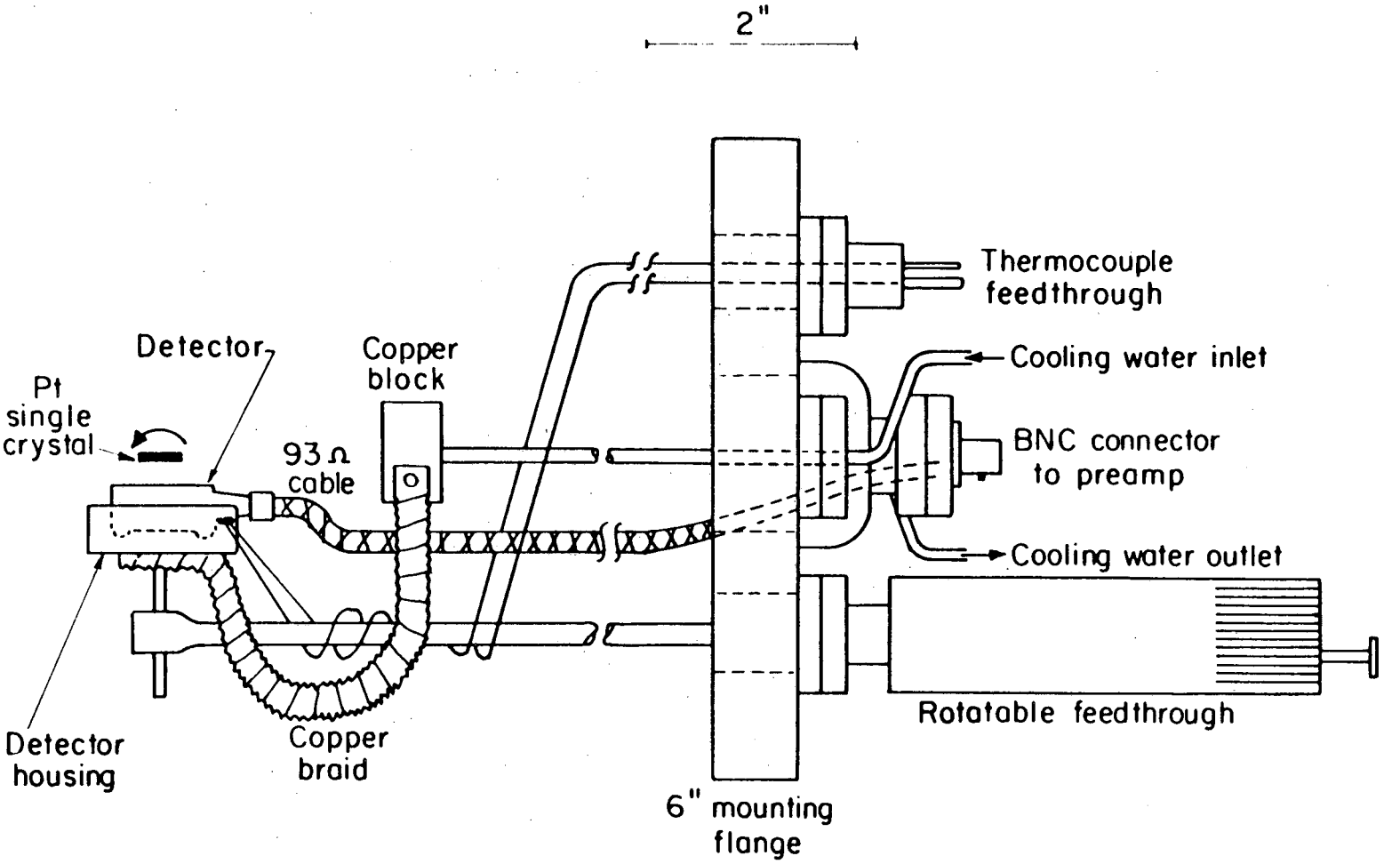
2"
Thermocouple feedthrough
Detector
Copper block
Cooling water inlet
Pt single crystal
93 Ω cable
BNC connector to preamp
Cooling water outlet
Rotatable feedthrough
Detector housing
Copper braid
6" mounting flange
XBL 811-5001

fig. 2.19

2.3. Materials.

2.3.1. Reagents.

Hydrogen and hydrocarbon reagents used in this research were of the highest obtainable research purity. A listing of these reagents is presented in table 2.1 with sources, purities, and major detectable impurities. Liquid hydrocarbons, stored in pyrex vacuum flasks, were outgassed by repeated freeze-pumping cycles at 77 K before use. Most gases were used as supplied.

Carbon-14 labelled ethylene (Amersham; specific activity=128.5 mc/mmol) was supplied in a break seal tube adapted with vacuum stopcocks. Radiochemical purities for this hydrocarbon were stated to be in excess of 99%.

In high pressure reaction experiments, contamination levels well below 1 ppm in the reactants are sufficient to cause immediate contamination of the metallic catalyst surfaces. Auger electron spectroscopy was therefore always used in these experiments to monitor the sample composition after high pressure exposures. Only low levels of sulfur were detected after methylcyclopentane, cyclohexene and benzene reactions, never exceding 10% of a monolayer. Also small amounts of oxygen were present after most of the experiments, but this did not affect the kinetic results obtained [5]. The most important species deposited by the reaction mixtures were carbon and hydrogen, forming carbonaceous deposits characteristic of all hydrocarbon conversion reactions.

2.3.2. Catalysts samples.

A variety of foils, powders and single crystals were used throughout this research. Rhenium foils, used for high pressure hydrocarbon reactions, were 0.025 mm thick (Alfa). The main contaminants present on those foil surfaces were carbon and/or oxygen, as detected by Auger elecron spectroscopy. Rhenium oxides, used in order to obtain reference x-ray photoelectron spectra, were in the powder form, and were pressed onto a platinum foil surface previous to insertion in the UHV chamber (Alfa products, 99.9% purity for ReO_2 and ReO_3, and 99.99% purity for Re_2O_7). Since Re_2O_7 is hygroscopic, handling of these samples outside vacuum were done in a glove box using He as an inert atmosphere. The platinum foils, that existed on my arrival to the group, were mainly contaminated with calcium and carbon, as seen by AES. Impurities were removed in all cases prior to performing the experiments by using the cleaning procedures described below.

The platinum single crystal samples used in this research either existed upon my arrival of were prepared by me. Spark erosion was used to slice thin oriented disks (0.3-0.9 mm thick) from 0.48 or 0.63 cm diameter platinum single crystal rods that were obtained from Material Research Corporation (MRC, 99.996% purity). Laue x-ray back diffraction was used to ensure that both crystal faces were within 0.5^{o} of the specified orientation. Examples of these diffraction patterns are shown in fig. 2.20, together with their respective LEED patterns. The crystals were polished to a mirror finish using standard metallographic procedures, with the final step using an aqueous slurry of 0.05 μm alumina

powder in an ultrasonic vibrator. After etching for 15-30 sec. in concentrated aqua regia, the samples were rinsed in water, acetone and ethanol, and then mounted in a manipulator and inserted in the vacuum chamber.

Auger electron spectra of platinum and rhenium samples obtained from new materials revealed surface contamination with some of the following elements: silicon (93 eV), phosphorous (119 eV), sulfur (154 eV), chlorine (181 eV), carbon (273 eV), calcium (295 eV), and/or oxygen (510 eV). These impurities were removed to whithin AES detection limits by repeated cycles of argon ion sputtering (0.5-1.5 KeV) at 900-1300 K, annealing at 1300-1400 K for platinum and 1800 K for rhenium, and treatment with $1\text{-}10\times10^{-7}$ torr O_2 at 900-1100 K. Sometimes, sputtering in the presence of about 1×10^{-7} torr O_2 was used to induce calcium and silicon segregation to the surface for easier removal by the argon ions. After initial cleaning of the samples, only occasional sputtering or oxygen treatment was necessary to mantain the samples clean.

Catalyst surface areas were needed for calculation of the high pressure reaction rates. The geometrical area of both faces and edges, together with the supporting wires (that were of the same material as the sample) were considered. Total areas on the order of 1-2 cm^2 were obtained, with 20-30% of polycrystalline surface in the case of the single crystals. A conversion factor of 1.5×10^{15} metal atoms per square centimeter was used.

2.3.3. Dosing materials and procedure.

Volatile gases were dosed through a variable leak valve from the gas manifold into the vacuum chamber, either by backfilling the chamber or by introduction through a 0.125 inch O.D. stainless steel tube doser pointed towards the sample.

All potassium dosing was done by heating a commercial SAES Getter source which consists of a powdered mixture of potassium chromate and a zirconium-16% aluminum alloy getter, enclosed in a tantalum dispenser. The doser was positioned about 5 cm from the platinum sample, and heated by passing a 4-8 Amps. current through it, giving dosing rates of 0.05-0.20 monolayers per minute. The amount of potassium deposited was monitored by AES, and calibrated from the shape of the uptake curves, as described in detail elsewhere [23].

Rhenium was deposited onto the platinum samples in one of three ways: by thermal decomposition of dirhenium decacarbonyl, by ion sputtering, or by evaporation from a rhenium filament.

Chemical deposition using metal carbonyls have been reported for nickel deposition on copper surfaces [35]. Dirhenium decacarbonyl, a white solid, sublimes at 413 K and decomposes quantitatively at 673 K [36-38]. The $Re_2(CO)_{10}$ (Alfa, > 95% purity) was evaporated by heating the sample container and the lines to the leak valve to 350-400 K, and the platinum substrate to 500-650 K. Only small amounts of rhenium could be deposited this way (10-50% of a monolayer) due to carbon codeposition from the carbonyl decomposition.

A commercial planar magnetron sputter source (US' Gun, model 200) was used for sputtering deposition of rhenium over platinum single crystals. A 5 cm diameter by 0.5 mm thick rhenium foil was used as the source, and was located about 10 cm away from the platinum surface, positioned at a glancing angle ($\simeq 70^{o}$). Deposition rates below 10 monolayers/minute were not possible, even operating at the lowest power possible ($2x10^{-2}$ torr Ar, 220 V and 0.03 Amps.). Codeposited carbon had to be burned off during deposition. A typical uptake curve is shown in fig. 2.21.

The third and most succesfull method for rhenium deposition was using a rhenium filament as a source. Re was evaporated by resistively heating the filament placed 5 cm from the platinum substrate, to 2500-2800 K (Re vapor pressures of $5x10^{-7}$-$2x10^{-5}$ torr). The temperature of the filament was calibrated using an optical pyrometer (Leeds & Northrop, model 8622-C) at low temperatures (1600-2100 K), and extrapolating to higher temperatures using either reported resistivities [39] or Stefan's law for power dissipation, together with reported emittances [54] (figs. 2.22 and 2.23). Uptake curves, obtained using Auger electron spectroscopy, are shown in fig. 2.21. Due to the overlap of most platinum and rhenium peaks, the calibration was not very accurate. However, the rhenium coverages could be estimated within 50% error.

FIGURE CAPTIONS

Fig. 2.20. Laue x-ray backscattering diffraction (left) and LEED patterns (right) for (111) and (755) platinum single crystal surfaces.

Fig. 2.21. Auger uptake curves for rhenium deposited on Pt(111). Various platinum peaks (at 44, 66 and 150 eV energies) and rhenium deposition techniques were used.

Fig. 2.22. Resistance vs. temperature calibration of a rhenium filament used for rhenium evaporation.

Fig. 2.23. Dissipated power vs. temperature calibration of a rhenium filament used for rhenium evaporation. The experimental results are compared with those obtained using Stefan's law. ξ is the emissivity coefficient ($\simeq 0.1$).

Fig. 2.24. Auger electron spectra for four different coverages of rhenium deposited over a Pt(111) single crystal surface.

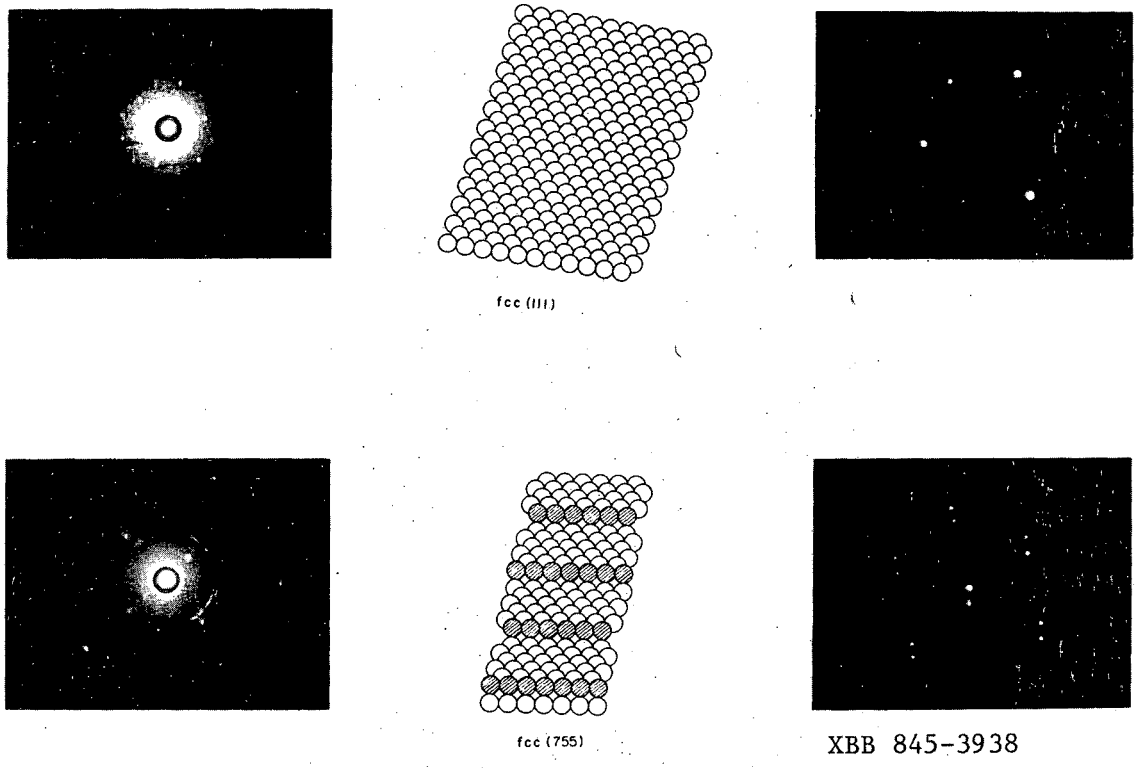

Fig. 2.20

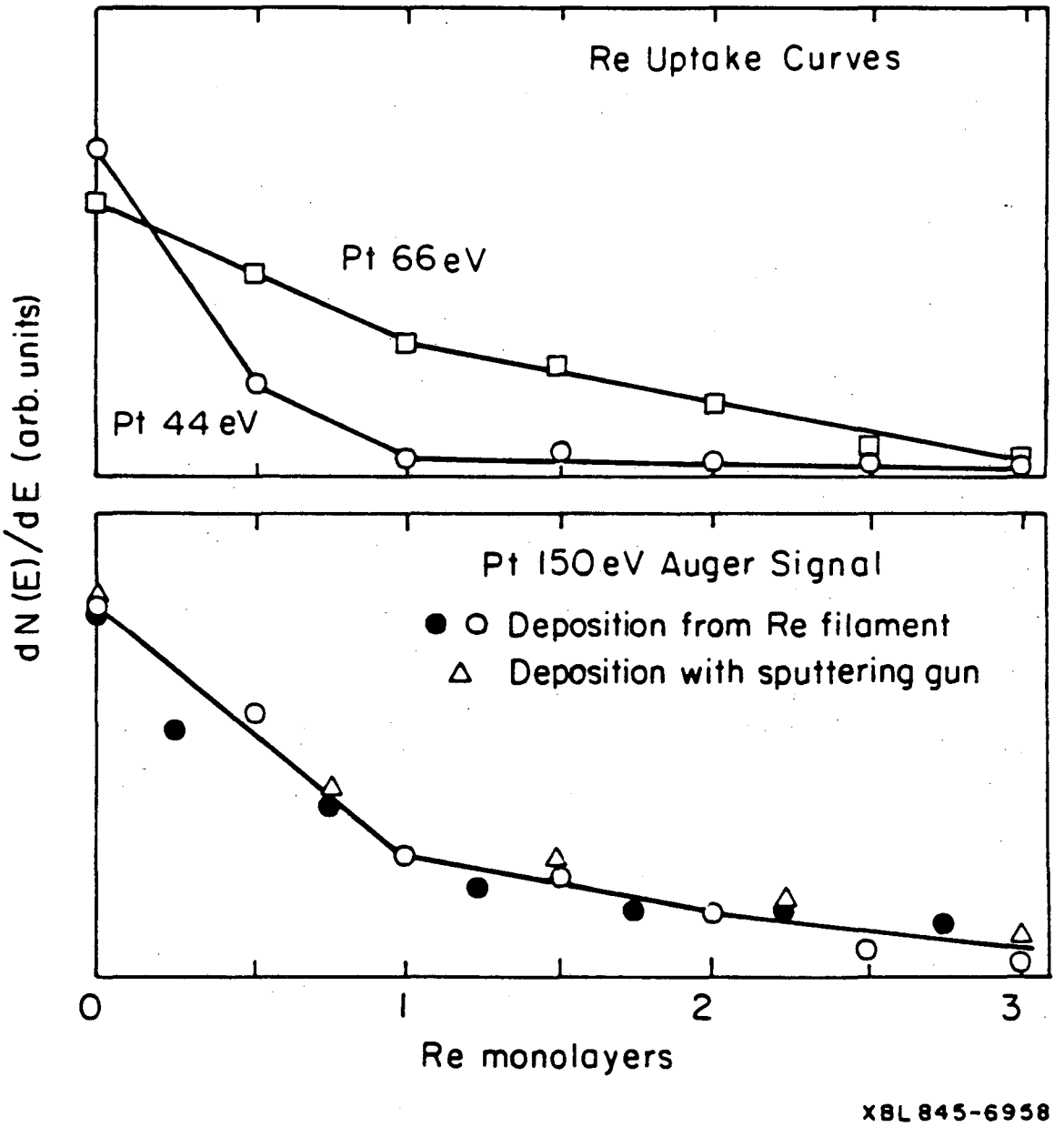
Re Uptake Curves
Pt 66 eV
Pt 44 eV
Pt 150 eV Auger Signal
● ○ Deposition from Re filament
△ Deposition with sputtering gun
dN(E)/dE (arb. units)
0
1
2
3
Re monolayers
XBL 845-6958

fig. 2.21

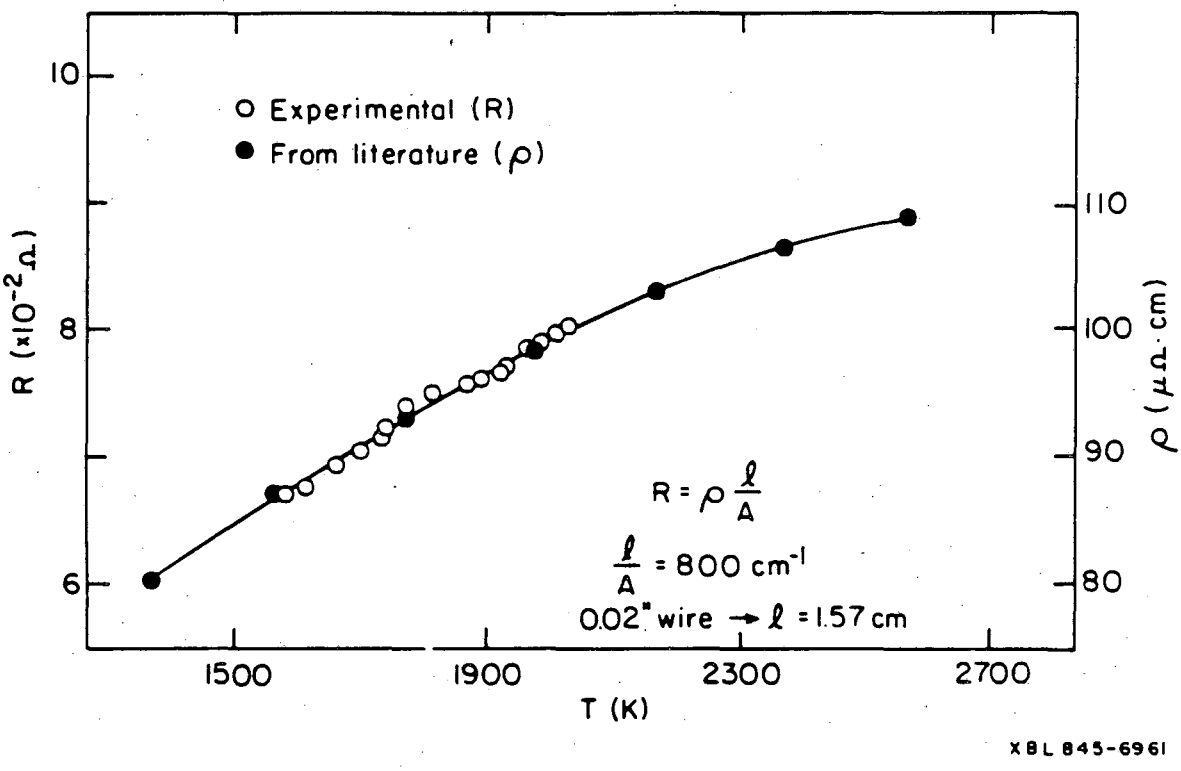
O Experimental (R)
● From literature (ρ)
R = ρ ℓ/A
ℓ/A = 800 cm⁻¹
0.02" wire → ℓ = 1.57 cm
R (×10⁻² Ω)
ρ (μΩ·cm)
T (K)
10
8
6
110
100
90
80
1500
1900
2300
2700
XBL 845-6961

fig. 2.22

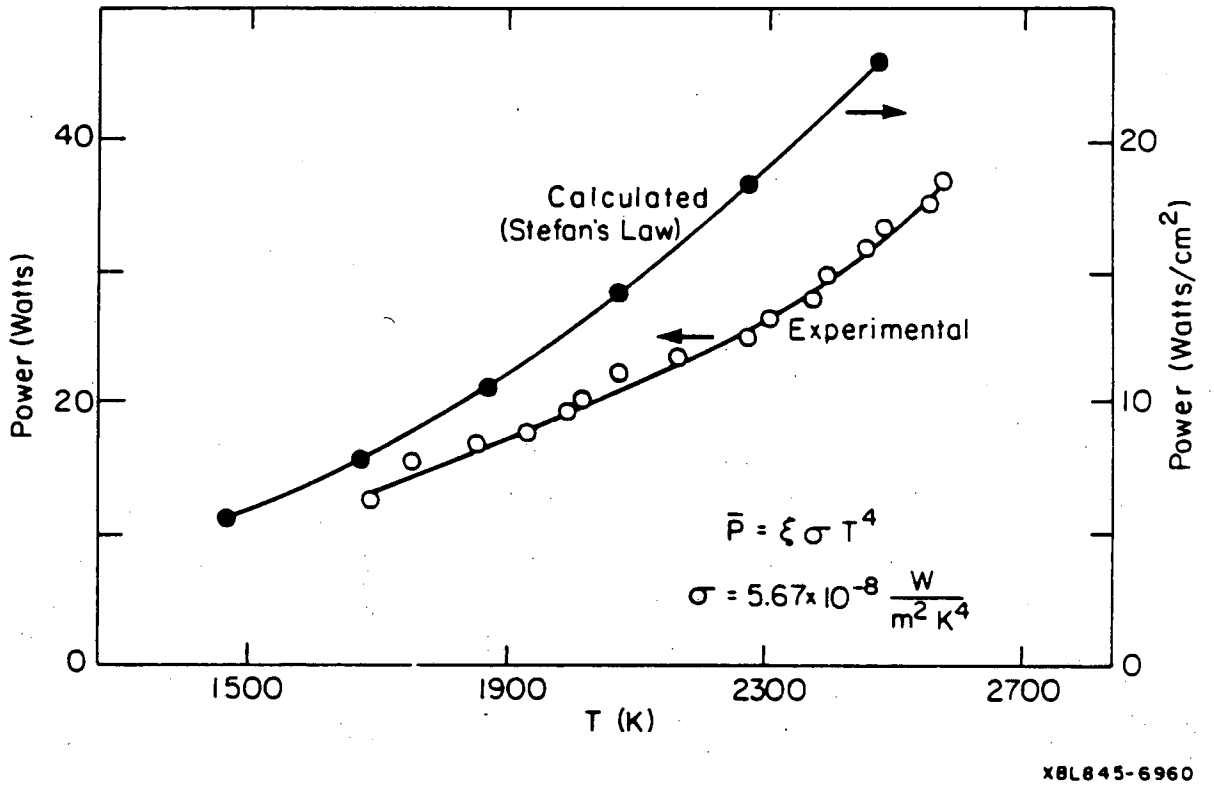
Power (Watts)
40
20
0
1500
1900
2300
2700
T (K)
20
10
0
Power (Watts/cm²)
Calculated
(Stefan's Law)
Experimental
$\bar{P} = \xi \sigma T^4$
$\sigma = 5.67 \times 10^{-8} \frac{W}{m^2 K^4}$
XBL845-6960

fig. 2.23

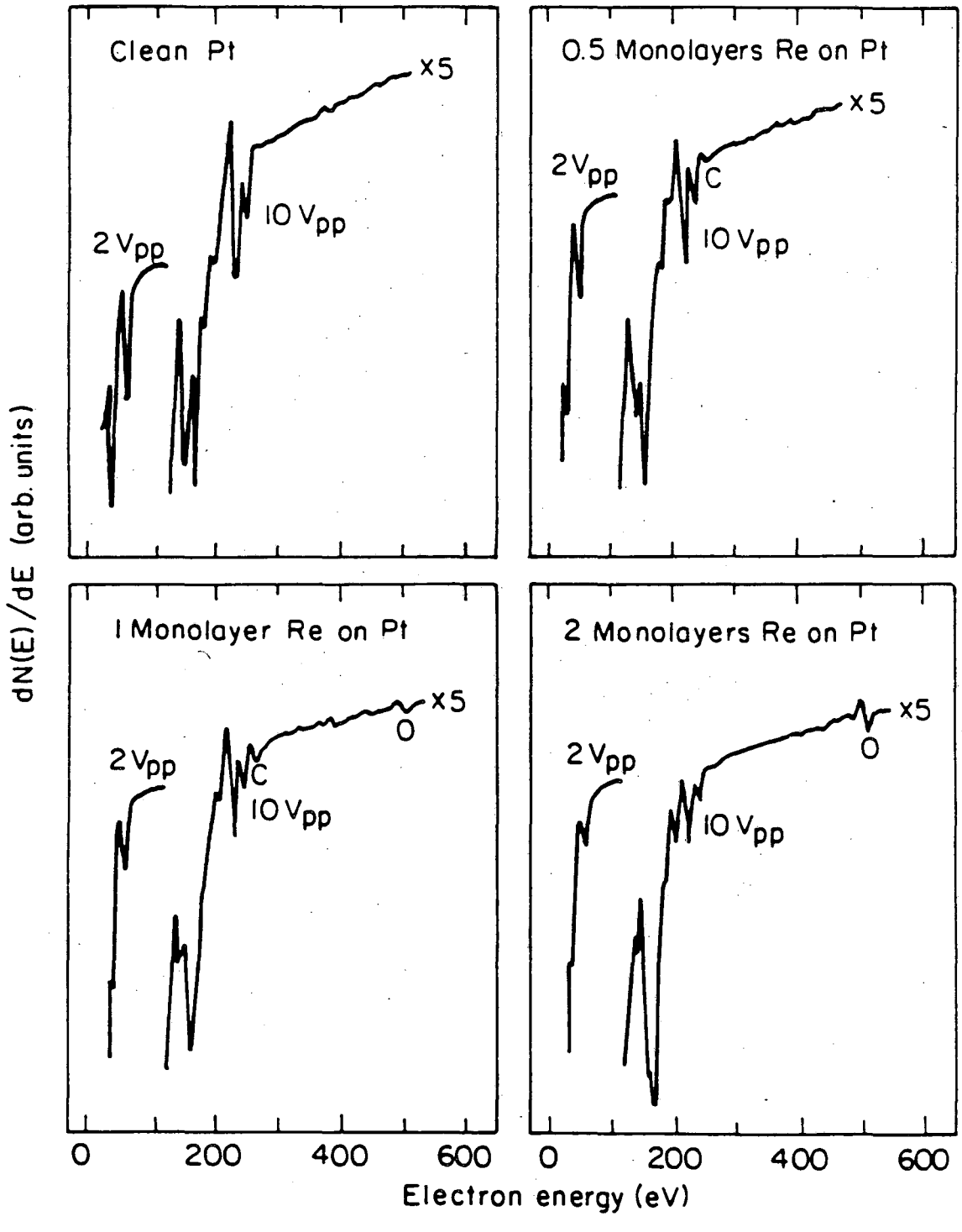
Clean Pt
x5
2 Vpp
10 Vpp
0.5 Monolayers Re on Pt
x5
2 Vpp
C
10 Vpp
1 Monolayer Re on Pt
x5
O
2 Vpp
C
10 Vpp
2 Monolayers Re on Pt
x5
O
2 Vpp
10 Vpp
dN(E)/dE (arb. units)
0
200
400
600
0
200
400
600
Electron energy (eV)
XBL845-6959

fig. 2.24

2.4. Procedures.

2.4.1. Low pressure chemisorption experiments.

Prior to each chemisorption experiment, the metallic samples were cleaned in UHV as described earlier using a combination of argon ion sputtering, oxygen treatment and annealing cycles. After cleaned, the surface composition was characterized by AES and subsequently flashed to remove any adsorbed background gases. In the rhenium film studies, Re was then evaporated onto the platinum substrate, cleaned and checked again by using AES. The sample was then cooled down to 100-150 K and flashed again. Gases could be exposed at either low or high pressures, using the environment cell in the latter case. In some cases a background gas pressure was maintained while performing thermal desorption experiments. LEED and AES were also used both before and after most reaction or thermal desorption experiments.

2.4.2. High pressure reactions.

For high pressure reaction experiments, the isolation cell was quickly closed after cleaning and characterizing the surface. An atmosphere af hydrogen was sometimes used to cool the metallic sample and supports to room temperature. In those cases, the hydrogen was removed after about one minute (AES analysis at this point never revealed more than 10% carbon on the surface). Hydrocarbon vapors and hydrogen (or deuterium) were introduced in that order up to the desired pressures, and circulation was started to allow complete mixing of the gases. Special care was taken to ensure that the first gas introduced was not isolated in the corners of the reaction loop, checing homogeneity with

the gas chromatrograph and/or the mass spectrometer. For total reactant pressures below 110 torr nitrogen was added as an inert diluent so that the circulation pump could operate effectively without overheating. After a few minutes of mixing, a gas sample was analyzed by gas chromatography, and the metal was then heated to the desired temperature. Zero reaction time was taken as the time at which the crystal or foil reached reaction temperature. The reaction temperature was continuously regulated to ±3 K using a precision temperature controller with a DVM display referenced to a chromel-alumel thermocouple spotwelded to the sample. Gas chromatographic samples were subsequently taken at periodic intervals of 5-30 minutes depending on the reaction studied. For mass spectrometric follow up of the deuteration and deuterium exchange reactions, the gas mixture was leaked into the main chamber at a rate of about 50 mm^3/min (UHV chamber pressure of about $1x10^{-7}$ torr) and mass spectra in the 1-50 amu range were recorded periodically. The reactions were allowed to proceed 60-240 minutes, after which the sample was rapidly cooled in the reaction mixture to room temperature, and the loop was then evacuated. The pumping procedure consisted of rough pumping to 10^{-2} torr with a mechanical pump followed by an additional 5-60 minutes of pumping with a liquid nitrogen cooled sorption pump until pressures in the 10^{-4} torr range were reached. Upon opening the isolation cell the pressure in the main chamber rose to $10^{-8}5x10^{-7}$ torr and then rapidly decayed to $5x10^{-9}$-$3x10^{-8}$ torr. LEED photographs and Auger electron spectra of both crystal faces were taken. The carbonaceous deposits formed during reactions were then further characterized by subsequent H_2 (or D_2) TDS and/or by CO titrations (The crystal was

flashed to about 400 K, followed by a 36 L expossure of CO and finally by CO TDS).

2.4.3. Mass spectrometer calibration.

An attempt was made to calibrate the mass spectrometer signal to perform quantitative measurements using thermal desorption spectroscopy. Most mass spectra were taken with a 70 V ionization voltage and emission currents to maximize the signal (1.5-2.5 mAmp.). To calculate the response factors, gases were leaked into the chamber to a known pressure (measured using the ion gauge) and the mass spectrometer signal was then recorded. The response factors were calculated from the slope of pressure versus signal plots for different current amplification ranges. Examples of these results are summarized in table 2.2. The electron multiplier had a gain of about 3000.

Using the response factors for the mass spectrometer and the previously reported pumping speeds, S, the total amount of gases desorbing during TDS experiments, n, can be calculated, by using the following equation [41]:

$$n = [S/(A \cdot k \cdot T_g)] \int p \cdot dt \qquad (2.22)$$

where n is in molecules/cm^2, A is the area of the desorbing surface, k is Boltzman constant, and T_g is the gas phase temperature. The integral is obtained from the area under the TDS trace, after being corrected for ion gauge sensitivities. Due to the uncertainty in the quantities involved in these calculations, absolute coverages obtained this way are

not too reliable. Relative coverages, however, are easy to determine using the described procedure.

Measurements were made for H_2 and CO desorption after adsorption of these gases or from methanol decomposition, and for H_2 desorption from adsorbed ethylene. The corresponding TDS are shown in figs. 2.25 and 2.26, and the saturation coverages obtained from them are tabulated in table 2.3. The ion gauge was also used in these experiments to measure the pressure gradient in the UHV chamber while the desorption was taken place.

The CO coverage obtained, Θ_{sat}=0.46-0.61, is in agreement with values reported in the literature [42]. The hydrogen saturation coverage, on the other hand, is belived to be Θ_{sat}=0.5 rather than 0.25, as was obtained in this work [41,43]. Ethylene TDS yields approximately the same amount of hydrogen molecules as a saturated overlayer of H_2 chemisorbed. Using the reported value for H_2 saturation an ethylene saturation coverage of a quarter of a monolayer is obtained, in agreement with results from other techniques [44-48]. Methanol decomposition produced exclusively H_2 and CO [49], and the TD spectra agree well with those reported in the literature (fig. 2.26). The absolute coverage, however, was not reported. No definitive conclusion can be obtained in this case from our data, since different values were obtained depending on whether H_2 or CO were used: Θ_{sat}=0.07 using the CO TDS data, or Θ_{sat}=0.04 using the H_2 trace for the calculations (relative to the value Θ_{sat}=0.5 for hydrogen chemisorption). Similar

results were obtained for Rh(111).

2.4.4. Mass spectrometry for kinetic studies.

Ethylene deuteration and ethane deuterium exchange reactions were followed using the mass spectrometer by leaking the gases into the vacuum chamber during the experiments, at a rate of about 50 mm^3/min (see above). Mass spectra in the 1-50 amu range like the one in fig. 2.27 were recorded periodically. The electron energy of the ionizer was set at 70 eV. The composition of the mixtures were obtained by deconvoluting the data between 26 and 36 amu using spectra for the pure gases reported in ref 50 and summarized in table 2.4. The standard spectra for pure ethylene and ethane were similar to those obtained using the experimental spectrometer ioniser settings. The table provides the intensity of the different peaks for each pure compound referred to the parent peak. No attempts were made to try to refer all values to a single parent peak. Isotopic effects or differences in sensitivity for ethane versus ethylene were not taken into consideration. This latter factor would cause an overestimation of the rates for ethylene deuteration, since the ethylene signal has been reported to be about two thirds as big as the one obtained from the same pressure of ethane [51]. However, kinetic studies performed simultaneously using both mass spectrometric and gas chromatographic detection were in very good agreement (see chapter 3).

The ethane product distribution was deconvoluted from spectra like fig. 2.27 using a recurrent method based on the set of equations:

$$D_n = (1/\alpha^n_{30+n}[M_{30+n} - \sum_{i=n+1}^{6} D_i \cdot \alpha^i_{30+n}] \qquad (n=6 \text{ to } 0) \qquad (2.23)$$

where α^n_{30+n} is the signal intensity of d_n at 30+n amu (from table 2.4) and M_{30+n} is the signal of the mixture spectrum at 30+n amu. D_n is proportional to the amount of the corresponding deuterated ethane, d_n, so the final composition can later be normalized to 100%. An example of the data obtained after ethane deuterium exchange, using fig. 2.27, is shown in table 2.5.

As a further test of the accuracy of the previous analysis, a mass balance was performed to check that the amount of hydrogen and deuterium atoms in the reaction mixtures remained constant at all times. Examples for ethane deuterium exchange and ethylene hydrogenation are presented in tables 2.5 and 2.6 respectively. The proportion of deuterium atoms in the H_2-D_2 mixture was calculated from the relative heights of the 2,3 and 4 amu peaks in the spectra, after correcting for different sensitivities (1 for H_2, 1.3 for HD and 1.7 for D_2). In the case of ethylene deuteration, ethylene deuterium exchange was also considered (20% of the rate of deuteration, as reported in chapter 3), although this contribution was negligible. The results agree for both cases within 5-10%, although higher hydrogen equivalent pressures were always obtained at high reaction conversions.

A more detailed analysis of the reaction mixture was attempted for ethane deuterium exchange by using high resolution mass spectrometry and H- and ^{13}C-NMR. The sample was trapped from the reaction loop

using a glass "U"-shaped tube with two stopcocks at each end, by cooling it with liquid nitrogen. This sample was then transfered to either a vacuum pyrex flask or to a 10 mm NMR glass tube that was then sealed. The sample pressure was about 2-3 atm. A summary of the mass spectrometric data from this experiment is presented in table 2.7. From the data for the 30-36 amu range, a distribution similar to the one shown previously can be obtained. In this case the set of equations used were of the form

$$D_n = M_{30+n} \cdot f_n \qquad (n=0 \text{ to } 6) \qquad (2.24)$$

where f_n is the fraction of the M_{30+n} signal that corresponds to the molecular peak of d_n (table 2.7). A cracking probability to form CX_3 from C_2X_6 in the ioniser can be calculated by

$$\chi_{15} = 2[\sum C_2X_6 / \sum CX_3] \qquad (2.25)$$

where CX_3 are calculated using equations similar to 2.24. Finally, the following set of equations are used to obtain the amounts of symetrically (s) and asymetrically (a) deuterated ethanes:

$$\begin{aligned}
\chi_{15} \cdot CD_3 &= 2d_6 + d_5 + d_4^a + d_3^a \\
\chi_{15} \cdot CD_2H &= d_5 + 2d_4^s + d_3^s + d_2^a \\
\chi_{15} \cdot CDH_2 &= d_4^a + d_3^s + 2d_2^s + d_1 \\
\chi_{15} \cdot CH_3 &= d_3^a + d_2^a + d_1 + 2d_0
\end{aligned} \qquad (2.26)$$

Unfortunately, two of the previous equations are dependent on the other two (since one is used to calculate χ_{15} and the other is set by the fact that the H/D ratio is fixed). Therefore, no definite answer can

be obtained. Using other fragments only complicate the calculations by introducing new cracking probability parameters. It seems, however, that at least half of the total $d_2+d_3+d_4$ is assymetrically substituted (that is, they are in the form of CD_2HCH_3, CD_3CH_3 and CD_3CDH_2).

H- and ^{13}C-NMR analysis were also performed on the same sample. The spectra, taken at 250 MHz, are shown in fig. 2.28. The proton NMR signal shifts with the number of deuterium substitutions, on the order of 2 Hz per deuterium, as has been seen for methane [52]. However, the spectra from our experiments merely broaden. The ^{13}C signal, on the other hand, couples with both H and D nucleii (coupling constants of 125 and 19 Hz respectively, as seen for methane [53]). Due to the low natural abundance of ^{13}C isotopes, the signal from our sample is too weak to obtain an aceptable signal to noise ratio. The spectrum presented was taken by decoupling the proton signal, and was averaged over a period of 16 hours. No conclusion can be obtained from these results.

FIGURE CAPTIONS.

Fig. 2.25. Hydrogen thermal desorption spectra (2 amu) after H_2 (a) and C_2H_4 (b) saturation of a Pt(111) surface at 130 K. The heating rate was about 35 K/sec.

Fig. 2.26. Hydrogen (2 amu) and CO (28 amu) thermal desorption spectra from a Pt(111) surface saturated with methanol at 130 K. Heating rate ≈ 35 K/sec.

Fig. 2.27. Mass spectrum of an ethane deuterium exchange reaction mixture. Taken after 20 minutes. The reaction mixture was composed of 200 torr C_2H_6 + 2000 torr D_2, on a rhenium covered platinum surface at 573 K.

Fig. 2.28. Proton and ^{13}C NMR spectra of an ethane deuterium exchange reaction mixture. Taken after 125 minutes of reaction of 200 torr C_2H_6 with 2000 torr D_2 over Pt(111) at 573 K.

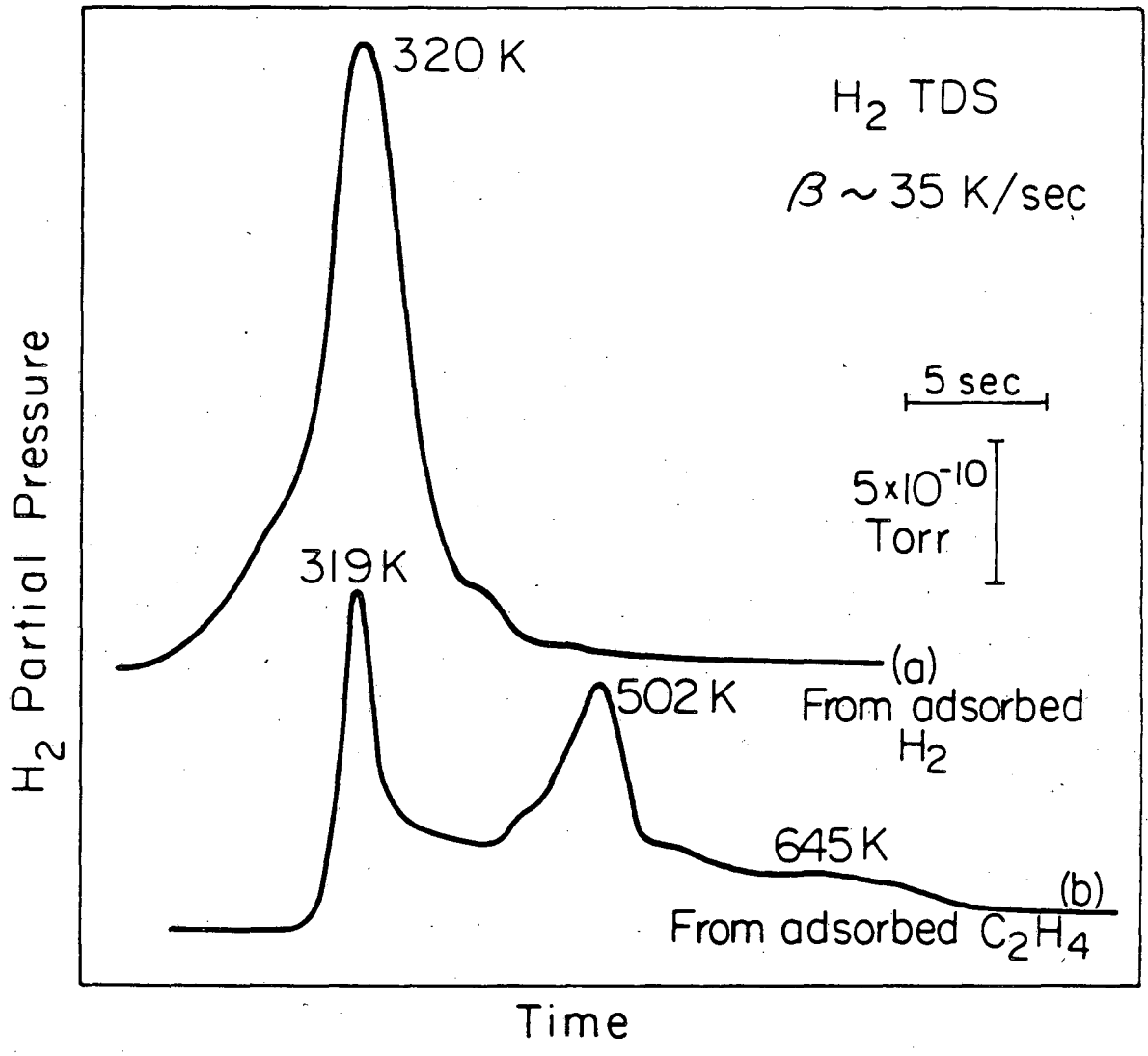

XBL8312-6667

fig. 2.25

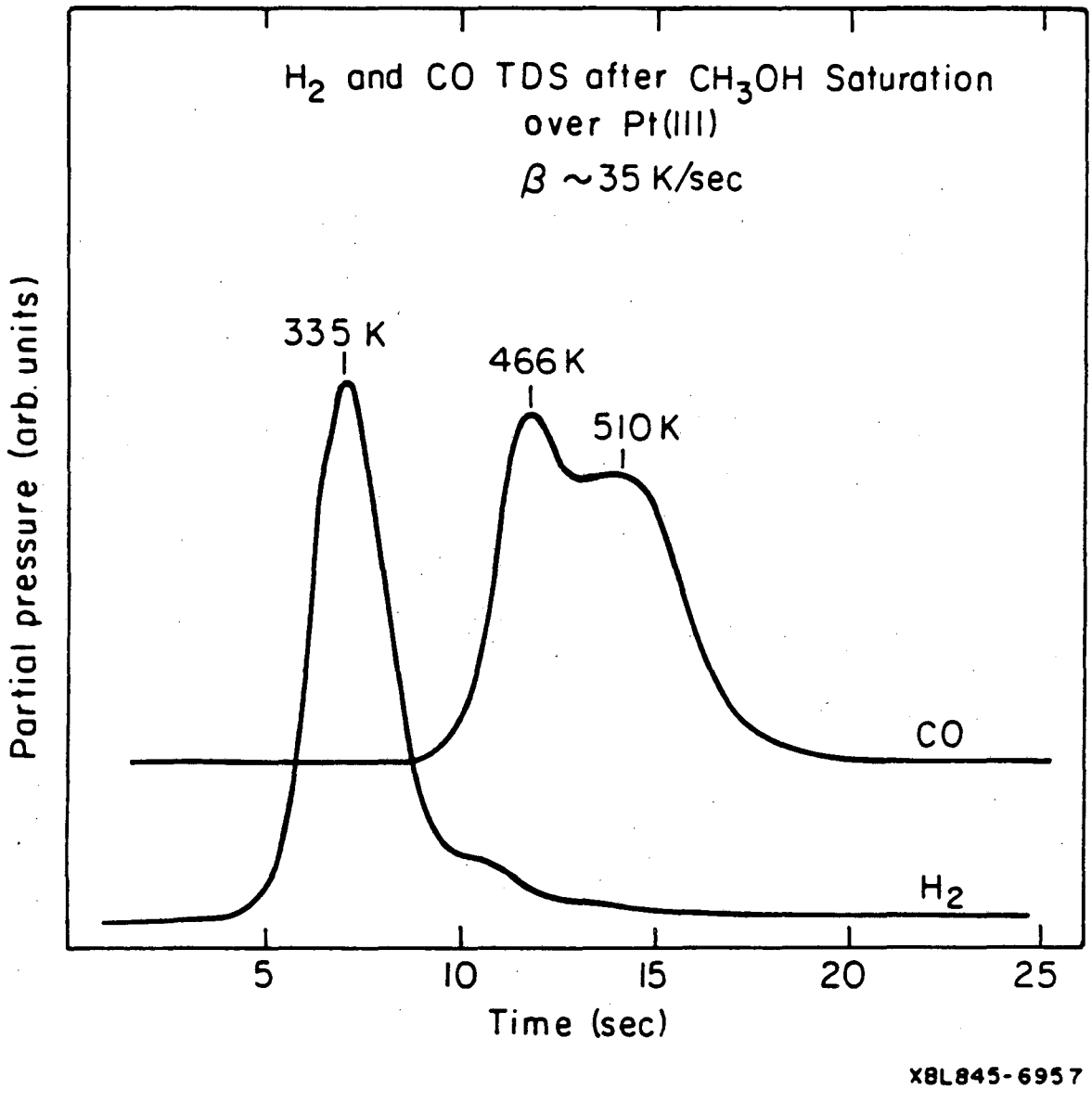
H2 and CO TDS after CH3OH Saturation
over Pt(111)
β ~35 K/sec
335 K
466 K
510 K
CO
H2
Partial pressure (arb. units)
5
10
15
20
25
Time (sec)
XBL845-6957

fig. 2.26

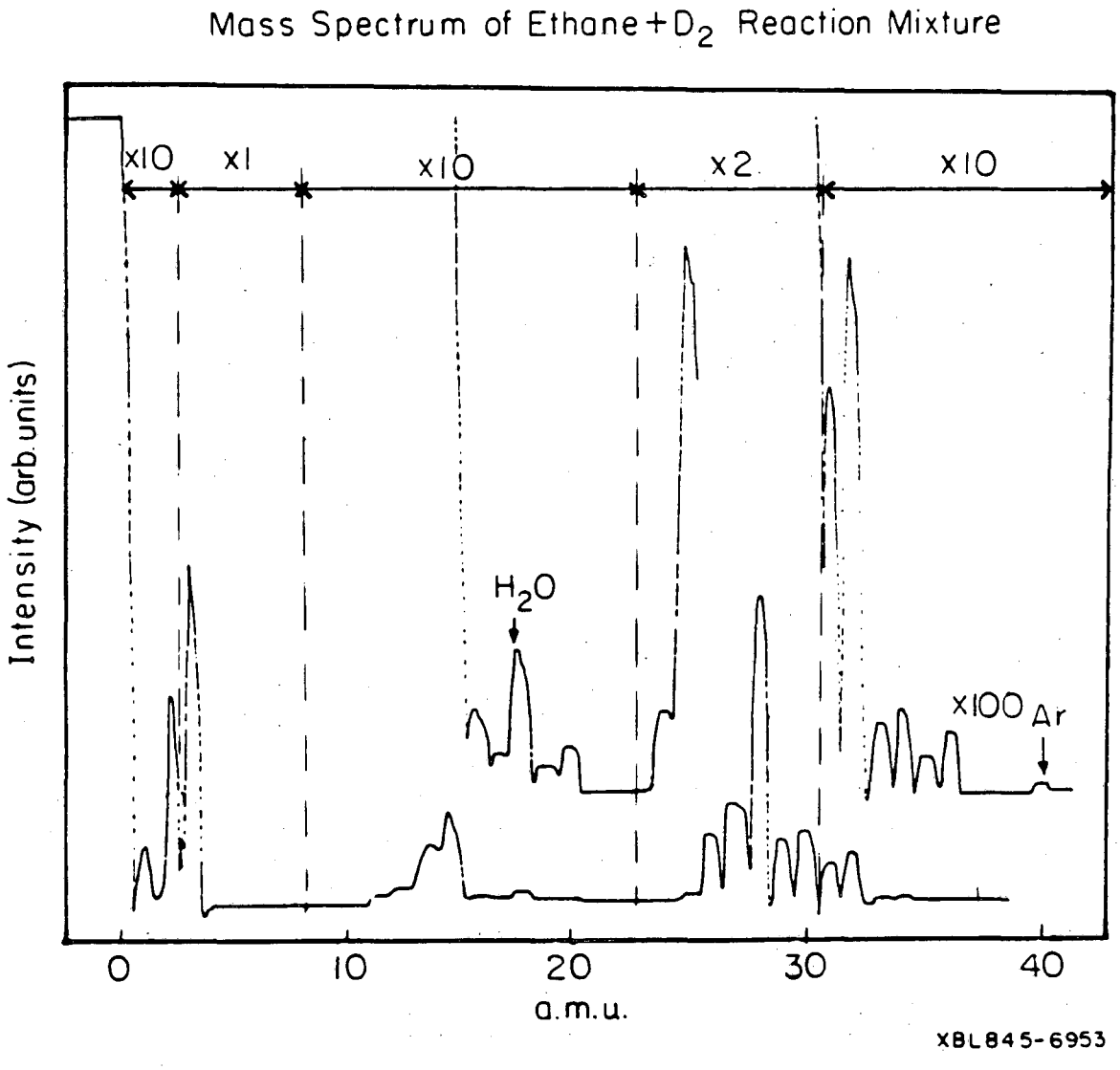
Mass Spectrum of Ethane+D_2 Reaction Mixture
x10
x1
x10
x2
x10
H_2O
x100 Ar
Intensity (arb.units)
0
10
20
30
40
a.m.u.
XBL845-6953

fig. 2.27

NMR Spectra of Ethane + D_2 Reaction Mixture

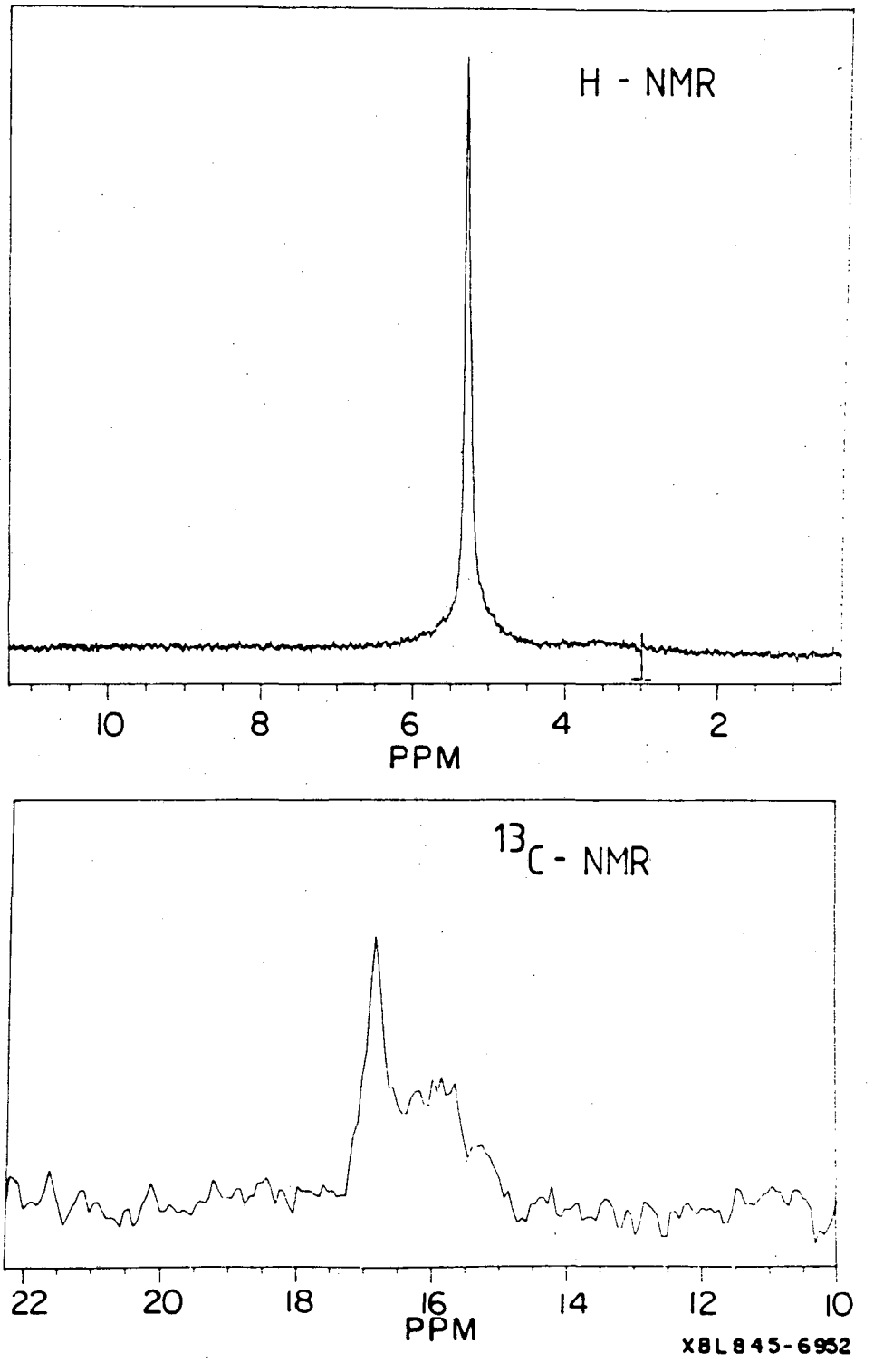

fig. 2.28

Table 2.1

List of reagents with sources, purities and major impurities

Reagent	Source	Purity[a]	Impurities[a]
O_2	Matheson-LBL	>99.9	CO
H_2	Matheson-LBL	>99.99	-
D_2	Matheson	>99.5 D_2 >99.95 D_2+HD+H_2	-
CO	Matheson-LBL	>99.5	-
C_2H_4	Matheson	>99.98	-
C_2H_6	Matheson	>99.96	-
i-C_4H_{10}	Matheson	>99.96	C_2H_6, i-C_4H_8
neo-C_5H_{12}	Matheson	>99.92	n-C_4H_{10}, n-C_4H_8
n-C_6H_{14}	Phillips	>99.95	methylcyclopentane 3-methylpentane C_6H_6
Methylcyclopentane	Aldrich	>99.5	cyclohexane, n-C_6H_{14}, C_6H_6
	Phillips	>99.96	Same as Aldrich
Cyclohexane	Matheson	>99.8	C_6H_6, n-C_6H_{14}
Cyclohexene	Matheson	>99.6	cyclohexane, C_6H_6 methylcyclopentane
C_6H_6	Matheson	>99.8	methylcyclopentane cyclohexane

a) In weight percent, as measured by gas chromatography

Table 2.2

Response factors for mass spectrometry[a].

Gas (amu)	Mass spectrometer amplification[b] 10^{-7}	10^{-8}	10^{-9}	σ[c]
CO (28)	0.943	0.862	-	1.01
H_2 (2)	2.70	2.38	-	0.41
D_2 (4)	1.59	1.41	-	0.41
C_2H_4 (27)	-	0.200	0.123	-
C_2H_6 (30)	-	0.079	0.060	-

a) Relative to N_2 when using a resolution of $\Delta M/M=0.02$.

b) In Amps/torr

c) Sensitivity of the ion gauge, refered to N_2, from ref. 40.

Table 2.3

Absolute saturation coverages of hydrogen, carbon monoxide and methanol adsorption over Pt (111)[a].

Gas adsorbed	Gas desorbed	S(l/s)	detection method I.G.	detection method M.S.
CO	CO	450	0.46	0.61
H_2	H_2	850	0.25	0.28
CH_3OH	CO	450	0.074	0.066
	H_2	850	0.15	0.11
C_2H_4	H_2	850	0.36	0.21
C_2H_3 (Ethylidyne)	H_2	850	-	0.10

a) in molecules/Pt atom. S is the pumping speed, and I.G. and M.S. are ion gauge and mass spectrometer, respectively.

Table 2.4

Mass spectrum cracking patterns of ethanes and ethylene[a].

	Ethane							
amu	d_0	d_1	d_2	d_3	d_4	d_5	d_6	Ethylene
26	23	14	10	3	3	3	3	62.3
27	33.3	24	23	13	12	8	0.2	64.8
28	100	48	37	16	68	23	21	100
29	2.2	100	78	20	68	78	0.7	2.2
30	26.2	22	100	100	68	27	27	-
31	0.6	31	24	21	100	100	1	-
32	-	-	38	15	51	89	100	-
33	-	-	-	29	27	27	2	-
34	-	-	-	-	44	7	15	-
35	-	-	-	-	-	47	0.8	-
36	-	-	-	-	-	-	19	-

a) Signal intensity relative to the parent peak.

Table 2.5

Mass spectrum intensity data from fig. 2.27.

i(amu)	30	31	32	33	34	35	36
M_i[a]	790	90.5	119.5	21	19	8.5	14

Gas composition

Ethane	d_0	d_1	d_2	d_3	d_4	d_5	d_6
d_i[b]	24.6	1.249	0.458	0.373	0.154	0.168	0.737
d_1(%)	88.7	4.50	1.65	1.35	0.55	0.61	2.66

Deuterium mass balance

A.- Initial: 200 torr C_2H_6 + 2000 torr D_2

Pressure equivalent: D_2 = 2000 torr

H_2 = 600 torr

B.- Final: 11.3% conversion, $\overline{M}$ = 2.89, D in H_2-D_2 mixture = 96.7%[c]

Pressure equivalent: $D_2 = 0.967 \times 2000 + 0.113 \times 2.89 \times 200/2$
$= 1967$ torr

$H_2 = 0.033 \times 2000 + 0.113 \times (6-2.89) \times 200/2$
$= 633$ torr

a) Signal intensity, in arbitrary units.

b) Calculated using eq. 2.23.

c) From mass spectrum, fig. 2.27.

Table 2.6

H_2-D_2 mass balance after ethylene deuteration.

A.- Initial conditions: 10 torr C_2H_4 + 20 torr D_2

Pressure equivalent: D_2 = 20 torr

H_2 = 2x10 = 20 torr

B.- Final conditions: 68.5% conversion to ethane, $\bar{M}$ = 1.92, D atoms in H_2-D_2 mixture = 85.9%.

Pressure equivalent:

D_2=(20-0.685x10)x0.859	=11.30	(in H_2-D_2)
+10x0.685x1.92/2	= 6.58	(in C_2H_6)
+10x(1-0.685)x0.2x0.685/2	= 0.22	(in (C_2H_4)
Total	=18.10 torr	

H_2=Total initial - D_2 final

=(20+20) - 18.10 =21.90 torr

Table 2.7

High resolution mass spectrum of an ethane mixture after deuterium exchange reaction.

amu	Total intensity	Fragment	% signal
12	1.1		
13	1.1		
14	8.0	CD	44
		CH_2	56
15	5.5	CHD	23
		CH_3	77
16	5.7	CD_2	74
		CH_2D	26
17	2.9		
18	4.8		
28	100	C_2D_2	28
		C_2H_2D	8
		C_2H_4	64
29	43.7	$^{13}CCH_4$	2
		C_2HD_2	34
		C_2H_3D	36
		C_2H_5	28
30	62.6	C_2D_3	45
		$C_2H_2D_2$	37
		C_2H_4D	4
		C_2H_6	14
31	53.4	C_2HD_3	91
		$C_2H_3D_2$	4
		C_2H_5D	5
32	74.3	C_2D_4	92
		$C_2H_2D_3$	5
		$C_2H_4D_2$	3

Table 2.7 (cont.)

amu	Total intensity	Fragment	% signal
33	10.9	$^{13}CCD_4$	12
		C_2D_4H	65
		$C_2D_3H_3$	23
34	12.0	C_2D_5	60
		$C_2D_4H_2$	40
35	6.8		
36	6.4		

2.5. References.

1) D.W. Blakely, E. Kozak, B.A. Sexton and G.A. Somorjai, J. Vac. Sci. Technol., 13, 1091 (1976).

2) W.D. Gillespie, Ph.D. Thesis, University of California, Berkeley 1980.

3) "Vacuum Physics and Technology", G.L. Weissler and R.W. Carlson, eds., Academic Press, New York 1979.

4) R.K. Herz, W.D. Gillespie, E.E. Petersen and G.A. Somorjai, J. Catal., 67, 371 (1981).

5) S.M. Davis, Ph.D. Thesis, University of California, Berkeley 1981.

6) S.M. Davis, F. Zaera and G.A. Somorjai, J. Am. Chem. Soc., 104, 7453 (1982).

7) W.A. Dietz, J. Gas Chromatography, 5, 68 (1967).

8) A.L. Cabrera, N.D. Spencer, E. Kozak, P.W. Davis and G.A. Somorjai, Rev. Sci. Instrum., 53, 1888 (1982).

9) A.L. Cabrera, H. Heinemann and G.A. Somorjai, J. Catal., 75, 7 (1982).

10) J.E. Crowell, Ph.D. Thesis, University of California, Berkeley 1984.

11) R.D. Kelley and D.W. Goodman, in "The Chemical Physics of Solid Surfaces and Heterogeneous Catalysis", D.A. King and D.P. Woodruff, eds., Elsevier, Amsterdam 1982.

12) G. Ertl and J. Küppers, "Low Energy Electrons and Surface Chemistry", Verlag-Chemie, Germany 1974.

13) R. Weissmann and K. Müller, Surf. Sci. Reports, 105, 251 (1981).

14) P.B. Needham, T.J. Driscoll and N.G. Rao, Appl. Phys. Lett., 21, 502 (1972).

15) T.E. Gallon, Surf. Sci., 17, 486 (1969).

16) M.A. Van Hove and S.Y. Tong, "Surface Crystallography by LEED", Springer-Verlag, Berlin 1979.

17) G. Comsa, Surf, Sci., 81, 57 (1979).

18) G.A. Somorjai, "Chemistry in Two Dimensions: Surfaces", Cornell University Press, Ithaca 1981.

19) D. Menzel, in "Interactions on Metal Surfaces", R. Gomer, ed., Springer-Verlag, New York 1975.

20) P.A. Redhead, Vacuum, 12, 203 (1962).

21) D. Edwards, Jr., Surf. Sci., 54, 1 (1976).

22) C.-M. Chan, R. Aris and W.H. Weinberg, Appl. Surf. Sci., 1, 360 (1978).

23) E.L. Garfunkel, Ph.D. Thesis, University of California, Berkeley 1983.

24) M. Salmeron, R.J. Gale and G.A. Somorjai, J. Chem. Phys., 70, 2807 (1979).

25) "Handbook of X-Ray and Ultraviolet Photoelectron Spectroscopy", D. Briggs, ed., Heyden, London 1978.

26) T.A. Carlson, "Photoelectron and Auger Spectroscopy", Plenum Press, New York 1975.

27) C.D. Wagner, W.M. Riggs, L.E. Davis, J.F. Moulder and G.E. Muilenberg, "Handbook of X-Ray Photoelectron Spectroscopy", Perkin Elmer Corp., Minnesota 1978.

28) H. Ibach and D.L. Mills, "Electron Energy Loss Spectroscopy and Surface Vibrations", Academic Press, New York 1982.

29) P. Tétényi and L. Babernics, J. Catal., 8, 215 (1967).

30) B.H. Davis, J. Catal., 29, 398 (1973).

31) S.V. Norval, S.J. Thompson and G. Webb, Appl. Surf. Sci., 4, 51 (1980).

32) K. Klier, A.C. Zettlemoyer and H. Leidheiser Jr., J. Chem. Phys., 52, 589 (1970) and references therein.

33) S.M. Davis, B.E. Gordon, M. Press and G.A. Somorjai, J. Vac. Sci. Technol., 19, 231 (1981).

34) Silicon Charged Particle Radiation Detectors Instruction Manual, E.G. & G. Ortec Corp.

35) C.A. Pietersen, C.M.A.M. Mesters, F.H.P.M. Habraken, O.L.I. Gijzeman, J.W. Geus and G.A. Bootsma, Surf. Sci., 107, 353 (1981).

36) P. Lemoine, J. Brenet and M. Gross, C. R. Acad. Sc. Paris, 274, Ser C, 1 (1972).

37) P. Lemoine and M. Gross, J. Thermal Anal., 6, 159 (1974).

38) A.K. Baev, V.V. Dem'yanchuk, G. Mirzoev, G.I. Novikov and N.E. Kolobora, Russ. J. Phys. Chem., 45, 777 (1971).

39) "Rhenium", B.W. Gonser, ed., Elsevier, Amsterdam 1962, pp 23-35.

40) R. Holanda, J. Vac. Sci. Technol., 10, 1133 (1973).

41) K. Christmann, G. Ertl and T. Pignet, Surf. Sci., 54, 365 (1976).

42) See, for instance, R.A. Shigeishi and D.A. King, Surf. Sci., 58, 379 (1976).

43) J. Lee, J.P. Cowin and L. Wharton, Surf. Sci., 130, 1 (1983).

44) P.C. Stair and G.A. Somorjai, J. Chem. Phys., 66, 2036 (1977).

45) L.L. Kesmodel, P.C. Stair, R.C. Baetzold and G.A. Somorjai, Phys. Rev. Lett., 36, 1316 (1976).

46) L.L. Kesmodel, R.C. Baetzold and G.A. Somorjai, Surf. Sci., 66, 299 (1977).

47) S.M. Davis, F. Zaera, B.E. Gordon and G.A. Somorjai, Submitted to J. Catal.

48) W.T. Tysoe, F. Zaera, S.M. Davis and G.A. Somorjai, Submitted to Surf. Sci.

49) B.A. Sexton, Surf. Sci., 102, 271 (1981).

50) "Registry of Mass Spectra Data", Vol 1, E. Stenhagen, S. Abrahamson and F.M. McLafferty, eds., pp 1-3 (1974).

51) "API 44 Selected Mass Spectral Data", Thermodynamics Research Center, Department of Chemistry, Texas A&M University, 1969.

52) R.A. Bernheim and B.J. Lavery, J. Chem. Phys., 42, 1464 (1965).

53) M. Alei, Jr., and W.E. Wageman, J. Chem. Phys., 68, 783 (1978).

54) "Thermal Radiative Properties. Metallic Elements and Alloys", Y.S. Touloukian and D.P. DeWitt, eds., IFI/Plenum, New York 1970, pp. 559-570.

CHAPTER THREE: THE ROLE OF ETHYLIDINE IN HIGH PRESSURE REACTIONS.

3.1. Ethylidyne formation and stability.

3.1.1. Introduction.

Extensive effort in several research groups have lead to a fairly complete understanding on the details of ethylene chemisorption over (111) metallic surfaces. In particular, similarities have been observed for the Pd (111) [1-5], Rh (111) [6-8] and Pt (111) [9-17] systems. Ethylene adsorbs molecularly over those surfaces with a sticking coefficient close to unity. At low temperatures, the molecules lay parallel to the metal surface almost undistorted from the gas phase structure [2,5, 6,9,14,18]. This configuration is stable up to close to room temperature, when the desorption of one hydrogen atom per ethylene molecule is detected by TDS [13], a process that is accompanied with a complete rearrengement of the remaining moiety. LEED [6-8,10], HREELS [1,3,6,12], angle-resolved ultraviolet photoemission spectroscopy (ARUPS) [4,14], TDS [6,13], near-edge X-ray adsorption fine structure spectroscopy (NEXAFS) [16], and secondary ion mass spectrometry (SIMS) [17], all indicate the formation of ethylidyne on these surfaces. In this structure one of the carbon atoms, triply bonded to the metal, sits on top of a three-fold hollow site, and the carbon-carbon bond is perpendicular to the surface so that the terminal carbon is in a methyl group. A schematic representation of such chemisorbed species is shown in fig. 3.1. Ethylidyne is then stable under ultra-high vacuum up to around 450 K, when further dehydrogenation and rearrangement occurs, possibly including carbon-carbon bond breaking, and C-H fragments are the predominant species on the surface [18]. The dehydrogenation continues with increa-

sing temperature, until eventually graphite is formed above 700 K. Similar processes are known to occur with heavier olefins [18].

The understanding of the role of ethylidyne in high pressure reactions is of primordial interest for catalysis, and is one of the major goals of this research project. For this purpose, its stability under high pressure was studied using TDS, LEED, HREELS and a radiotracer technique. It was found that a monolayer of adsorbed ethylidyne on Pt (111) (and Rh (111)) does not rehydrogenate or desorb from the surface when exposed to 1 atm. H_2 or D_2 near room temperature. The methyl group hydrogens exchange with deuterium only slowly. The extent of the exchange depends strongly on the ethylidyne coverage, but not on the deuterium pressure. A detailed TDS study of the ethylene decomposition, a careful measurement of the saturation coverage of ethylidyne, and some coadsorption experiments were also performed.

3.1.2. Results.

Thermal desorption spectra after adsorption of ethylene (6×10^{-6} Torr·sec.=6 L) over Pt (111) at 150 K are shown in fig. 3.2. The hydrogen (2 amu) and ethylene (27 amu) traces have been reported and discussed in previous publications [13]. Ethane formation (30 amu) was followed here as well. The temperature maxima for both ethylene and ethane desorption occur at 300 K, which corresponds to an activation energy of 12.0 Kcal/mole for the case of ethylidyne. Since ethane formation is not expected to be a first order process, the activation energy for this reaction was not calculated. The hydrogen TDS shows three regions with maxima at 320, 500 and above 600 K, corresponding to ethy-

lidyne formation, its decomposition into CH fragments, and total dehydrogenation, respectively. The activation energies associated with those steps are 18.4, 22.0 and 33-43 Kcal/mole [13]. The relative areas under the different TDS also contain information concerning the relative yields for each process. The total hydrogen desorption corresponds to the equivalent of 1/4 ethylene saturation coverage over Pt (111), from which one hydrogen atom per ethylene molecule is desorbed when ethylidyne forms, at 320 K (see section 2.4.3). The same quantitative measurements could not be made for ethane and undissocited ethylene, since pumping speeds (S) and ion gauge sensitivities (σ) are needed for the calculation (eq. 2.22), but rough estimates were obtained by using values of S≈400 l/s and σ=1, and the mass spectrometer response factors tabulated in table 2.2. That way values of 10 and 0.14 molec/Pt atom•sec were obtained for ethylene and ethane, respectively.

If hydrogen is preadsorbed over Pt (111) prior to C_2H_4 exposure, some changes are observed in the resulting TDS, as seen in fig. 3.3. Both ethylene and ethane peaks get broader, and disply maxima at lower temperatures. The hydrogen curve also changes, even when D_2 is used for coadsorption: the relative areas of the peaks at 320 and 500 K change, the latter being less intense on the D_2 predosed surface. The total area under the TDS decreases due to some exchange, as will be discussed latter.

The absolute value for the saturation coverage of ethylidyne was measured using several other techniques besides TDS. The XPS C 1s signal was used in order to measure the total amount of carbon over a

platinum foil surface after room temperature exposure to C_2H_4, and CO was used for calibration. XPS spectra for both ethylene and CO saturated surfaces are shown in fig. 3.4. The C 1s peak for each adsorbate were obtained at two resolutions: 0.3 and 1.1 V (pass energies of 40 and 160 V, respectively). The high resolution spectra required long data aquisition times (a couple of hours), and we found that additional carbon was deposited onto the surface. Low resolution spectra (10 minutes aquisition time) were obtained and corroborated this; they were used to estimate the amount of carbon on the surface in both cases. The results gave area ratios (normalized to the same ordinates) of $A_{ethylene}/A_{CO}=0.93$ for the low resolution spectra, and $A_{ethylene}/A_{CO}=1.24$ for the high resolution ones. Further confirmation of the increase in amount of carbon on the surface with time for ethylene adsorption was obtained using AES. Fig. 3.5 shows typical Auger spectra for saturation CO and ethylene. It is worth noticing the different shapes of the carbon 273 eV peak for the two cases. The C(273eV)/Pt(237eV) peak height ratio (R_{AES}) were used to monitor surface carbon. The results are as follow: for saturation CO, $R_{AES}=0.54$, and saturation ethylene $R_{AES}=0.63$. However, after obtaining the high resolution ethylene XPS spectrum, $R_{AES}=2.48$. This shows that, using both the C 1s XPS peak area ratios and the Auger carbon signal, the amount of carbon on the foil surface after CO and ethylene saturation at room temperature are identical to within 10%, before the surface becomes further contaminated. If it is assumed for CO $\theta_{sat}=0.5$, this implies that ethylene saturates at a coverage of 0.25.

Radiotracer experiments were carried out using the solid state detector described in the experimental section for measuring the β decay

of ^{14}C labeled compounds. Isotherms obtained for ^{14}C-ethylene chemisorption on Pt(111) at 330-570 K are shown in fig. 3.6. At temperatures below 450 K, the initial sticking coefficient was s_o=0.9±0.2, satuating at C_s=4x10^{14} molec/cm^2 [19]. This corresponds to θ_{sat}=0.27, consistent with the proposed coverage by LEED [10].

Carbon Auger signals were monitored with a retarding field analyzer, using a 10 V peak to peak modulation. The shape of the peaks were similar to those obtained using a cylindrical mirror analyzer and a foil, as shown in fig. 3.5. This limits the accuracy of the reported measurements. For CO saturation at 150 K, R_{AES}=0.48±0.04. This ratio was 0.50±0.07 for ethylene adsorbed at 150 K, and did not vary significantly as the surface was warmed to 1000 K. The electron beam was defocussed to a spot size of about 1 mm to minimize electron stimulated desorption (ESD). To further confirm that there was no ESD, CO TDS were obtained before and after taking AES spectra. These yielded identical desorption peak areas.

Since different LEED patterns were obtained for CO adsorption, there is some uncertanty in its absolute saturation coverage, but its value can certainly be placed between 0.5 and 0.6 [20,21]. This then corresponds to an ethylene saturation coverage of between 0.26 and 0.31 of a monolayer, in agreement with a value of θ_{sat}=1/4.

The stability of ethylidyne when exposed to high pressures of hydrogen was studied using the radiotracer detector and HREELS. Radiotracer decay curves representing the rehydrogenation and removal of

ethylidyne over Pt (111) surfaces are shown in fig. 3.7. These species were prepared by chemisorbing ^{14}C-ethylene at 335-345 K and 10^{-7} torr using a constant expossure of 6 L. The rehydrogenation reactions were carried out at 300-470 K in the presence of 1 atm of flowing hydrogen. The reactions were interrupted at intervals of 1-10 minutes so that the residual coverages ($\theta(t)/\theta(t=0) = \theta/\theta_o$ in cpm/cpm_o) of the radioactive surface species could be determined as a function of total reaction time. Two observations are significant: (1) the ethylidyne species became highly reactive only at temperatures higher than about 340 K, and (2) the rehydrogenation was not a first-order process. At 300 K only about 25% of the surface moieties were removed by rehydrogenation in a 30 minute reaction time. By contrast, at 370 K or higher temperatures, the same surface species underwent esentially complete rehydrogenation in just 3-5 minutes. From the initial slopes of the decay curves the activation energy for ethylidyne hydrogenation can be very roughly estimated to be 5-10 Kcal/mole.

The preceeding results were confirmed by using HREELS. Vibrational spectra of a saturation coverage of ethylidyne on Pt (111) before and after expossure to 1 atm H_2 for 7 minutes at 310 K are shown in fig. 3.8. The spectra are nearly identical, indicating that if any changes in the chemisorbed species occur during the high pressure treatment, they are reversible, and ethylidyne forms back when the sample is returned to vacuum. The only noticable changes observed are an increase in the CO signal and a peak at 735 cm^{-1}, which have been atributted to species comming from contaminants from the reaction loop. At higher temperatures, above 330 K, ethylidyne rehydrogenation becomes fast enough so

considerable amounts of CO and CH fragments from contaminants are observed in the HREELS after hydrogen treatment. Similar studies on Rh (111) show that ethylidyne is even more stable on this metal, remaining virtually intact after 1 atm H_2 exposure at up to 370 K [22].

Both Pt (111) and Rh (111) surfaces, after saturated with ethylidyne, are not able to further adsorb ethylene or CO, even after high pressure exposure to these gases. Chemisorption studies of ethylene on an ethylidyne saturated Pt (111) surface were performed by exposing such surface to both UHV and atmospheric pressures of C_2H_4 while cooling to 150 K. TDS detected at 27 amu revealed no signal due to coadsorbed ethylene. Similar studies were made using HREELS. Fig. 3.9 shows the vibrational spectrum of a deuterated ethylidyne overlayer after exposed to 10 Torr C_2H_4 for 5 minutes at room temperature. Only one new peak at 1218 cm^{-1} due to CH deformation modes could be detected, coming from either coadsorption, displacement or exchange reactions. However, most of the features coming from CCD_3 fragments remain unchanged.

Hydrogen and deuterium coadsorption experiments were performed as well. H_2 could not be adsorbed on an ethylidyne saturated surface under UHV conditions, but some coadsorption occured when 1 atm H_2 or D_2 was used. Fig. 3.10 shows both H_2 and D_2 TDS after these treatments. The 2 amu TDS obtained from CCH_3 and H_2 coadsorption (middle trace) is the sum of the contributions from ethylidyne decomposition (upper trace) and hydrogen (or deuterium) coadsorption (as seen from the 4 amu TDS when D_2 was used instead of H_2, lower trace). Some deuterium exchange in the methyl group was also observed, as illustrated in fig. 3.11.

Atmospheric H_2 exposure of an ethylidyne saturated Rh (111) surface at 310 K did not modify the overlayer structure (fig. 3.11 a and b), but when D_2 was used instead, some new peaks appeared in the HREEL spectrum, indicating the presence of C-D bonds (fig. 3.11 c). The exchange seems to occur in a stepwise fashion, with incorporation of one deuterium atom at a time. It also requires a critical deuterium coverage on the surface, because exchange is not possible under UHV on an ethylidyne saturated surface, but if partially hydrocarbon covered surfaces are used, the reaction readily takes place. Fig. 3.12, taken from ref. 13, illustrates this fact. 0.1 L (1 L=10^{-6} Torr·sec) of ethylene was used to produce a Pt (111) surface partially covered with ethylidyne. These chemisorbed species were stable at 388 K under UHV, as manifested by the similar H_2 TDS obtained before and after the heating treatment (two lower traces). When exposed to 30 L D_2, the 2 amu TDS signal decreased significantly, and the 4 amu TDS resembled that obtained from ethylidyne before exchange. The stoichiometry of the final exchanged ethylidyne was estimated to be $CCHD_2$.

3.1.3 Discussion.

As mentioned in the introduction, adsorption of ethylene over Pt (111) and Rh (111) surfaces at low temperatures is molecular [6,9,14, 18]. No changes are observed on the chemisorbed overlayer until these surfaces are heated to about 300 K, when the TDS traces indicate drastic changes in the hydrocarbon species (fig. 3.2). At 300 K some ethylene desorbs intact, the activation energy for this process being about 12 Kcal/mole. At the same temperature a small amount of ethane desorption was also detected. Since this reaction occurs at a lower tempera-

ture than that for hydrogen desorption from ethylene decomposition, it can be concluded that the ethane is produced from self-hydrogenation of ethylene, perhaps a concerted mechanism. Self-hydrogenation of ethylene have been previously reported over several metallic films, including Ni [23-26], Pd [27], W [28] and Ir [29]. A recent study of ethylene self-hydrogenation over Ni (111) single crystals concluded that this process occurs through a recombination of ethylene gas molecules with hydrogen atoms adsorbed on the surface coming from dissociative chemisorption [30]. A similar mechanism is highly improbable for the platinum case, since hydrogen desorption rates at the temperatures at which ethane forms are very high, and a H_2 peak should therefore be present in the 2 amu TDS at 300 K. Ethylidyne is also not involved in the self-hydrogenation reaction, because it is formed at temperatures 20 K higher. 30 amu TDS from an ethylidyne saturated Pt (111) surface never displayed any features, even when the experiments were carried out in an ethylene background (about 10^{-7} Torr), not surprising since no coadsorption of ethylene was ever observed.

Ethylidyne formation occurs at 320 K, as manifested by the first peak in the H_2 TDS (fig. 3.2). The changes in the TDS peak with coverage indicate that this reaction in the ethylene decomposition is a first order process, and then it can be assumed that the rate limiting step is the breaking of C-H bonds [13]. Additional evidence comes from White's group, where it was demostrated that the formation of CH_3 radicals occur at the same temperature of the hydrogen desorption by using SIMS [17]. The desorption of H_2 occurs then by hydrogen atoms recombination on the platinum surface. The activation energy for the overall process is 18.4

Kcal/mole. Further decomposition of ethylidyne is seen at much higher temperatures, probably also involving C-C bond breaking. The activation energy for the formation of CH fragments is 22 Kcal/mole, indicating the great stability of ethylidyne.

The absolute saturation coverage of ethylidyne over the (111) surface has important consequences for catalytic studies. In the original LEED work reporting the existence of ethylidyne, Somorjai and coworkers proposed that the (2x2) overlayer observed at saturation corresponded to a quarter of a monolayer [31-33]. However, Bonzel et. al. have recently measured the amount of carbon on the surfasce using XPS [14,34], and, by comparing with a CO saturated surface, reported ethylidyne saturation values of half monolayer. They then explained the LEED results as the superposition of three (2x1) domains with different orientations, rather than just one (2x2) superstructure. We have used XPS in a similar way to Bonzel and found, by contrast, that the saturation coverage is closer to 0.25 than to 0.5. We also found that long exposures of the surface to the X-rays increased the deposition of carbon from the background gases, a factor that could explain the discrepancies between our results and those from refs. 15 and 34. To further check our results, we employed several different techniques to obtain independent corroboration of this value of 0.25, including an absolute calibration using radioactive ^{14}C-ethylene. All experiments were in excellent agreement.

A saturation coverage of a quarter of a monolayer with the formation of a (2x2) ordered overlayer is effective in blocking further

adsorption of most gaseous molecules. In fig. 3.13 the Van der Waals radii have been used to represent a top view of an ethylidyne saturated surface. Although quite open at first glance, ethylene or CO molecules can not be inserted in the free spaces between the ethylidyne moieties. The experimental results confirm this statement: no further ethylene or CO could be adsorbed together or on top of an ethylidyne saturated surface. Only some hydrogen could be coadsorbed at high pressures. This conclusion is of paramount importance for the understanding of high pressure catalytic reactions, as will be discussed in detail in the following section.

Rehydrogenation and deuterium exchange of ethylidyne saturated surfaces are slow processes over both Pt and Rh (111). Atmospheric rehydrogenation rates could be estimated from the radioactivity (fig. 3.7) and HREELS experiments (figs. 3.8 and 3.11). Precise quantitative measurements from the vibrational spectra are difficult to obtain; the cross sections and dynamic dipoles for each vibrational mode are not known. However, estimates of the relevant rates were obtained on the basis of some assumptions [22]. Turnover frecuencies on the order of 10^{-4} for platinum and 10^{-5} for Rh were obtained at near room temperature. Similar calculations for hydrogen-deuterium exchange of the methyl group gave values of 10^{-5} for Pt and 10^{-4} for Rh, all rates expressed in molecules/metal atom·sec. It can be seen that all these processes are very slow as compared to the rates for ethylene hydrogenation over the same surfaces, since these are on the order of 10 for Pt and 100 or more for Rh (see fig. 3.14 and section 3.2). This conclusion is a key ingredient in the elucidation of a mechanism for ethylene

hydrogenation presented in the next section. It is also interesting that both hydrogenation of ethylene and deuterium exchange were faster over Rh as compared to Pt, but rehydrogenation of ethylidyne followed the opposite trend. This suggests that the former reactions may have a common limiting step, but one that is not important for the rehydrogenation process.

Concerning the mechanism for exchange in the methyl group of ethylidyne, it has been stated that dehydrogenation can not preceed the incorporation of the new deuterium atom [13]. If that were the case, heating of ethylidyne in vacuum would cause the removed hydrogen atoms to recombine on the surface and desorb, thus modifying the structure of the remaining hydrocarbon fragment. These changes were not observed (fig. 3.12). In addition, the incorporation process must be stepwise, since exchange of CCH_3 moieties yielded mainly CCH_2D species in the earlier stages of the reaction, and similarly, $CCHD_2$ was obtained after CCD_3 exposure to H_2 [22]. The need for H_2 or D_2 to reach the metallic surface in order to dissociate was also established. All these conclusions are in excellent agreement with the results by White et. al. [35], who followed the exchange of an ethylidyne surface with 10^{-6} Torr D_2 at 350-400 K using SIMS. They also observed stepwise deuterium incorporation in the methyl group, with rates on the order of 10^{-2} exchanges/Pt atom·sec. at 383 K. Dehydrogenation of ethylidyne as the first step was ruled out, and an ethylidene intermediate, $CDCH_3$, was proposed. We propose a similar mechanism (fig. 3.15), involving the formation of ethylidene, followed by a concerted displacement of one of the hydrogen atoms in the methyl group by the deuterium in the α carbon. This mechanism is analogous to the one proposed in the next section for ethlene hydrogenation.

FIGURE CAPTIONS

Fig. 3.1. Atomic surface structure for ethylidyne adsorbed over Pt (111) single crystal surfaces.

Fig. 3.2. H_2 (2 amu), C_2H_4 (27 amu) and C_2H_6 (30 amu) TDS curves corresponding to the decomposition of C_2H_4 adsorbed on Pt (111) surfaces at 150 K. The exposure was 6 L (1 L=10^{-6} Torr•sec.).

Fig. 3.3. C_2H_4 (27 amu) and C_2H_6 (30 amu) TDS curves corresponding to the decomposition of C_2H_4 adsorbed over clean (dashed lines) and hydrogen predosed Pt (111) surfasces at 150 K. Expossures were 6 L for C_2H_4 and 30 L for hydrogen.

Fig. 3.4. Carbon C 1s XPS spectra after room temperature saturation on a platinum foil: a) ethylene, 40 V pass energy, b) CO, 40 V pass energy, c) ethylene, 160 V pass energy, d) CO, 160 V pass energy. Vertical bars represent 1000 counts.

Fig. 3.5. Auger spectra of a Pt(111) single crystal surface after saturation at 150 K with ethylene (a) and CO (b). The spectra were obtained with a retarding field analyzer and 10 V modulation.

Fig. 3.6. Adsorption isotherms (left frame) for ^{14}C-C_2H_4 chemisorption on Pt(111) at 330-570 K. The adsorption behavior below 420 K is well described by a first order langmuir model (right frame).

Fig. 3.7. Radiotracer decay curves illustrating the rehydrogenation of ^{14}C-ethylidyne chemisorbed on Pt (111) under 1 atm H_2.

Fig. 3.8. Vibrational spectra of ethylidyne over Pt (111) at 310 K. a) Saturated overlayer; b) after 7 min. treatment with 1 atm H_2.

Fig. 3.9. Vibrational spectrum of deuterated ethylidyne over Rh (111) after room temperature expossure to 10 Torr C_2H_4 (middle trace). CCD_3 and CCH_3 spectra are also shown as references.

Fig. 3.10. TDS demonstrating the coadsorption of hydrogen and ethylidyne. Shown is the 4 amu TDS after 1 atm D_2 exposure of ethylidyne (lower trace) and the 2 amu TDS after the same treatment with H_2 (middle). Ethylidyne H_2 TDS is given for comparison (top).

Fig. 3.11. Vibrational spectra of ethylidyne on Rh (111) spectra illustrating the deuterium exchange in the methyl group. Spectra B and C were obtained from ethylidyne after exposure to 1 atm H_2 and D_2, respectively. CCH_3 and CCD_3 spectra are shown for comparison.

Fig. 3.12. H_2 and D_2 TDS from the decomposition of ethylidyne before and after deuterium exchange. Shown are ethylidyne H_2 TDS before (lower) and after (2^{nd} trace) heating in vacuum, and H_2 and D_2 TDS after exposure to 30 L D_2 at 388 K.

Fig. 3.13. Structure of the (2x2) CCH_3 overlayer over Pt (111). Approximated Van der Waals radii were used in the drawing.

Fig. 3.14. Comparison of hydrogenation and exchange rates over Pt and Rh (111) single crystal surfaces at near room temperature.

Fig. 3.15. Schematic representation of the mechanism for deuterium exchange in the methyl group of ethylidyne over Pt and Rh (111).

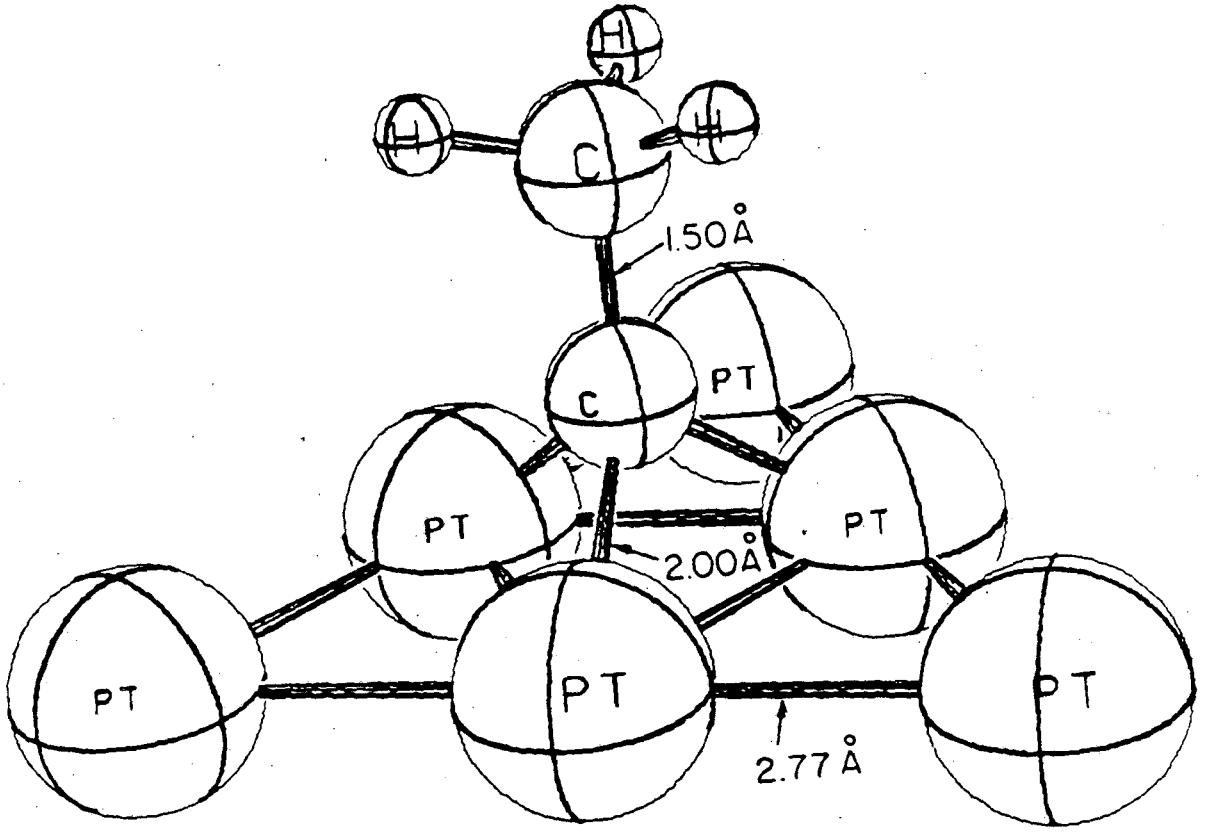

Pt (111) + ethylidyne

XBL794-6167

fig. 3.1

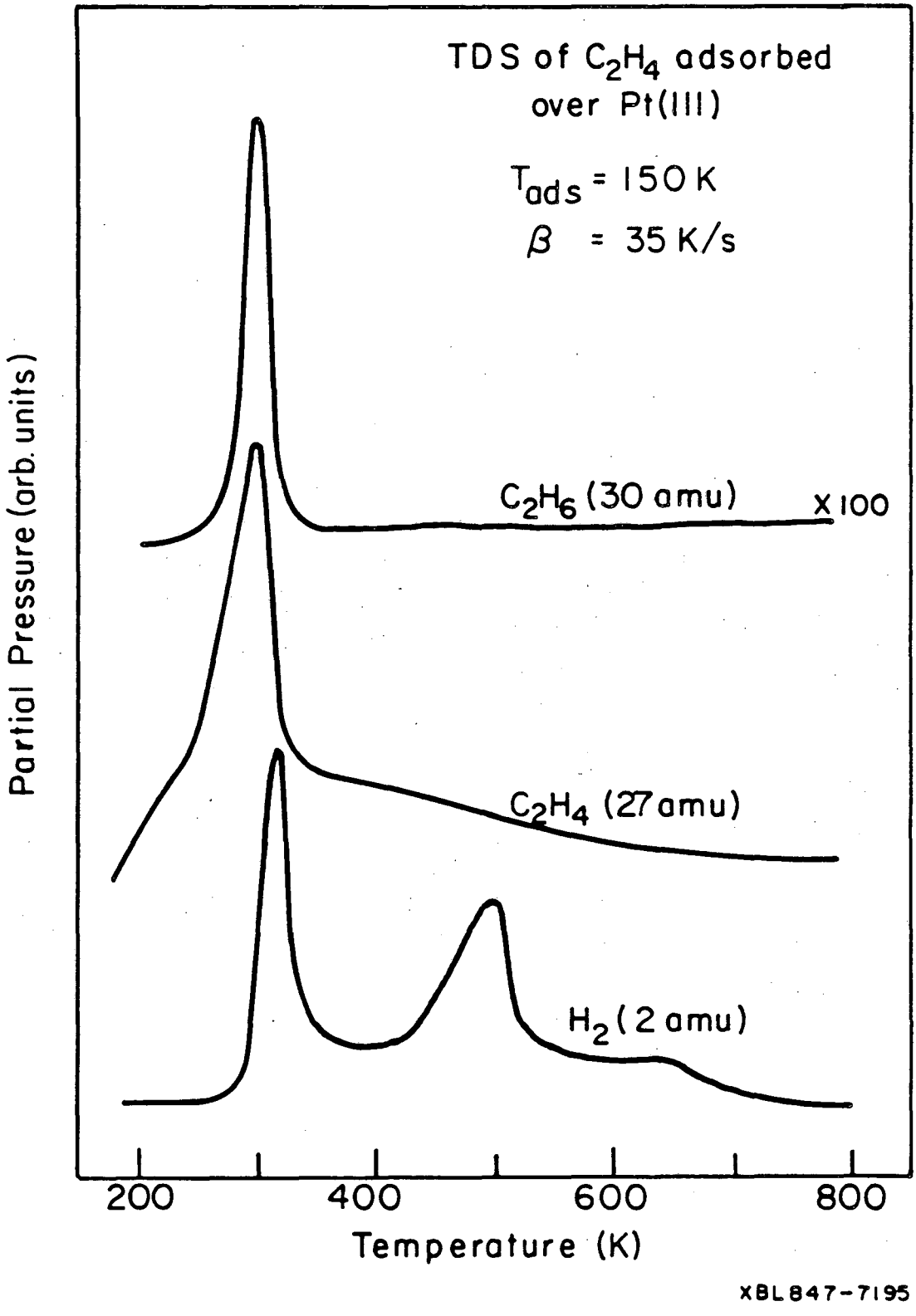
TDS of C_2H_4 adsorbed over Pt(111)
T_{ads} = 150 K
β = 35 K/s
C_2H_6 (30 amu)
x100
C_2H_4 (27 amu)
H_2 (2 amu)
Partial Pressure (arb. units)
200
400
600
800
Temperature (K)
XBL847-7195

fig. 3.2

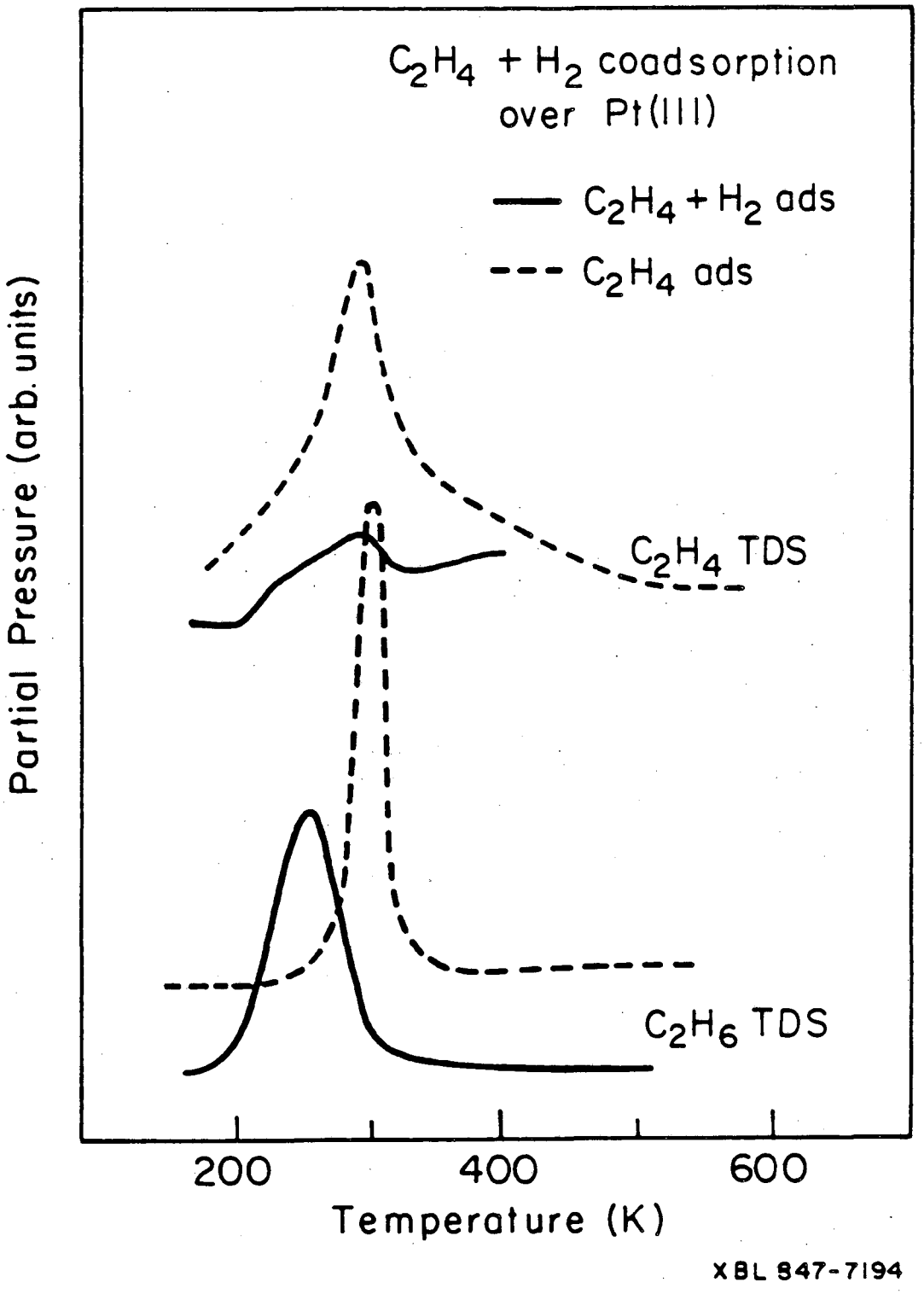
$C_2H_4 + H_2$ coadsorption
over Pt(111)
$C_2H_4 + H_2$ ads
C_2H_4 ads
C_2H_4 TDS
C_2H_6 TDS
Partial Pressure (arb. units)
200
400
600
Temperature (K)
XBL 847-7194

fig. 3.3

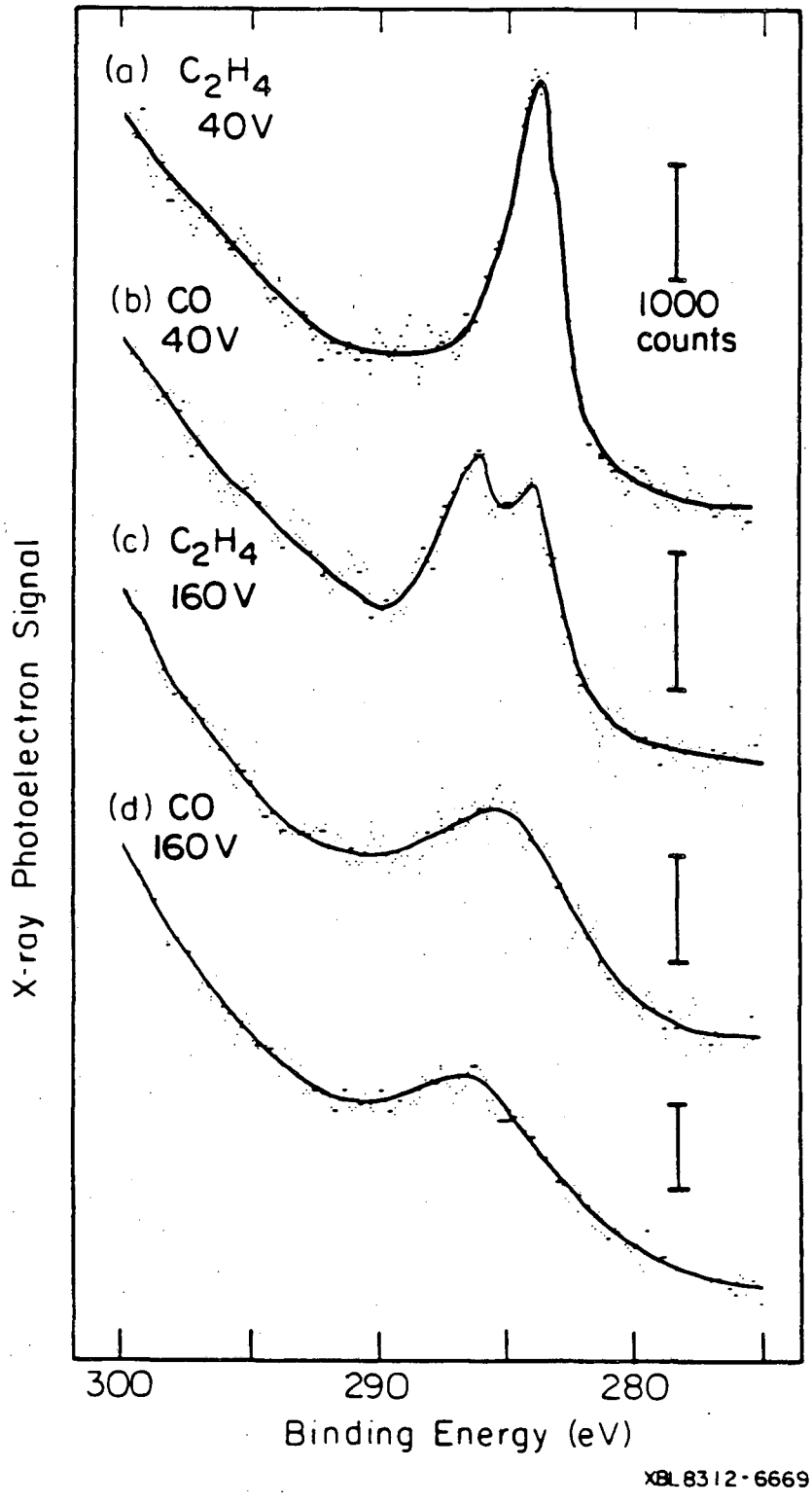
(a) C_2H_4
40V
(b) CO
40V
(c) C_2H_4
160V
(d) CO
160V
1000
counts
X-ray Photoelectron Signal
300
290
280
Binding Energy (eV)
XBL8312-6669

fig. 3.4

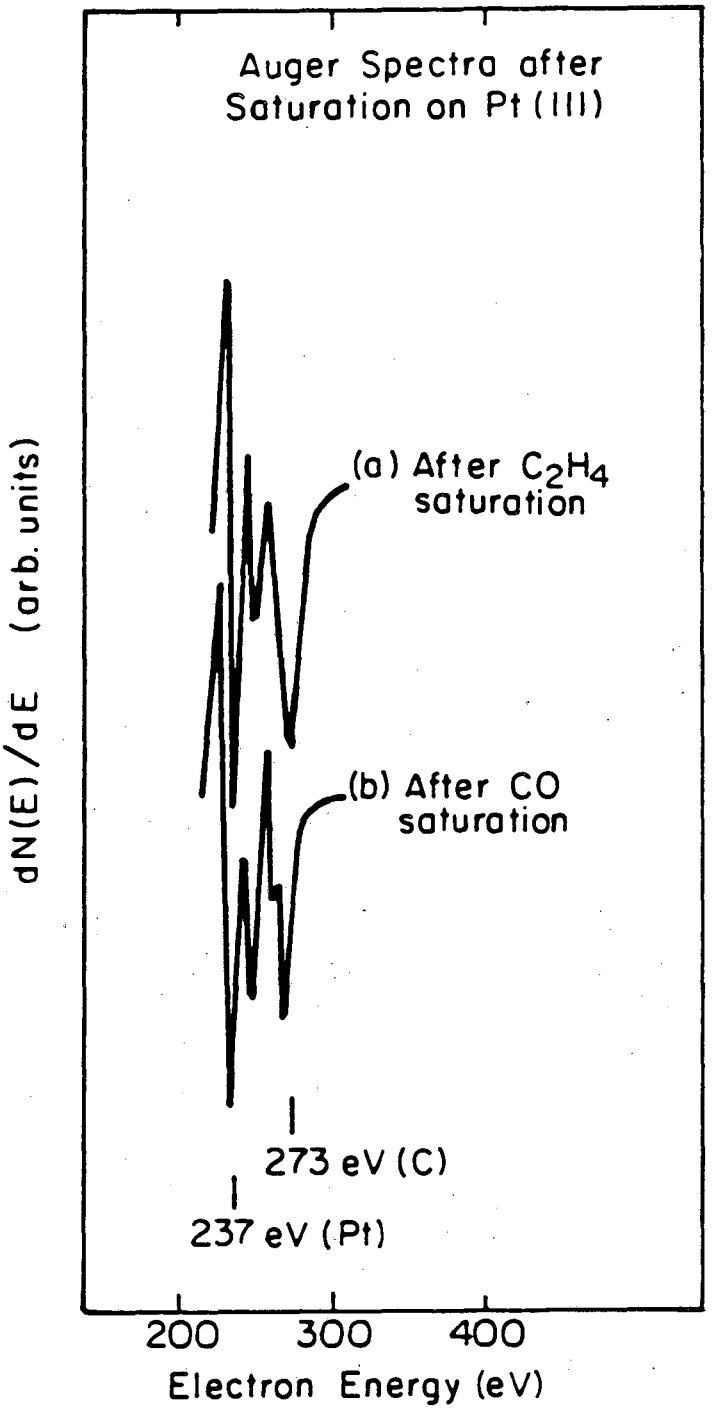
Auger Spectra after
Saturation on Pt (111)
(a) After C_2H_4
saturation
(b) After CO
saturation
273 eV (C)
237 eV (Pt)
dN(E)/dE (arb. units)
200
300
400
Electron Energy (eV)
XBL8312-6668

fig. 3.5

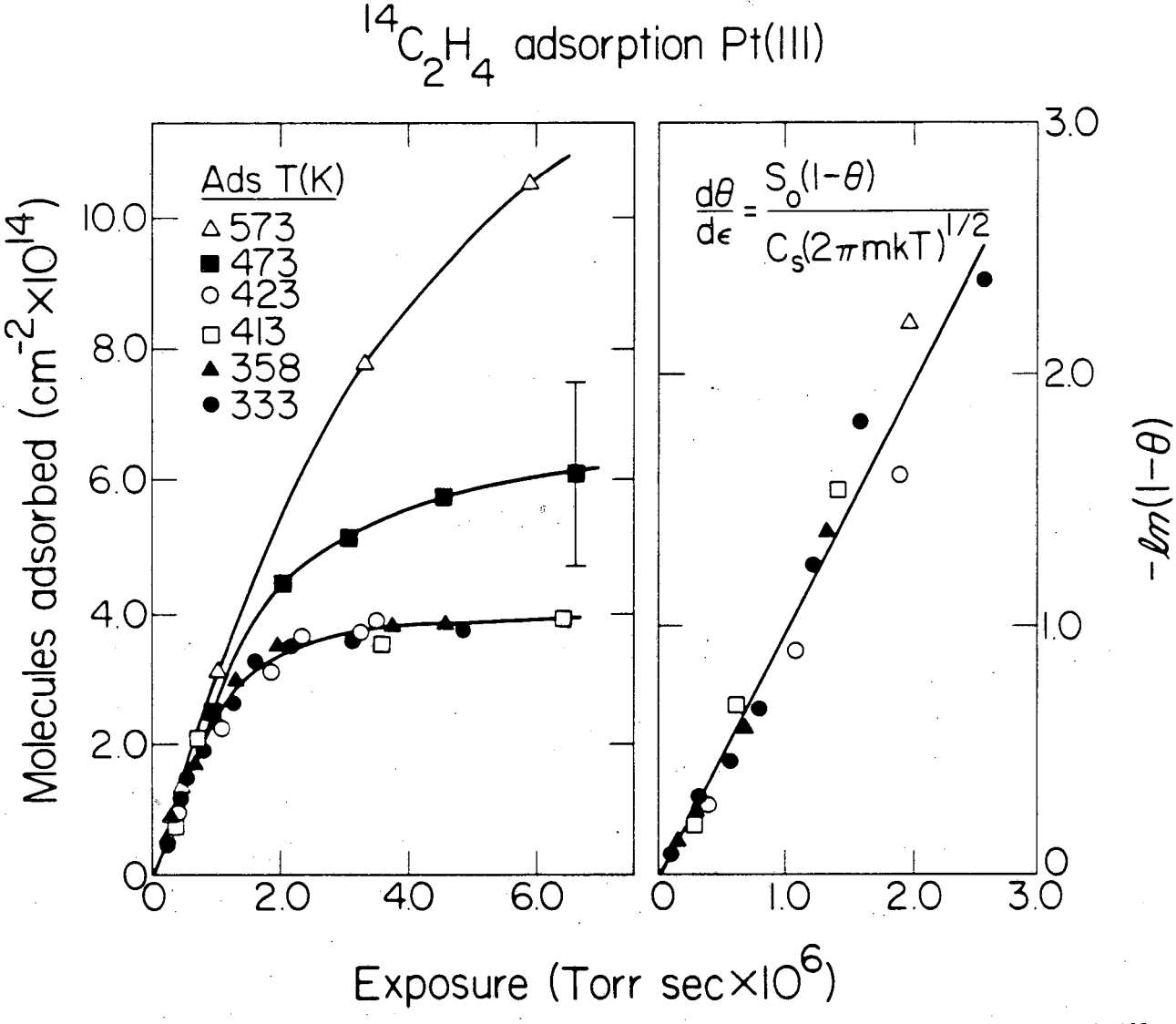

XBL 818-1105

fig. 3.6

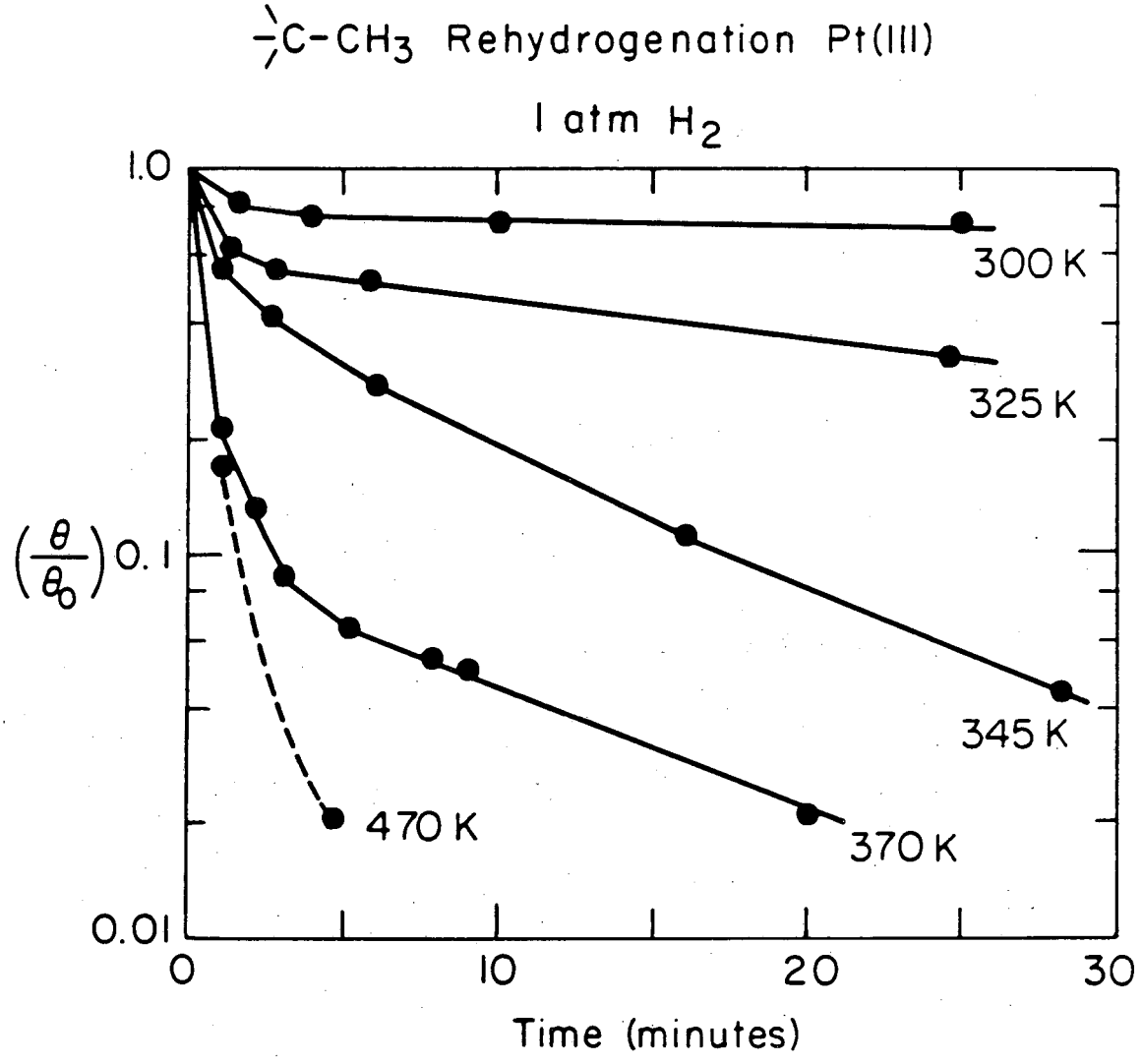
C-CH3 Rehydrogenation Pt(III)
1 atm H2
1.0
0.1
0.01
(θ/θ0)
300 K
325 K
345 K
370 K
470 K
0
10
20
30
Time (minutes)
XBL813-5385

fig. 3.7

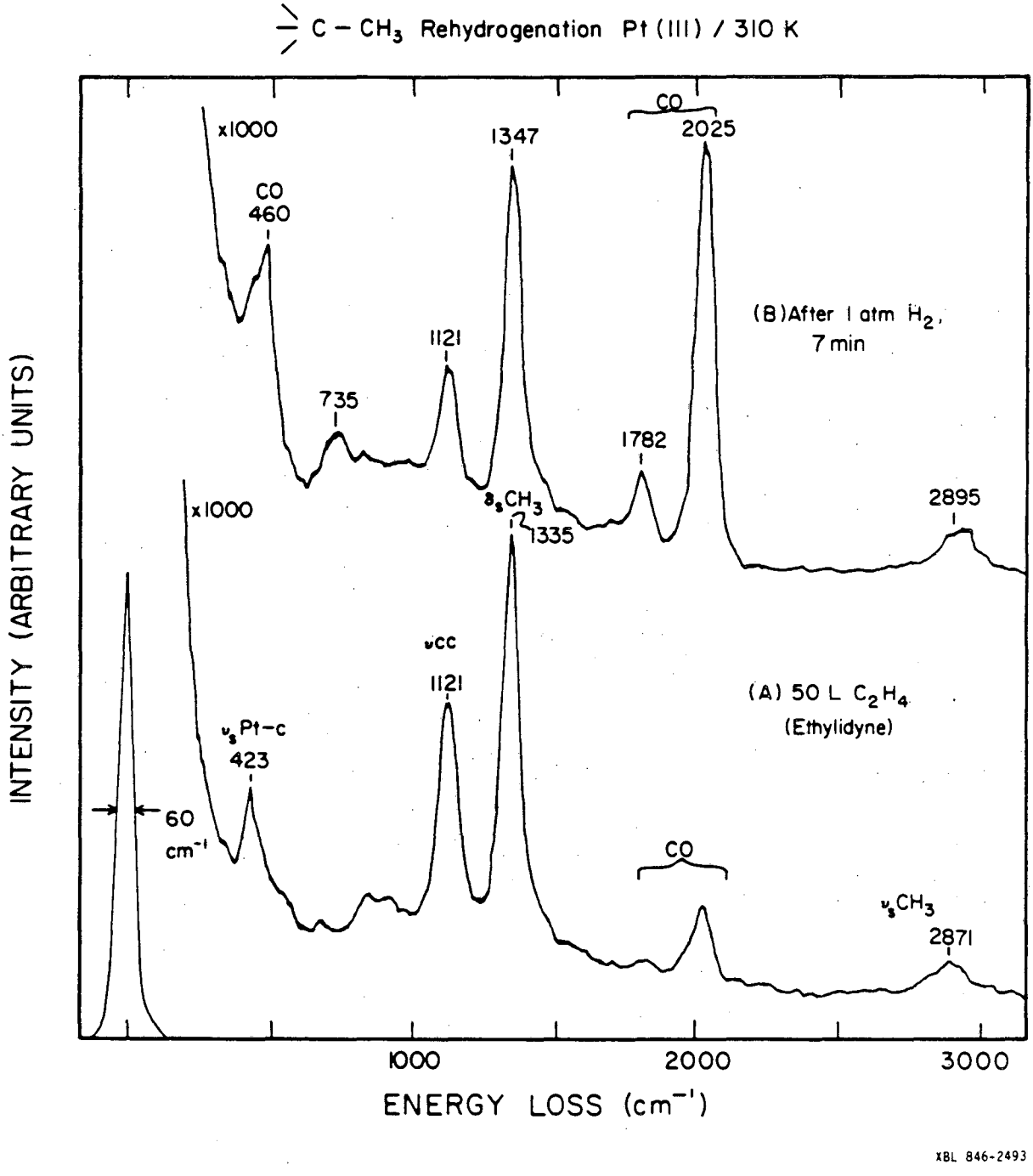
C – CH3 Rehydrogenation Pt (111) / 310 K
x1000
CO
460
735
1121
1347
CO
2025
1782
2895
(B) After 1 atm H2,
7 min
δs CH3
1335
x1000
νCC
1121
νs Pt-c
423
60
cm-1
(A) 50 L C2H4
(Ethylidyne)
CO
νs CH3
2871
INTENSITY (ARBITRARY UNITS)
1000
2000
3000
ENERGY LOSS (cm-1)
XBL 846-2493

fig. 3.8

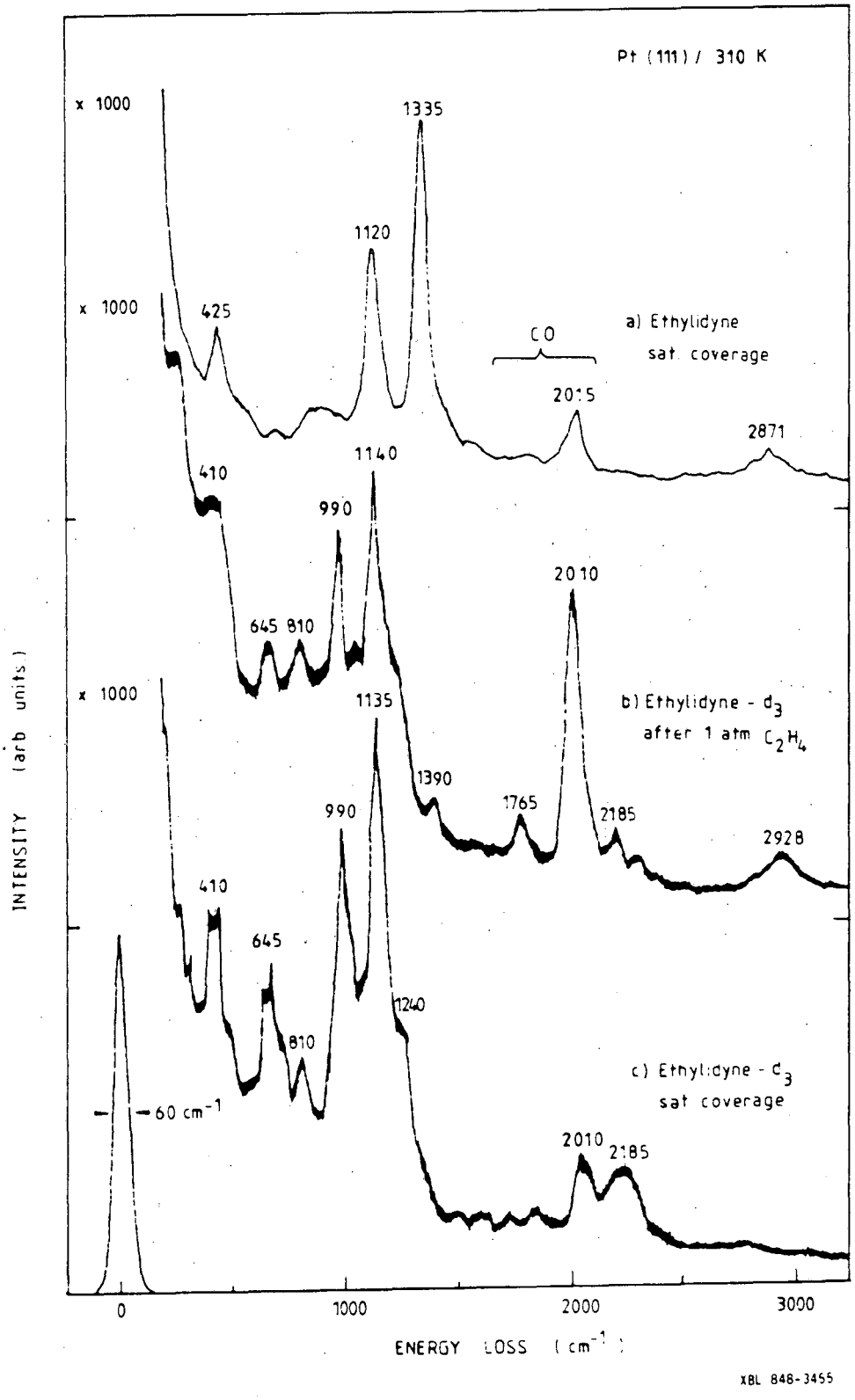
Pt (111) / 310 K
x 1000
1335
1120
425
CO
a) Ethylidyne
sat. coverage
2015
2871
x 1000
410
1140
990
2010
645 810
x 1000
b) Ethylidyne - d_3
after 1 atm C_2H_4
1135
1390
990
1765
2185
2928
410
645
1240
810
c) Ethylidyne - d_3
sat coverage
60 cm^{-1}
2010
2185
INTENSITY (arb units)
0
1000
2000
3000
ENERGY LOSS (cm^{-1})
XBL 848-3455

fig. 3.9

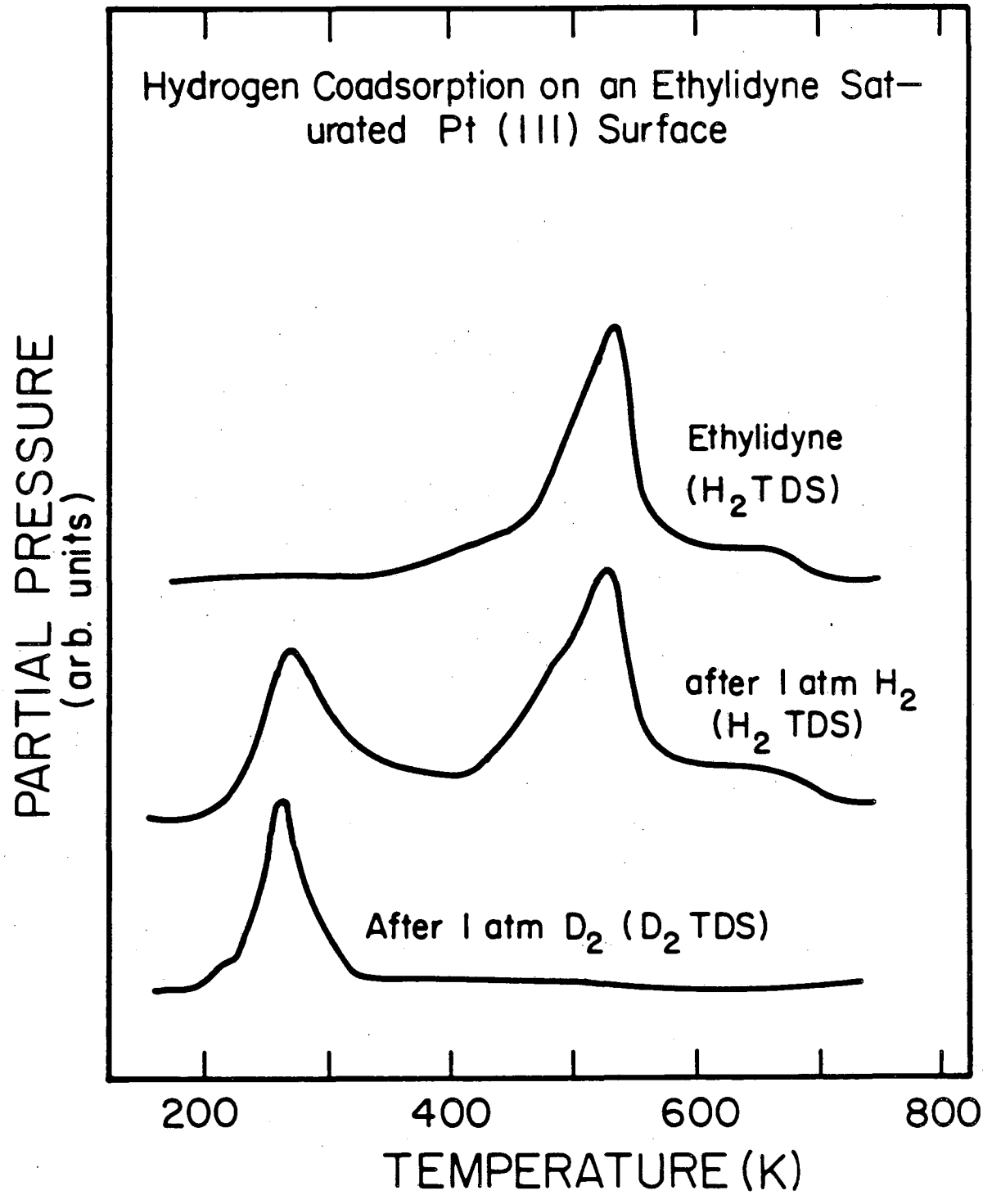

XBL 846-2491

fig. 3.10

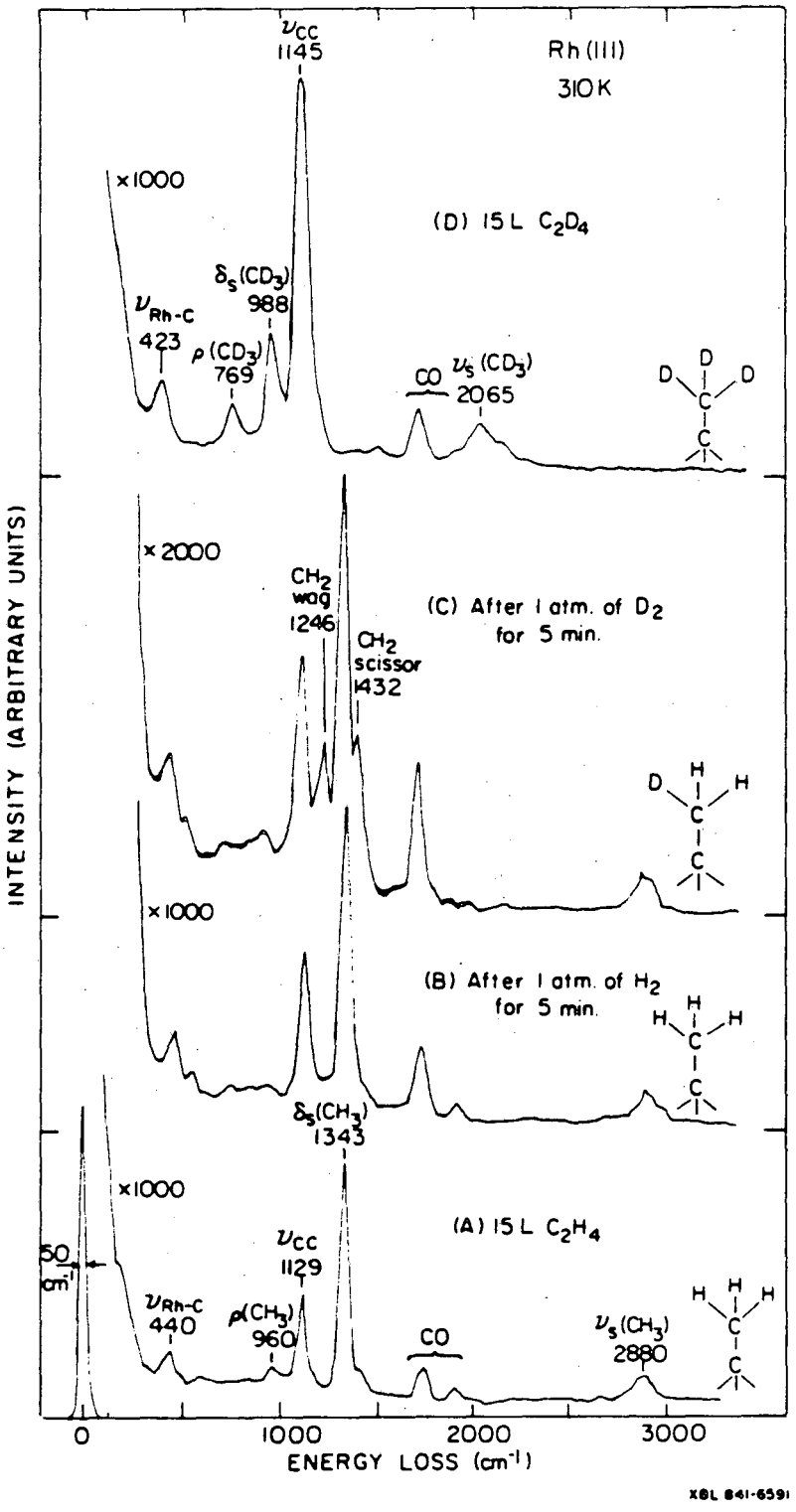
ν_{CC} 1145
Rh(111)
310K
×1000
(D) 15 L C_2D_4
$\delta_s(CD_3)$ 988
ν_{Rh-C} 423
$\rho(CD_3)$ 769
CO
$\nu_s(CD_3)$ 2065
×2000
CH_2 wag 1246
CH_2 scissor 1432
(C) After 1 atm. of D_2 for 5 min.
×1000
(B) After 1 atm. of H_2 for 5 min.
$\delta_s(CH_3)$ 1343
×1000
(A) 15 L C_2H_4
50 cm^{-1}
ν_{CC} 1129
ν_{Rh-C} 440
$\rho(CH_3)$ 960
CO
$\nu_s(CH_3)$ 2880
INTENSITY (ARBITRARY UNITS)
0
1000
2000
3000
ENERGY LOSS (cm^{-1})
XBL 841-6591

fig. 3.11

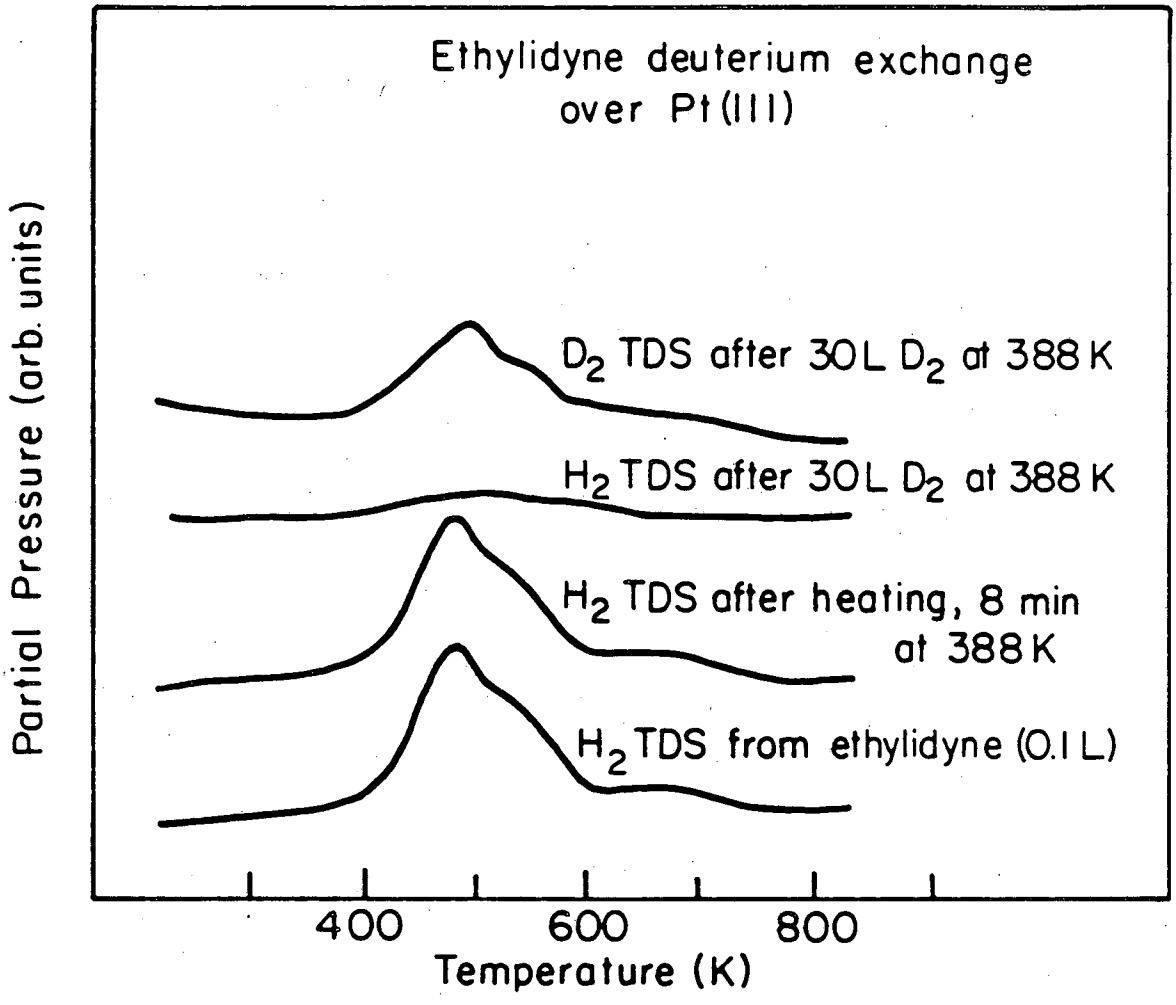

XBL847-7193

fig. 3.12

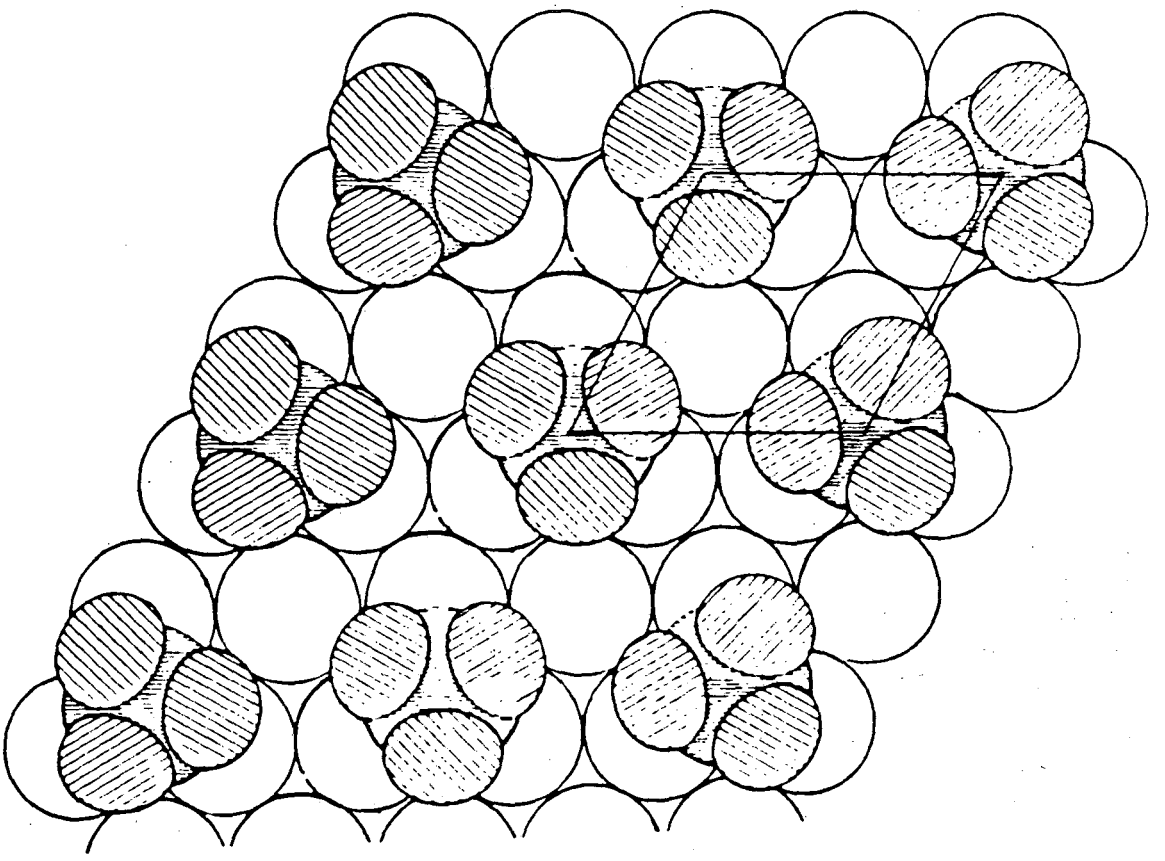

XBL 846-2628

fig. 3.13

Comparison of Hydrogenation Rates
over Pt(111) and Rh(111) Single-Crystal Surfaces

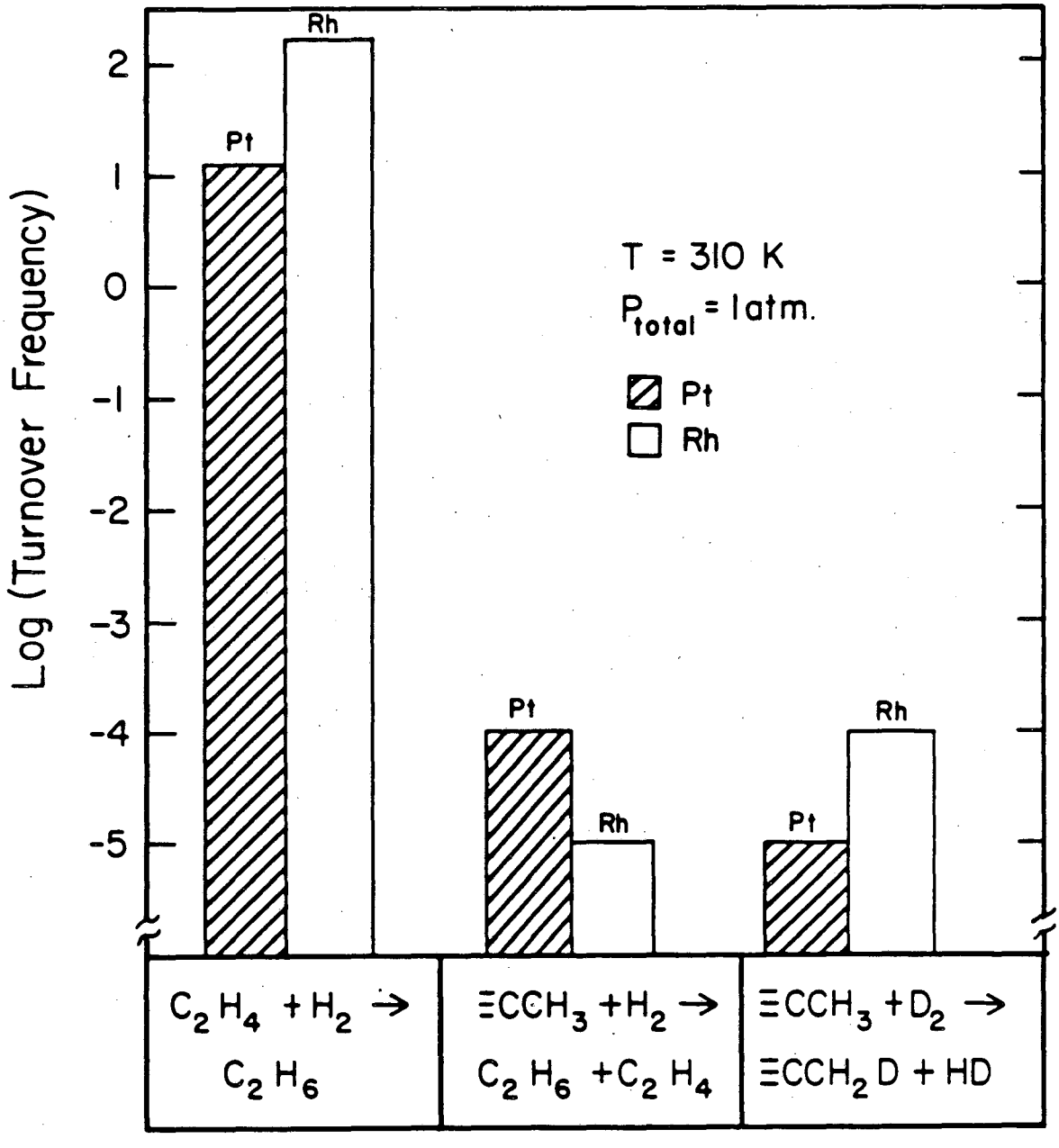

XBL 846-2487

fig. 3.14

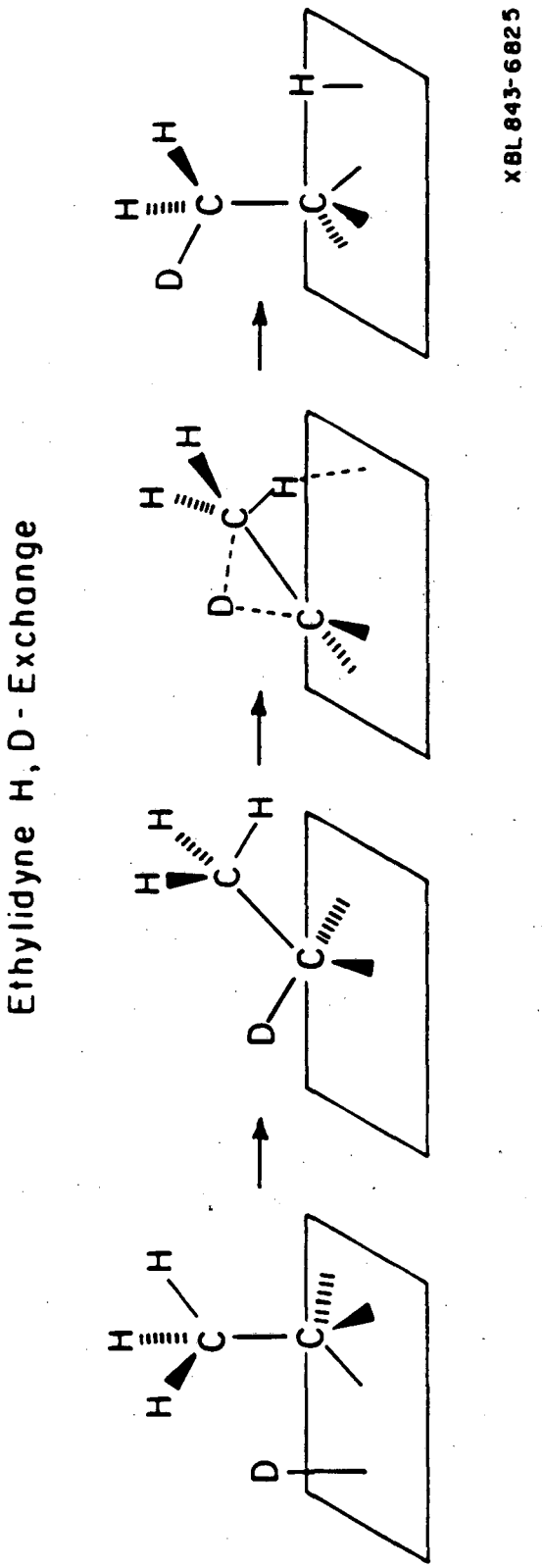

fig. 3.15

3.2. Hydrogenation of ethylene.

3.2.1. Introduction.

Although many chemisorption studies have been carried out using surface science techniques such as Auger Electron Spectroscopy (AES), Low Energy Electron Diffraction (LEED), and Ultraviolet and X-Ray Photoelectron Spectroscopy (UPS and XPS), the direct application of their results to interpret catalytic processes is not straightforward. One of the problems is that most of these studies are carried out over clean surfaces and under ultra-high vacuum conditions. Catalytic reactions, on the other hand, generally take place on surfaces covered with adsorbed species, and at several atmospheres of reactant gases. In this case, the intermediates in the reactions need not necessarily be related to the chemisorbed states of the reactants present under vacuum conditions. In this section we attempt to find the relationship between the chemisorption process that occurs on clean surfaces and the mechanism of the catalytic reaction under high pressures for the case of the hydrogenation of ethylene over platinum surfaces.

Since its discovery by Sabatier and Senderens in 1897, the hydrogenation of ethylene over high surface area metallic catalysts has been extensively studied [36]. However, up to now, the mechanistic details of the surface reaction are still unknown. In contrast, appreciable research effort has focused on the adsorption of ethylene on clean metallic surfaces under vacuum and ultra-high vacuum conditions [18,37]. On (111) single crystal faces of most noble metals, alkenes are believed to lose one hydrogen atom at around room temperature and form stable alkylidyne species on the surface [38]. It was shown in the previous section that

this ethylidyne is stable towards rehydrogenation in the presence of atmospheric pressures of hydrogen.

In the present work, the kinetic parameters for the hydrogenation of ethylene with hydrogen and deuterium were obtained on the Pt (111) crystal surface, and were found to be in the range of those reported for supported platinum catalysts [39]. Evidence was obtained that partially hydrogenated carbonaceous deposits (most probably including ethylidyne fragments) cover the surface during reactions, but do not participate directly in the reaction mechanism. Also important is the fact that, from LEED evidence, the carbonaceous fragments were at least partially ordered after the high pressure reactions, and it is, to the best of our knowledge, the first case where the presence of ordered overlayers after catalytic reactions has been reported. Finally, it is proposed that the hydrogenation reaction takes place on top of these carbonaceous residues rather than on the clean platinum surface. A mechanism involving ethylidene moities as intermediates is proposed to explain the specific details for hydrogen transfer and incorporation into the ethylene molecule.

3.2.2. Results.

The hydrogenation of ethylene to ethane using both hydrogen and deuterium was investigated over the flat close packed platinum (111) surface at temperatures between 300 and 373 K. The total pressure of the gases was kept constant at 110 Torr by adding nitrogen to the reaction mixture when necessary. The standard reaction conditions were pressures of 10 Torr of ethylene and 20 Torr of hydrogen (or deuterium), unless

indicated otherwise. A typical product accumulation curve, determined as a function of reaction time, is shown in fig. 3.16. The reaction rates, which were constant up to high conversions (see appendix), were calculated from the slopes of these plots. Arrhenius plots of the initial rates of hydrogenation using both hydrogen and deuterium are shown in fig. 3.17, and yield activation energies of 10.8 ± 0.1 Kcal/mole. The reaction exhibits a normal isotope effect, the reaction with hydrogen being about 1.3 times faster than with deuterium. The dependences of the rates on H_2 and C_2H_4 partial pressures were also studied. The data is sumarized in table 3.1. From these, the following kinetic equation was obtained:

$$\text{Rate} = (8 \pm 4)\times 10^{8} \exp[-(10.8 \pm 0.1)/RT] P_{C_2H_4}^{(-0.60 \pm 0.05)} P_{H_2}^{(1.31 \pm 0.05)}$$

where the rate is expressed in molec/Pt atom.sec, R is the gas constant ($R=1.987\times10^{-3}$ Kcal/mole.K), T is the reaction temperature in degrees Kelvin, and P_{H_2} and $P_{C_2H_4}$ are the hydrogen and ethylene partial pressures in atm, respectively.

For reactions with deuterium, the product distribution in the resulting ethane was studied mass spectrometrically. A typical distribution is shown in fig. 3.18. Most of the ethane contains either one or two deuterium atoms per molecule, although products up to d_6 are also present. From these distributions, an average number of deuterium atoms per ethane molecule, M, can be calculated. Fig. 3.19 shows the change of this average as a function of reaction time for a typical case. As it can be seen, M increases slightly with time due to some

deuterium exchange in the reactant ethylene. The rate of this side reaction can be estimated from the slope in the figure to be about 25% of the rate of hydrogenation (see appendix for details). The deuterium distribution also changes as a function of temperature (fig. 3.20), and deuterium partial pressure (table 3.2).

The reaction did not self-poison (within the experimental error) under the reported conditions. After completion of a reaction, and evacuation of the cell, a second run using a fresh reaction mixture yields similar reaction rates. An experiment was performed in which the crystal was saturated with ethylene (1 minute at $2x10^{-7}$ Torr, that is, 12 L exposure) before closing the reaction cell and starting the reaction. Again, the activity was equal to that obtained when starting with a clean platinum surface.

LEED pictures of the platinum (111) surface were taken after each reaction. A poorly ordered (2x2) pattern was always obtained. This is shown in fig. 3.21, together with the pattern resulting from room temperature exposure of the clean surface to ethylene, that leads to the formation of ethylidyne [38].

A vibrational spectrum after reactions is shown in the bottom part of fig. 3.22. Again, the spectrum for ethylidyne is shown in the upper part for comparison. Peaks for ethylidyne at 423 cm^{-1} (Pt-C symmetric stretching, $\nu(MC)$), ~ 960 cm^{-1} (methyl group rock, $\rho(CH_3)$), 1121 cm^{-1} (C-C stretching, $\nu(CC)$), 1335 cm^{-1} (symmetric methyl hydrogen bending, $\delta_s(CH_3)$) and 2871 cm^{-1} (symmetric and asymmetric C-H streching

modes, $\nu(CH_3)$), all are seen in the spectrum obtained after reactions. Additionally, peaks at 815 and 1436 cm^{-1}, from CH and C_xH fragments, were seen as well. The extra features are indicative of adsorbates coming from contamination from the high pressure cell [22].

Hydrogen (2 amu) and deuterium (4 amu) TDS were obtained after reactions by heating the crystal at a constant rate of ~ 40 K.sec. (fig, 3.23). These desorption profiles, which exibit maxima at 530 and 670 K, were similar to those obtained from adsorbed ethylidyne [38]. The only new feature in the spectra is the shoulder at about 450 K, probably due to desorption from coadsorbed hydrocarbon fragments. The upper spectrum was obtained after a series of reactions of ethylene with H_2, between 300 and 370 K, whereas the lower one was obtained after similar reactions using D_2. To compare the spectra, it should be pointed out that the mass spectrometer sensitivity for H_2 is about 1.7 times that of the sensitivity for D_2. The 4 amu (D_2) TDS for reactions with D_2 are very similar to the 2 amu (H_2) traces using H_2 as a reactant, except that the area under the deuterium peak is about 10-20% of that of the area under the hydrogen peak. However, the sum of areas under the 2 and 4 amu curves after deuteration is nearly equal to the area under the 2 amu TDS trace when the reaction is performed with H_2.

Auger spectra indicated that the amount of carbon on the surface after reactions did not change significantly with reaction temperature or hydrogen partial pressures. The average value for the $I_C(273\ eV)/I_{Pt}(237\ eV)$, where I is the Auger intensity peak-to peak height, was always 0.74 ± 0.20. This represents an atomic ratio of θ_C=0.46 carbon atoms/

Pt atom [40], or roughly one carbon atom for every two platinum atoms. These carbon residues are partially hydrogenated, with hydrogen to carbon ratio (obtained by measurement of the H_2 TDS area and the C/Pt AES ratio) very close to that for ethylidyne (that is, 1.5 H atoms/C atom).

3.2.3. Discussion.

The hydrogenation of ethylene using either hydrogen or deuterium on Pt (111) single crystal surfaces was found to have an activation energy of 10.8 Kcal/mole, and orders of 1.3 with respect to hydrogen (or deuterium) and -0.6 with respect to ethylene partial pressures. The reaction also displays a normal isotope effect, the reaction with hydrogen being about 1.3 times faster than that with deuterium. All these kinetic data compare favorably with results reported previously by other workers on supported platinum catalysts (Table 3.3). For instance, most of the reported activation energies lie between the values of 9 and 11 Kcal/mole [23,41-44]. Bond and coworkers studied the reaction of ethylene with deuterium over different platinum catalysts, and reported reaction rate orders in hydrogen and ethylene partial pressures of 1.2 and -0.5, respectively [39,45]. They also reported a deuterium distribution in the resulting ethane that qualitatively agrees with that obtained in our work. Also, the hydrogenation over five different types of catalysts gave similar results, showing that the reaction is essentially structure insensitive. In that respect, it is of interest to note that the absolute reaction rates obtained here for platinum single crystals are within the range of those reported in the literature already cited for supported high surface area polycrystalline platinum catalysts.

The AES spectra after reactions always reveal the presence of surface carbon. Furthermore, when reactions were started on surfaces precovered by hydrocarbon fragments, either by retaining the carbonaceous deposits from previous reactions or by predosing the surface with ethylene under UHV conditions, the rates were identical to those when starting with a clean surface. In addition, hydrogenation of these fragments is much slower than the rates of ethylene hydrogenation (fig. 3.14). On the other hand, no reaction self-poisoning was detected during the experiments (i.e., over several hours). These observations suggest that the hydrogenation reaction takes place on a surface covered with partially hydrogenated carbon fragments. The (2x2) LEED pattern and the vibrational spectra obtained after reactions, the shape of the H_2 TDS spectra that results from the thermal decomposition of these adsorbates, and the similar kinetic results for the ethylene hydrogenation obtained with a clean Pt (111) surface and with a surface precovered with ethylene under UHV conditions, all suggest that the carbonaceous species are, in fact, ethylidyne moieties, as obtained by dosing ethylene onto a clean Pt (111) surface in UHV [10-17,38]. One difference between the low pressure and the high pressure studies is the presence of a small amount of CH or C_xH fragments in the latter case, as manifests by a low temperature shoulder in the thermal desorption spectrum of H_2 (fig. 3.23). Since the surface is analyzed after returning the platinum crystal to UHV conditions, there is always the possibility that changes take place on the surface during the pumping process. However, it is known that ethylidyne on Pt (111) is stable between about 300 and 400 K, and experiments of repeated pressurization with H_2 and subsequent evacuation show that its composition and structure remains unchanged while resto-

ring vacuum, as checked by LEED and HREELS. This implies that if any changes do occur during the high pressure exposures, they are reversible. Also, since there is a high pressure of ethylene present during reactions (10-20 torr) and ethylidyne rehydrogenation at room temperature is slow, the platinum surface is believed to be saturated with ethylidyne during and after reactions. This fact rules out the posibility of readsorption of the residual gases. They are: ethylene (that would produce ethylidyne as it adsorbs), ethane (that does not adsorb readily on the clean platinum surface), and hydrogen. The only possible difference in the platinum surface between the time the reactions are taking place and when the surface is analyzed, is that the overlayer of weakly adsorbed hydrocarbons is lost as it is pumped away. Optical spectroscopies might be used to study the surface in situ during reactions to obtain more detailed information on the structure of this second layer.

The role of the carbonaceous deposits in the mechanism of the hydrogenation reactions is not yet well understood. Experiments with ^{14}C-ethylene have shown that the hydrogenation of ethylidyne under 1 atmosphere H_2 is very slow at room temperature (previous section). Also, if ethylidyne were to be a direct intermediate for the hydrogenation, the reaction with D_2 would have yield ethane containing at least three deuterium atoms per molecule, instead of one or two, as was obtained experimentally. On the other hand, the ability of the carbonaceous fragments chemisorbed on the surface to facilitate atomic hydrogen transfer has been demonstrated by the exchange experiments reported in section 3.1. Very little exchange takes place in an ethylidyne saturated surface at room temperature either in an atmosphere of D_2 or under UHV conditions.

Even after long D_2 exposures at temperatures as high as 370 K, the extent of exchange was never more than 40% (fig. 3.23). It seems that the rate of this deuterium exchange depends on the dissociated deuterium coverage, being slower when the surface is saturated with ethylidyne (that is the situation that prevails during hydrogenation reactions). This indicates that the hydrogen atoms in the methyl group of ethylidyne are not labile, and that they cannot act as hydrogen transfer agents. By contrast, H or D bonded to the α carbon in ethylidene, the precursor for hydrogen-deuterium exchange, may be easier to remove, and may incorporate into gas phase ethylene molecules to form ethane.

In view of all the evidence, a main conclusion of this work is that the hydrogenation of ethylene does not take place on the clean metallic surface, but rather on top of a layer of carbonaceous fragments, which TDS, LEED and AES results strongly suggest are composed of ethylidyne adsorbates. The bond of unsaturated hydrocarbons to metals is too strong to allow them to desorb at room temperature, but a bond to the carbonaceous overlayer could, on the other hand, be within the energetic range required for the catalytic reaction to take place. If that is the case, perhaps future surface science work should focus not only on chemisorption on clean surfaces, but on surfaces that have been already exposed to reactant gases. The main problem is that the weak reversible chemisorption expected in the latter case is hard to achieve under UHV conditions. One way around this could be to work at lower temperatures, but the question still remains as if this is equivalent to having higher gas pressures. Also, molecular beam experiments on covered surfaces should be helpful in elucidating the details of the chemical reactions.

Even, if the reaction takes place on a covered surface, the presence of the metal still has to be important, because the reaction rates are known to change with different metals [26]. Fig. 3.9 shows that the metal atoms cannot be reached by the gaseous ethylene molecules. However, this surface is able to adsorb a small amount of hydrogen (fig. 3.10). Also, hydrogen is most probably involved in the limiting step of the reaction, since this would account for the pressure dependence and the isotope effect on the rates. It seems highly improbable that this chemisorbed hydrogen will jump from the surface to an ethylene molecule adsorbed on a second layer without the intervention of the ethylidyne in the first layer. On the other hand, the hydrogen atoms in the methyl group of the ethylidyne do not directly participate in the hydrogenation of gaseous ethylene. One possible explanation that reconciles these conclusions is that the adsorbed deuterium atoms α-incorporates into the ethylidyne, forming ethylidene intermediates that subsequently transfer the deuterium to the ethylene. A scheme of this mechanism is presented in fig. 3.24, and can be written as:

$$D_2\ (g) \rightarrow 2D\ (ads)$$

$$Pt_3 \equiv C\text{-}CH_3\ (ads) + D\ (ads) \rightarrow Pt_n\text{=}CD\text{-}CH_3\ (ads)$$

$$2Pt_n\text{=}CD\text{-}CH_3\ (ads) + C_2H_4\ (weakly\ ads) \rightarrow 2Pt_3 \equiv C\text{-}CH_3 + C_2H_4D_2$$

Such an ethylidene intermediate has been proposed by Salmeron and Somorjai to explain the ethylidyne deuterium exchange under UHV conditions [13]. In their case, however, the incorporation of deuterium at the carbon of ethylidyne is followed by β abstraction of a hydrogen atom from the methyl group, and this can be a slow step at high ethylene pressures, since it may be necessary for the ethylidyne to tilt so that

the H atom can reach the surface and exchange can occur. A more detailed explanation of this process was given in section 3.1. Therefore, while the exchange rates at high pressures are small, ethylene hydrogenation is still a fast process.

Our results also indicate that the hydrogenation of ethylene over platinum (111) single crystal surfaces is very similar to that on supported catalysts. Since the reaction takes place on a surface covered by carbonaceous deposits, we propose that the carbon deposit masks the surface structure, making the reaction surface insensitive.

The mechanism we proposed for the hydrogenation of ethylene on platinum may be extended to other metals and to other olefins. The existence of ethylidyne and its analogs, propylidyne and butylidyne, have been demonstrated for Pt (111) and Rh(111) surfaces [18]. On Pd (111), ethylidyne formation was reported, but the observation of alkylidynes from heavier olefins has not been reported. On Ni(111), on the other hand, the most probable species on the surface are acetylenic complexes [46]. In all these cases, the hydrogen transfer mechanism previously proposed for hydrogenation could still, with small modifications, be valid. Also, the fact that most olefin hydrogenation reactions are structure insensitive, and that they have similar kinetic parameters on all group VIII transition metals catalysts (see table 3.4 for some examples), support the previous statement about the reactions having similar mechanisms. It would be worthwhile to perform similar experiments to the ones reported here for other similar systems.

3.2.4. Appendix.

Estimation of the rate of ethylene deuterium exchange. When kinetic studies are carried out in a batch reactor, the intermediate products accumulate with time in the reactant mixture, modifying the rate of subsequent reactions. This is the reason why the amount of extra deuterium in the ethane coming from deuterated ethylene is not merely directly proportional to the deuterium exchange rate of the ethylene. In the following appendix, we estimate this exchange rate out of the data in fig. 3.19.

If there were no deuterium exchange of the ethylene, the deuterium content of the resulting ethane would be constant, $C_2H_{6-M'}D_{M'}$, where M' would ideally be 2, but was found experimentally to be about 1.64. However, due to the incorporation of deuterium atoms in the ethylene, M increases with time, as seen in fig. 3.19. The side reaction involved can be written as

$$C_2H_4 + D_2 \rightarrow C_2H_3D + HD \qquad \text{Rate}=R_{exc} \qquad (3.1)$$

The exchange of ethane with deuterium can be ruled out as a source of deuterated ethane, since this reaction does not take place until much higher temperatures (above 550 K, see next section).

We will assume in our derivation that R_{hyd} is constant, as found experimentally, since $R_{hyd} = kP_{D_2}^{1.31}P_{C_2X_4}^{-0.60}$, and the two pressure factors almost cancel out up to 80% conversion (see table 3.5). R_{exc} will be assumed to be either constant or linearly dependent on $P_{C_2X_4}$.

The rate of formation of ethane with an extra deuterium atom will be

$$\frac{d}{dt}(P_{ed}) = R_{hyd} \frac{P_{C_2H_3D}}{P_{C_2X_4}} \qquad (3.2)$$

where P_{ed} is the partial pressure of the ethane with the extra deuterium, R_{hyd} is the rate of hydrogenation of ethylene, and X is either H or D. For constant R_{exc}:

$$P_{C_2H_3D} = R_{exc} \cdot t - P_{ed} \qquad (3.3)$$

and

$$P_{C_2X_4} = P^{*}_{C_2H_4} - R_{hyd} \cdot t \qquad (3.4)$$

where the asterisk denotes initial pressure. Substituing eqs. (3.3) and (3.4) into eq. (3.2):

$$\frac{d}{dt}(P_{ed}) = R_{hyd} \frac{R_{exc} \cdot t - P_{ed}}{P^{*}_{C_2H_4} - R_{hyd} \cdot t} \qquad (3.5)$$

This equation is hard to solve as written, since there are some cross terms involved. However, using a Taylor series expansion around t=0, and assuming that the rate of formation of P_{ed} is constant at least at the begining of the reaction, eq. (3.5) is reduced to:

$$\frac{d}{dt}(P_{ed}) = \frac{R_{hyd}}{P^{*}_{C_2H_4}} \left\{R_{exc} - \frac{d}{dt}(P_{ed})\right\}\left(t + \frac{R_{hyd}}{P^{*}_{C_2H_4}} t^2 + \frac{R^2_{hyd}}{P^{*2}_{C_2H_4}} t^3 \ldots\right) \qquad (3.6)$$

Integrating the previous equation, substituing for the conversion fraction of ethylene to ethane, $F = (R_{hyd} \cdot t)/P^{*}_{C_2H_4}$, and taking the limiting

case when F<<1:

$$P_{ed} = F \cdot R_{exc} \cdot t(1/2 + F/3 + F^2/4 + \ldots) \qquad (3.7)$$

From this, the rate of exchange is:

$$R_{exc} = \frac{P_{ed}}{F \cdot t} \; (1/2 + F/3 + F^2/4 + \ldots)^{-1} \qquad (3.8)$$

If the rate of exchange is slow enough, only one deuterium per ethylene molecule will be present in the reaction mixture, and

$$P_{ed} = (M-M')R_{hyd} \cdot t = (M-M')F \cdot P^{*}_{C_2H_4} \qquad (3.9)$$

and

$$R_{exc} = \left\{\frac{(M-M')}{t} \; P^{*}_{C_2H_4}\right\}(1/2 + F/3 + F^2/4 + \ldots)^{-1} \qquad (3.10)$$

The first factor in this expresion can be estimated form the fig. 3.19 to be about 0.016 torr/min, or 1.06 molec/Pt atom•sec, and the second term varies from 2 at zero conversion to about 1 when F=0.95. Since the rate of hydrogenation under the same conditions is $R_{hyd} \sim 7.95$ molec/Pt atom•sec, the ratio R_{exc}/R_{hyd} lies between 0.13 and 0.25.

If R_{exc} depends linearly on $P_{C_2X_4}$, $R_{exc} = k_{exc}P_{C_2X_4}$, the only difference in equation (3.5) is that R_{exc} has to be substituted by

$$R_{exc} = k_{exc}(P^{*}_{C_2H_4} - R_{hyd} \cdot t) \qquad (3.11)$$

Following the same procedure as before

$$k_{exc} = \{2(M-M')/t\}(1/2 - F/3 - F^2/4...) = 0.0032\ min^{-1} \quad (3.12)$$

and

$$R_{exc} = k_{exc} P^{*}_{C_2H_4} (1-F) \quad (3.13)$$

Then, R_{exc}/R_{hyd} varies between 0.25 at F=0, and 0.23 at F=0.5.

Table 3.1

Pressure dependence of the initial reaction rates of ethylene hydrogenation over platinum (111) single crystal surfaces

$P_{C_2H_4}$ (torr)	P_{D_2} (torr)	T (K)	Rate (molec/Pt atom.sec)
10	10	300	0.42
10	20	300	1.24
10	100	300	7.95
10	10	333	2.63
10	20	333	6.80
10	40	333	17.53
10	100	333	> 65
20	20	333	4.56

Table 3.2

Pressure dependence of the deuterium atom distribution of the resulting ethane from the ethylene hydrogenation with D_2 over platinum (111) single crystal surfaces. T = 300K, $P_{C_2H_4}$ = 10 torr.

	Composition (%)				
P_{D_2} (torr)	d_0	d_1	d_2	d_3	d_4
20	0	45	39	11	2
100	0	43	46	6	4

Table 3.3

Comparison of ethylene hydrogenation kinetic parameters for different platinum catalysts.

Catalyst	Log Rate[a]	a[b]	b[b]	E_a (Kcal/mole)	Ref.
Platnized foil	1.9	-0.8	1.3	10	41
Platinum evaporated film	2.7	0	1.0	10.7	23
1% Pt/Al_2O_3	---	-0.5	1.2	9.9	39
Platinum wire	0.6	-0.5	1.2	10	42
3% Pt/SiO_2	1.0	----	---	10.5	43
0.05% Pt/SiO_2	1.0	0	---	9.1	44
Pt (111)	1.4	-0.6	1.3	10.8	Our work

a) Rate in molec/Pt atom.sec, corrected for the following conditions:

$T = 323$ K, $P_{C_2H_4} = 20$ torr, $P_{H_2} = 100$ torr.

b) Orders in ethylene (a) and hydrogen (b) partial pressures.

Table 3.4

Comparison of ethylene hydrogenation kinetic parameters over different metals.

Metal	Form	a^a	b^a	E_a(Kcal/mole)	Ref.
Ni	wire	0	0.97	11-15	47
	powder	-0.6	0.98	6	48
	Evap. film	0	1	9-10	49
	on SiO_2	-0.08	0.67	8.4	50
Pt	foil	-0.8	1.3	10	41
	wire	-0.5	1.2	10	42
Pd	thimble	0	1	5-7	51
	on SiO_2	-0.03	0.66	8.4	50
Rh	on Al_2O_3	0	1	12	52
Fe	film	-0.6	0.87	7.3	53
Ir	on Al_2O_3	-0.4	1.6	13.8	45
Ru	on Al_2O_3	-0.2	1	8.7	54
Co	on SiO_2	-0.19	0.55	8.4	50

a) Order in ethylene (a) and hydrogen (b) partial pressures.

Table 3.5

Ratio R_{hyd}/R_{hyd}^* as a function of ethylene conversion for the initial conditions $P_{D_2}^* = 20$ torr and $P_{C_2H_4}^* = 10$ torr.

Conversion fraction of ethylene (F)	P_{D_2} (torr)	$P_{C_2H_4}$ (torr)	R_{hyd}/R_{hyd}^*
0	20	10	1.000
0.20	18	8	0.996
0.40	16	6	1.014
0.60	14	4	1.086
0.80	12	2	1.345

FIGURE CAPTIONS

Fig. 3.16. Product accumulation curve as a function of time for ethylene hydrogenation to ethane over Pt(111) single crystal surfaces. T=333 K, $P_{C_2H_4}$ = 10 Torr, P_{D_2} = 20 Torr, P_{N_2} = 80 Torr. The product was measured by gas chromatography (.) and mass spectrometry (o).

Fig. 3.17. Arrhenius plots for ethylene hydrogenation with H_2 and D_2 over Pt(111). $P_{C_2H_4}$ = 10 Torr, P_{H_2} or D_2 = 20 Torr, P_{N_2} = 80 Torr.

Fig. 3.18. Deuterium atom distribution in the resulting ethane from the hydrogenation of ethylene with deuterium over Pt(111). Same conditions as fig. 3.16

Fig. 3.19. Average number of deuterium atoms incorporated per ethane molecule produced (M) as a function of reaction time for the hydrogenation of ethylene with deuterium over Pt(111). T=300 K, $P_{C_2H_4}$ = 10 Torr, P_{D_2} = 100 Torr.

Fig. 3.20. Temperature dependence of the deuterium atom distribution in the resulting ethane from the deuteration of ethylene over Pt (111). Same conditions as in fig. 3.17.

Fig. 3.21. a) (2x2) LEED pattern resulting from the adsorption of ethylene on a Pt(111) surface at room temperature and under UHV conditions. b) Diffuse (2x2) LEED pattern obtained after ethylene hydrogenation reactions over Pt(111) surfaces at 300-370 K. Electron energy ~ 70 eV.

Fig. 3.22. Vibrational spectra of ethylidyne (upper frame) and fragments formed during high pressure ethylene hydrogenation (lower frame) over Pt (111) at 310 K.

Fig. 3.23. a) 2 amu thermal desorption spectrum after ethylene hydrogenation with H_2. b) 4 amu TDS after ethylene reaction with D_2. Reactions over Pt (111) surfaces, T=300-370K, same conditions as fig. 3.17. The heating rate was ~ 40 K/sec.

Fig. 3.24. Schematic representation of the mechanism for ethylene hydrogenation over Pt and Rh (111) single crystal surfaces.

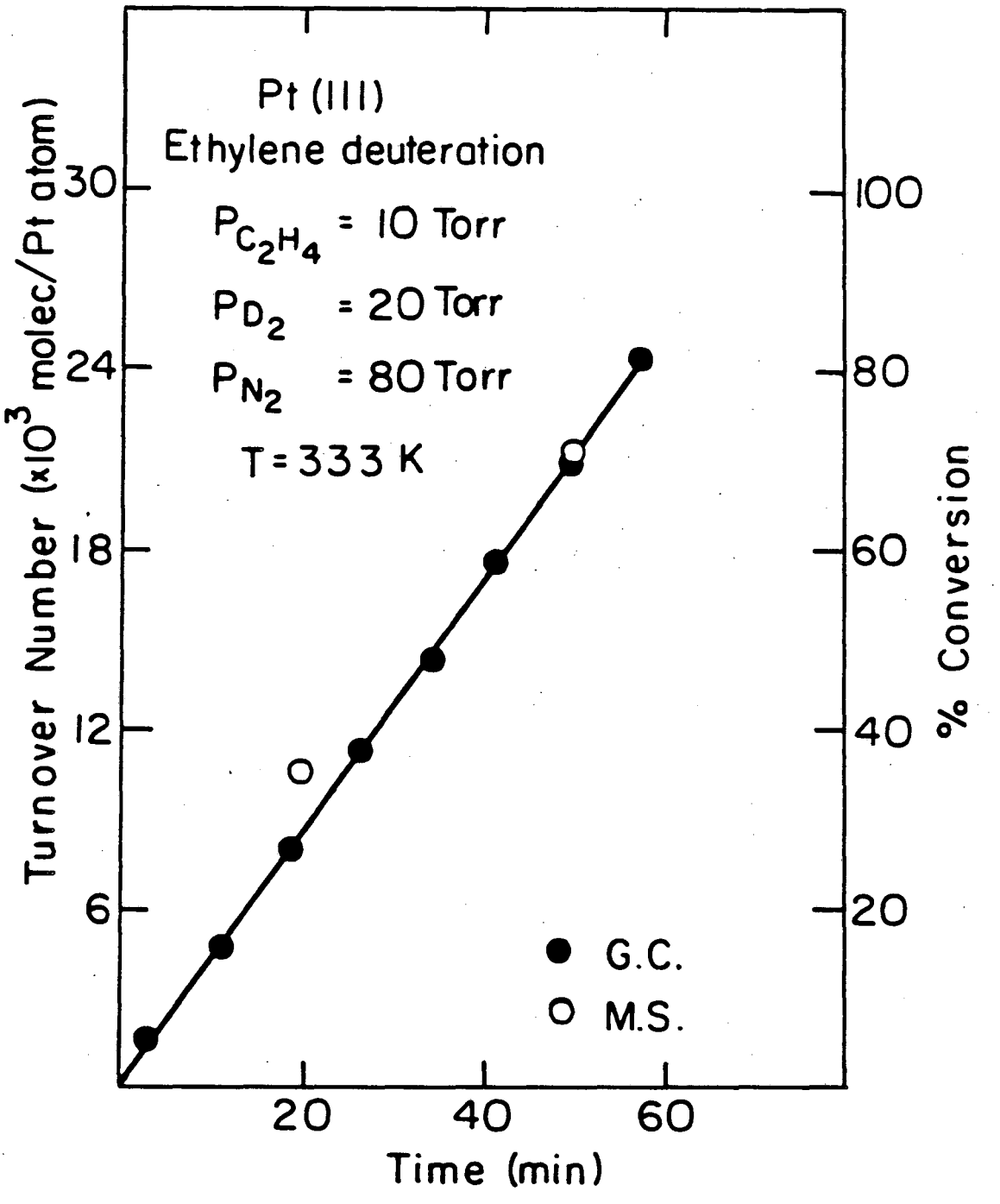

XBL 835-5636

fig. 3.16

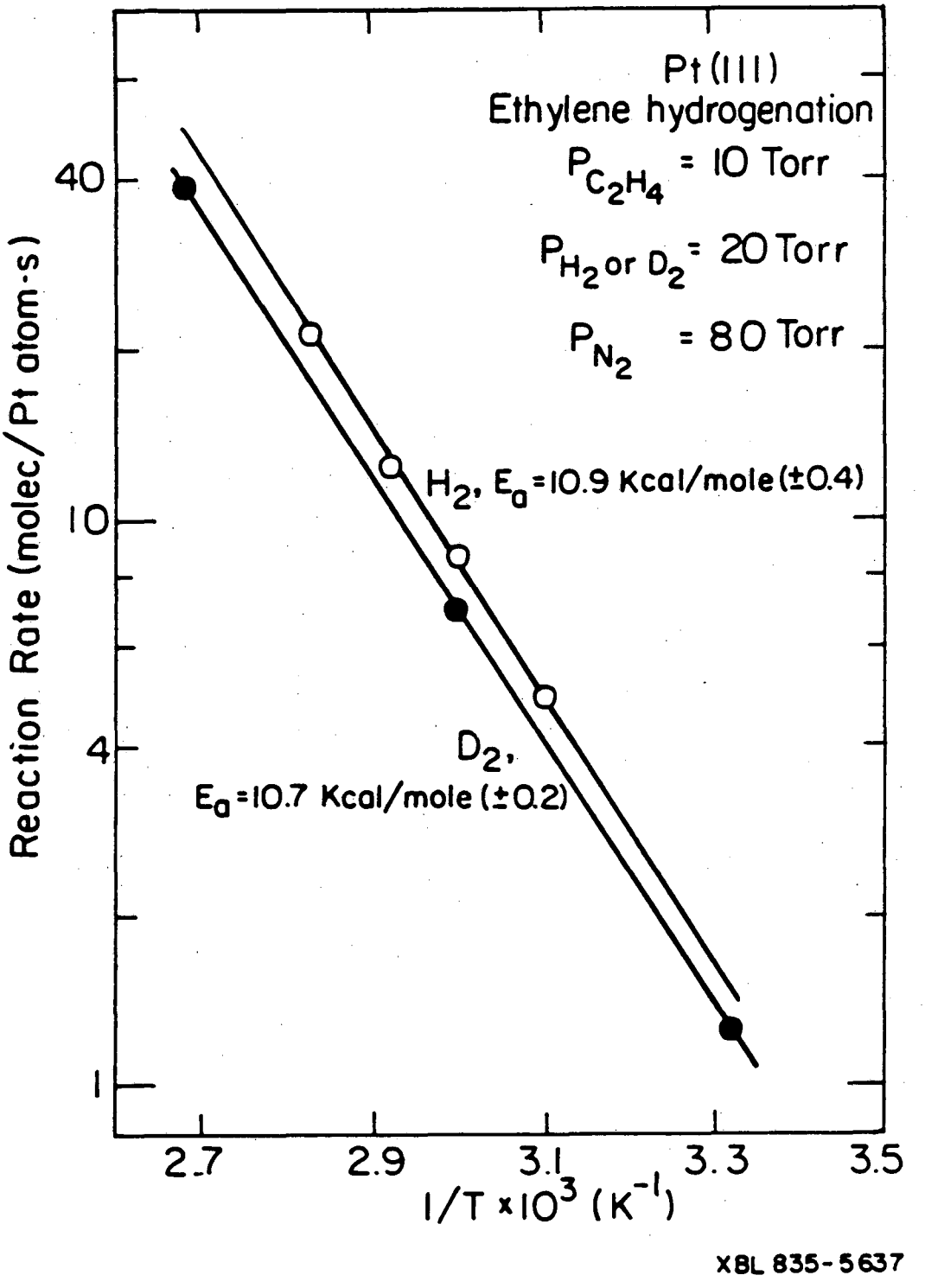
Pt(111)
Ethylene hydrogenation
$P_{C_2H_4}$ = 10 Torr
$P_{H_2 \text{ or } D_2}$ = 20 Torr
P_{N_2} = 80 Torr
H_2, E_a = 10.9 Kcal/mole (±0.4)
D_2,
E_a = 10.7 Kcal/mole (±0.2)
Reaction Rate (molec/Pt atom-s)
40
10
4
1
2.7
2.9
3.1
3.3
3.5
1/T x 10^3 (K^{-1})
XBL 835-5637

fig. 3.17

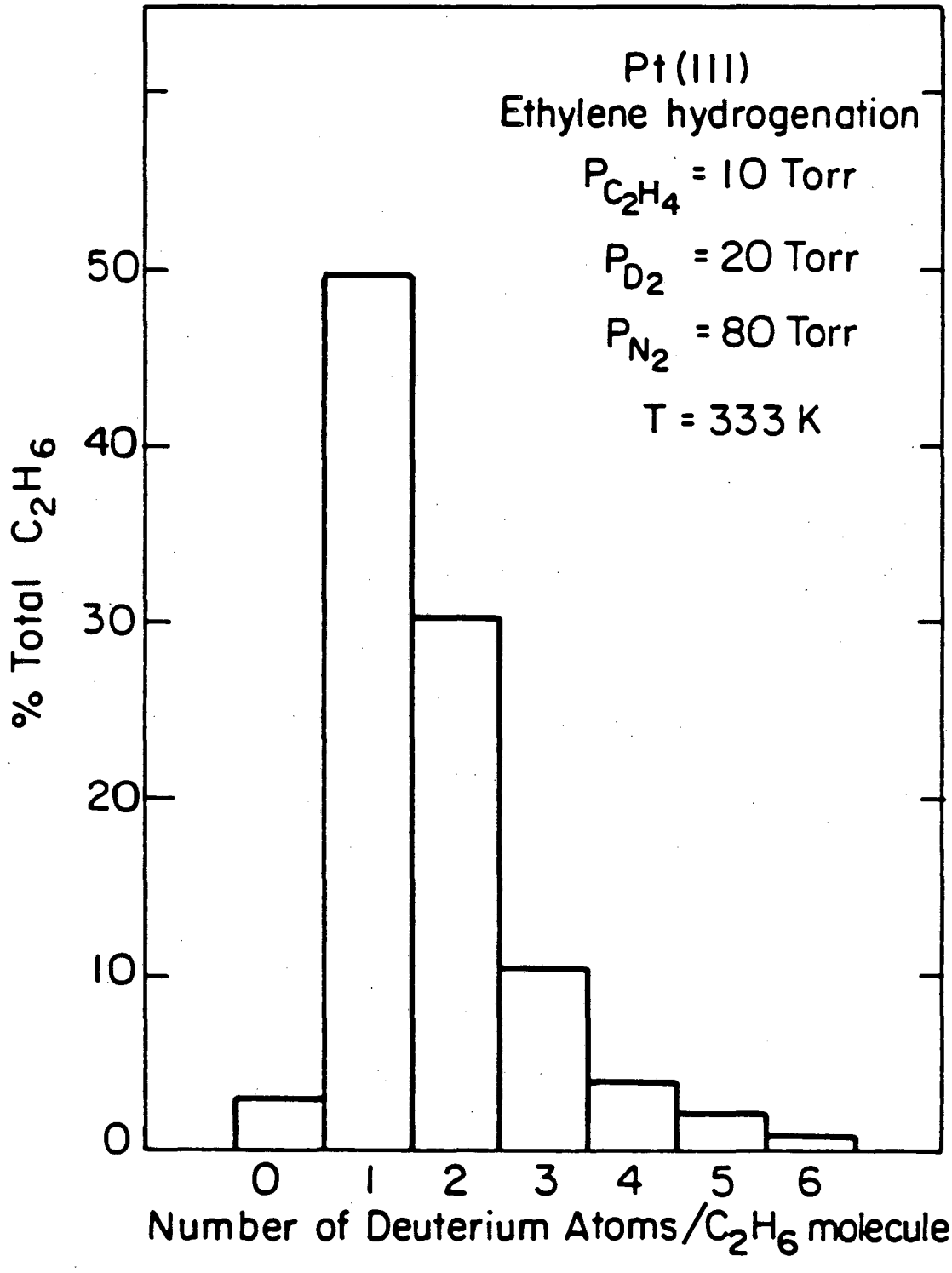
Pt(111)
Ethylene hydrogenation
$P_{C_2H_4}$ = 10 Torr
P_{D_2} = 20 Torr
P_{N_2} = 80 Torr
T = 333 K
% Total C_2H_6
0
10
20
30
40
50
0 1 2 3 4 5 6
Number of Deuterium Atoms/C_2H_6 molecule
XBL 835-5638

fig. 3.18

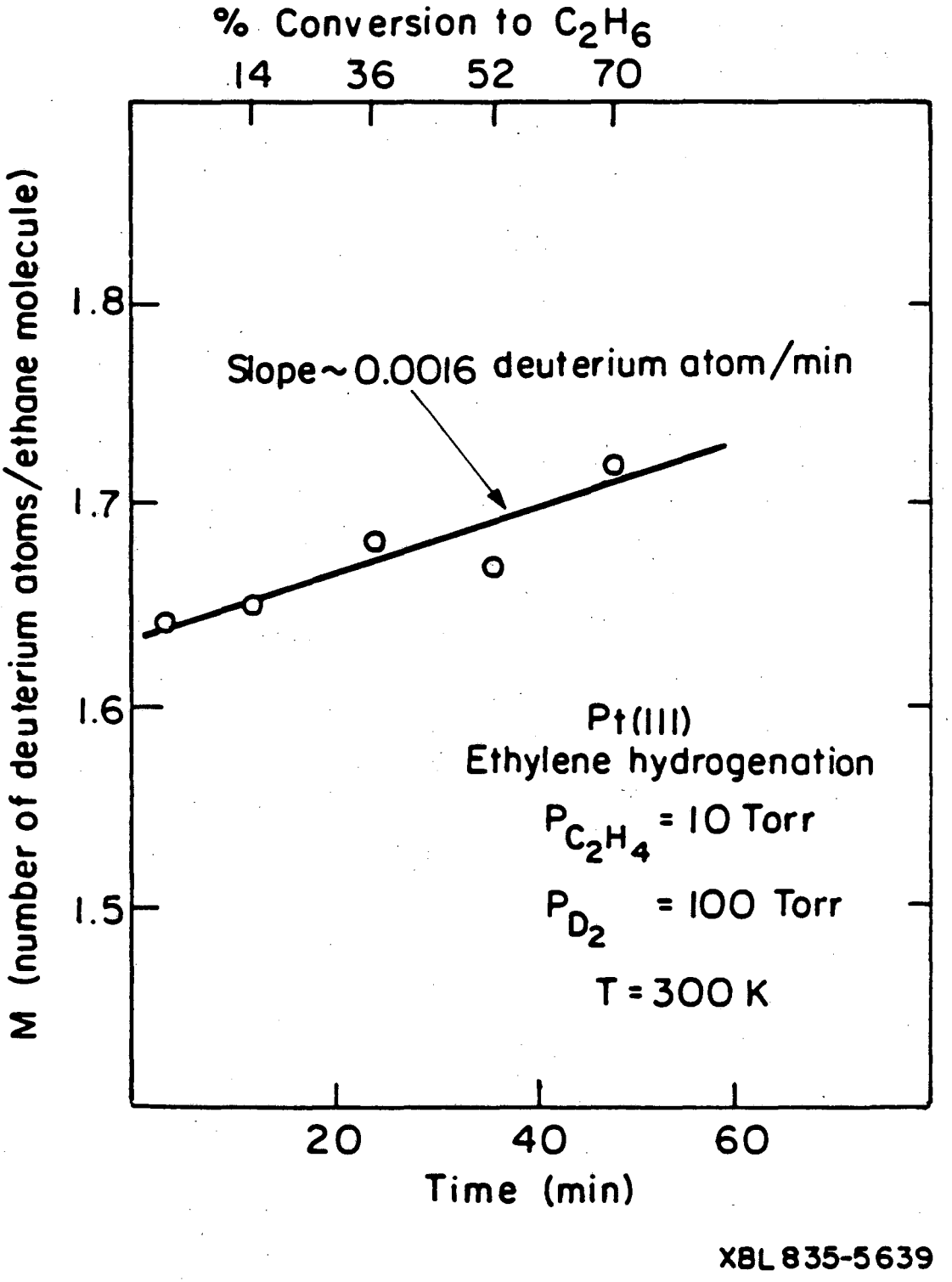
% Conversion to C_2H_6
14
36
52
70
M (number of deuterium atoms/ethane molecule)
1.8
1.7
1.6
1.5
Slope ~ 0.0016 deuterium atom/min
Pt(111)
Ethylene hydrogenation
$P_{C_2H_4}$ = 10 Torr
P_{D_2} = 100 Torr
T = 300 K
20
40
60
Time (min)
XBL 835-5639

fig. 3.19

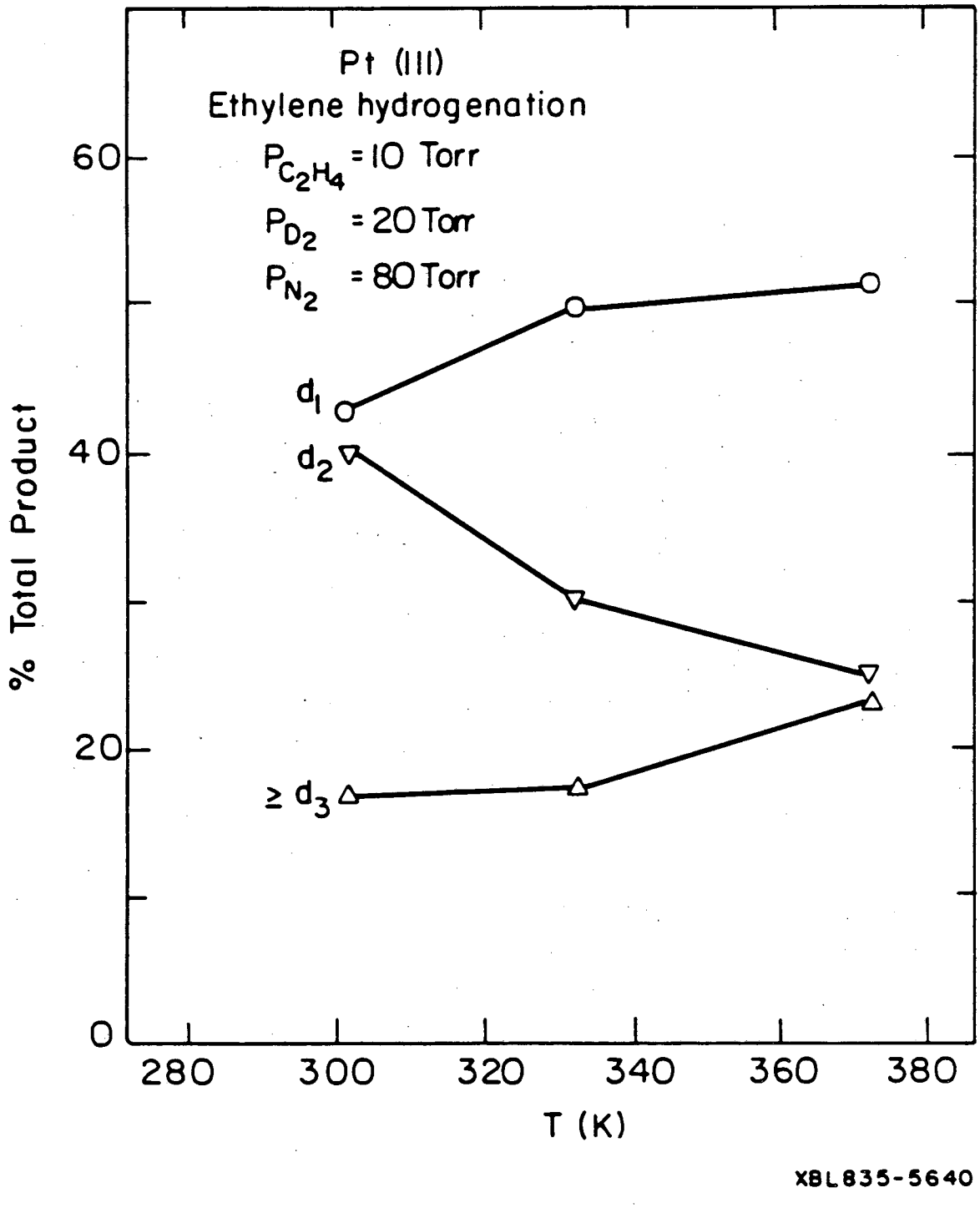
Pt (111)
Ethylene hydrogenation
$P_{C_2H_4}$ = 10 Torr
P_{D_2} = 20 Torr
P_{N_2} = 80 Torr
d_1
d_2
$\geq d_3$
% Total Product
0
20
40
60
280
300
320
340
360
380
T (K)
XBL835-5640

fig. 3.20

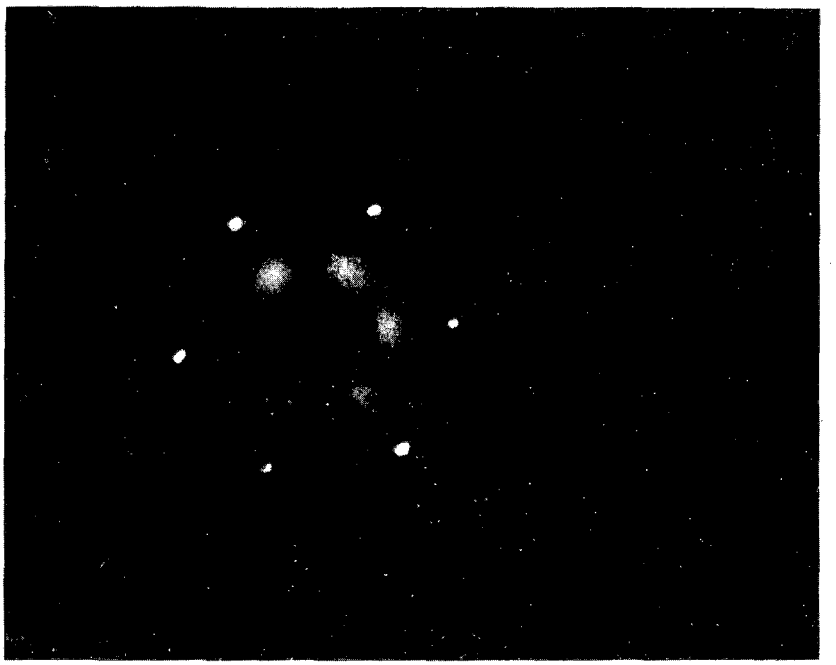

(a)

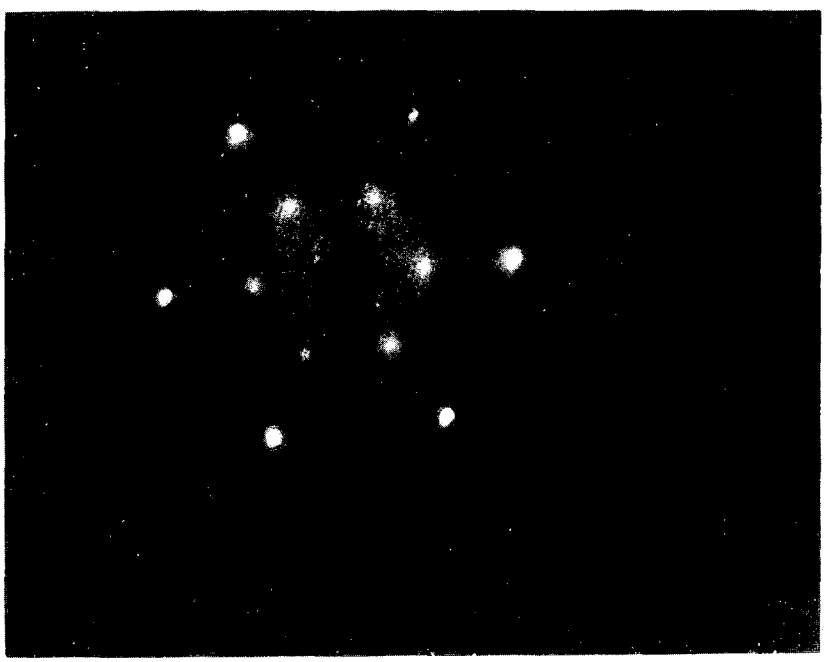

(b)

XBB 835-4421

Fig. 3.21

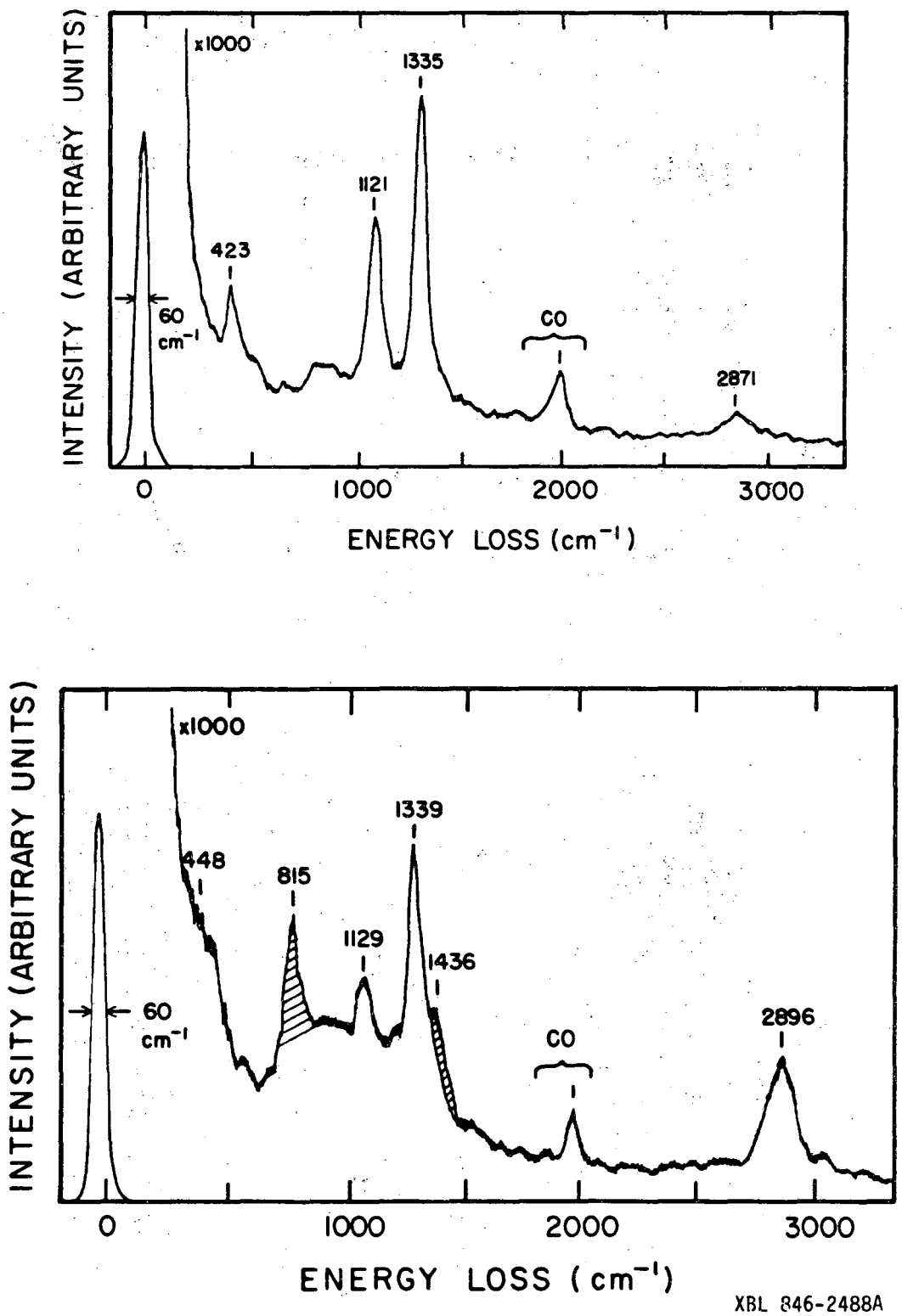
INTENSITY (ARBITRARY UNITS)
x1000
1335
1121
423
60
cm⁻¹
CO
2871
0
1000
2000
3000
ENERGY LOSS (cm⁻¹)
x1000
1339
448
815
1129
1436
60
cm⁻¹
CO
2896
0
1000
2000
3000
ENERGY LOSS (cm⁻¹)
XBL 846-2488A

fig. 3.22

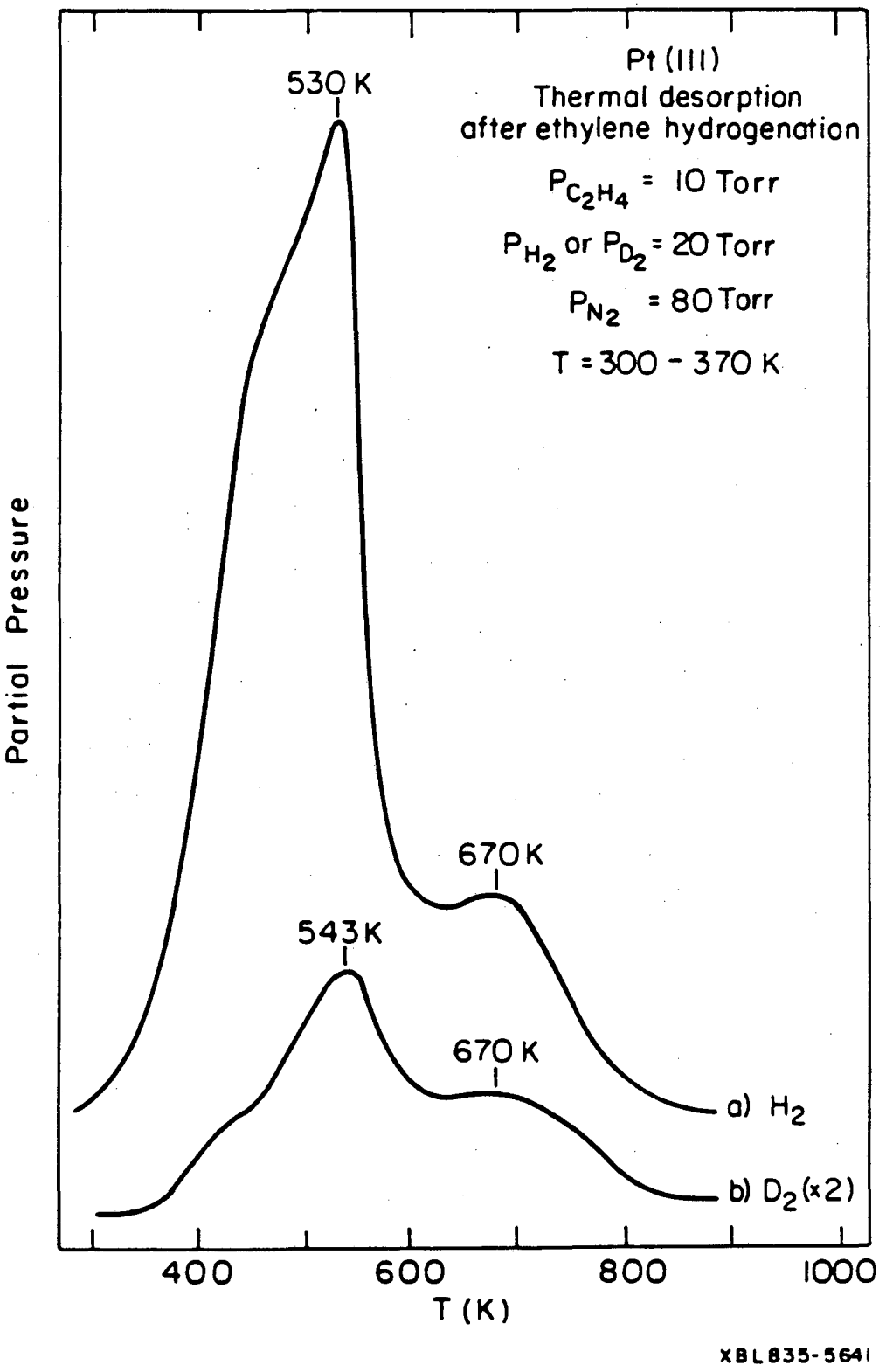
Pt (111)
Thermal desorption
after ethylene hydrogenation
$P_{C_2H_4}$ = 10 Torr
P_{H_2} or P_{D_2} = 20 Torr
P_{N_2} = 80 Torr
T = 300 - 370 K
530 K
670 K
543 K
670 K
a) H_2
b) D_2 (x2)
Partial Pressure
400
600
800
1000
T (K)
XBL835-5641

fig. 3.23

PROPOSED MECHANISM FOR ETHYLENE HYDROGENATION

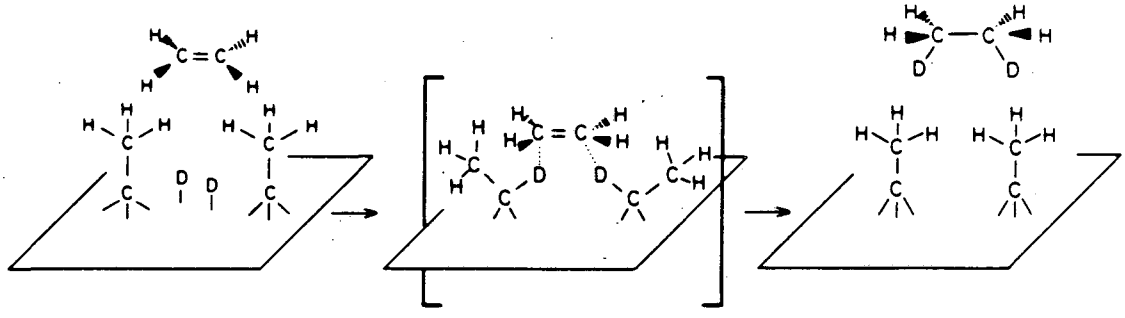

XBL 846-2494

fig. 3.24

3.3. Reaction of ethane with deuterium.

3.3.1. Introduction.

The development of apparatuses in which samples can be transferred from ultra-high vacuum (UHV) to high pressure reactors and back without exposure to air, together with the powerful tools of surface science, allows a more detailed examination of the mechanism of catalytic surface reactions. In the study of ethylene hydrogenation over Pt (111) single crystal surfaces, we concluded that ethylidyne (a hydrocarbon fragment which forms under UHV when ethylene is adsorbed at room temperature) is also present during high pressure reactions, and covers the metallic surface. Since ethylidyne is stable in the presence of high pressures of H_2 below 350 K, the hydrogenation of gas phase ethylene takes place on top of this first chemisorbed layer.

In this section we report a similar study of the ethane deuterium exchange reaction. An activation energy of 19 Kcal/mole was obtained, consistent with values reported previously on supported platinum, platinum films or foils [55-59]. Furthermore, a U-shaped product distribution was obtained, with maxima at one and six D atoms per ethane molecule, indicating the existence of two competitive exchange reactions. LEED and TDS suggest the presence of ethylidyne fragments on the surface after these reactions. Since the initial step for exchange muust be the dissociative adsorption of ethane, the reaction requires temperatures above about 400 K. Under these conditions ethylidyne moieties present during the high pressure reaction are readily rehydrogenated. We propose a mechanism for the exchange reaction in which initially adsorbed ethane either desorbs immediately, yielding monodeuterated ethane, or undergoes

sequential hydrogen exchange which involves ethylidyne as an intermediate, finally producing fully deuterated ethane.

3.3.2. Results.

Deuterium exchange and hydrogenolysis (to produce methane) of ethane were investigated over the close packed (111) platinum crystal surfaces at temperatures between 473 and 623 K. The standard reaction conditions were pressures of 100 Torr deuterium and 10 Torr ethane, unless otherwise indicated. Typical product accumulation curves are shown in fig. 3.25 for both reactions. These curves are plotted using the total number of ethane molecules that underwent reaction as a function of time. As expected, deuterium exchange is more than three orders of magnitude faster than hydrogenolysis over the temperature range studied.

For hydrogenolysis, the initial reaction rates were determined from the slope at zero time from plots like the one shown in fig. 3.25. Due to the high conversions for exchange, the rates for those reactions were calculated using first order kinetics for the disappearance of the light alkane (d_0). The reverse reactions, namely, the production of light alkane from deuterated ones, were neglected, since the equilibrium concentration of d_0 under our conditions is less than 0.02% of the total ethane (as calculated using the method described by Kemball [60]). The corresponding semilogarithmic plots are linear up to very high conversions, as can be seen in fig. 3.26, where the data from fig. 3.25 has been replotted to obtain the reaction rate constant. The rates estimated using this procedure were within 20% of the values obtained in a similar

way as for hydrogenolysis, i.e., by taking the slope at t=0 from fig. 3.25. First order kinetics are justified by the first order dependence of the reaction rates on ethane pressure, as will be reported later.

Arrhenius plots of the initial rates for both reactions are shown in fig. 3.27; these gave activation energies of 19±2 Kcal/mole for deuterium exchange, and 34±1 Kcal/mole for hydrogenolysis. The dependence of the exchange rate on reactant pressures was also studied; the data is summarized in table 3.6. The rate is almost linearly dependent on the ethane partial pressure, and inversely proportional to the square root of the deuterium pressure. All kinetic parameters obtained for the two reactions are displayed in table 3.7.

The product distribution of the resulting ethane from deuterium exchange was followed mass spectrometrically. A typical distribution is shown in fig. 3.28. This distribution has an "U" shape, with maxima at one (d_1) and six (d_6), and a minimum at three (d_3) deuterium atoms per ethane molecule. This distribution changes as a function of time of reaction and temperature, as can be seen from figs. 3.29 and 3.30. As the time of the reaction increases, d_1 increases while d_2 decreases, the other ethanes remaining approximately constant. This may be explained by exchange with the scrambled HD and H_2 formed as byproducts and accumulated during reactions. An increase in temperature decreases the production of totally deuterated ethane, and increases d_1, d_4 and d_5 products, while d_2 and d_3 remain almost unchanged. The distribution is also slightly affected by changes in reactant pressures, as shown in

table 3.8.

LEED pictures of the platinum (111) surface were taken after each reaction. A very diffuse (2x2) pattern was obtained, the half order extra spots being sharper for reactions performed at lower temperatures. An example of these diffraction patterns is shown in fig. 3.31, together with one obtained after ethylidyne formation on platinum for comparison.

The Auger spectra taken after reactions always indicated the presence of carbon on the surface. About half of these carbonaceous deposits were reversibly adsorbed, since they could be removed by flashing to high temperature in UHV. The ratio of carbon to platinum atoms, calculated from the Auger spectra taken after flashing, increases as a function of reaction temperature, from about 0.25 at 500K to 0.6 at 620 K (fig. 3.32).

Hydrogen (2 amu) and deuterium (4 amu) TDS were also taken after reactions. Examples are shown in fig. 3.33. Both TDS exhibit three main peaks: the first one around 470 K (A), possibly due to CH or CH_x fragments from contaminants in the reaction loop, and two others at 530-550 K (B) and above 640 K (C). The shape and relative contribution of each peak to the total desorption does not change appreciably as a function of reaction temperature. However, the total area and hydrogen (or deuterium) to carbon ratio on the surface decrease when the reactions are performed at higher temperature. The (H+D)/C ratio changes from about 1.5 at T<500 K, to 0.9 at 575 K, where ethylidyne is used as a standard (H/C=1.5). The fact that the mass spectrometer is 1.7 times

more sensitive to H_2 than to D_2 was also taken into account for the D/C calculations. A summary of the thermal desorption data is presented in table 3.9.

3.3.3. Discussion.

Ethane deuterium exchange on Pt (111) single crystal surfaces was found to have an activation energy of 19 Kcal/mole, and kinetic orders of -0.55 and 1.2 with respect to deuterium and ethane pressures, respectively. These values compare favorably with those obtained on films and supported catalysts (table 3.10). In the case of hydrogenolysis, on the other hand, activation energies between 53 and 55 Kcal/mole have been reported (see, for instance, refs. 61-63), as compared to the value of 34 Kcal/mole obtained here on Pt (111). However, since hydrogenolysis was about three orders of magnitude slower than exchange, it appears that the limiting step for carbon-carbon bond breaking is not the initial chemisorption of the saturated hydrocarbon [63]. Deuterium pressure dependences of -0.3 to -0.6 for ethane deuterium exchange were obtained on silica and cab-o-sil supported platinum [59], and are also consistent with our value of -0.55.

Where the product distribution has been studied, U-shaped curves similar to fig. 3.28 were obtained [55,56,58]. Anderson and Kemball [55] studied this reaction using different metal catalysts, obtaining three different product distribution shapes: a) predominantly ethane with one deuterium atom (d_1) (Mo, Ta); b) mostly fully deuterated ethane (d_6) (Pd, Rh); and c) maxima in the ethane distribution at both d_1 and d_6 (W, Zr, Cr, V, Pt). In order to explain these results, they proposed the

following mechanism for exchange:

$$CH_3CH_3\ (g) \underset{k_{-1}}{\overset{}{\rightleftharpoons}} CH_2CH_3\ ^* \overset{k_2}{\underset{k_{-2}}{\rightleftharpoons}} CH_2CH_2\ ^*\ ^*$$

where the asterisks identifies adsorption sites. They then introduced a parameter P, defined as the probability for adsorbed C_2H_5 species to undergo a $C_2H_5(ads) \rightarrow C_2H_4(ads) \rightarrow C_2H_5(ads)$ cycle, rather than directly desorbing and forming ethane ($P=k_2/k_{-1}$, if k_{-2} is fast). Using this scheme, a value of $P<1$ reproduces the type (a) product distribution, namely, a maximum at d_1. $P>1$, on the other hand, accounts for the results for the second group (mainly production of d_6). Finally, to obtain the U-shaped distribution characteristic of the third group, they postulate that two different mechanisms occur on different crystal faces with different values for P. To explain the distribution obtained for platinum it was necessary to propose that 54% of the products form via a reaction path with $P_1=2.0$, and the other 46% from a second branch with $P_2=20.0$.

The fact that a similar U-shaped product distribution was obtained on a flat hexagonal close packed platinum (111) crystal surface mediates against this argument. The partially ordered (2x2) overlayer observed by LEED after reactions indicates the presence of a short range periodicity, strongly suggesting the presence of only one main moiety on the surface (or at least a common intermediate) which leads to the formation of both d_1 and d_6 ethanes. If this hypothesis is valid, it is kinetically necessary to propose more than one dehydrogenated surface intermediate to reproduce the experimental product distribution. Miya-

hara [64] has offered an alternative kinetic model to account for the results of Anderson and Kemball, in which intermediates with 5,4 and 3 hydrogen atoms per surface moiety were postulated. The full kinetic treatment of this system succesfully reproduced the U-shaped curve, but it was later questioned because the existence of adsorbed C_2H_3 fragments was thought unlikely [65].

Recent surface studies have shown that such highly dehydrogenated intermediates are, in fact, stable and easy to obtain. Ethylidyne formation, for instance, is now well established (section 3.1). It has also been clearly shown that this moiety exists during ethylene hydrogenation (section 3.2). In this reaction the ethylidyne layer formed is too stable to be rehydrogenated, so that the gas phase ethylene hydrogenates on top of an ethylidyne covered platinum surface. In the present case, the (2x2) LEED pattern obtained after reactions, together with the thermal desorption results, lead us to propose ethylidyne as a reaction intermediate for exchange as well. Unlike room temperature ethylene hydrogenation, H/D exchange reaction temperatures are much higher (around 500 K) and ^{14}C radiotracer experiments have shown that CCH_3 fragments can be easily rehydrogenated and removed from the surface under those conditions (fig. 3.7). However, the diffuse nature of the extra spots in the LEED pictures indicates some disorder, probably due to the presence of other species. For that reason, the TDS cannot be unambiguously interpretated. Although the peaks in both H_2 and D_2 TDS are in the expected temperature ranges for ethylidyne, the relative areas are different. For instance, the high temperature peak in the D_2 trace is considerably bigger than expected. This could be explained by

the presence of CD fragments on the platinum surface, produced by of some ethylidyne decomposition at the high reaction temperatures, as obtained in UHV chemisorption studies [13]. These fragments would then account for the production of methane, the end product of hydrogenolysis.

It is therefore suggested that in the case of exchange reactions, associative desorption of the C_2H_5 adsorbate formed during the initial adsorption of ethane with a surface deuterium atom would yield mainly d_1 products, while the formation and rehydrogenation of ethylidyne could account for the formation of fully deuterated molecules. The proposed mechanism could be described as follows:

$$CX_3CX_3\ (g) \underset{k_{-1}}{\overset{k_1}{\rightleftharpoons}} \underset{*}{CX_2} + \underset{*}{X} \underset{k_{-2}}{\overset{k_2}{\rightleftharpoons}} \underset{**}{CX} + 2X \underset{k_{-3}}{\overset{k_3}{\rightleftharpoons}} \underset{***}{C} + 3X$$

$$\underset{***}{C}X_3 \xrightarrow{k_4} \underset{***}{2C} + \underset{*}{X} \xrightarrow{k_5} 2CX_4\ (g) + 5X$$

where X can be either H or D. The limiting step for exchange would be given by k_1, while the shape of the final distribution would depend on the k_2/k_{-1} ratio. The constants k_3, k_{-3}, and k_{-2} are postulated to represent fast reactions. For the d_6 production, once ethylidyne is formed, hydrogen exchange in the methyl group should be much more rapidly than ethylidyne rehydrogenation. The slow step for hydrogenolysis would be the carboncarbon bond breaking, k_4. A postulated energy diagram for this mechanism is shown in fig. 3.34. It is analogous to one previously proposed for methane deuterium exchange [66], except that in this case the limiting step for the formation of both d_1 and d_6 is the same, namely, the dissociative adsorption of ethane. This also explains why

methane d_4 and d_1 production have different activation energies, but ethane d_1 and d_6 pathways have the same value.

In the energy diagram presented in fig. 3.34, the initial dissociative chemisorption of ethane is the proposed limiting step for the exchange [57], therefore, an activation energy of 19 Kcal/mole has been assigned to it. Also, the resulting C_2X_5 moiety (an ethyl radical) has to be less stable than ethane gas, since its desorption is faster than the adsorption. Once formed, this initial adsorbed species can either rehydrogenate and form ethane again, or undergo further dehydrogenation. These are the two competitive pathways responsible for the U-shaped distribution of products, so that the activation barriers for these processes must be similar. Using the temperature dependence data of the product distribution shown in fig. 3.30, it can be seen that the barrier for rehydrogenation should be slightly higher than that for multiple exchange, by about 2 Kcal/mole, because less d_6 is produced at higher temperatures. The relative energies of other adsorbed species can be estimated using values of $D^{o}_{298}(H-H)$= 104 Kcal/mole [67], E_{act}=17.5 Kcal/mole for hydrogen desorption from Pt(111) [68], ΔH^{o}_{f} (C_2H_6)=-20 Kcal/mole and $\Delta H^{o}_{f}(C_2H_2)$=54 Kcal/mole [69], and calculations reported by Gavezotti and Simonetta for the adsorbed hydrocarbons [70], giving:

$$C_2H_6(g) \rightarrow CHCH_3(ads) + 2H(ads) \qquad \Delta H=29 \text{ Kcal/mole}$$

and

$$CHCH_3(ads) \rightarrow CCH_3(ads) + H(ads) \qquad \Delta H= 9 \text{ Kcal/mole}$$

Although the absolute values may not be accurate, the relative stabilities of the species involved have been used in the drawing of our diagram. The

equilibrium between different adsorbates may also change as a function of hydrogen pressure. Thus, ethylidyne, which is very stable under UHV conditions, may hydrogenate under an atmosphere of H_2 to yield ethylidene ($CXCX_3$), or further to form an ethyl radical (CX_2CX_3). The deuterium exchange in the methyl group of ethylidyne is assumed to go through an ethylidene intermediate, as proposed previously in section 3.1, and must be faster than ethylidyne rehydrogenation. If this were not the case, a large proportion of d_3 would be observed at low conversion, in contrast to the experimental results (no maximum in d_3 in fig. 3.29 was obtained).

It is important to point out that the intermediates proposed in the preceeding paragraph for exchange are 1,1 and 1,1,1 adsorbed species, as opposed to the 1,2 and 1,1,2 adsorption modes that have been previously reported. In other words, the multiadsorbed fragments bond to the metal through one of the carbon atoms only. These new species are well doccumented in chemisorption studies under UHV, as discussed earlier. Ethylidyne, that can be formed at room temperature, is triply bonded to the surface through one of the carbon atoms, and only at higher temperatures, above 450 K, does it "tip over" and further decompose to CH fragments [13,71]. These intermediates can also explain the thermal desorption results. The large peak at 691 K in the 4 amu trace corresponds to the CD fragments from ethylidyne decomposition, after having exchanged with D_2. They constitute the intermediates for methane formation, a reaction which is much slower than the exchange. It is worth noticing that the calculated activation energy from the high temperature peak in the TDS is 33 Kcal/mole [13], close to the value for hydrogenolysis over the

(111) surface. It is also interesting that, according to our model, the mechanisms for ethane deuterium exchange and ethylene hydrogenation are not directly related, since in the latter case the ethylidyne is stable on the surface, while ethylene hydrogenates on a second layer through a hydrogen transfer process. Finally, recent HREELS work in our group has shown that chemisorption of ethyl iodide over Pt(111) results in the formation of ethylidyne under UHV [72]. This means that once a C_2H_5 ethyl moiety is formed on the surface (product of the C-I bond breaking), further dehydrogenation of the α carbon is a facile process, easier than the formation of adsorbed ethylene over the same surface.

Further testing of the previously proposed ethane H/D exchange mechanism is difficult. The identification of adsorbed species on the platinum surface is complicated by the presence of different types of fragments. Preliminary HREELS studies have been inconclusive. A careful analysis of the resulting gas phase ethane mixture could provide some insight to the problem. ^{13}C-NMR can, in theory, differentiate between 1,1 and 1,2 dideuterated ethanes (and, analogously, between 1,1,1,2 and 1,1,2,2 d_4) [73,74]. However, due to the low pressure of the total gas produced in our reactions, the peaks in the final spectra broaden and overlap, due to free internal rotation of the molecules around the carbon-carbon axis. Again, preliminary work proved to be inconclusive (section 2.4). Infrared spectroscopy is another useful technique for distinguishing the different products, but spectra of these mixtures appear to be much too complicated to interpret [75,76]. A third technique to be used could be high resolution mass spectrometry. Guczi et. al. [77] have used it to determine the product distribution from the ethane

deuterium exchange over platinum black catalyst. They found that the 1,2 adsorption is predominant at 390 K, while 1,1 adsorbed intermediates become more important at higher temperatures (520 K). However, there are two main problems with the interpretation of their experimental results: a) the ionization of ethane in the mass spectrometer induces considerable scrambling of the hydrogen atoms in the molecules [78]; and b) the results obtained by Guczi et. al. are very sensitive to the values chosen for the required parameters, f_{14} and f_{15} (fragmentation probabilities for CX_2^+ and CX_3^+, respectively). They used a value $f_{14}/f_{15}=0.63$, while in the paper by Amenomiya and coworkers a value of 0.21 is reported for that ratio. That latter number would make the interpretation of Guczi's results difficult. We also try to perform such detailed analysis of the products, but the deconvolution of the resulting mass spectrum was not satisfactory (section 2.4.4). It seems, however, that at least half of the total $d_2+d_3+d_4$ mixture in the reaction mixture are asymmetrically substituted, a result that would support our mechanism.

Table 3.6

Pressure dependence of the initial reaction rates for ethane deuterium exchange over platinum (111) single crystal surfaces at 550 K.

$P_{C_2H_6}$ (Torr)	P_{D_2} (Torr)	Rate (C_2H_6 molec./Pt atom·sec)
10	100	8.94
10	300	4.78
10	600	3.46
20	300	10.96

Table 3.7

Kinetic parameters for the reactions of ethane with deuterium over platinum (111) single crystals.

Reaction	E_a (Kcal/mole)	$LogA^a$	a^b	b^b
D_2 exchange	19±2	9.8±0.5	-0.55±0.05	1.2±0.2
Hydrogenolysis	34±1	11.2±0.2[c]		

a) Preexponential factor, in molec/Pt atom•sec. (Pressures in atm.).

b) orders in deuterium (a) and ethane (b) partial pressures.

c) includes pressure dependence, $P_{C_2H_6}$=10 Torr, and P_{D_2}=100 Torr.

Table 3.8

Pressure dependence of the deuterium atom distribution for ethane deuterium exchange over Pt (111) single crystal surfaces. T=550 K

$P_{C_2H_6}$ (Torr)	P_{D_2} (Torr)	Composition (%)					
		d_1	d_2	d_3	d_4	d_5	d_6
10	100	29	10	1	4	11	46
10	300	27	14	2	3	6	48
10	600	27	14	4	4	7	44
20	300	28	8	2	4	9	49

Table 3.9

Compilation of thermal desorption data obtained after ethane deuterium exchange reactions on Pt (111).

m/e (molec.)	T[b]	Peak A[a] Area%	Peak B[a] Area%	Peak B[a] E_a[c]	Peak C[a] Area%	Peak C[a] E_a[c]	H or D/C
2 (H_2)	473	17	60	21.6	23	36.9	0.65
	533	12	64	22.7	24	36.6	0.44
	548	19	56	21.9	25	37.1	0.45
	623	22	54	21.9	24	36.9	0.24
	Average	18	59	22	24	37	
4 (D_2)	513	9	46	22.2	45	39.8	0.91
	548	13	41	22.7	46	40.4	0.78
	573	9	42	22.2	49	40.4	0.70
	Average	10	43	22	47	40	

a) Peak A at 470 K, peak B at 540 K, peak C above 640 K.

b) Reaction temperature, in K.

c) Activation energy, in Kcal/mole, assuming first order desorption kinetics, and $\nu=2\times10^{9}$ for peak B and $\nu=10^{13}$ for peak C, as for ethylidyne.

Table 3.10

Comparison of ethylene deuterium exchange kinetic parameters for different platinum catalysts.

Catalyst	E_a (Kcal/mole)	LogA^a	M^b	Ref.
Pt film	12.5	4.32	3.5 (415 K)	55
Pt black	19.0	7.03	2.6 (373-413 K)	56
Pt powder	18.9	3.18	1.7 (377 K) 2.7 (551 K)	57
Pt film	26.2	7.82	2.12 (573 K)	58
1% Pt/SiO_2	17.7	7.07	---	59
1% Pt/Cab-O-Sil	17.1	5.26	---	59
Pt (111)	19	9.8	3.74 (523 K) 4.30 (573 K)	our work

a) Preexponential factor, including pressures, in C_2H_6 molec./Pt atom·sec.

b) Average number of deuterium atoms incorporated per ethane molecule.

FIGURE CAPTIONS

Fig. 3.25. Product accumulation curves as a function of reaction time for ethane deuterium exchange and hydrogenolysis over Pt (111) single crystal surfaces. T=573 K, $P_{C_2H_6}$=10 Torr and P_{D_2}=100 Torr.

Fig. 3.26. First order kinetic plot of the product accumulation curve for ethane deuterium exchange over Pt (111). Same conditions as in fig. 3.25.

Fig. 3.27. Arrhenius plots for ethane deuterium exchange and hydrogenolysis over Pt (111). $P_{C_2H_6}$=10 Torr and P_{D_2}=100 Torr.

Fig. 3.28. Deuterium atom distribution in the resulting ethane from the exchange with deuterium over Pt (111). Same pressures as in fig. 3.27, T=550 K.

Fig. 3.29. Deuterium atom distribution of ethane as a function of reaction time for deuterium exchange over Pt (111). Same conditions as in fig. 3.28.

Fig. 3.30. Temperature dependence of the deuterium atom distribution in ethane deuterium exchange over Pt (111). Same conditions as in fig. 3.27.

Fig. 3.31. a) (2x2) LEED pattern resulting from the adsorption of ethylene on a Pt (111) surface at room temperature and UHV. b) diffuse (2x2) LEED pattern obtained after ethane reactions with

deuterium over Pt (111) surfaces at 500-650 K. Electron energy ~ 70 eV.

Fig. 3.32. Amount of carbon on the Pt (111) surface after ethane deuterium exchange as a function of reaction temperature, measured using Auger electron spectroscopy. Same conditions as in fig. 3.27.

Fig. 3.33. 2 amu (H_2, trace a) and 4 amu (D_2, trace b) thermal desorption spectra after ethane reactions with deuterium over Pt (111). Same conditions as in fig. 3.27. Heating rate ~ 40 K/sec.

Fig. 3.34. Schematic energy diagram for the reaction of ethane with deuterium. X represents either H or D.

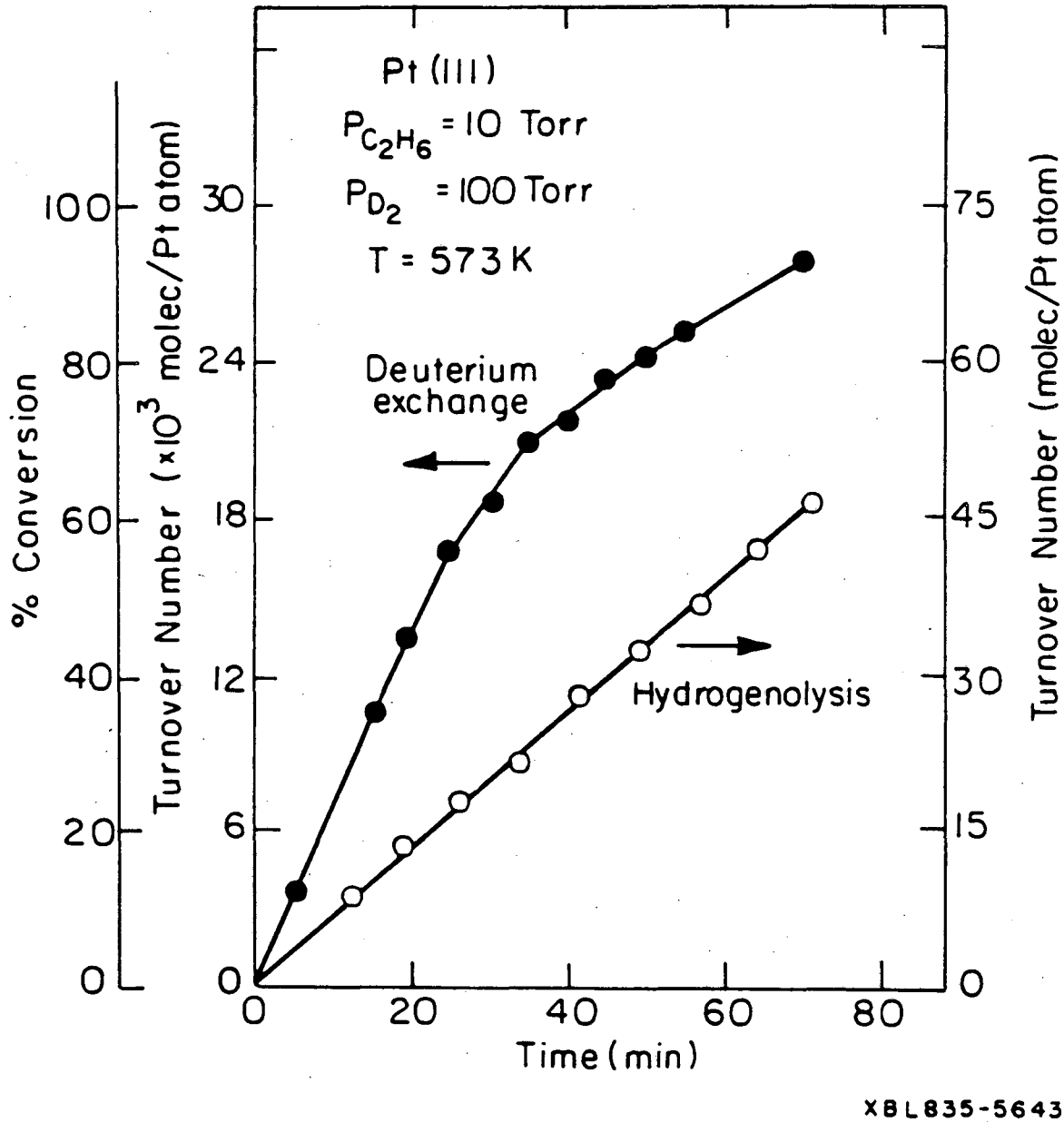
Pt (111)
$P_{C_2H_6}$ = 10 Torr
P_{D_2} = 100 Torr
T = 573 K
Deuterium exchange
Hydrogenolysis
% Conversion
Turnover Number (×10³ molec/Pt atom)
Turnover Number (molec/Pt atom)
Time (min)
0
20
40
60
80
100
30
24
18
12
6
75
60
45
30
15
XBL835-5643

fig. 3.25

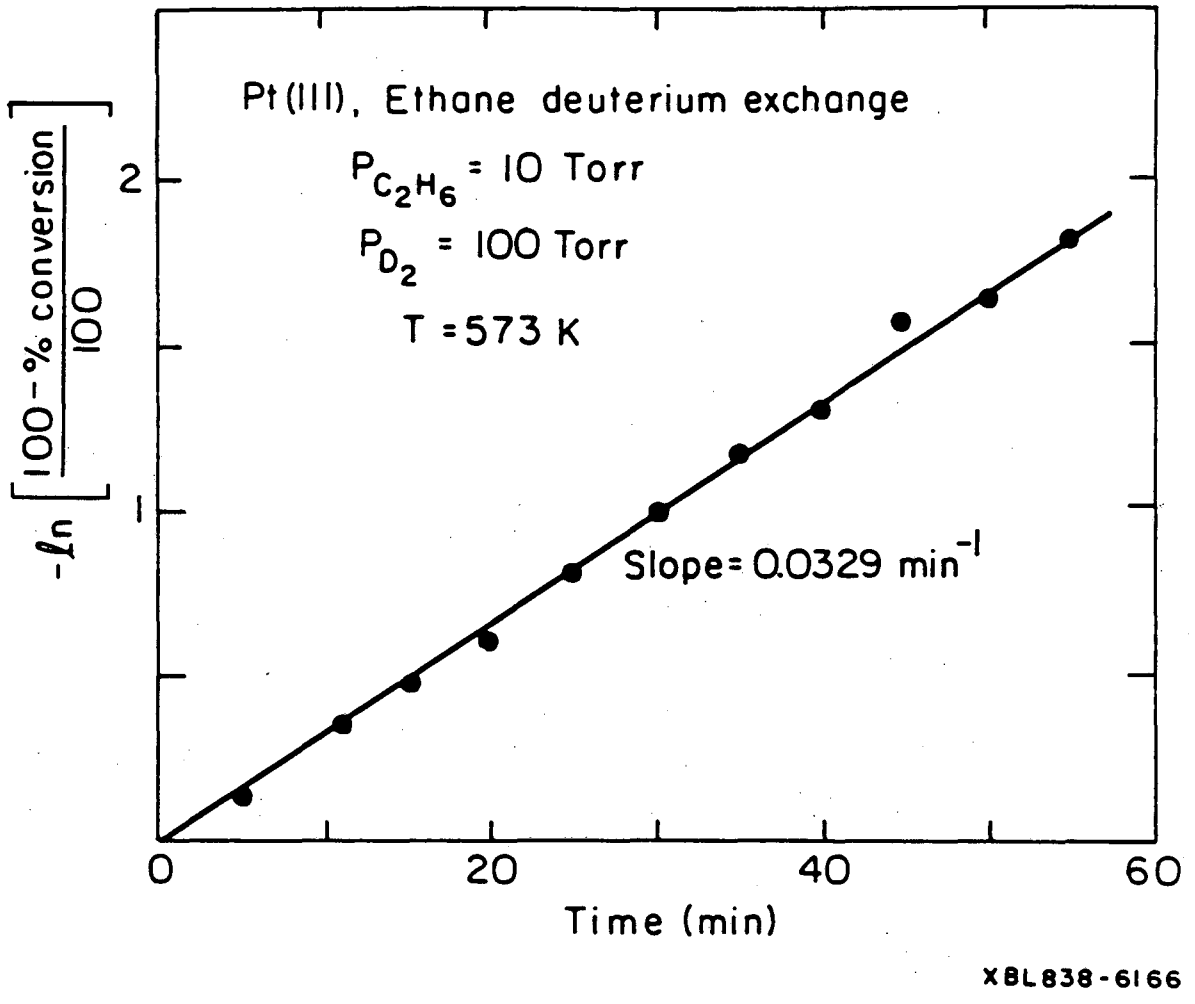
Pt(111), Ethane deuterium exchange
$P_{C_2H_6}$ = 10 Torr
P_{D_2} = 100 Torr
T = 573 K
Slope = 0.0329 min^{-1}
$-\ln\left[\frac{100-\%\text{ conversion}}{100}\right]$
0
1
2
0
20
40
60
Time (min)
XBL838-6166

fig. 3.26

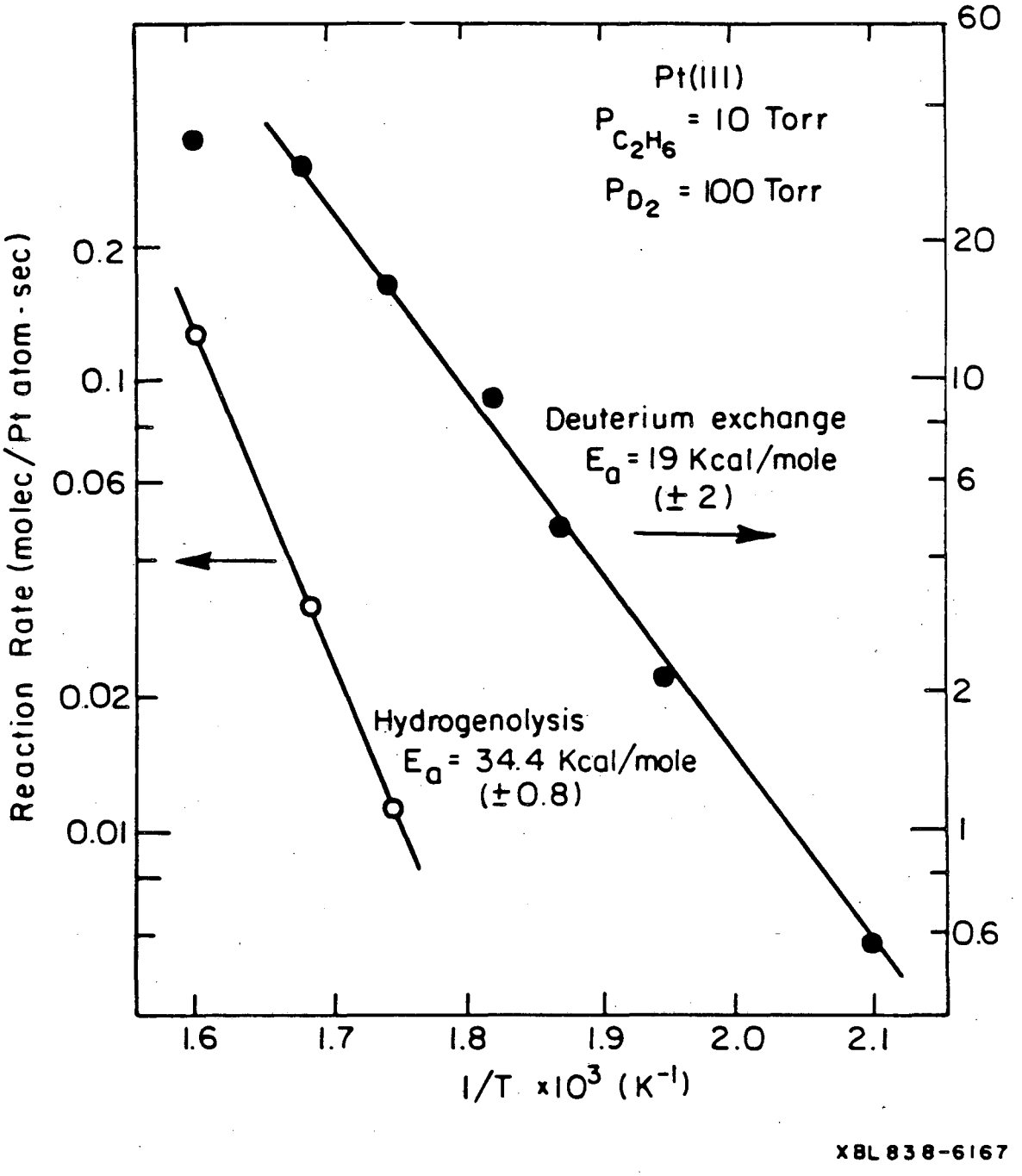
Pt(111)
$P_{C_2H_6}$ = 10 Torr
P_{D_2} = 100 Torr
Deuterium exchange
E_a = 19 Kcal/mole
(± 2)
Hydrogenolysis
E_a = 34.4 Kcal/mole
(±0.8)
Reaction Rate (molec/Pt atom - sec)
0.2
0.1
0.06
0.02
0.01
60
20
10
6
2
1
0.6
1.6
1.7
1.8
1.9
2.0
2.1
1/T x10^3 (K^{-1})
XBL838-6167

fig. 3.27

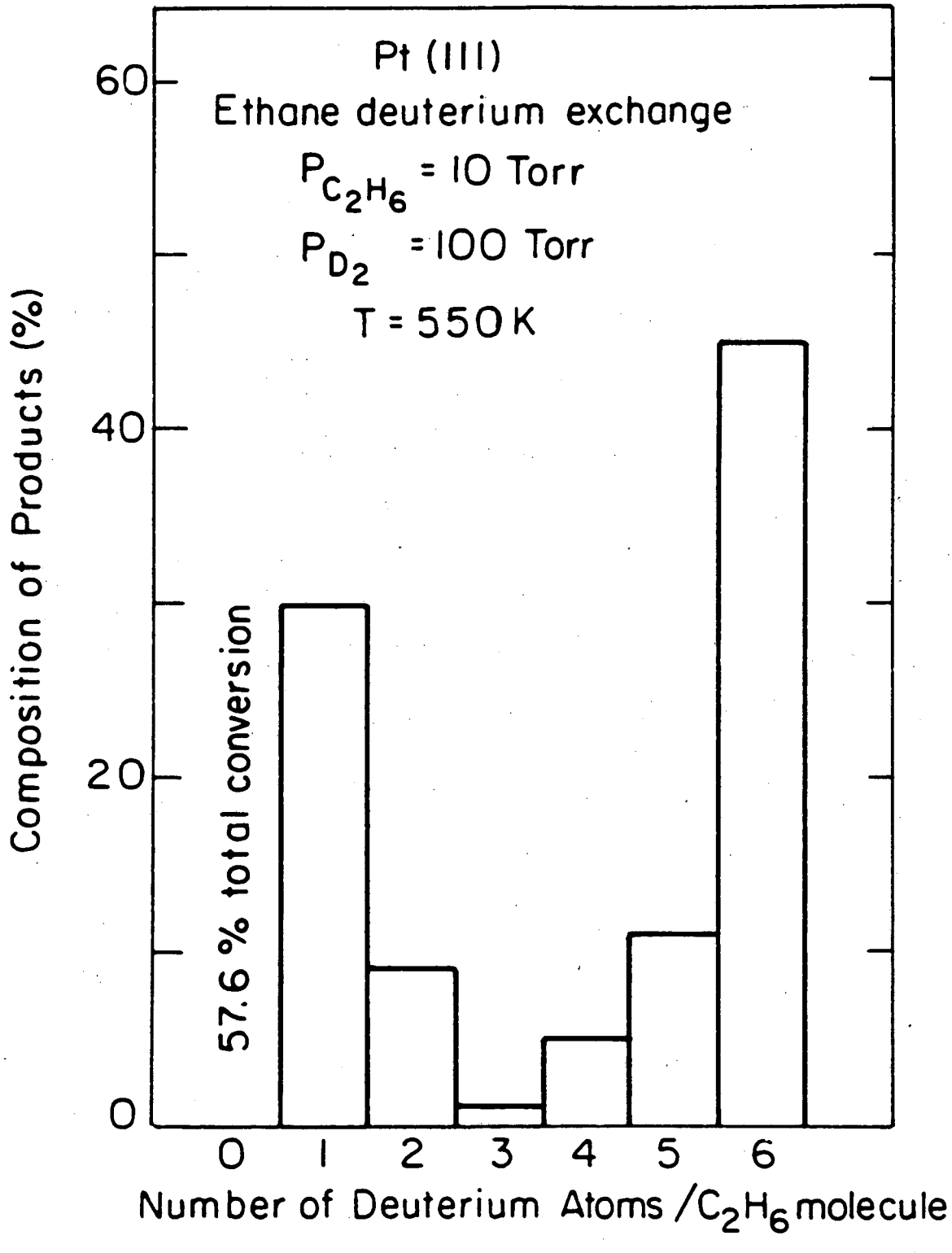
Pt (111)
Ethane deuterium exchange
$P_{C_2H_6}$ = 10 Torr
P_{D_2} = 100 Torr
T = 550 K
57.6 % total conversion
Composition of Products (%)
0
20
40
60
0 1 2 3 4 5 6
Number of Deuterium Atoms /C_2H_6 molecule
XBL835-5647

fig. 3.28

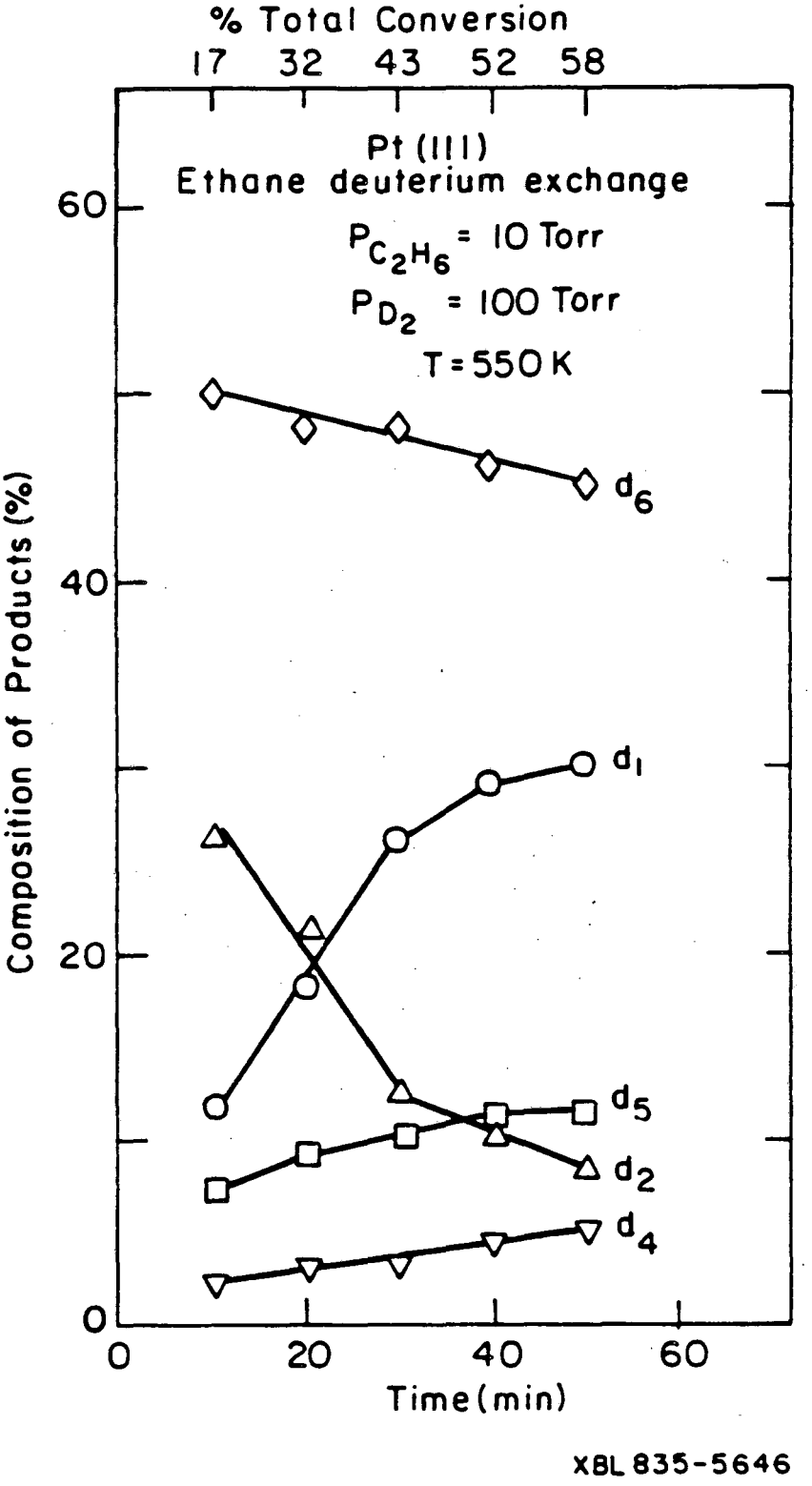
% Total Conversion
17 32 43 52 58
Pt (111)
Ethane deuterium exchange
$P_{C_2H_6}$ = 10 Torr
P_{D_2} = 100 Torr
T = 550 K
Composition of Products (%)
0
20
40
60
d_6
d_1
d_5
d_2
d_4
0
20
40
60
Time (min)
XBL 835-5646

fig. 3.29

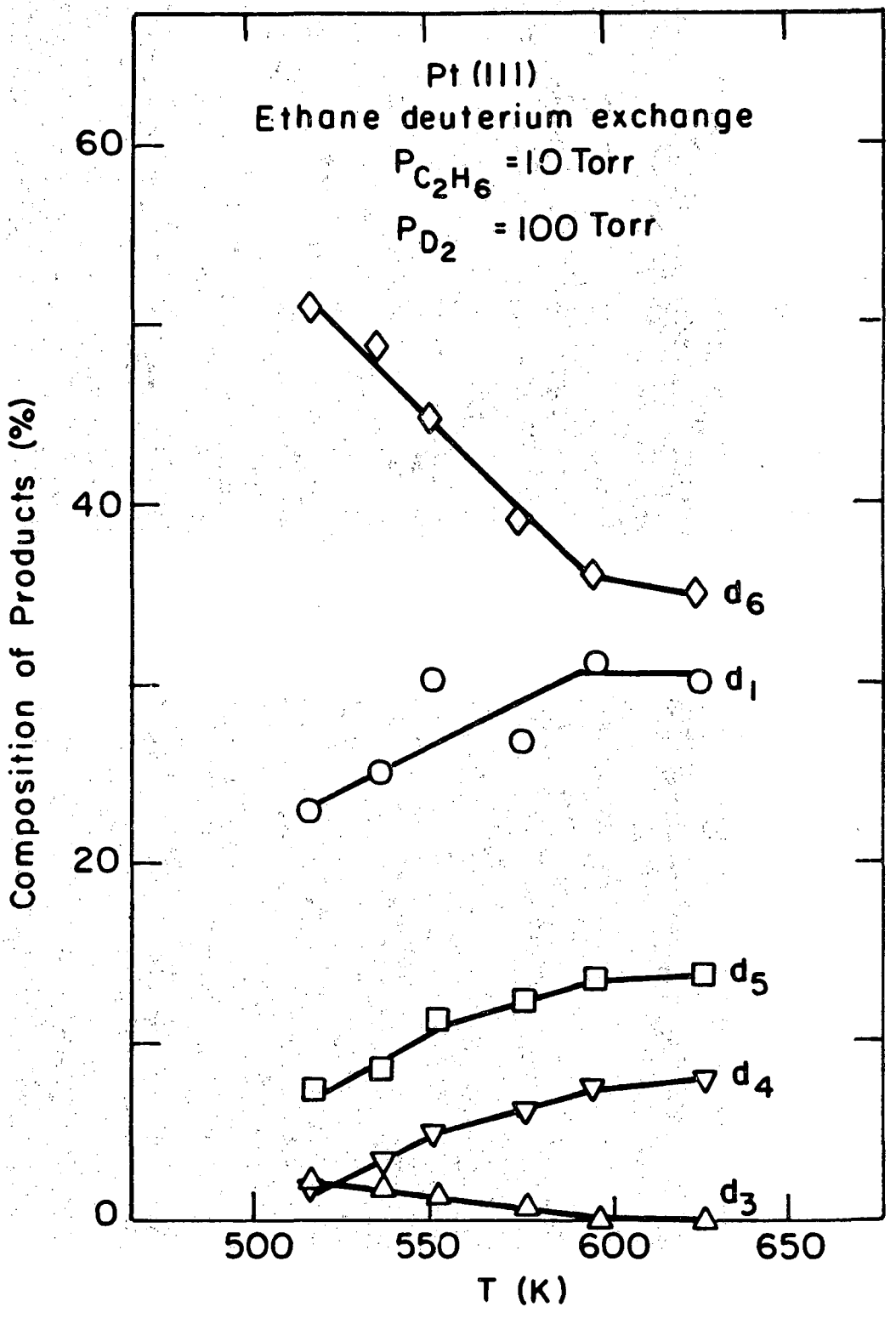

fig. 3.30

XBL835-5645

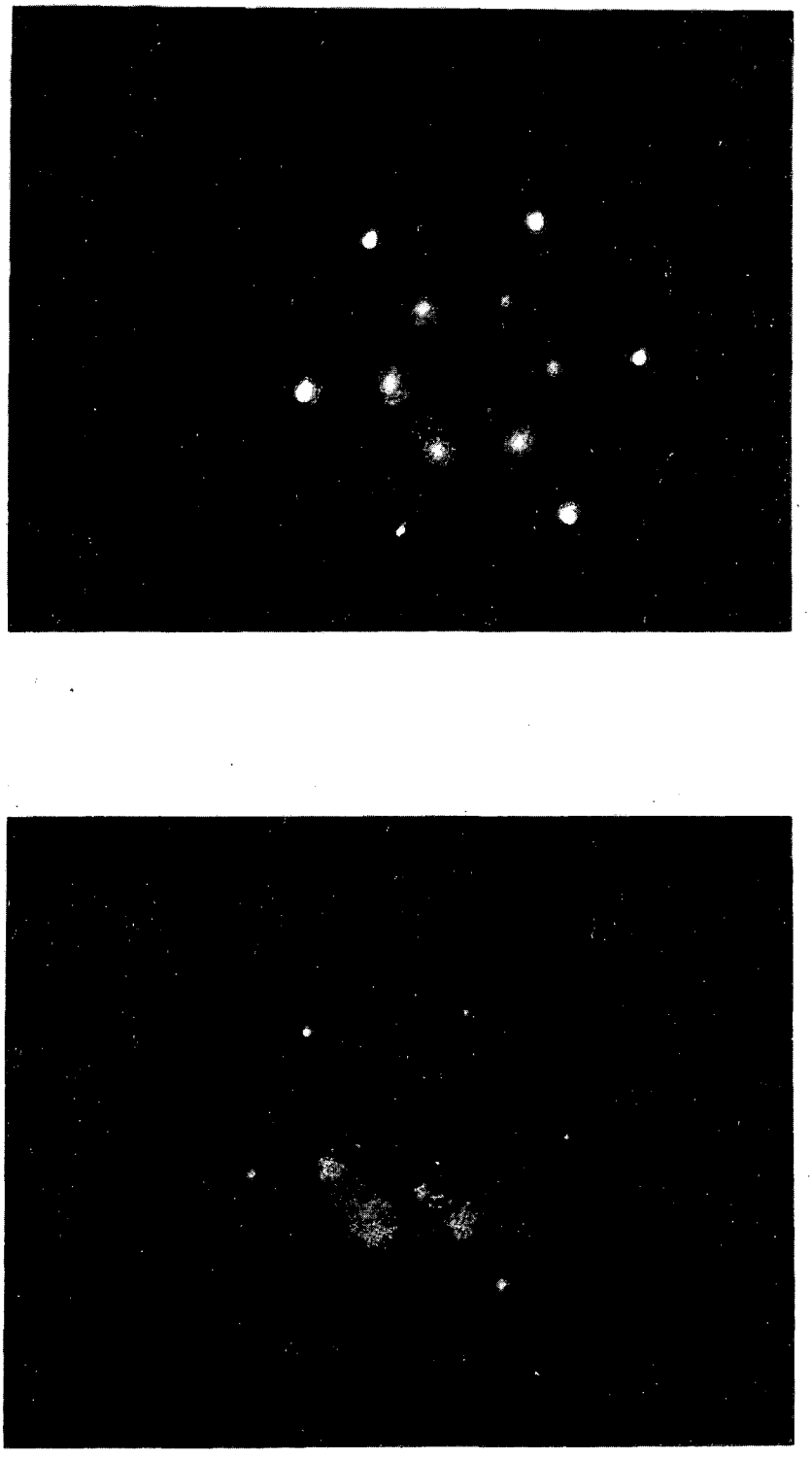

XBB 839-1999A

Fig. 3.31

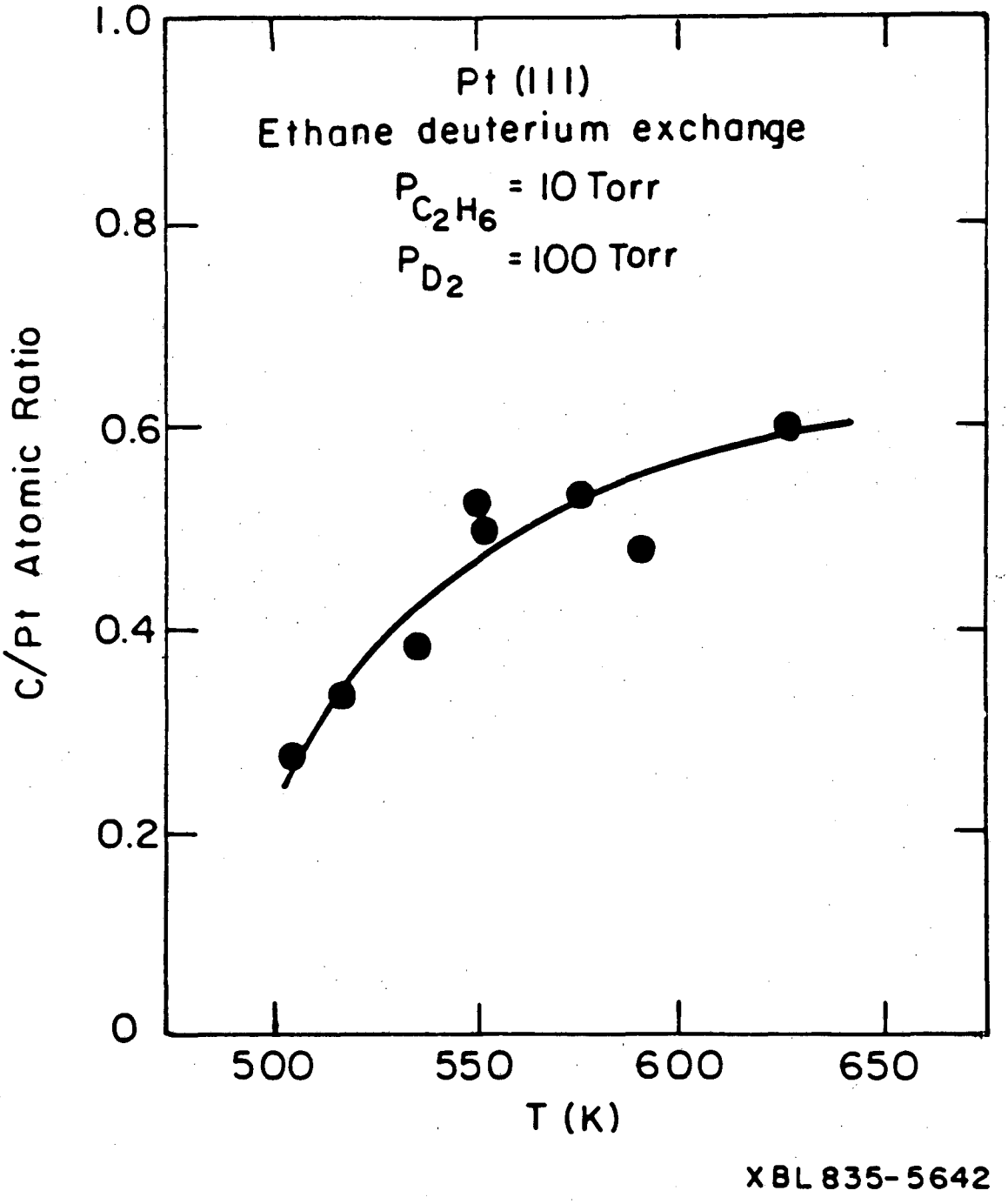
Pt (111)
Ethane deuterium exchange
$P_{C_2H_6}$ = 10 Torr
P_{D_2} = 100 Torr
C/Pt Atomic Ratio
1.0
0.8
0.6
0.4
0.2
0
500
550
600
650
T (K)
XBL 835-5642

fig. 3.32

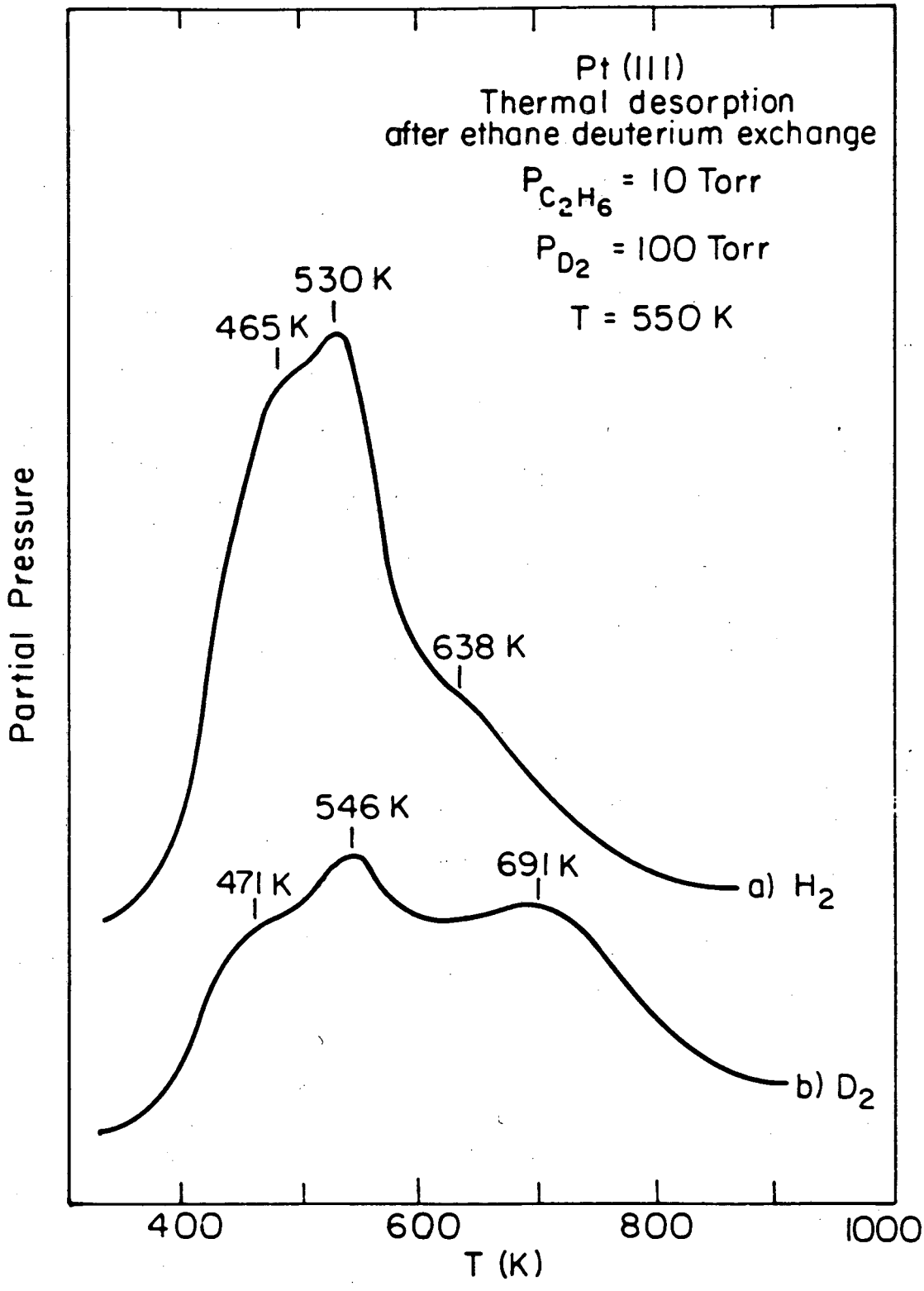
Pt (111)
Thermal desorption
after ethane deuterium exchange
$P_{C_2H_6}$ = 10 Torr
P_{D_2} = 100 Torr
T = 550 K
530 K
465 K
638 K
546 K
471 K
691 K
a) H_2
b) D_2
Partial Pressure
400
600
800
1000
T (K)
XBL 835-5648

fig. 3.33

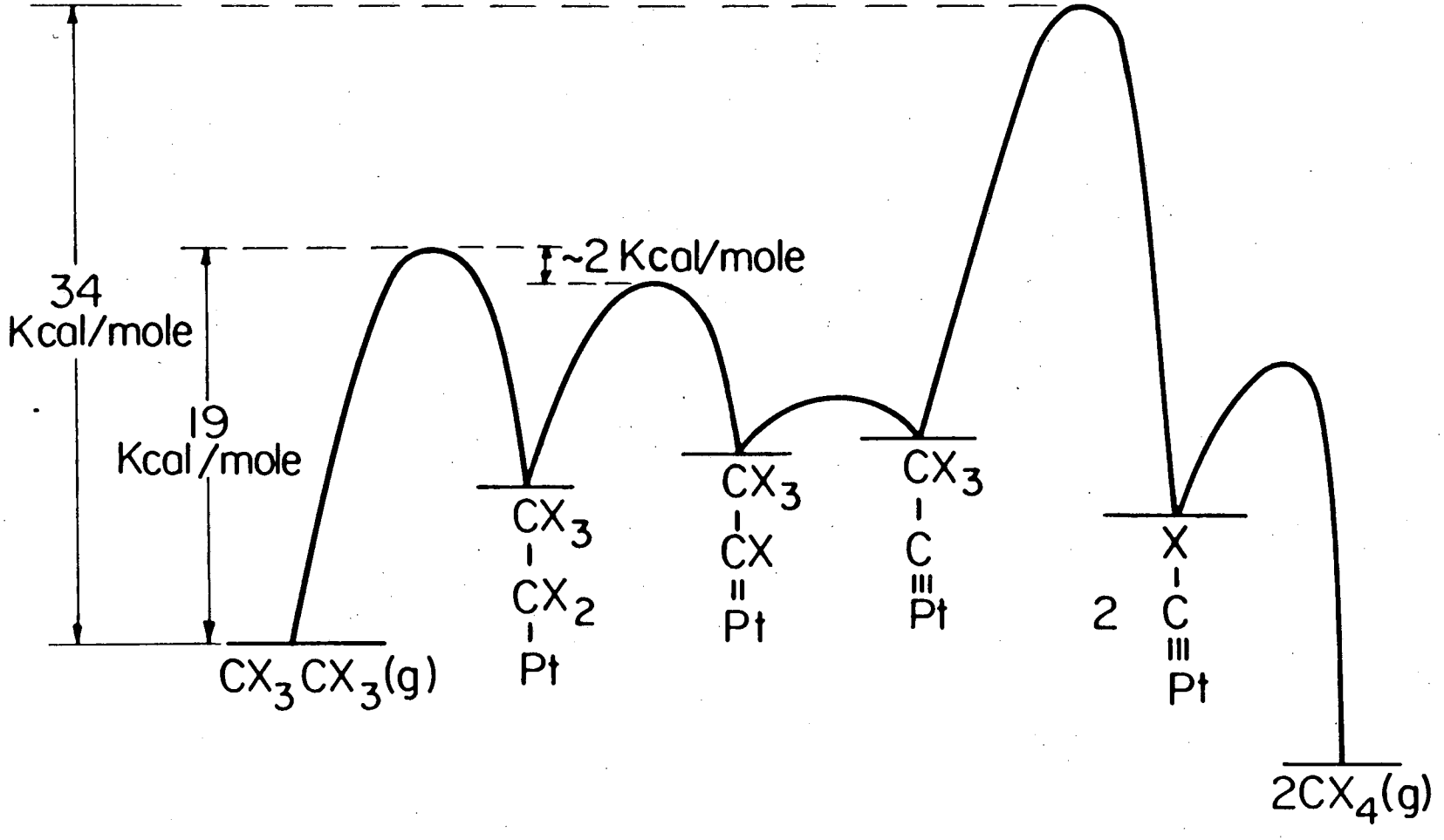

XBL 842-6613

Fig. 3.34

3.4. References.

1) L.L. Kesmodel and J.A. Gates, Surf. Sci., 111, L747 (1981).

2) J.A. Gates and L.L. Kesmodel, Surf. Sci., 120, L461 (1982).

3) J.A. Gates and L.L. Kesmodel, Surf. Sci., 124, 68 (1983).

4) D.R. Lloyd and F.P. Netzer, Surf. Sci., 129, L249 (1983).

5) W.T. Tysoe, G.L. Nyberg and R.M. Lambert, J. Phys. Chem., 88, 1960 (1984).

6) L.H. Dubois, D.G. Castner and G.A. Somorjai, J.Chem. Phys., 72, 5234 (1980).

7) M.A. Van Hove, R.J. Koestner and G.A. Somorjai, J. Vac. Sci. Technol., 20, 886 (1982).

8) R.J. Koestner, M.A. Van Hove and G.A. Somorjai, Surf. Sci., 121, 321 (1982)

9) H. Ibach and S. Lehwald, J. Vac. Sci. Technol., 15, 407 (1978).

10) L.L. Kesmodel, L.H. Dubois and G.A. Somorjai, J. Chem. Phys., 70, 2180 (1979).

11) J.E. Demuth, Surf. Sci., 80, 367 (1979).

12) P. Skinner, M.W. Howard, I.A. Oxton, S.F.A. Kettle, D.B. Powell and N. Sheppard, J. Chem. Soc., Faraday Trans. 2, 77, 1203 (1981).

13) M. Salmerón and G.A. Somorjai, J. Phys. Chem., 86, 341 (1982).

14) M.R. Albert, L.G. Sneddon, W. Eberhardt, F. Greunter, T. Gustafsson and E.W. Plummer, Surf. Sci., 120, 19 (1982).

15) N. Freyer, G. Pirug and H.P. Bonzel, Surf. Sci., 126, 487 (1983).

16) R.J. Koestner, J. Stöhr, J.L. Gland and J.A. Horsley, Chem. Phys. Lett., 105, 332 (1984).

17) J.R. Creighton and J.M. White, Surf. Sci., 129, 327 (1983).

18) R.J. Koestner, M.A. Van Hove and G.A. Somorjai, J. Phys. Chem., 87, 203 (1983).

19) S.M. Davis, F. Zaera, B.E. Gordon and G.A. Somorjai, Submitted to J. Catal.

20) P.R. Norton, J.W. Goodale and E.B. Selkirk, Surf. Sci., 83, 189 (1979).

21) G. Ertl, M. Neumann and K.H. Streit, Surf. Sci., 64, 393 (1977).

22) B.E. Koel, B.E. Bent and G.A. Somorjai, Submitted to Surf. Sci.

23) O. Beek, Rev. Mod. Phys., 17, 61 (1945).

24) G.I. Jenkins and E.K. Rideal, J. Chem. Soc., 2490 (1955).

25) O. Beek, Discuss. Faraday Soc., 8, 118 (1950).

26) G.C. Bond, "Catalysis by Metals", Academic Press, London 1962.

27) S.J. Stephens, J. Phys. Chem., 63, 512 (1959).

28) B.M.W. Trapnell, Trans. Faraday Soc., 48, 160 (1952).

29) R.W. Roberts, J. Phys. Chem., 67, 2035 (1963).

30) W. Hasse, H.-L. Günter and M. Henzler, Surf. Sci., 126, 479 (1983).

31) L.L. Kesmodel, P.C. Stair, R.C. Baetzold and G.A. Somorjai, Phys. Rev. Lett., 36, 1316 (1976).

32) P.C. Stair and G.A. Somorjai, J. Chem. Phys., 66, 2036 (1977).

33) L.L. Kesmodel, R.C. Baetzold and G.A. Somorjai, Surf. Sci., 66, 299 (1977).

34) N. Freyer, G. Pirug and H.P. Bonzel, Surf. Sci., 125, 327 (1983).

35) J.R. Creighton, K.M. Ogle and J.M. White, Surf. Sci., 138, L137 (1984).

36) For a review, see J. Horiuti, K. Miyahara, "Hydrogenation of Ethylene on Metallic Catalysts", NSRDS-NBS, 13, (1968).

37) J.R. Anderson, B.G. Baker, in "Chemisorption and reactions on Metallic Films", Vol. 2, J.R. Anderson, ed., Academic Press, London 1971, p. 63.

38) L.L. Kesmodel, L.H. Dubois, and G.A. Somorjai, Chem. Phys. Lett., 56, 267 (1978).

39) G.C. Bond, Trans. Faraday Soc., 52, 1235 (1956).

40) S.M. Davis, B.E. Gordon, M. Press, and G.A. Somorjai, J. Vac. Sci. Technol., 19, 231 (1981).

41) A. Farkas, L. Farkas, J. Am. Chem. Soc., 60, 22 (1938).

42) V.B. Kazanskii, V.P. Strunin, Kinet & Catal, 1, 517 (1960).

43) T.A. Dorling, M.J. Eastlake, and R.L. Moss, J. Catal., 14, 23 (1969).

44) J.C. Schlatter, M. Boudart, J. Catal., 24, 482 (1972).

45) G.C. Bond, J.J. Phillipson, P.B. Wells, and J.M. Winterbottom, Trans. Faraday Soc., 60, 1847, (1964).

46) J.E. Demuth, H. Ibach, Surf. Sci., 85, 365 (1979).

47) G.M. Schwab, W. Schmaltz, H. Noller, Z. Physik Chem (N.F.), 29, 356 (1961).

48) O. Toyama, Rev. Phys. Lett. Chem. Japan, 11, 353 (1937).

49) E. Crawford, M.W. Roberts, C. Kemball, Trans. Faraday Soc., 58, 1761 (1962).

50) G.C.A. Schuit, L.L van Reijen, Adv. in Catal., 10, 298 (1958).

51) M. Kowaka, M.I. Joncich, Mem. Inst. Sci. Res., Osaka Univ., 16, 107 (1959).

52) G.C. Bond, J.J. Phillipson, P.B. Wells, J.H. Winterbottom, Trans. Faraday Soc., 62, 443 (1966).

53) K.J. Laidler, R.E. Townshend, Trans. Faraday Soc., 57, 1590 (1961).

54) G.C. Bond, G. Webb, P.B. Wells, Trans. Faraday Soc., 61, 999 (1965).

55) J.R. Anderson and C. Kemball, Proc. Royal Soc., A223, 361 (1954).

56) L. Guczi, A. Sárkány and P. Tétényi, J. Chem. Soc. Faraday

Trans. I, 70, 1971 (1974).

57) L. Babernics, L. Guczi, K. Matusek, A. Sárkány and P. Tétényi, Proc. 6th Int. Cong. Catal., Vol. 1, paper A36, London, 1976.

58) L. Guczi and Z. Karpiński, J. Catal., 56, 438 (1979).

59) L. Guczi and J. Sárkány, J. Catal., 68, 190 (1981).

60) C. Kemball, in "Advances in Catalysis", Vol. 11, D.D. Eley, H. Pines and P.B. Weisz, eds., Academic Press, New York 1959, pp 223-262.

61) G. Leclerq, L. Leclerq and R. Maurel, J. Catal., 44, 68 (1976).

62) P. Tétényi, L. Guczi and A. Sárkány, Acta Chim. Acad. Scient. Hung., 97, 221 (1978).

63) J.H. Sinfelt, in "Advances in Catalysis", Vol. 23, D.D. Eley, H. Pines and P.B. Weisz, eds., Academic Press, New York 1980, p. 91.

64) K. Miyahara, J. Res. Inst. Catal., Hokkaido Univ., 4, 143 (1956).

65) C. Kemball, J. Res. Inst. Catal., Hokkaido Univ., 4, 222 (1957).

66) C. Kemball, Catal. Rev., 5, 33 (1971).

67) "Handbook of Chemistry and Physics", 64th edition, C.R.C. Press, Florida 1983.

68) K. Christmann, G. Ertl and T. Pignet, Surf. Sci., 54, 365 (1976).

69) D.R. Stull, E.F. Westrum, Jr. and G.C. Sinke, "The Chemical Thermodynamics of Organic Compounds", John Willey & Sons, Inc., New York 1969.

70) A. Gavezotti and M. Simonetta, Surf. Sci., 99, 453 (1980).

71) A.M. Baro and H. Ibach, J. Chem. Phys., 74, 4194 (1981).

72) B. Bent and G.A. Somorjai, private communications.

73) R.A. Berheim and B.J. Lavery, J. Chem. Phys., 42, 1464 (1965).

74) M. Alei, Jr., and W.E. Wageman, J. Chem. Phys., 68, 783 (1978).

75) R. Van Riet, Ann. Soc. Sci. Bruxelles, Ser. 1, 71, 102 (1957).

76) J.L. Duncan, D.C. McKean and A.J. Bruce, J. Mol. Spectros., 74, 361 (1979).

77) L. Guczi and K. Ujszáski, React. Kin. & Catal. Lett., 8, 489 (1978).

78) Y. Amenomiya and R.F. Pottie, Can. J. Chem., 46, 1741 (1968).

CHAPTER FOUR: SATURATED HYDROCARBON REACTIONS OVER CLEAN PLATINUM SINGLE CRYSTALS

4.1. Structure sensitivity of hydrocarbon reactions.

4.1.1. Introduction.

Hydrocarbon reactions have been extensively studied over many types of platinum catalysts, including powders, films and supported particles of platinum alone or alloyed with a second metal. A comprehensive review of the work done in this area has been recently published by Davis and Somorjai [1]. The skeletal rearrangement of saturated hydrocarbons over these catalysts is generally believed to be structure sensitive, that is, the activity and selectivity for such reactions depend strongly on the microscopic structure of the metal surface. In supported catalysts this effect becomes manifest by a change in catalyst performance as a function of particle size as observed many times for reactions like butane [2] and neopentane [3,4] conversions. For n-hexane, Dautzenberg and Platteuw [5,6] and Ponec and coworkers [7] did not find significant structure sensitivity over a platinum particle size range of 15 to 80 Å, but Anderson [8] and Santacessaria [9], on the other hand, reported significant variations in catalytic activity for ultra-thin films and for Pt/SiO_2 catalysts with particle sizes of 10 Å and less.

In order to obtain a better underestanding of the nature of the structure sensitivity, we have recently studied hydrocarbon reactions over various exposed surfaces of platinum single crystals. Davis [10] has studied the conversion of n-butane, isobutane, neopentane and n-he-

xane over four different surfaces including Pt(111), Pt(100) and stepped and kinked surfaces. He found that isomerization and consecutive rearrangement reactions of light alkanes were maximized on platinum surfaces with high concentrations of (100) microfacets [11]. n-Hexane isomerization, by contrast, was structure insensitive, but its aromatization was enhanced by the presence of (111) terraces [12]. In the present work, an extension of these studies was performed, with focus on the study of the effect of steps on these reactions. For that purpose, the catalytic activity of isobutane, neopentane and n-hexane over Pt(111), Pt(557) and Pt(332) was added to similar studies reported by Davis on Pt(13,1,1), Pt(100) and Pt(10,8,7). A schematic representation of all these six surfaces is shown in fig. 4.1.

4.1.2. Results.

The conversion of isobutane, neopentane and n-hexane were investigated over the above mentioned platinum single crystal surfaces at temperatures between 550 and 620 K (fig 4.2). Standard pressures for these reactions were 20 Torr of the hydrocarbon and either 200 or 600 Torr H_2. Typical product accumulation curves obtained as a function of time are shown in fig. 4.3 for isobutane isomerization and hydrogenolysis at 573 K over the six platinum surfaces. Initial rates were calculated from the slope of these curves at low conversions, and are summarized in tables 4.1 to 4.3. The conversion rates displayed significant structure sensitivities in the cases of isobutane and neopentane, with initial rates differing by a factor of four between the least and most active surfaces under similar conditions. In contrast, most reaction rates for n-hexane were within a factor of two for all the surfaces.

Initial activities for the six platinum surfaces studied are also shown in figs. 4.4 to 4.6. Pressure and temperature dependences can also be seen from the data reported; an example is shown in fig. 4.7 for isobutane conversion over Pt(332).

Auger analysis of the surface composition following these reactions always revealed the build-up of an overlayer of strongly chemisorbed carbonaceous species (from one to six carbon atoms per surface platinum atom, depending on the reactants and on the reaction conditions). No ordering in these layers could be detected with LEED. The slow but continuous deactivation that was observed for all reactions over the platinum surfaces indicates that at least part of the carbon deposits were bound irreversibly and acted as deactivating residues. The rate of deactivation was similar for all reactions studied, and appeared to be essentially independent of surface structure. As an example the deactivation of isobutane conversion as a function of time is shown, together with the carbon build-up on the surface and the uncovered platinum area, in fig. 4.8. This data was obtained by running the same reaction many times, starting with the clean surface, and stopping at different times in order to characterize the resulting surface. There is good correlation between activity and catalytically active area, and between the amount of carbon on the surface and the other two parameters.

CO titrations in order to determine the bare platinum sites were performed after each reaction. The area under the resulting CO TDS measures the total amount of platinum surface uncovered by the carbonaceous layer; the data in fig. 4.8 was obtained this way. Also, when stepped

surfaces are used, this experiment allow us the identification of active sites on the surface, because the binding energy for CO at low coordination sites is higher than that on (111) terraces. This is illustrated in fig. 4.9, which shows the results of CO TDS from these titrations obtained after reactions using various hydrocarbons. The top curve was obtained from a CO saturated Pt(755) surface. It has a main peak at about 440 K due to CO molecules desorbing from the (111) terraces, and a shoulder at around 540 K that arises from desorption from steps. This high temperature peak is also seen after isobutane and neopentane reactions, but it is absent for the methylcyclopentane and n-hexane cases. Similar results were obtained using a Pt(332) surface.

4.1.3. Discussion.

Most of the implications of these structure sensitivity results have been discussed in detail in previous publications [10-12]. For light alkanes it was concluded that (100) terraces were in general more active in catalyzing isobutane and n-butane isomerization, but the effect was not as significant when neopentane was used as a reactant. The differences may be related to the hydrocarbon structure, since n-butane and isobutane dehydrogenate readily to form the corresponding olefins, while this is not possible for neopentane. Also the orientation of the d orbitals of the metal surface change with crystallographic face, so the change in overlap with the molecular orbitals of the hydrocarbons can be used to explain the structure sensitivity observed. In the case of n-hexane, no structure dependence was observed for isomerization and methylcyclopentane formation. A different mechanism is involved in these reactions, in which a cyclic intermediate is formed (a five or six

membered ring), instead of a bond-shift mechanism responsible for light alkane reactions [13-17] (fig. 4.10). In the case of benzene formation, (111) terraces displayed activities that were several times higher than those over (100) surfaces, possibly due to the different binding energies of hydrogen on both surfaces, or to a template effect. Finally, the results obtained on single crystals were compared with those reported using other types of catalysts, and agreement was found with the work of Anderson and Avery for butane isomerization [2]; of Foger and Anderson for neopentane conversion [3]; and of Ponec et. al. [7] and Dautzenberg and Platteeuw [5,6] for n-hexane reactions. Discrepencies were found between our results and those of Anderson [8] and Santacessaria [9], where significant variations in catalytic activity were found for n-hexane isomerization, hydrogenolysis and C_5-cyclization as a function of particle size.

The present work emphazises the role of steps and other low coordination number platinum atoms in these reactions. Generally, different mechanisms have been proposed for different sites on the metallic surfaces. It has been suggested, for instance, that corner atoms with very few (3 or 4) nearest neighbours may be responsible for the exceptional C_5-cyclization selectivity that has often been reported for supported catalysts with very high dispersions [7,15-25]. These theories could be tested with our experimental instrumentation by carefully selecting different exposed surfaces of platinum single crystals and correlating the changes in activities and selectivities with the morphology of the carbonaceous deposits formed during the reaction conditions [26].

Figs. 4.5 and 4.6 show that the turnover frecuencies for all n-hexane reactions do not change considerably when steps and kinks are introduced on the surface, that is, these reactions display similar rates for all three (111), (332) and (10,8,7) surfaces. It can also be seen from fig. 4.9 that the carbonaceous residues formed cover all defects, leaving only patches of (111) terraces uncovered and thus active for catalysis. In other words, n-hexane conversion proved to be structure insensitive over these surfaces because any low coordination platinum atom is covered with strongly adsorbed hydrocarbons and therefore is deactivated for further catalytic activity. In the case of the light alkanes isobutane and neopentane, the situation is the opposite to that of n-hexane. Surfaces with defects show up to a three-fold increase in activity for both hydrogenolysis and isomerization, a fact that correlates very well with the presence of uncovered steps and kinks on the surfaces after reactions (fig. 4.9).

As already pointed out, the light alkane isomerization can only occur via a bond-shift mechanism. That is, an alkyl group is transferred from one carbon to the adjacent one after the formation of a three carbon ring intermediate. Our results suggest that, although these reactions take place on terrace sites, they in fact proceed more rapidly on steps and kinks, as inferred from the observed structure sensitivity. The situation is slightly more complicated in the case of hydrocarbons with carbon chains of six or more atoms long since the relative importance of the cyclic and bond-shift mechanisms has to be stablished. However, data from ours and other groups supports the idea that the preponderance of cyclic mechanisms dominates for isomerization of n-he-

xane and heavier compounds (see section 4.2 and refs. 12,15 and 27). Therefore, it seems likely that the cyclic mechanism takes place on terraces, since all other metallic atoms are covered by the carbonaceous residues. This conclusion can be extended to supported catalysts with low dispersion, where the platinum particles behave similarly to single crystal surfaces.

The preceeding conclusion is at variance with previous results. Anderson [16,20], Santacesaria [21], and Rooney's [17,22] groups, all concluded that the cyclic mechanism takes place on low coordination sites. They base their conclusion on results showing an increase in isomerization rate for n-hexane over highly dispersed ultra-thin films and over supported platinum catalysts. Gault et. al. [13-15,24,25] have used ^{13}C isotopically labelled hydrocarbons to study the mechanism for these reactions, and have concluded that there were two types of sites involved: a first type (A), present in small particles, responsible for the non-selective cyclic mechanism (statistical splitting of the intermediate ring), and a second type (B), present on low dispersion catalysts, in which the bond shift and selective cyclic mechanisms operates. These type B sites are the ones modeled by our single crystal catalyst. We also observed a non-selective ring opening, as discussed in the following section, in which the results of methylcyclopentane conversion studies are reported. Site assigment on the flat terraces of the metallic surfaces is, to the best of our knowledge, the first based on direct evidence such as the CO titration (fig. 4.9). All other studies based their conclusions on changes in activity or selectivity as a function of particle size. More work is needed to extend these conclusions to highly dispersed catalysts.

Table 4.1

Initial reaction rates for isobutane conversion over platinum single crystal surfaces[a].

Surface	P_{H_2} (Torr)	T(K)	TF[b] Hydrogenolysis	TF[b] Isomerization
Pt (111)	200	573	3.6	32
Pt (10,8,7)	200	573	14	60
Pt (557)	200	568	13	60
		573	14	100
		583	14	160
	600	573	16	24
		593	17	63
Pt (332)	200	573	9.7	62
	600	573	8.3	16
		593	23	97

a) P_{HC} = 20 Torr

b) Turnover frecuency, $x10^{-3}$ molec/Pt atm·sec.

Table 4.2

Initial reaction rates for neopentane conversion over platinum single crystal surfaces[a].

Surface	P_{H_2} (Torr)	T(K)	TF[b] Hydrogenolysis	TF[b] Isomerization
Pt (111)	200	573	15	110
Pt (10,8,7)	200	573	26	200
Pt (557)	600	573	17	39
		613	140	920
Pt (332)	200	573	67	350
	600	578	35	170
		613	270	1140

a) P_{HC} = 20 Torr.

b) Turnover frecuency, $x10^{-3}$ molec/Pt atom sec.

Table 4.3

Initial reaction rates for n-hexane conversion over platinum single crystal surfaces[a].

Surface	P_{H_2} (Torr)	T(K)	TF^b Hyd	Iso	MCP	Bz
Pt (111)	200	553	5.2	6.1	5.6	2.5
		573	8.7	9.0	7.8	5.0
		593	17	12	10	9.3
	600	573	17	28	17	5.0
Pt (10,8,7)	200	573	6.3	5.8	12	6.3
	600	573	11	8.0	16	3.6
Pt (557)	600	573	5.4	4.5	5.8	1.8
		613	39	16	41	-
Pt (332)	600	573	7.8	4.7	3.4	6.0
	200	573	6.0	3.2	12	5.0

a) P_{HC} = 20 Torr.

b) Turnover frecuencies, $x10^{-3}$ molec/Pt atom sec. Hyd=hydrogenolysis; Iso=isomerization; MCP=methylcyclopentane formation; Bz=benzene formation.

FIGURE CAPTIONS

Fig. 4.1. Idealized atomic surface structures for the flat (100) and (111), stepped (332), (557) and (13,1,1), and kinked (10,8,7) platinum single crystal surfaces.

Fig. 4.2. Schematic representation of the reactions studied.

Fig. 4.3. Product accumulation curves obtained as a function of reaction time at 573 K for isobutane isomerization (left) and hydrogenolysis (right) catalyzed over platinum single crystal surfaces.

Fig. 4.4. Structure sensitivities for alkane hydrogenolysis reactions over platinum single crystal surfaces. Shown are the initial reaction rates as a function of crystallographic orientation.

Fig. 4.5. Structure sensitivities for alkane isomerization reactions over platinum single crystal surfaces.

Fig. 4.6. Structure dependence of n-hexane C_5-cyclization and aromatization rates over platinum single crystal surfaces.

Fig. 4.7. Product accumulation curves obtained as a function of reaction time for isobutane conversion, showing temperature and hydrogen pressure dependences.

Fig. 4.8. Self poisoning of isobutane conversion as a function of reaction time due to carbonaceous deposits growth. a) (Upper frame) Carbon accumulated on the platinum surface, as measured by AES; b) (middle frame) Fraction of uncovered platinum active for ca-

talysis, determined using CO titrations; c) (Lower frame) Turnover frecuencies, relative to the initial rate, for isobutane isomerization.

Fig. 4.9. Comparison between CO thermal desorption from the clean (557) platinum surface and Pt (557) following hydrocarbon reactions. The adsorption temperature was 310-315 K, 80 K/sec, and CO exposure=36 L.

Fig. 4.10. Bond-shift and cyclic mechanisms for isomerization. Also shown is the distinction between terminal and internal bond-scission during hydrogenolysis.

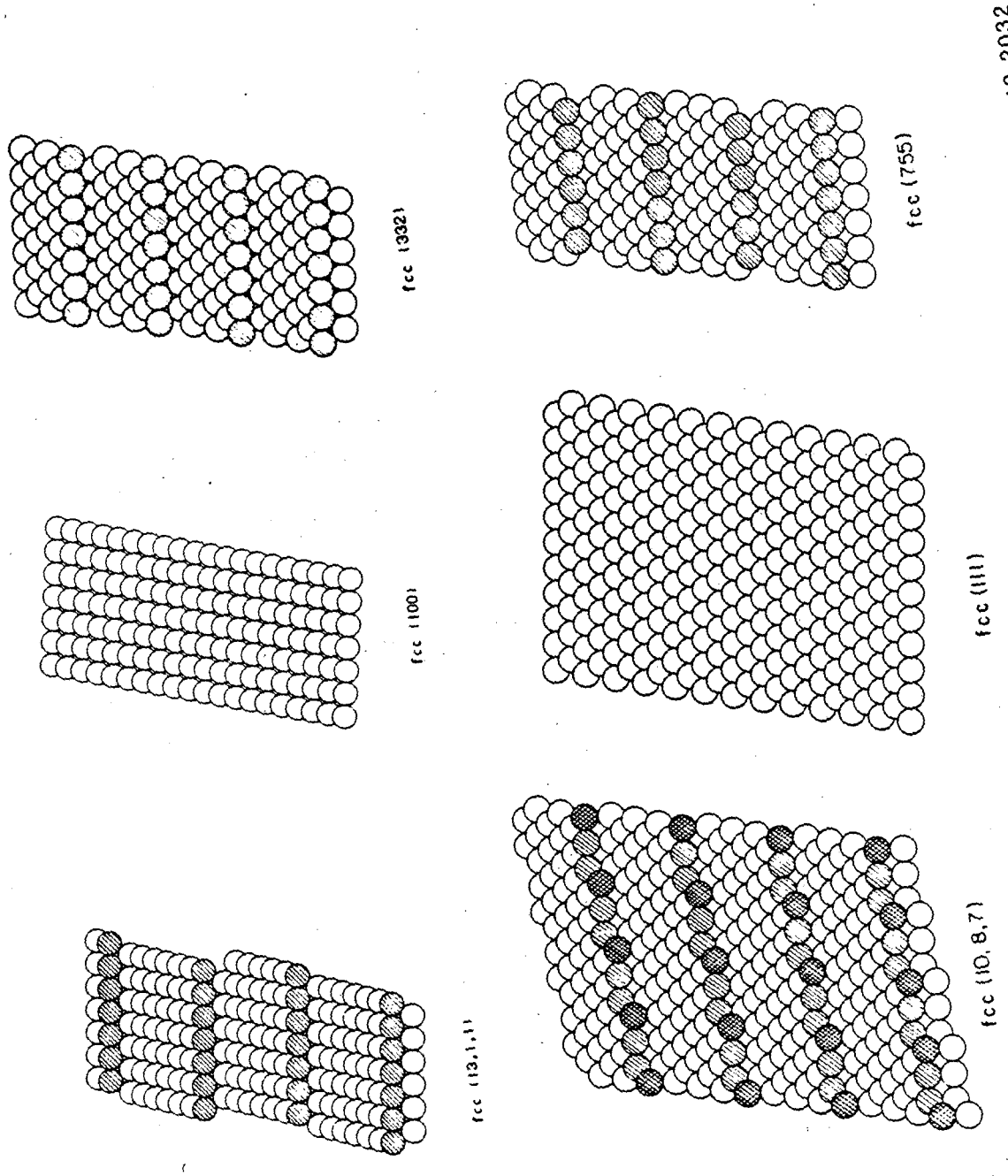

fig. 4.1

Reactions Studied

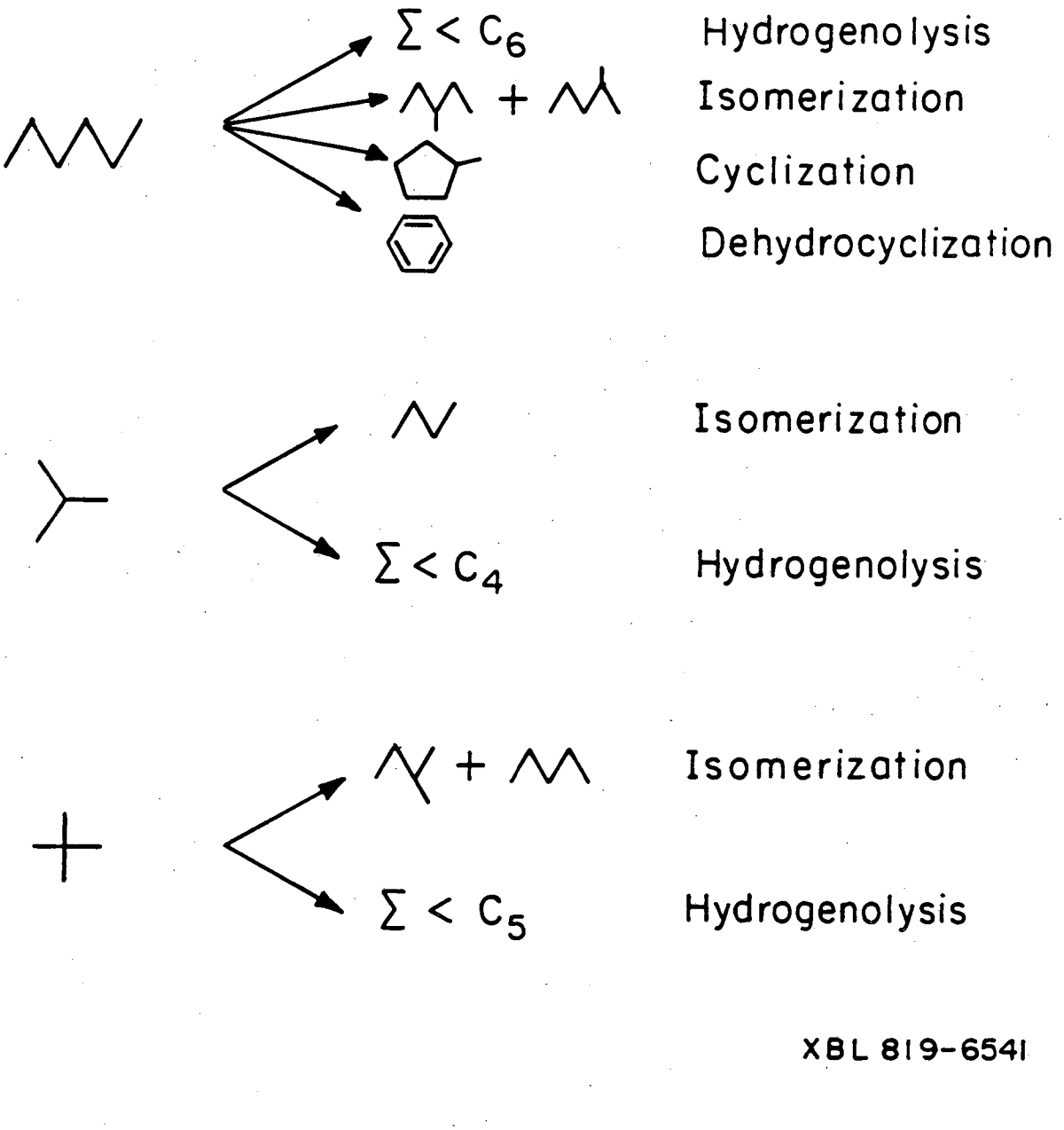

XBL 819-6541

fig. 4.2

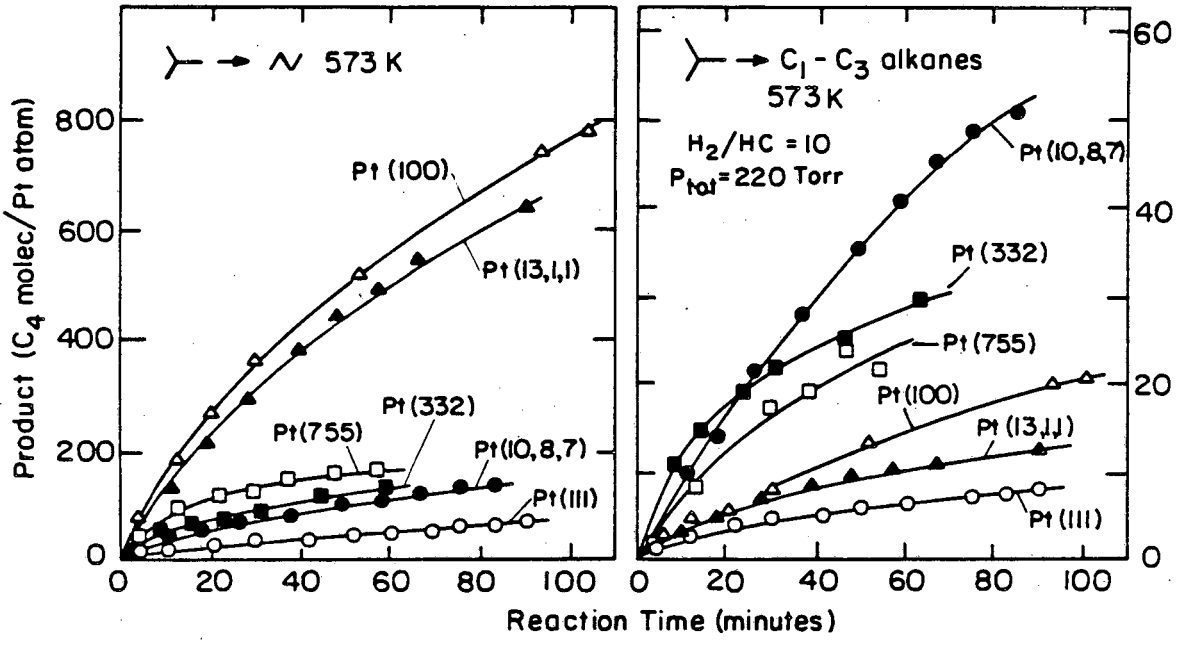

XBL 819-6629

fig. 4.3

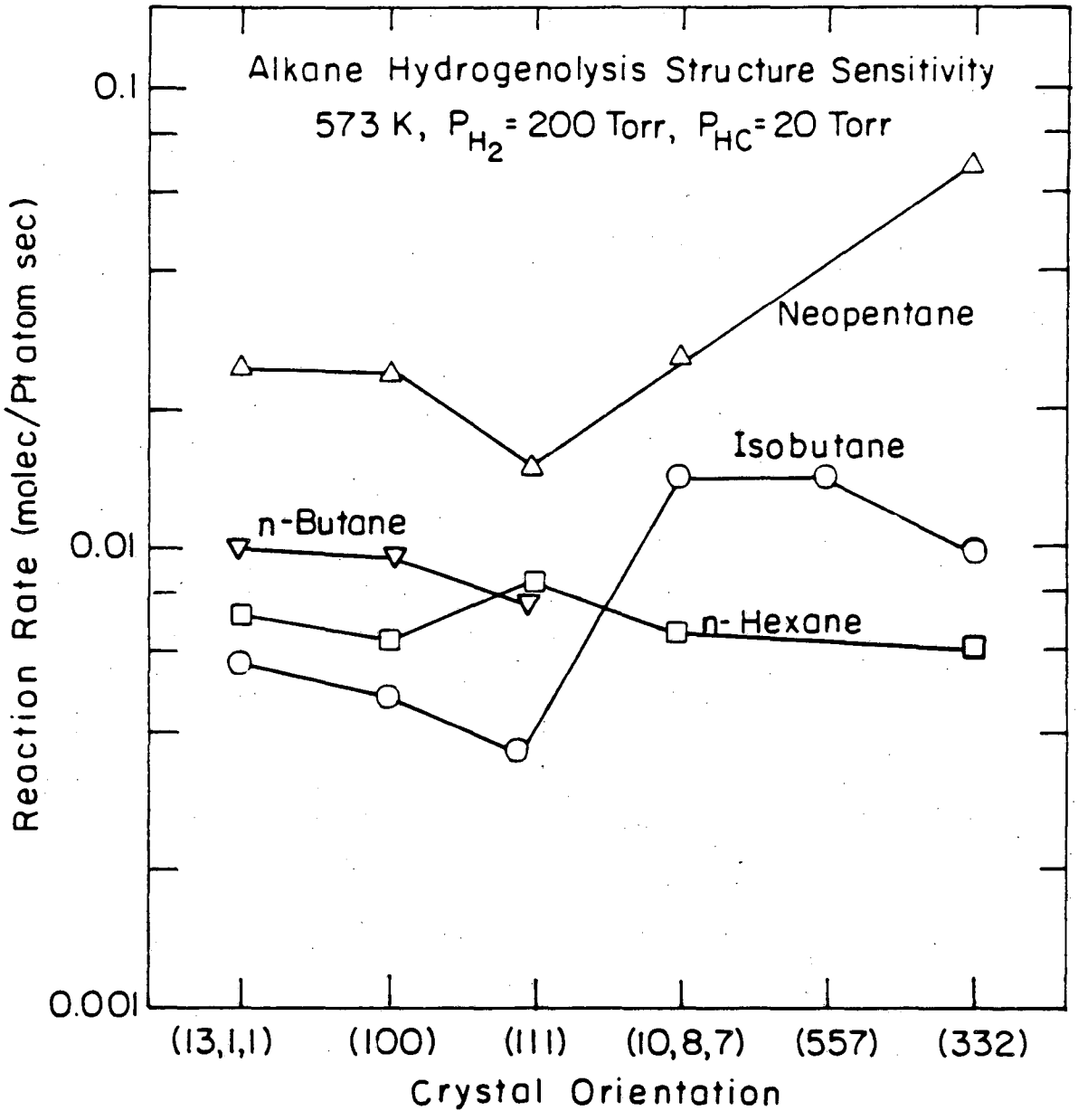
Alkane Hydrogenolysis Structure Sensitivity
573 K, P_{H_2} = 200 Torr, P_{HC} = 20 Torr
Reaction Rate (molec/Pt atom sec)
0.1
0.01
0.001
Neopentane
Isobutane
n-Butane
n-Hexane
(13,1,1)
(100)
(111)
(10,8,7)
(557)
(332)
Crystal Orientation
XBL 819-6632A

fig. 4.4

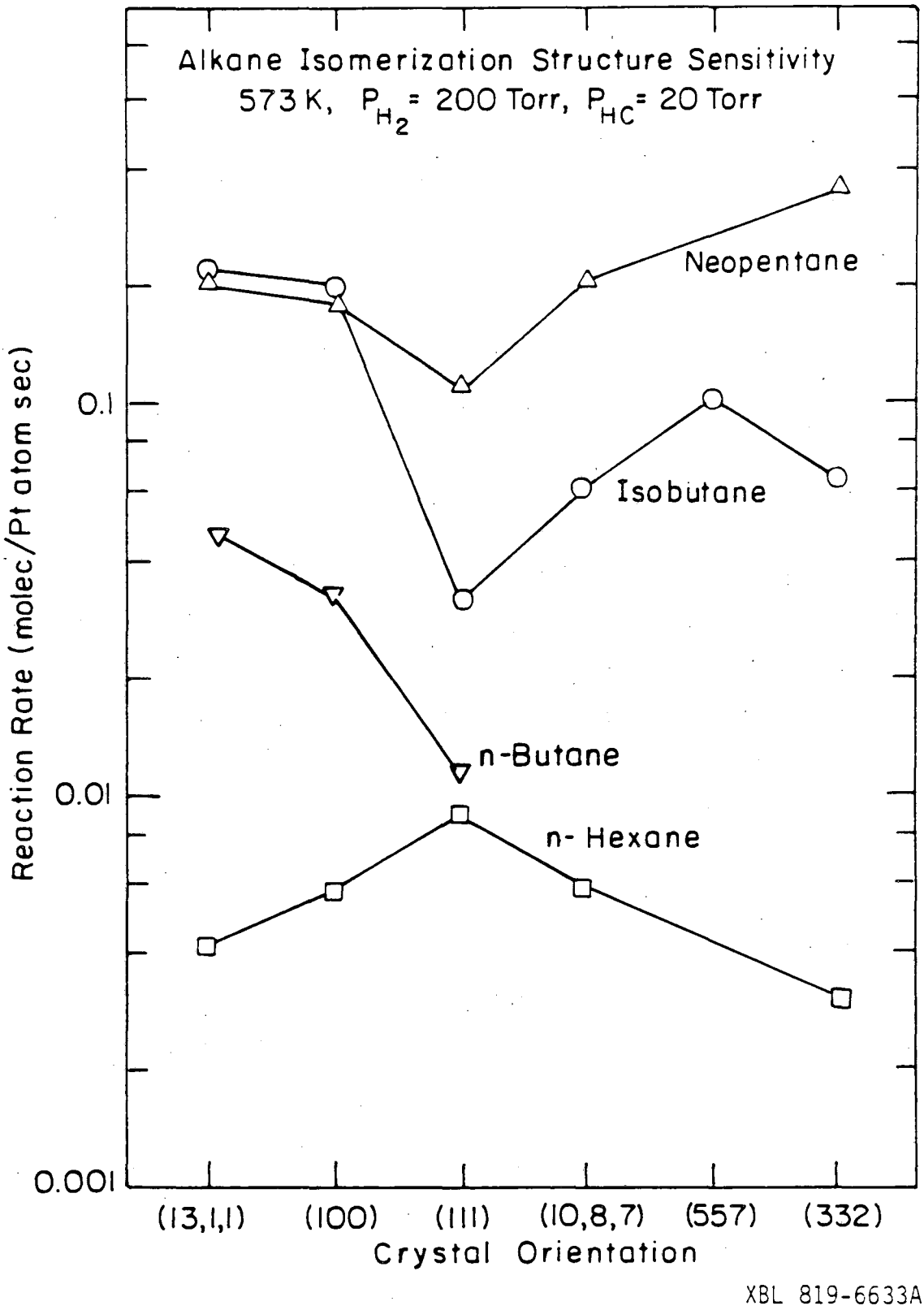
Alkane Isomerization Structure Sensitivity
573 K, P_{H_2} = 200 Torr, P_{HC} = 20 Torr
Neopentane
Isobutane
n-Butane
n- Hexane
Reaction Rate (molec/Pt atom sec)
0.1
0.01
0.001
(13,1,1)
(100)
(111)
(10,8,7)
(557)
(332)
Crystal Orientation
XBL 819-6633A

fig. 4.5

n-Hexane Cyclization Structure Sensitivity

573 K, H_2/HC = 10, P_{tot} = 220 Torr

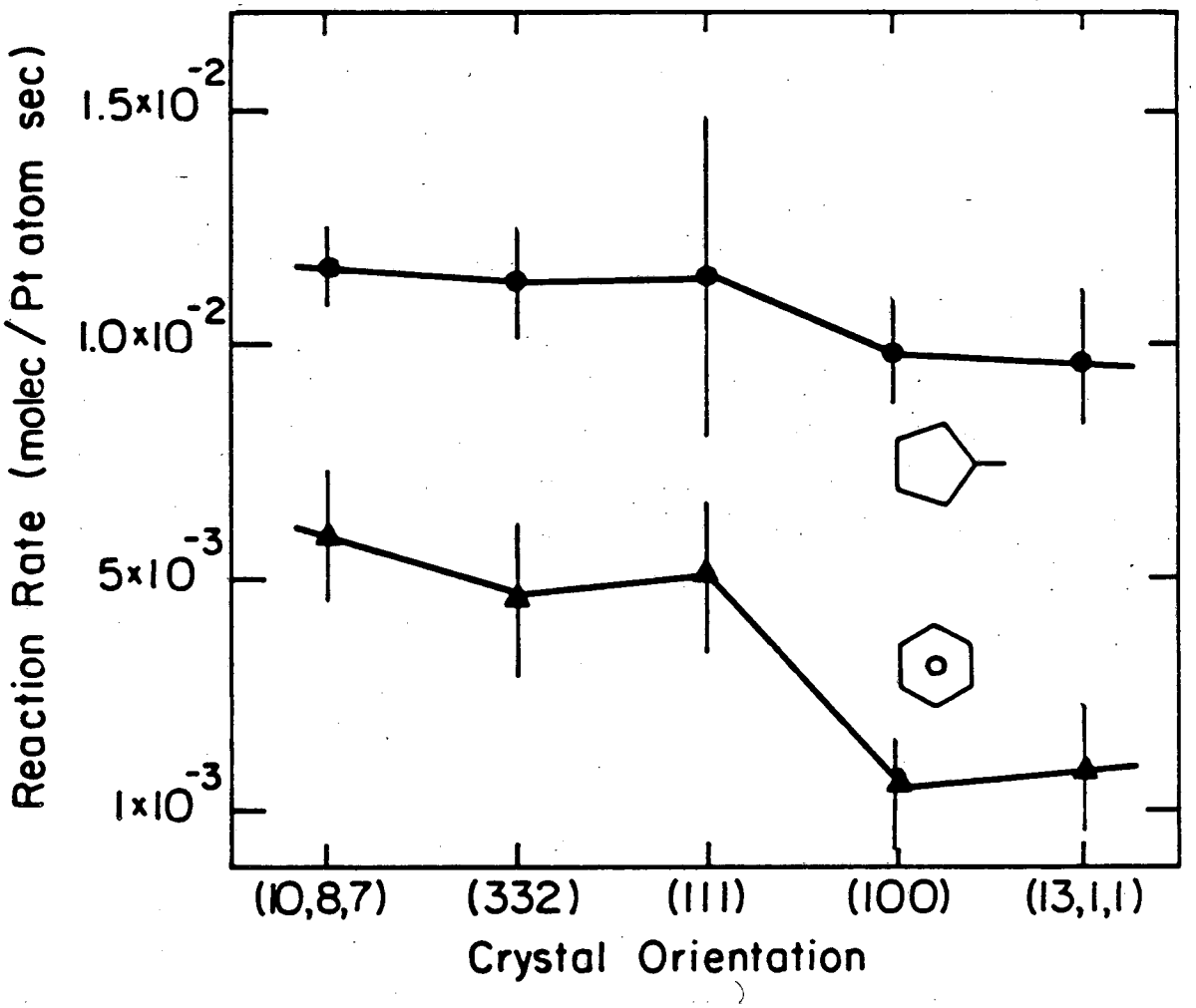

fig. 4.6

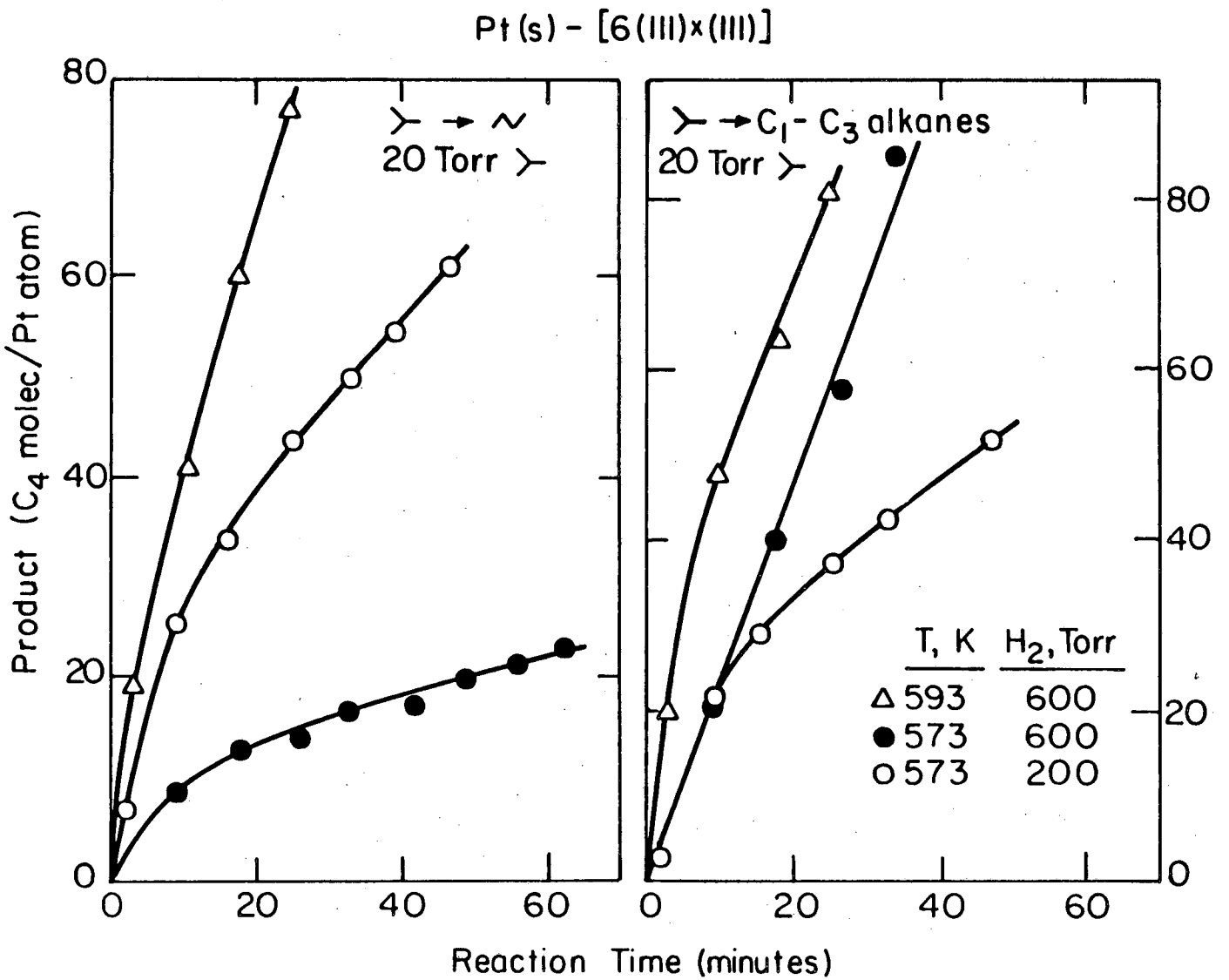

Fig. 4.7

XBL 819 - 6539

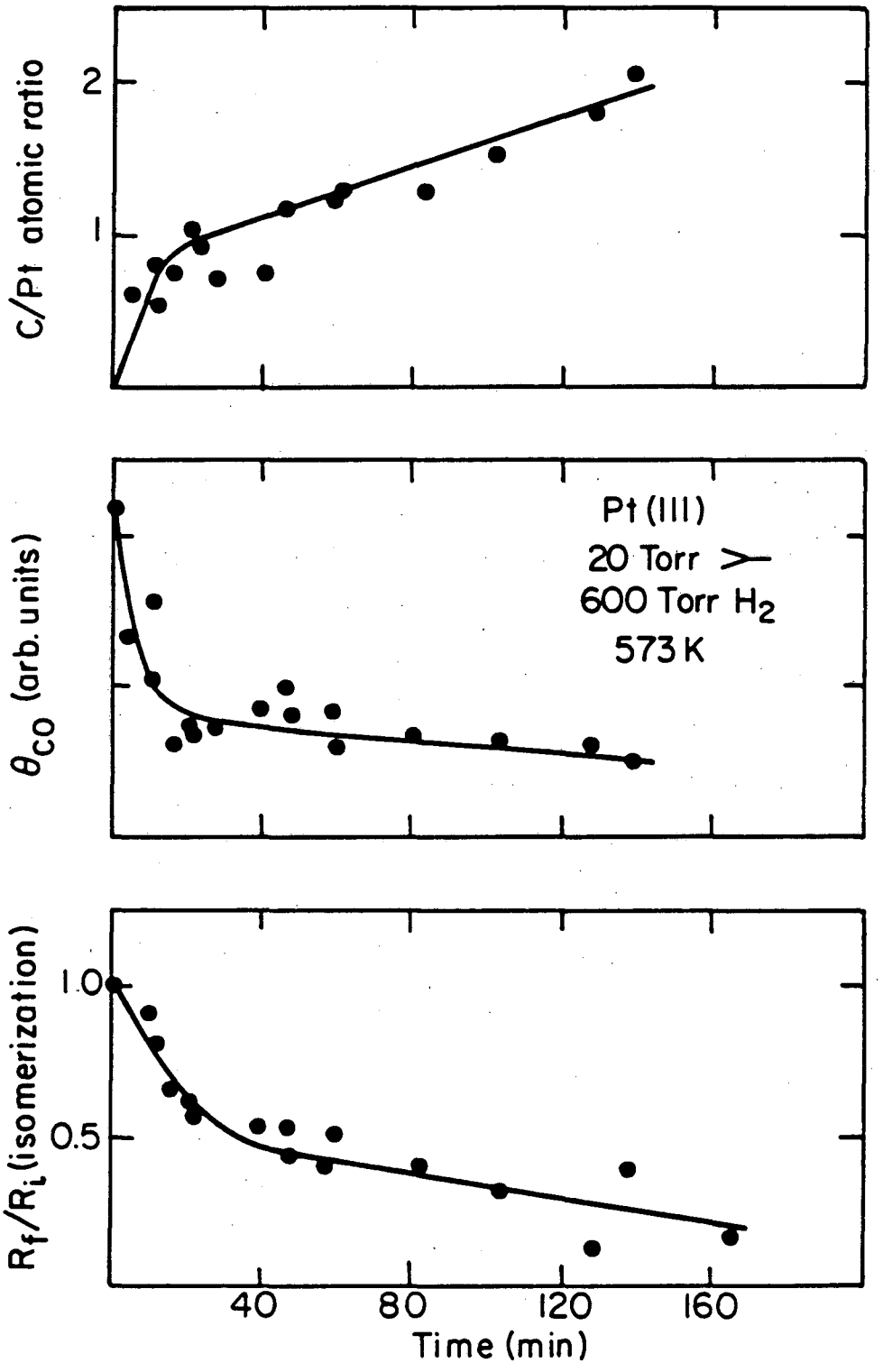

XBL 846-7054

fig. 4.8

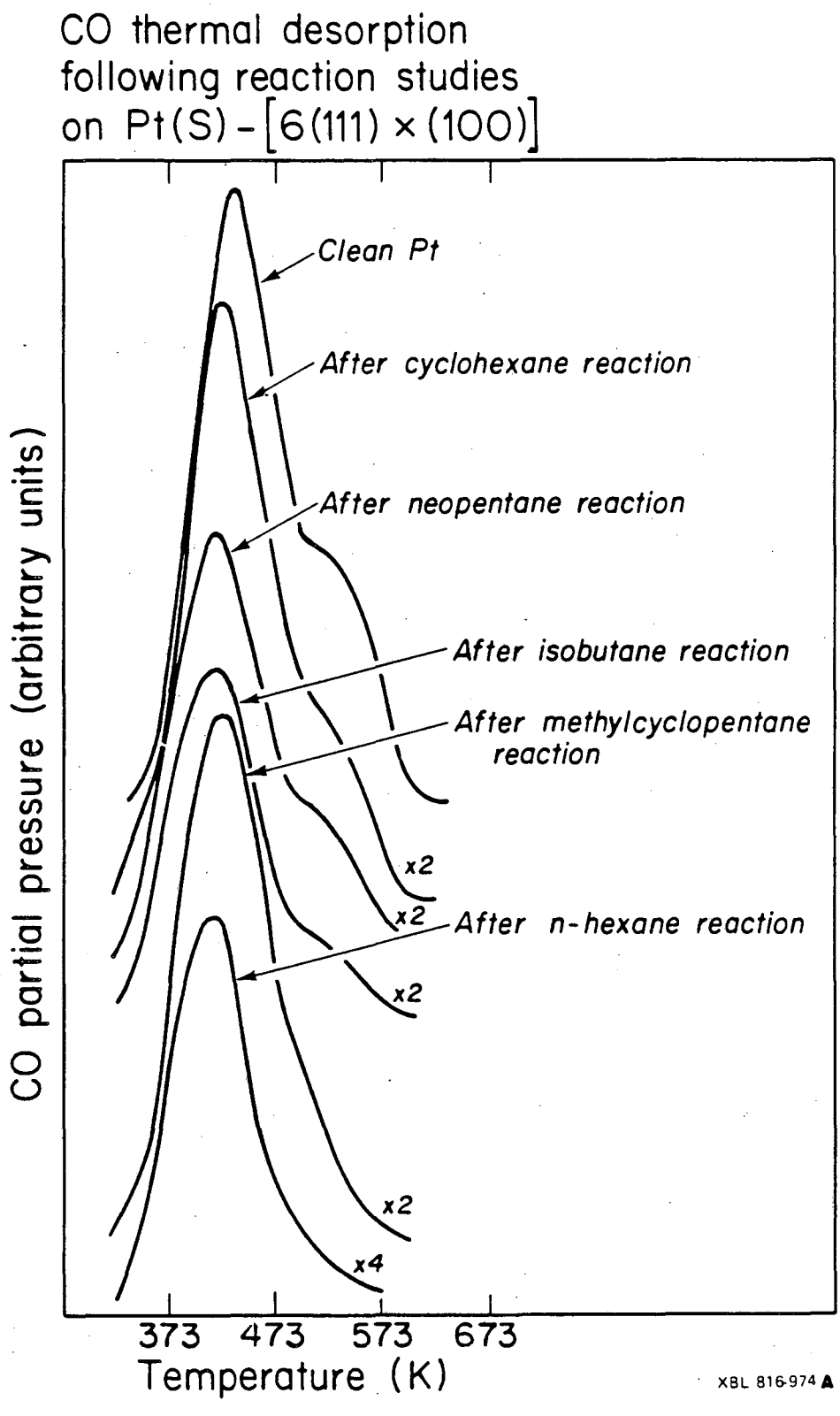
CO thermal desorption
following reaction studies
on Pt(S) - [6(111) × (100)]
Clean Pt
After cyclohexane reaction
After neopentane reaction
After isobutane reaction
After methylcyclopentane reaction
After n-hexane reaction
x2
x2
x2
x2
x4
CO partial pressure (arbitrary units)
373
473
573
673
Temperature (K)
XBL 816-974 A

fig. 4.9

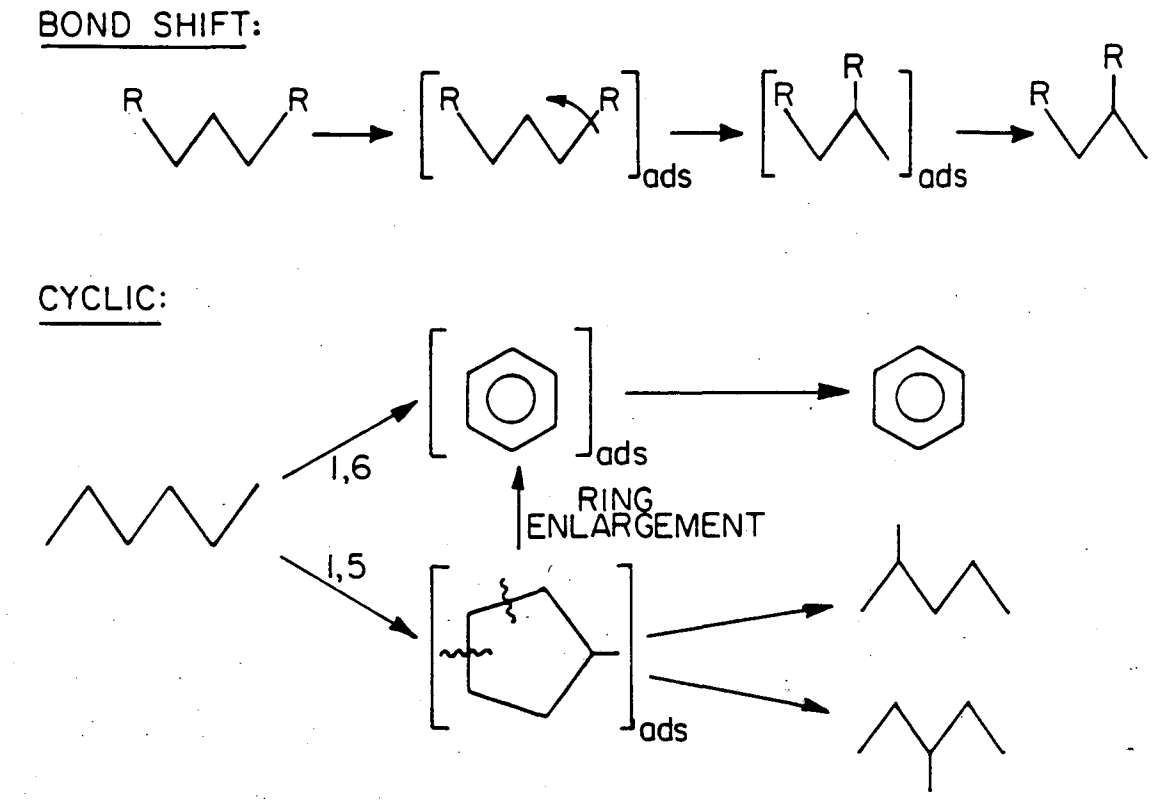
BOND SHIFT:
R
R
R
R
ads
R
R
ads
R
R
CYCLIC:
1,6
ads
RING
ENLARGEMENT
1,5
ads
BOND SCISSION:
TERMINAL
+ •
INTERNAL
+
or
+
XBL822-5249

fig. 4.10

4.2. Methylcyclopentane conversion and mechanistic implications.

4.2.1. Introduction.

The reactions of methylcyclopentane and hydrogen over platinum based catalysts have been extensively studied in the past [8,18-19,28-42]. Methylcyclopentane is a particularly important molecule because it is one of the simplest molecules from which a considerable structure sensitivity effect has been observed in its hydrogenolysis selectivity [28]. Furthermore, the understanding of its reactions have straightforward implications on the mechanism of hydrocarbon isomerization in general [15,16].

The study of hydrocarbon reactions over practical catalysts is complicated by the great number of variables involved. For methylcyclopentane conversion, many research groups have tried to isolate the effect of each individual factor contributing to changes in activity and/or selectivity. Changes in hydrogenolysis selectivity with particle size have been reported by Gault, Maire and coworkers [18-19,28-34]. They concluded that there are at least two carbon-carbon bond breaking mechanisms: a non-selective one occurring on highly dispersed catalysts, and a second one involving secondary carbons only, occurring predominantly on particles larger than about 20 Å in diameter. The acidity of the support, on the other hand, seems to have no effect on hydrogenolysis selectivity, although the bifunctionality of the catalysts is indispensable for benzene formation [41,42]. Hydrogen partial pressure (or surface coverage) is also crucial for the selectivity, as shown by Paál et. al. [35-37]. Finally, Kramer et. al. [38-40] have performed experiments indicating that the change in selectivity as a function of particle size may be due to interface effects between the metal and the support.

In the present work methylcyclopentane conversion was studied over platinum single crystal surfaces. Kinetic parameters over Pt (111), Pt (332) and Pt (557) were measured. The results suggest that the sites active for hydrogenolysis are located on the terraces, since no significant structure sensitivity is observed. Implications for n-hexane isomerization mechanism are also discussed.

4.2.2. Results.

Product accumulation curves obtained as a function of time for methylcyclopentane (MCP) reactions catalyzed over platinum single crystal surfaces are examplified in figs. 4.11 and 4.12. Standard conditions were MCP pressures of 20 Torr, hydrogen pressures of either 200 or 600 Torr, and temperatures of 573 K, unless otherwise indicated. The reaction rate at a particular time is given by the slope of the product accumulation curve at that time. Table 4.4 summarizes initial reaction rates at 573 K over all these surfaces. No structure sensitivity was observed for any reaction within the experimental error; no difference larger than a factor of two was obtained for the same reaction over the three surfaces.

Arrhenius plots for methylcyclopentane hydrogenolysis and aromatization over the Pt (111) surface at a total pressure of 220 Torr are shown in fig. 4.13. For 2- and 3-methylpentane and benzene formation, the activation energies appear to decrease with increasing temperatures, probably due to competition between these reactions and catalyst deactivation from carbonaceous deposits formation. Activation energies were estimated for all reactions from the low temperature region

of these Arrhenius plots (table 4.4). Similarly, the hydrogen pressure dependence is shown in fig. 4.14 and kinetic orders are also summarized in table 4.4.

Continuous deactivation was observed with time for most reactions (fig. 4.11). Also, carbon was always present on the surface after reactions, similar to what has been observed for other hydrocarbons [26]. The amount of carbon increased with reaction temperature, as shown by AES (fig. 4.15). CO titration of the bare Pt sites also indicates a corresponding decrease in catalyst area available for reaction at higher temperatures (fig. 4.15). However, the increase in carbon deposited is not proportional to the total area cover by these deposits, indicating the formation of three dimensional islands [26].

Hydrogen thermal desorption experiments from the carbonaceous deposits were obtained. Examples of these are shown in fig. 4.16. Also shown in that figure are the H/C atomic ratio as a function of reaction temperature and hydrogen partial pressure. The total hydrogen area seems to increase with reaction temperature. The high temperature peak (around 470 K) is the main contributor to this area change, and the H/C ratio then increases accordingly. This is in contrast to results from n-hexane reactions [10,26]. The H/C ratio increases with hydrogen pressure, as would be expected.

4.2.3. Discussion.

Important new information about structure sensitivity of methylcyclopentane reactions has been obtained. The MCP conversion over flat

Pt (111) and stepped Pt (332) and Pt (557) surfaces did not show significant differences in activity for any of the hydrogenolysis reactions under our experimental conditions. Both stepped crystals have six atom wide (111) terraces, with either (111) or (100) monoatomic steps. The role of the steps in the different hydrocarbon reactions has been discussed in the previous section of this thesis. CO titrations indicate that, for n-hexane conversion, any defect on the surface becomes covered with carbon residues and deactivated within few minutes of starting the reaction. The same conclusion applies to the MCP conversion; no uncovered steps were seen on the catalytic surface after high pressure reactions (fig. 4.9). It is then not surprising that no changes in activity were observed with surface structure modifications, since only the flat terraces are active for hydrogenolysis and skeletal rearrangement of the reactive molecules.

The product distribution for MCP conversion over all three surfaces showed that carbon-carbon bond breaking occurs selectively between secondary carbons, that is, carbon atoms with two hydrogens attached. This becomes evident since the main reaction products were 2- and 3-methylpentane, and very little n-hexane and cyclopentane was formed. The same phenomenon has been observed over low dispersion supported catalysts [16,18,29,33-34,37-39], and has been attributed to the nonselective ring opening mechanism. Because such mechanism requires two secondary carbons, it has been suggested that the reaction intermediate is a highly dehydrogenated species, probably an $\alpha\alpha\beta\beta$ tetradsorbed moiety. Also, while the 3-methylpentane production decreases with reaction time, 2-methylpentane is formed at a constant rate over a period of at least

two hours (fig 4.11). This is clearly manifest in the ratio 3-/2-methylpentane, which has been plotted against time in fig. 4.17: the ratio starts at a very high value (>10), decreasing to a steady state value of about 0.5 after long reaction times, as expected statistically. This may imply that there is an alternative mechanism for hydrogenolysis requiring a specific site on the platinum surface, and that these sites get quickly covered by the carbon deposits during the first minutes of reaction. Consequently, this system would appear to be a logical choice for studying ensemble effects in catalysis when an active metal is diluted by a second unreactive one as, for instance, in the case of platinum-gold alloys. Also the different activation energies indicate that the mechanism for 2- and 3-methylpentane formation (E_a=15 Kcal/mole) differs from that for n-hexane and cyclopentane formation, the latter having activation energies three or four Kcal/mole larger than the former. It also can be seen that multiple carbon-carbon bond scission represents a very small fraction of the total conversion, as indicated by the fact that the rates for methane and cyclopentane formation were comparable, and that there was little production of other light alkanes. This is in agreement with results reported previously for other hydrocarbons [11]. Finally, only small amounts of benzene were produced, indicating that metallic platinum is not a good catalyst for ring enlargement. It has been shown [41,42] that both the dehydrogenation properties of platinum and the acidic sites of the support are needed for this unique reaction to occur.

All the preceeding conclusions have important consequences for the understanding of the mechanism for hydrocarbon isomerization. As has

already been discussed in the previous section, light alkanes isomerize by a bond-shift mechanism, but hydrocarbons with chains longer than six carbon atmos can alternativly isomerize through a five or six member ring intermediate. In fact, Gault et. al. have used ^{13}C labelled compounds to prove that, for most platinum catalysts, this cyclic mechanism is predominant for heavy hydrocarbon isomerization [15,27]. Several pieces of evidence suggest that this is also true in our case. For instance, the change in the 3-/2-methylpentane ratio as a function of reaction time for methylcyclopentane hydrogenolysis parallels the same trend obtained for n-hexane isomerization (fig. 4.17). Also, n-hexane isomerization, MCP formation from n-hexane, and MCP hydrogenolysis are all structure insensitive, and all take place on surface terraces rather than over kinks or steps [12]. Finally, the temperature and hydrogen pressure dependence for isomerization and MCP formation from n-hexane are very similar (Fig. 4.18) [10,12]. In conclusion, n-hexane isomerization over platinum single crystal surfaces seems to proceed preferebly via a five member ring intermediate, i.e., a cyclic mechanism that takes place on the close packed terraces of the metal, with no appreciable dependence on surface defect concentration. Similar conclusions have been reported for low dispersion platinum catalysts, where selective carbon-carbon bond breaking is the predominant mechanism [18,19,28,34]. The same studies concluded that there is some bond-shift contribution to the total isomerization activity when catalysts with large metallic particles were used. Therefore, the structure sensitivity reported by the French group is manifested by two parallel trends as the particle size increases, the transition from non-selective to selective ring opening, together with the increased importance of bond-shift

for isomerization. However, recent experiments by Kramer et. al. indicate that the structure sensitivity observed could be attributed to the metal-support boundary [39,40]. By independently varying the interface area for the same catalyst dispersion, they concluded that selective hydrogenolysis of MCP could be assigned to the platinum metal, while the non-selective bond scissions are catalyzed by the sites at the platinum-support interface. This conclusion is consistent with our results, in which only non-selective hydrogenolysis was observed.

Another important conclusion that derives from our results is the fact that benzene is not an important product from MCP conversion over pure metallic platinum. It has been previously shown that the acidic function is also necessary for this reaction [41,42]. The MCP molecule can dehydrogenate over platinum, but ring enlargement involves the formation of a carbonium intermediate that latter undergoes rearrangement over acidic sites on the support. This implies that benzene formation from n-hexane does not proceed via a five member intermediate, as opposed to the isomerization. Dautzenberg and Platteeuw [5,6] reached a similar conclusion based on the fact that while n-hexane produces both MCP and benzene, 2-methylpentane only produces MCP over the same catalyst. Sinfelt group [43], using n-heptane, and Davis et. al. [44], using even larger hydrocarbons, observed the same behavior, but Gault and co-workers [45] and Davis [46,47], using labelled compounds, concluded that some 1,5 ring closure was important for the total aromatic production.

Recently Garin and co-workers have studied hydrocarbon reforming over platinum (111), (119) and (557) single crystal surfaces [19]. They concluded that the cyclic mechanism for isomerization is important on these surfaces too, since it accounts for 80% or more of all isomerization products in most cases. They also reported some structure sensitivity, in which the bond-shift mechanism became most important over the Pt (557) crystal. They explain their result by postulating a surface reconstruction that takes place under high pressures of hydrogen. We have not observed such reconstructions in our laboratory, but CO titrations indicate that even if the reconstruction does happens it should not be relevant to the reactivity of the surface, since carbonaceous deposits block all low coordination platinum atoms. No new features were observed in those CO TDS. Most of the other results they report for methylcyclopentane hydrogenolysis qualitatively agree with ours. The product distribution indicates the predominance of the non-selective cracking, with 2- and 3-methylpentane as major products, some n-hexane and cyclopentane production, and very small amounts of benzene.

In conclusion, our results lead us to conclude that methylcyclopentane hydrogenolysis proceed through a selective bond breaking mechanism and that it occurs preferentially over the flat (111) terraces of platinum single crystals studied. n-Hexane isomerization is then believed to involve a five membered cycle as an intermediate, but it appears that such pathway is not relevant for aromatization reactions.

Table 4.4

Initial reaction rates and kinetic parameters for methylcyclopentane conversion over platinum single crystal surfaces[a].

Surface	Turnover frecuency[b]					
	2MP+3MP	n-H	CH_4	CP	Hyd	Bz
Pt (111)	210	20	0.7	0.2	0.1	1
Pt (332)	250	13	0.3	0.2	-	-
Pt (557)	350	15	0.6	0.5	-	3
Approximate kinetic parameters						
E_a[c]	15	-	18	19	25	<34
$n(H_2)$[d]	-0.7	-	0.6	-0.3	0.7	-

a) Conditions: P_{H_2} = 600 Torr, P_{MCP} = 20 Torr, T = 573 K.

b) $x10^{-3}$ molec/Pt atom·sec; 2MP+3MP=2-+3-methylpentane, n-H=n-hexane, CP=cyclopentane, Hyd=multiple hydrogenolysis, Bz=benzene.

c) Activation energies, in Kcal/mole. P_{H_2} = 200 Torr.

d) Dependence in hydrogen pressure.

FIGURE CAPTIONS

Fig. 4.11. Product accumulation curves measured as a function of reaction time at 573 K for methylcyclopentane conversion over Pt (557). P_{MCP} = 20 Torr and P_{H_2} = 600 Torr.

Fig. 4.12. Product accumulation curves measured as a function of reaction time at 573 K for 3-methylpentane and n-hexane formation from methylcyclopentane over platinum single crystal surfaces. Same conditions as fig. 4.11.

Fig. 4.13. Arrhenius plots for methylcyclopentane conversion over Pt (111). P_{MCP} = 20 Torr, P_{H_2} = 200 Torr.

Fig. 4.14. Order plots at 573 K for Pt (111) showing the dependence of methylcyclopentane reaction rates on hydrogen pressure. P_{MCP} = 20 Torr.

Fig. 4.15. Temperature dependence of the C/Pt atomic ratio and fraction of uncovered platinum surface measured following methylcyclopentane reaction studies over Pt (111) single crystals.

Fig. 4.16. Hydrogen thermal desorption spectra (lower frame) recorded after methylcyclopentane reaction studies at 573 and 653 K over Pt (111) surfaces. The H/C atomic ratio of the carbonaceous deposits formed were calculated as a function of temperature and hydrogen partial pressure by using the total desorption peak areas (upper frame).

Fig. 4.17. 2- to 3-methylpentane ratio as a function of reaction time from n-hexane isomerization (left frame) and methylcyclopentane hydrogenolysis (right frame) reaction studies over Pt (332) single crystal surfaces. The ratio of reaction rates is also shown for the methylcyclopentane case. P_{MCP} = 20 Torr, P_{H_2} = 600 Torr, and T = 573 K.

Fig. 4.18. Arrhenius plots for n-hexane isomerization (left) and methylcyclopentane formation (right) catalyzed over platinum single crystal surfaces. P_{HC} = 20 Torr and P_{H_2} = 200 Torr.

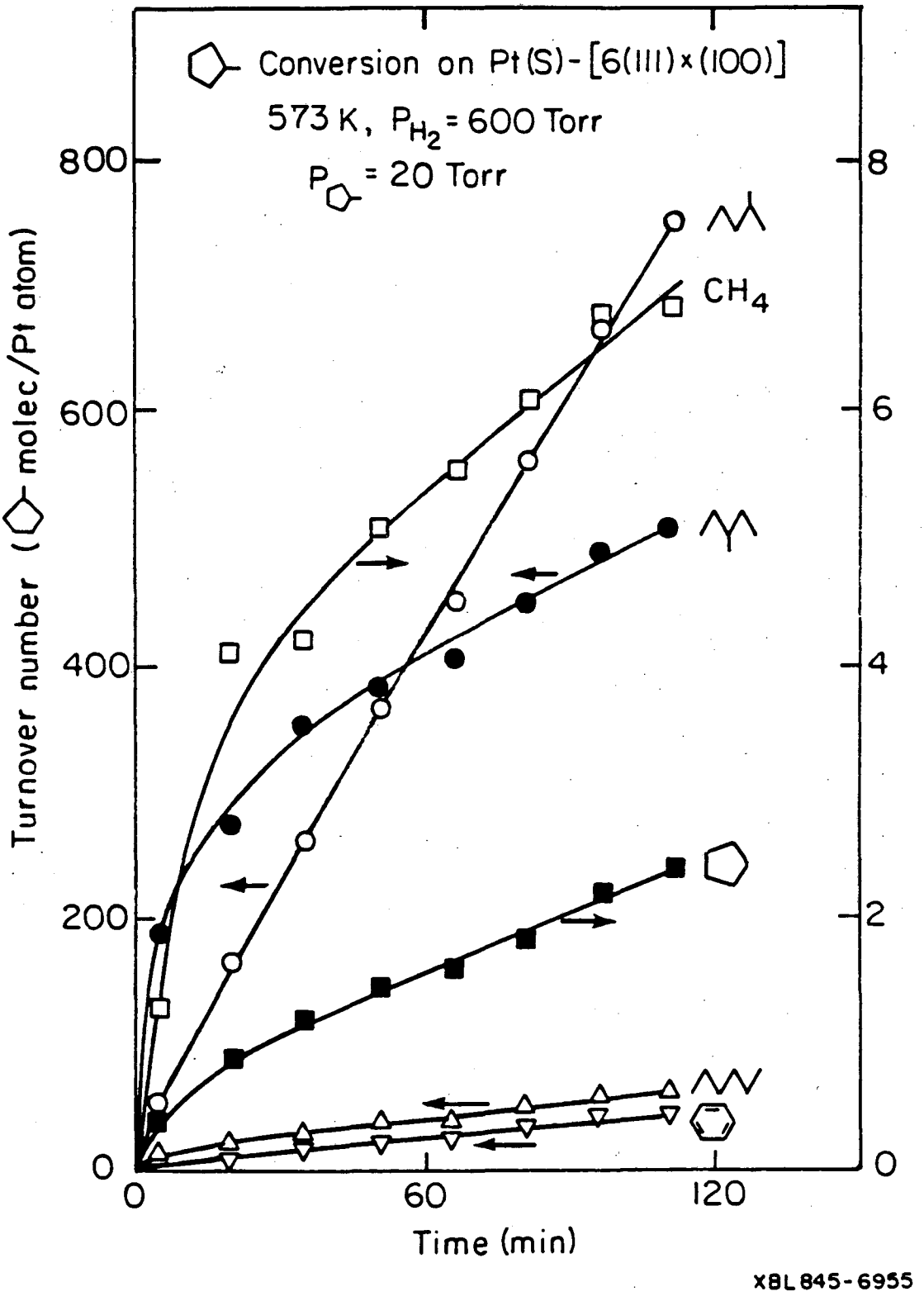
Conversion on Pt(S)-[6(111)x(100)]
573 K, P_{H_2} = 600 Torr
$P_{\hexagon}$ = 20 Torr
CH_4
Turnover number (molec/Pt atom)
Time (min)
0
60
120
200
400
600
800
2
4
6
8
XBL845-6955

fig. 4.11

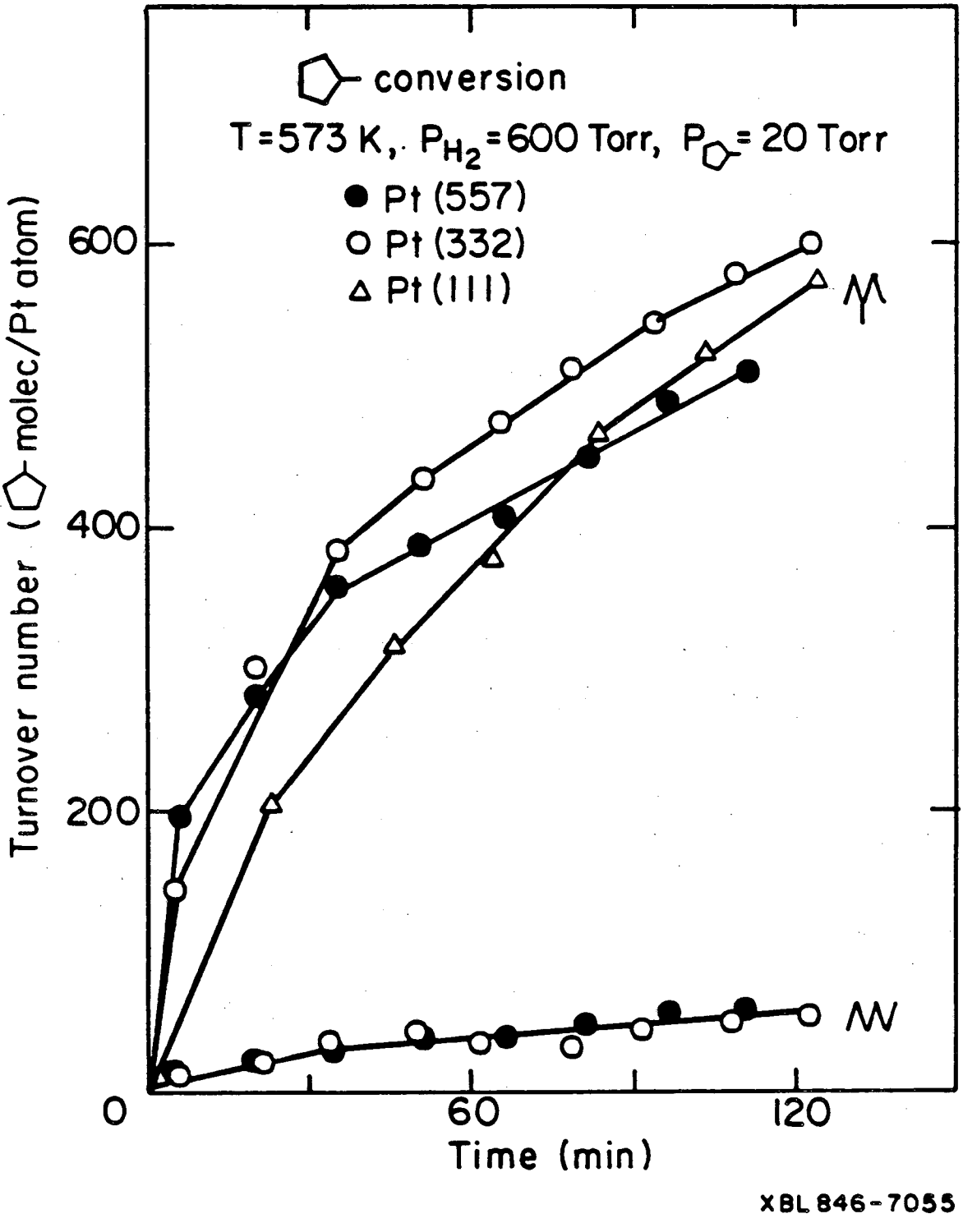
conversion
T=573 K, P_{H_2}=600 Torr, $P_{\hexagon}$= 20 Torr
Pt (557)
Pt (332)
Pt (111)
M
W
Turnover number (⬡ molec/Pt atom)
600
400
200
0
60
120
Time (min)
XBL 846-7055

fig. 4.12

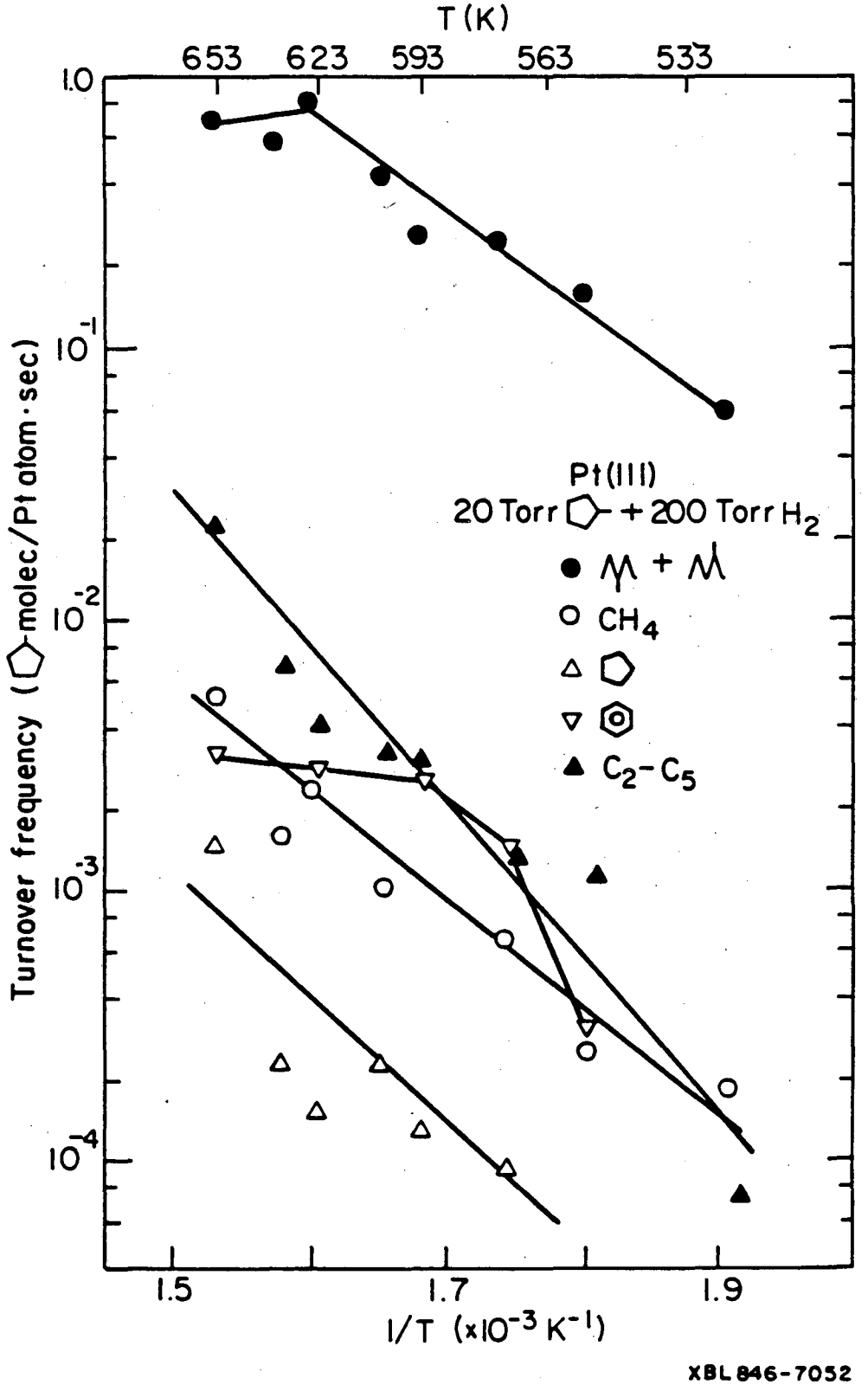
T (K)
653
623
593
563
533
1.0
10^{-1}
10^{-2}
10^{-3}
10^{-4}
Turnover frequency (⬡-molec/Pt atom·sec)
Pt(111)
20 Torr ⬡- + 200 Torr H_2
● ⩚ + ⩚
○ CH_4
△ ⬡
▽ ⬢
▲ C_2-C_5
1.5
1.7
1.9
1/T (x10^{-3} K^{-1})
XBL 846-7052

fig. 4.13

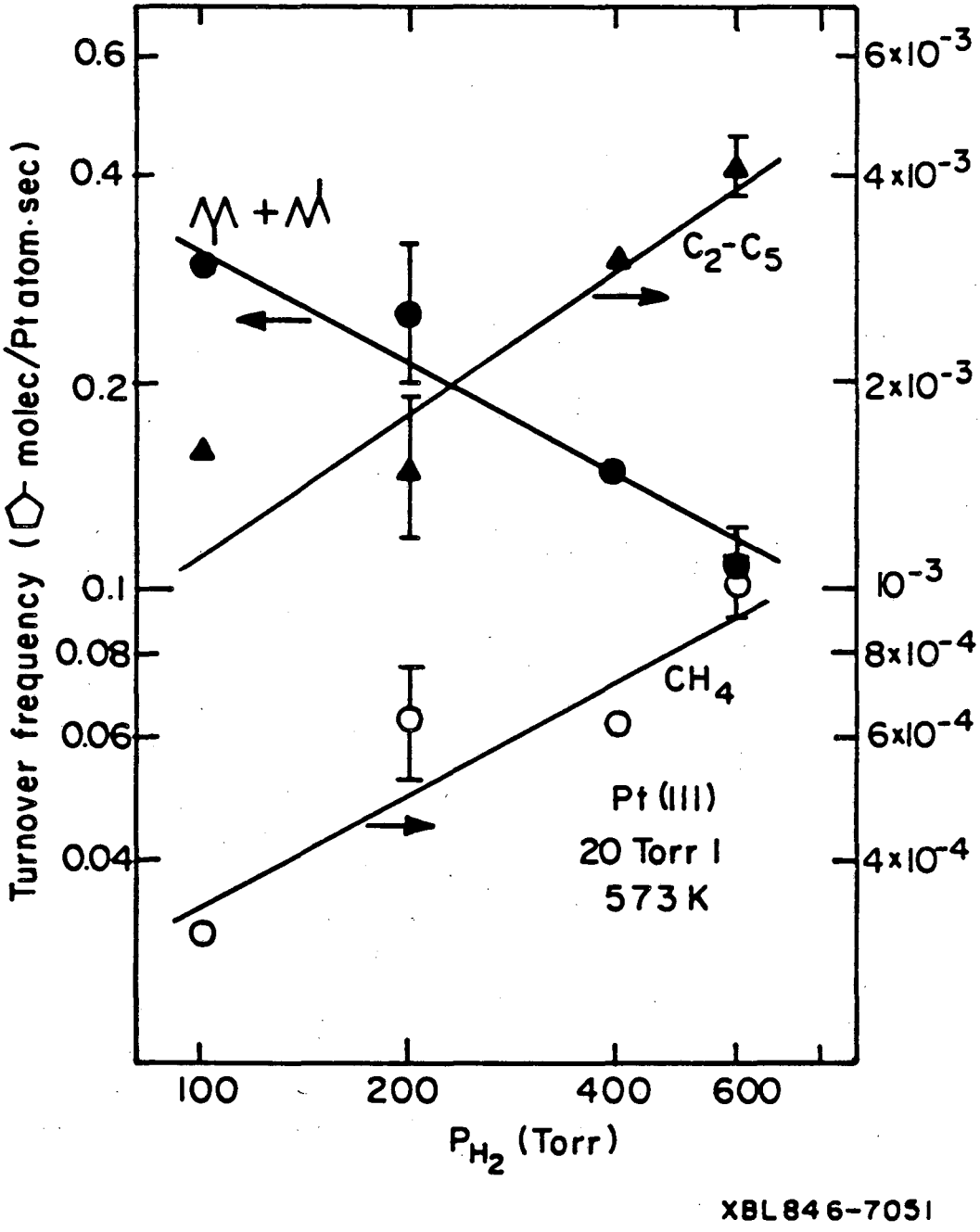
0.6
0.4
0.2
0.1
0.08
0.06
0.04
Turnover frequency (molec/Pt atom·sec)
6x10-3
4x10-3
2x10-3
10-3
8x10-4
6x10-4
4x10-4
M + M
C2-C5
CH4
Pt (111)
20 Torr I
573 K
100
200
400
600
PH2 (Torr)
XBL846-7051

fig. 4.14

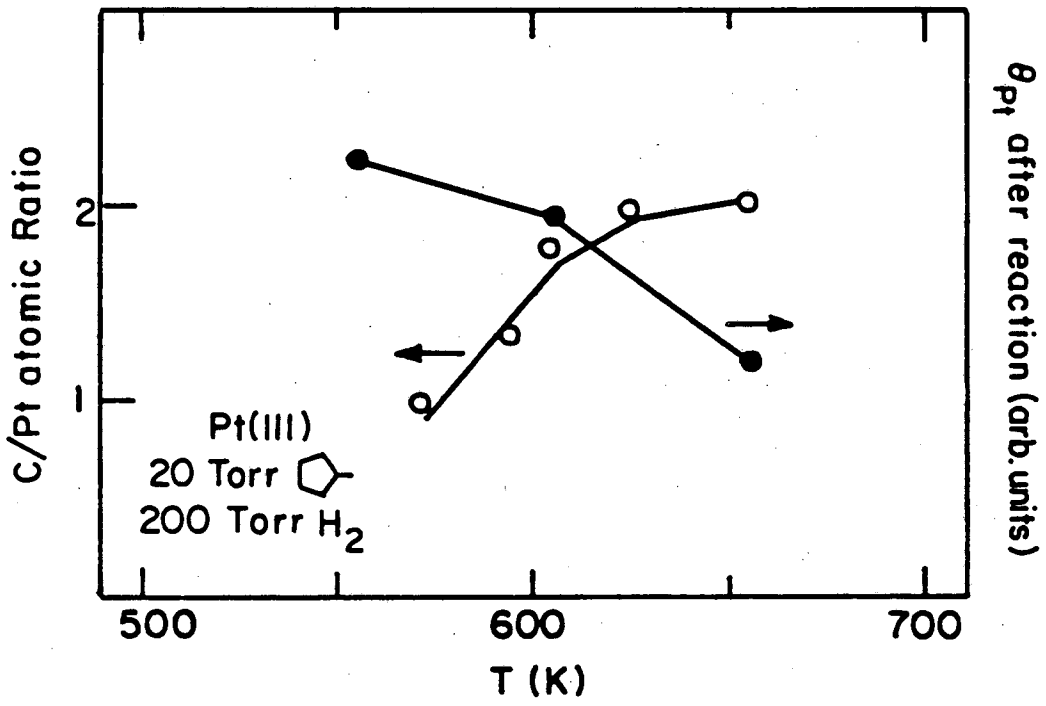
C/Pt atomic Ratio
2
1
Pt(111)
20 Torr
200 Torr H_2
500
600
700
T (K)
θ_{Pt} after reaction (arb. units)
XBL 846-7053

fig. 4.15

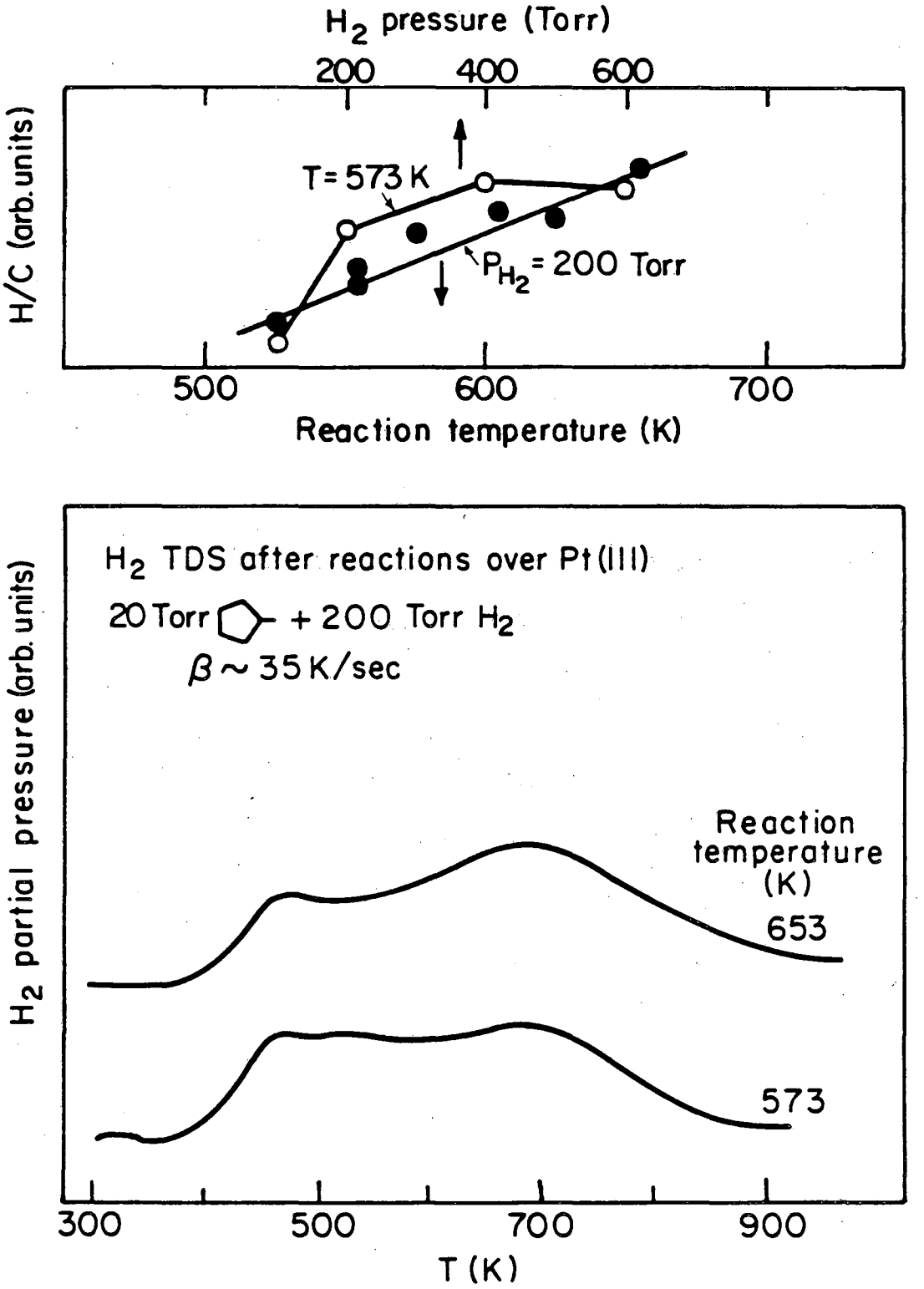
H2 pressure (Torr)
200
400
600
H/C (arb.units)
T=573 K
PH2 = 200 Torr
500
600
700
Reaction temperature (K)
H2 TDS after reactions over Pt(111)
20 Torr
+ 200 Torr H2
β ~ 35 K/sec
H2 partial pressure (arb.units)
Reaction temperature (K)
653
573
300
500
700
900
T (K)
XBL 846-7056

fig. 4.16

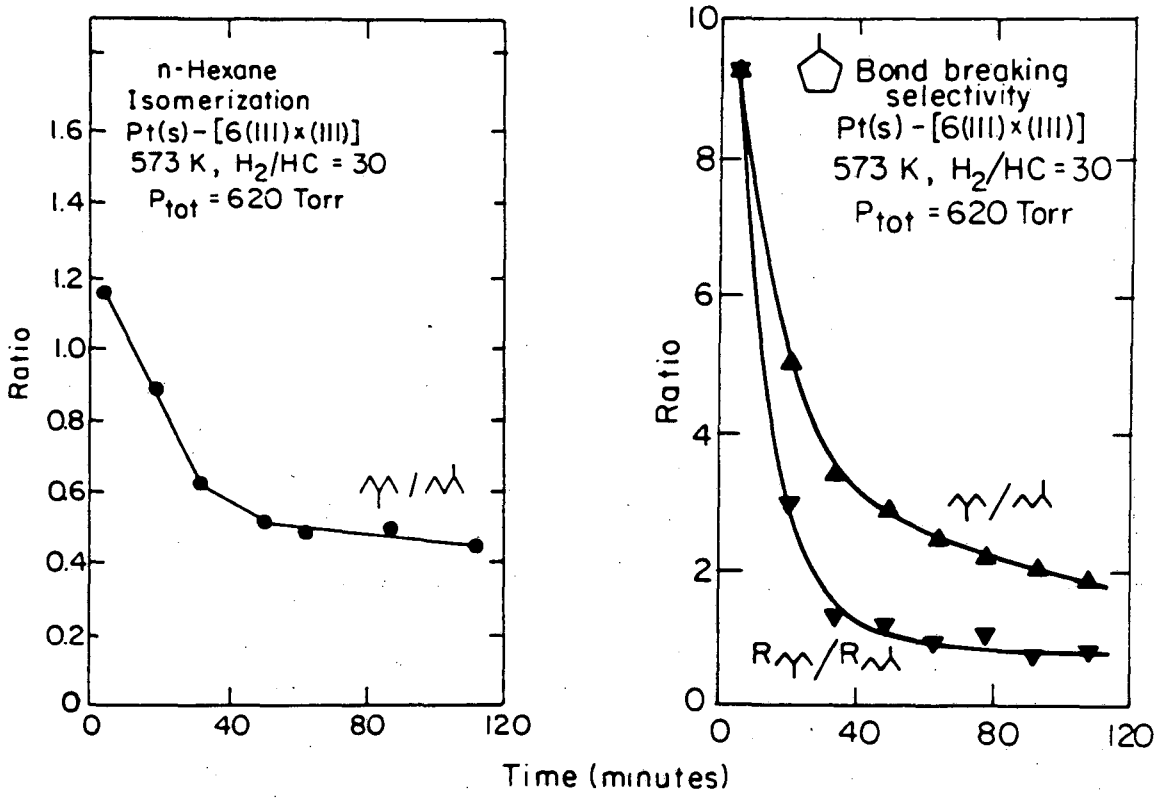

XBL819-6540B

fig. 4.17

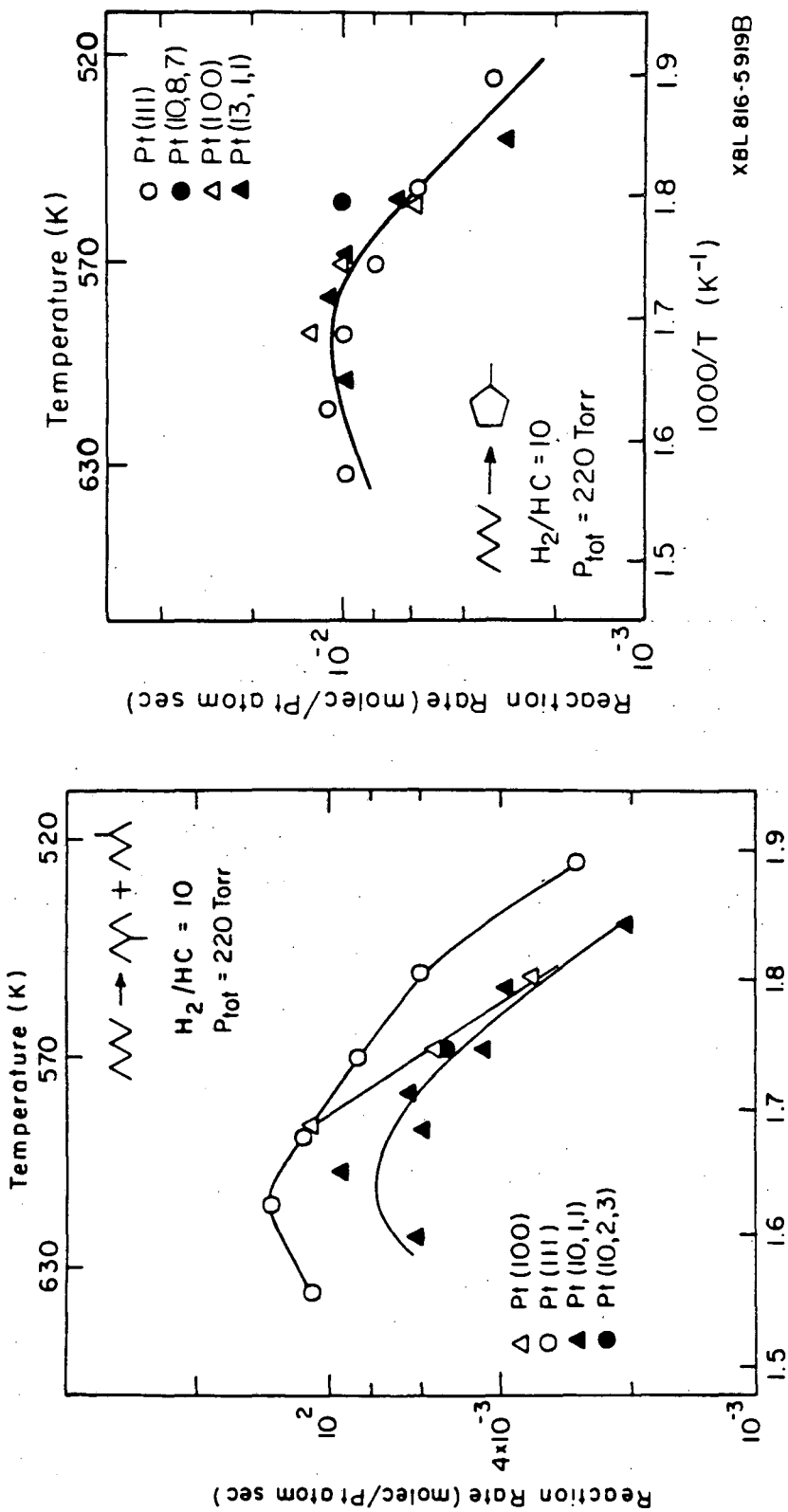
Temperature (K)
520
570
630
Pt (111)
Pt (10,8,7)
Pt (100)
Pt (13, 1, 1)
H_2/HC = 10
P_{tot} = 220 Torr
Reaction Rate (molec/Pt atom sec)
10^{-2}
10^{-3}
1.5
1.6
1.7
1.8
1.9
1000/T (K^{-1})
XBL 816-5919B
Temperature (K)
520
570
630
H_2/HC = 10
P_{tot} = 220 Torr
Pt (100)
Pt (111)
Pt (10, 1, 1)
Pt (10, 2, 3)
Reaction Rate (molec/Pt atom sec)
10^{2}
4×10^{-3}
10^{-3}
1.5
1.6
1.7
1.8
1.9
1000/T (K^{-1})

fig. 4.18

4.3. References.

1) S.M. Davis and G.A. Somorjai, in "The Chemical Physics of Solid Surfaces and Heterogeneous Catalysis", Vol. 4, D.A. King and D.P. Woodruff, Eds., Elsevier, Amsterdam 1982.

2) J.R. Anderson and N.R. Avery, J. Catal., 5, 446 (1966).

3) K. Foger and J.R. Anderson, J. Catal., 54, 318 (1978).

4) M. Boudart, A.W. Aldag, L.D. Ptak and J.E. Benson, J. Catal., 11, 35 (1968).

5) F.M. Dautzenberg and J.C. Platteeuw, J. Catal., 19, 41 (1970).

6) F.M. Dautzenberg and J.C. Platteeuw, J. Catal., 24, 264 (1972).

7) P.P. Lankhorst, H.C. DeJongste and V. Ponec, in "Catalyst Deactivation", B. Delmont and G.C. Froment, Eds. Elsevier, Amsterdam 1980.

8) J.R. Anderson and Y. Shimoyama, "Proc. 5th Int. Cong. Catal., Miami 1972", J.W. Hightower, ed., North Holland, Amsterdam 1973, p 695.

9) E. Santacessaria, D. Gelosa and S. Carra, J. Catal., 39, 403 (1975).

10) S.M. Davis, Ph.D. Thesis, University of California, Berkeley 1981.

11) S.M. Davis, F. Zaera and G.A. Somorjai, J. Am. Chem. Soc., 104, 7453 (1982).

12) S.M. Davis, F. Zaera and G.A. Somorjai, J. Catal., 85, 206 (1984).

13) Y. Barron, D. Coronet, G. Maire and F.G. Gault, J. Catal., 2, 152 (1963).

14) V. Amir-Ebrahami, F. Garin, F. Weisang and F.G. Gault, Nouv. J. Chemie, 3, 529 (1979).

15) F.G. Gault, in "Advances in Catalysis", Vol. 30, D.D. Eley, H. Pines and P.B. Weisz, eds., Academic Press, New York, 1981 p. 1.

16) J.R. Anderson, in "Advances in Catalysis", Vol. 23, D.D. Eley, H. Pines and P.B. Weisz, eds., Academic Press, New York 1973, p. 1.

17) J.K.A. Clarke and J.J. Rooney, in "Advances in Catalysis", Vol. 25, D.D. Eley, H. Pines and P.B. Weisz, eds., Academic Press, New York 1976, p. 125.

18) J.M. Dartigues, A. Chambellan, S. Corolleur, F.G. Gault, A. Renouprez, B. Moraweck, P. Bosch Giral and G. Dalmai-Imelik, Nouv. J. Chemie, 3, 591 (1979).

19) F. Garin, S. Aeiyach, L. Legare and G. Maire, J. Catal., 77, 323 (1982).

20) J.R. Anderson and R.J. MacDonald, J. Catal., 20, 147 (1971).

21) E. Santacessaria, D. Gelosa, S. Carra and I. Adami, Ind. Eng. Chem. Prod. Res. Develop., 17, 68 (1978).

22) F.E. Shepard and J.J. Rooney, J. Catal., 3, 129 (1964).

23) C. Corolleur, F.G. Gault, D. Juttard, G. Maire and J.M. Muller, J. Catal., 7, 466 (1967).

24) C. Corolleur, S. Corolleur and F.G. Gault, J. Catal, 24, 385 (1972).

25) C. Corolleur, D. Tomanova and F.G. Gault, J. Catal., 24, 401 (1972).

26) S.M. Davis, F. Zaera and G.A. Somorjai, J. Catal., 77, 439 (1982).

27) A. Chambellan, J.M. Dartigues, C. Corolleur and F.G. Gault, Nouv. J. Chimie, 1, 41 (1977).

28) F.G. Gault, Ann. Chim. (Paris), 5, 645 (1960).

29) G. Maire, G. Plouidy, J.C. Prudhomme and F.G. Gault, J. Catal., 4, 556 (1965).

30) D. Tomanova, C. Corolleur and F.G. Gault, C. R. Acad. Sc. Paris, 269, Ser. C, 1605 (1969).

31) G. Maire, C. Corolleur, D. Juttard and F.G. Gault, J. Catal., 21, 250 (1971).

32) C. Corolleur, F.G. Gault, D. Juttard, G. Maire and J.M. Muller, J. Catal., 27, 466 (1972).

33) J.-M. Dartigues, A. Chambellan and F.G. Gault, J. Am. Chem. Soc., 98, 856 (1976).

34) F. Garin, O. Zahraa, C. Crouzet, J.L. Schmitt and G. Maire, Surf. Sci., 106, 466 (1981).

35) Z. Paál and P. Tétényi, J. Catal., 29, 176 (1973).

36) Z. Paál, G. Székely and P. Tétényi, J. Catal., 58, 108 (1979).

37) O.V. Bragin, Z. Karpinski, K. Matusek, Z. Paál and P. Tétényi, J. Catal., 56, 219 (1979).

38) H. Glassi, K. Hayek and R. Kramer, J. Catal., 68, 397 (1981).

39) R. Kramer and H. Zuegg, J. Catal., 80, 446 (1983).

40) R. Kramer and H. Zuegg, J. Catal., 85, 530 (1984).

41) G.B. McVicker, P.J. Collins and J.J. Ziemiak, J. Catal., 74, 156 (1982).

42) S.G. Brandenberger, W.L. Callender and W.K. Meerbott, J. Catal., 42, 282 (1976).

43) J.H. Sinfelt, H. Hurwitz and J.C. Rohrer, J. Catal., 1, 481 (1962).

44) B.H. Davis and P.B. Venuto, J. Catal., 15, 363 (1963).

45) V. Amir-Ebrahami, A. Choplin, P. Pasayre and F.G. Gault, Nouv. J. Chimie, 4, 431 (1980).

46) B.H. Davis, J. Catal., 29, 398 (1973).

47) B.H. Davis, J. Catal., 46, 348 (1977).

CHAPTER FIVE: THE ROLE OF ADDITIVES IN HYDROCARBON CATALYSIS OVER PLATINUM SINGLE CRYSTAL SURFACES.

5.1. The effect of Potassium.

5.1.1. Introduction.

Alkali metals are frequently employed as promoters in the preparation of practical metal catalysts. Potassium is a well known additive to iron for ammonia synthesis [1,2] and to catalysts for the hydrogenation of carbon monoxide [3,4]. While the promotion effect of the elements like Ca, B, Al, Si, Ga and Bi on platinum reforming catalysts have been studied [5,6,7], the influence of alkali metals on the activity and selectivity of platinum for hydrocarbon conversion reactions has received less attention. A recent patent reported enhanced cyclization selectivity over Na_2O promoted platinum catalysts [8].

The effect of potassium over the flat Pt (111) single crystal surfaces on n-hexane conversion is reported here. The activity of the promoted catalyst was lower by a factor of two for all reactions when a small coverage ($\theta_K \sim 0.05$) of the alkali metal was deposited on the platinum surface. This decrease in reactivity was accompanied by an increase in the self-poisoning rate. The temperature dependence of the reaction rates was unaltered by the presence of potassium on the platinum surface between 550 and 625 K. The effect of oxygen on the catalysts was independent of that of potassium: while potassium decreased the overall activity, oxygen enhance hydrogenolysis.

A slightly larger amount of carbon, measured by Auger electron

spectroscopy, was seen after reactions when about 2% K atoms were present on the catalyst surface (as compared with the clean platinum case). This increase, however, was accompained by an increase of the bare platinum area available for catalytic activity. Also the H/C ratio of these carbonaceous deposits was higher in the presence of potassium. All this suggests a more three dimensional structure of the hydrocarbon fragments adsorbed, with less carbon to metal bonds. An inhibition of the dehydrogenation activity of platinum in the presence of potassium explains these results.

5.1.2. Results.

n-Hexane conversion on the Pt(111) face in the presence of coadsorbed potassium. The rates of hydrogenolysis, isomerization, cyclization and aromatization of n-hexane were investigated over the flat (111) platinum surfaces. The gas mixtures used for these reactions were 20 torr n-hexane and 600 torr of H_2, and reactions were carried out at 573 K unless otherwise indicated. Product accumulation curves, obtained as a function of reaction time for the (111) surface and different potassium coverages, are shown in figs. 5.1 to 5.4. From these, initial reaction rates, selectivities (as a percentage of desired accumulated product over the total conversion), and extent of self-poisoning (as the rate after two hours over initial rate), were obtained; they are shown in figs. 5.5, 5.6 and 5.7 respectively. All four reactions are strongly inhibited when only a small amount of potassium is present on the surface: about 5% of a monolayer of potassium reduces the total activity to one-half to that obtained on clean platinum. The selectivities for the different products did not change much, and, considering

the large decrease in overall activity, these changes were not significant. Self-poisoning of all the reactions was enhanced with the addition of potassium.

The temperature dependence for hydrogenolysis, isomerization and cyclization reaction rates were studied in the temperature range from 550 to 675 K for both clean platinum and for platinum with θ_K=0.05. Arrhenius plots are shown in figs. 5.8 to 5.10. Activation energies obtained for the low temperature region (550-625 K) are summarized in table 5.1; they were identical within experimental error, for clean and potassium covered platinum surfaces. In the high temperature region, there was a drop in activity for both cases from that predicted by the Arrhenius expression, being more pronounced for the potassium covered surface.

The dehydrogenation of n-hexane to olefins under the same conditions was also studied. The respective product accumulation curves are shown in fig. 5.11. Since olefin formation is much faster than the other reactions, initial reaction rates could not be accurately determined. It can be seen, however, that the potassium coverage was not too important in this case. The total olefin accumulated after 30-60 minutes of reaction dropped to about one half when the potassium coverage reached θ_K=0.45, as compared with the value θ_K=0.05 for the other reactions. Also, a maximum in the product accumulation curves as a function of time was observed at high potassium coverages (θ_K>0.3), after approximately 60 minutes of starting the reactions. Similar observations were made for cyclohexane dehydrogenation experiments; the results are summari-

zed in table 5.2. Almost identical values for the initial rates were obtained with and without potassium, but poisoning due to benzene coadsorption was greatly inhibited by the alkaline metal on the surface [9].

Studies were performed also on the 6(111)x(111) stepped platinum surface. The results were qualitatively the same as those obtained on the Pt(111) crystal face (table 5.3). More work needs to be carried out to make a quantitative comparison between those two surfaces.

Morphology of the carbonaceous deposits formed during n-hexane reactions. Auger analysis of the surface composition following n-hexane reactions always revealed the build-up of about a monolayer of strongly bonded carbonaceous deposits. No ordering of this layer could be detected using LEED. The self-poisoning of all reactions strongly suggest that at least part of these carbonaceus species were bonded irreversibly as a deactivating residue. Fig. 5.12 shows the 273 eV carbon to 237 eV platinum Auger signal ratio (C_{273}/Pt_{237}), measured following reactions as a function of potassium coverage. These peak height ratios can be converted into approximated (±25%) atomic ratios, expressed as carbon equivalents per surface platinum atom, by multiplying them by 0.62 [10]. As can be seen, there was a slight increase in the amount of carbon deposited up to $\theta_K \sim 0.3$, followed by a decrease by a factor of three at high potassium coverages, probably due blocking of platinum sites by potassium atoms.

The fraction of the platinum surface that remains clean after n-hexane reactions was measured using the CO titration technique described

in detail previously [11]. CO thermal desorption spectra obtained from these titrations at various potassium coverages are shown in fig. 5.13. The temperature of the maxima and the shape of the spectra followed the expected tendency for CO adsorption on potassium precovered platinum surfaces (fig. 5.14) [12], i.e., the binding energy of CO to platinum increased in the presence of coadsorbed potassium. The area under each spectrum is proportional to the amount of CO desorbed, which is also proportional to the fraction of uncovered platinum surface. In this way it was possible to measure the fraction of bare platinum after reactions as a function of potassium coverage, since CO does not adsorb on potassium under our experimental conditions. The results are shown in fig. 5.15. There is a clear increase of the fraction of bare sites up to about θ_K=0.3, followed by a decrease as potassium obscures a larger fraction of the platinum surface.

Energetics of C-H bond breaking. Hydrogen thermal desorption spectra were also recorded following n-hexane reactions. These are shown in fig. 5.16 for various potassium coverages. The spectra represent the sequential dehydrogenation of the strongly adsorbed species that were deposited by the reaction mixture. The desorption takes place in at least two steps, with broad peaks around 500 and 650 K. As discussed in a previous paper [13], the first desorption peak mainly corresponds to β-hydrogen abstraction, while the second peak represents the decomposition of CH fragments and breaking of C-H bonds that have no easy access to metal sites.

The areas under these spectra are proportional to the amount of

hydrogen present in the carbonaceous deposits. This data can be converted to approximate hydrogen to carbon ratios using the AES carbon signal and a benzene adsorption calibration [7]. Fig. 5.17 was obtained this way. A rapid increase in the H/C ratio with increasing potassium coverage (up to θ_K~0.08) is seen, followed by a slower one thereafter.

The activation energy for hydrogen desorption by β-elimination could also be calculated by assuming first order desorption kinetics [13]. The potassium coverage dependence of this activation energy is shown in fig. 5.18. It starts at about 26 Kcal/mole for the clean platinum surface, followed by a sharp increase of about 2 Kcal/mole at θ_K≈0.02, and by a further increase of another 2 Kcal/mole at θ_K≈0.45.

Preliminary n-hexane adsorption experiments under ultra high vacuum conditions have also been performed. Since n-hexane adsorption is dissociative and activated, the results of these studies have to be analyzed cautiously. n-Hexane uptake curves, measured using the amount of carbon on the surface as a function of n-hexane exposure, increases with temperature as expected (fig. 5.19). At any given temperature, less adsorption for the potassium precovered surface was obtained as compared with the clean platinum case (by about a factor of five, fig. 5.20). Temperature dependence of the initial sticking probability for n-hexane over clean and potassium and oxygen precovered platinum surfaces is shown in fig. 5.21. The adsorbed hydrocarbons had a higher H/C ratio in the case of the potassium precovered surface, similar to what has been observed in the high pressure experiments. Rehydrogenation of the adsorbed species deposited under UHV conditions were performed by exposing the catalyst to 600 torr of H_2 and the same deposition temperature for

5-10 minutes. The fraction of irreversibly adsorbed carbon was always greater than 60% (fig. 5.22).

Effect of coadsorbed oxygen on the reactivity of the potassium-platinum system. It is well known that alkali metals greatly increase the sticking probability of molecular oxygen and water. The base pressure of our system, about 10^{-9} torr, did not allow us to keep clean metallic potassium in most of the runs, and more than half of the AE spectra revealed the presence of little oxygen before reaction. In any case, after inserting the sample in the high pressure loop, a higher background pressure (more than 10^{-3} torr) provides enough water for the oxygenated species to form: oxygen was always detected afterwards. To study the effect of oxygen on the n-hexane conversion, some experiments were carried out in which the K/Pt samples were pretreated with oxygen before reactions. The catalytic activity of a platinum surface that was preoxidized at about 1000K and then covered with Θ_K=0.03 potassium was also studied. The results are summarized in table 5.4. Except for an increase of hydrogenolysis activity with oxygen, all potassium-platinum systems had comparable reactivities. The increase in hydrogenolysis activity has been observed previously for platinum oxide alone and for calcium oxide on platinum [7].

5.1.3. Discussion.

Addition of potassium on the platinum catalyst surface mainly inhibits n-hexane conversion rates, and increases slightly self-poisoning. However, the self-poisoning can not be directly related to the presence of carbonaceous deposits because, although there was more carbon present

on the surface after reactions when the catalyst was predosed with potassium, there was also a larger area of uncovered platinum available for catalytic activity. The carbonaceous deposits also have higher hydrogen content and larger activation energy for C-H bond breaking that in the case of clean platinum. Ultra-high vacuum n-hexane adsorption results are consistent with the preceeing conclusions.

As already mentioned, the addition of potassium causes a large decrease in n-hexane conversion rates, even at potassium coverages as low as θ_K=0.03. The change of catalytic activity versus potassium coverage displayed a pronounced non linearity (The initial rates are roughly proportional to $\theta_K^{-1/3}$). This suggest that electronic, and not structural changes on the surfaces (caused by site blocking by potassium), are responsible for the differences observed.

Alkali metals are well known as electron donors on almost all metalic surfaces. One of the most extended uses of this property is in the fabrication of low work function photocathodes [14]. The same effect is believed to be responsible for the enhanced activity in ammonia synthesis [1,2] and Fisher-Tropsch [3,4] catalysts when alkali metals are used as promoters. The CO/K/Pt system has been carefully characterized recently in our laboratory using various surface sensitive techniques: thermal desorption spectroscopy (TDS), high resolution electron energy loss spectroscopy (HREELS), ultraviolet photoelectron spectroscopy (UPS), and isotope scrambling experiments [12,78]. A large change in electronic properties of platinum with adsorbed potassium was observed. This was inferred from the following observations: an increase in activation

energy of the CO desorption from 25 to 36 Kcal/mole with θ_K=0.5 (manifested by a 210 K shift in the desorption peak maximum of the CO TDS); and a decrease in the C-O vibrational frecuency, down to 1400 cm^{-1} at θ_K=0.3 and low CO coverages, the lowest ever reported for CO bonded to a metal. Also in the same work, a drop of about 4 eV in the work function of the metal at θ_K=0.3, and an increase in the scrambling probability for adsorbed CO, were reported.

Due to the complexity of the hydrocarbon system, some simplifications are needed before attempting to explain our results. To start with, we will adopt the two step mechanism for hydrocarbon conversion initially proposed by Cimino et. al. [15]. According to this scheme, following dissociative adsorption of the reactants, a further dehydrogenation of the adsorbed hydrocarbons can take place. These dehydrogenated intermediates then rearrange and desorb as products. The slow step, depending on the conditions of the reaction, can be either the dehydrogenation or the rearrangement of the adsorbed intermediates. Since different reactions proceed via different intermediates, and since potassium was found to be a non-selective poison, it seems that the presence of potassium on the platinum surface slows down the dehydrogenation steps, and therefore, we propose that dehydrogenation is the limiting step under our conditions.

Low pressure experiments on n-hexane adsorption showed a decrease in the apparent sticking coefficient with potassium on the surface. In this process, at least one C-H bond breaks, followed by the bonding of the dissociated molecule to the surface through the carbon atom.

Qualitative calculations [16,17], photoemission studies of energy level shifts [18], and work function changes [19,20] all suggest that this adsorption is accompanied by a charge transfer from the hydrocarbon to the platinum surface, leaving the former with a carbonium ion character. surface potassium, which acts as an electron donor, inhibits then this charge transfer. The effect should be more accentuated as the hydrocarbon dehydrogenates further, because the remaining hydrocarbon fraction is less able to interact with the extra negative charge provided by the potassium. This may be the reason why, while n-hexane adsorption at low pressures is severely inhibited by potassium, not much change in the high pressure dehydrogenation reactions was observed, in which high hydrogen pressures ensure that surface species are largely hydrogenated. Only when dealing with isomerization, cyclization, and hydrogenolysis reactions, which requires more dehydrogenated intermediates, does the poisoning effect of potassium become appreciable.

A further piece of information that supports the preceeding conclusion is the steep rise in the activation energy for hydrogen β elimination of the carbonaceous deposits shown in fig. 5.18. As in the adsorption experiments, potassium makes breaking the C-H bonds of adsorbed species more difficult.

The morphology of the carbonaceous deposits formed during the reactions also changes with the amount of potassium on the surface. Although there is a slight increase in carbon coverage up to $\theta_K \sim 0.04$ (fig. 5.12), this is accompanied by an increase, and not a decrease, in the fraction of uncovered platinum surface (fig. 5.15). This can be

explained as follows: less multiple site adsorption yields less hydrogenolysis and C-C bond breaking activity, leaving more adsorbed species on the surface, as shown by a grater amount of carbon in fig.5.12. However, these carbonaceous deposits do not block much of the platinum surface, because there are fewer carbon-metal bonds involved (less multiple adsorption); the molecules are "sticking out" instead of "lying down" on the surface, giving more 3-dimensional character to the deposits [11]. This also implies a higher hydrogen to carbon ratio of the adsorbed species, as observed.

The effect of adsorbed alkali metals and the electronic changes that they induce on platinum surfaces have been studied by other researchers. Foger and Anderson [21] studied the effect of different additives on the Pt/Y-zeolite catalyst for neopentane conversion. The electron deficiency of the platinum particles, measured by ESCA, was founded to follow the sequence La-Y>Ca-Y>Na-y zeolite. At the same time, the total activity for neopentane conversion decreased in that order. Since neopentane does not have secondary or tertiary carbon atoms, it is expected to react only on the metal surface. Their results are then in agreement with ours, namely, the activity for hydrocarbon conversion slows down with an increase in electron density on the platinum catalyst.

Finally, a patent [8] reports an enhancement in activity of a factor of three for benzene formation from n-hexane when few ppm of sodium are added to a carbon supported platinum catalyst. One possible explanation for the disagreement with our data is that, while sodium forms alloys with platinum, potassium remains as a separate phase (preferentially on the

surface), and desorbs above ~ 1000K [22]. Consequently, different electronic interactions between the alkali metals and platinum are to be expected, with corresponding changes in the catalytic behaviour of the two systems.

Some of our results remain unexplained. The temperature dependence of the reaction rates in the range of 600-675 K showed a decrease in activity as compared with that expected from the Arrhenius expression. This can be attributed to an increase in coke formation at higher temperatures, that poisons the platinum activity. However, it is not clear at this point why potassium accelerates this effect, as observed experimentally. Also it cannot readily explained why the olefin accumulation curves have a maximum at high potassium coverages. The fact that the total amount of olefin produced decreases with time means that they react to form other products. However, it is not clear why potassium favors these side reactions.

Table 5.1

Activation energies for n-hexane reactions over clean and potassium covered Pt (111) surfaces in the 550 - 625 K temperature range.

Reaction	Activation energy E_a (Kcal/mole)
Hydrogenolysis	29 ± 3
Isomerization	56 ± 5 → 25 ± 3
Dehydrocyclization	33 ± 3

Table 5.2

Effect of potassium on cyclohexane conversion over Pt (111) surfaces (T=473 K, P_{H_2} =600 Torr and P_{HC}=20 Torr).

Θ_K	Initial rate[a]		Rate after 1 hour[a]	
	Benzene	n-Hexane	Benzene	n-Hexane
0	550	11	≃ 0	≃ 0
0.013	550	≃ 0	7.4	≃ 0
0.35	420	≃ 0	25	≃ 0
0.35 (restart)	420	≃ 0	-	-

a) turnover fecuencies, $x10^{-3}$ molecules/Pt atom·sec.

Table 5.3

The effect of potassium on n-hexane conversion activity over Pt (332) surfaces (T=573 K, P_{H_2}=600 Torr, P_{HC}=20 Torr).

Surface	Time[a]	Turnover frecuency[b]			
		Hyd	MCP	Iso	Bz
Clean Pt	0	28	17	7.0	3.0
	120	8.5	6.0	4.0	2.0
θ_K=0.10	0	43	25	4.0	2.5
	120	8.5	5.0	4.0	2.0

a) reaction time in minutes

b) $x10^{-3}$ molec/Pt atom•sec. Hyd=hydrogenolysis, MCP=methylcyclopentane formation, Iso=isomerization, and Bz=benzene formation.

Table 5.4

Effect of oxygen on clean and potassium precovered Pt (111) surfaces for n-hexane conversion (T=573 K, P_{HC}=20 Torr, P_{H_2}=600 Torr).

Surface	Θ_K	O/Pt[a]	Initial TF[b]		
			Hyd	Iso	MCP
Clean Pt	0	0	14	17	19
K/Pt	0.02	≈ 0	3	6	6
K/Pt	0.03	≈ 0	4	5	6
K_xO/Pt[c]	0.02	0.08	11	5	8
K/PtO_x[d]	0.03	0.28	12	6	6

a) Ratio of Auger signal intensities I(515 eV)/I(237 eV).

b) Turnover frequencies, x10^{-3} molec/Pt atom·sec (±20%). Hyd= hydrogenolysis, Iso=isomerization and MCP=methylcyclopentane formation.

c) Saturated with oxygen at room temperature after potassium deposition.

d) Potassium deposited after preoxidizing the platinum surface at about 1000 K.

FIGURE CAPTIONS

Fig. 5.1. Product accumulation curves as a function of time for n-hexane hydrogenolysis over Pt (111) surfaces dosed with different amounts of potassium.

Fig. 5.2. Product accumulation curves as a function of time for n-hexane isomerization over Pt (111) surfaces dosed with different amounts of potassium.

Fig. 5.3. Product accumulation curves as a function of time for n-hexane methylcyclopentane formation over Pt (111) surfaces dosed with different amounts of potassium.

Fig. 5.4. Product accumulation curves as a function of time for n-hexane aromatization over Pt (111) surfaces dosed with different amounts of potassium.

Fig. 5.5. Initial reaction rates for hydrogenolysis, isomerization, dehydrocyclization and aromatization of n-hexane over Pt (111) surfaces as a function of potassium coverages.

Fig. 5.6. Selectivity of accumulated products after two hours of n-hexane reaction over Pt (111) as a function of potassium coverages.

Fig. 5.7. Stability to self-poisoning, expressed as the ratio of reaction rates after two hours over initial rates, for hydrogenolysis, isomerization, dehydrocyclization and aromatization of n-hexane over Pt (111) surfaces as a function of potassium coverages.

Fig. 5.8. Arrhenius plot for the initial rate of n-hexane hydrogenolysis catalyzed over Pt (111) clean and potassium dosed surfaces.

Fig. 5.9. Arrhenius plot for the initial rate of n-hexane isomerization catalyzed over Pt (111) clean and potassium dosed surfaces.

Fig. 5.10. Arrhenius plot for the initial rate of formation of methylcyclopentane from n-hexane catalyzed over Pt (111) clean and potassium dosed surfaces.

Fig. 5.11. Product accumulation curves as a function of reaction time for n-hexane dehydrogenation over Pt (111) surfaces covered with different amounts of potassium.

Fig. 5.12. Carbon to platinum AES signal ratio after n-hexane reaction over Pt (111) surfaces as a function of potassium coverage.

Fig. 5.13. CO thermal desorption spectra following CO saturation of the Pt (111) surface after two hours of n-hexane reaction for various potassium coverages. The adsorption temperature was 300-310 K the heating rate 80 K/sec.

Fig. 5.14. Temperature of the maxima and full width at half maximum as a function of potassium coverage for CO TDS after n-hexane reactions and 36 L CO exposure.

Fig. 5.15. Fractional concentration of uncovered platinum surface sites after n-hexane reactions (determined by CO titration) as a function of potassium coverage (relative to the same fractional concentration after reaction for the clean platinum case).

Fig. 5.16. Hydrogen thermal desorption spectra from the carbonaceous deposits after n-hexane reactions over Pt (111) surfaces with various potassium coverages. Heating rate = 80 K/sec.

Fig. 5.17. Hydrogen to carbon ratio for carbonaceous deposits formed after n-hexane reactions over Pt (111) surfaces, as a function of potassium coverage.

Fig. 5.18. Activation energy of hydrogen β-elimination from the carbonaceous deposits formed after n-hexane reactions over Pt (111) surfaces as a function of potassium coverages.

Fig. 5.19. n-Hexane uptake curves on Pt (111) surfaces at three different temperatures.

Fig. 5.20. n-Hexane uptake curves at 523 K over clean and potassium and oxygen predosed Pt (111) surfaces.

Fig. 5.21. Arrhenius plot of n-hexane initial sticking probabilities, S_O, over clean and predosed Pt (111) surfaces. S_O is in carbon atoms per Langmuir of exposure, uncorrected for ion gauge sensitivity.

Fig. 5.22. Fraction of irreversibly adsorbed carbon deposits after n-hexane exposure at 523 K over Pt (111) clean and predosed surfaces.

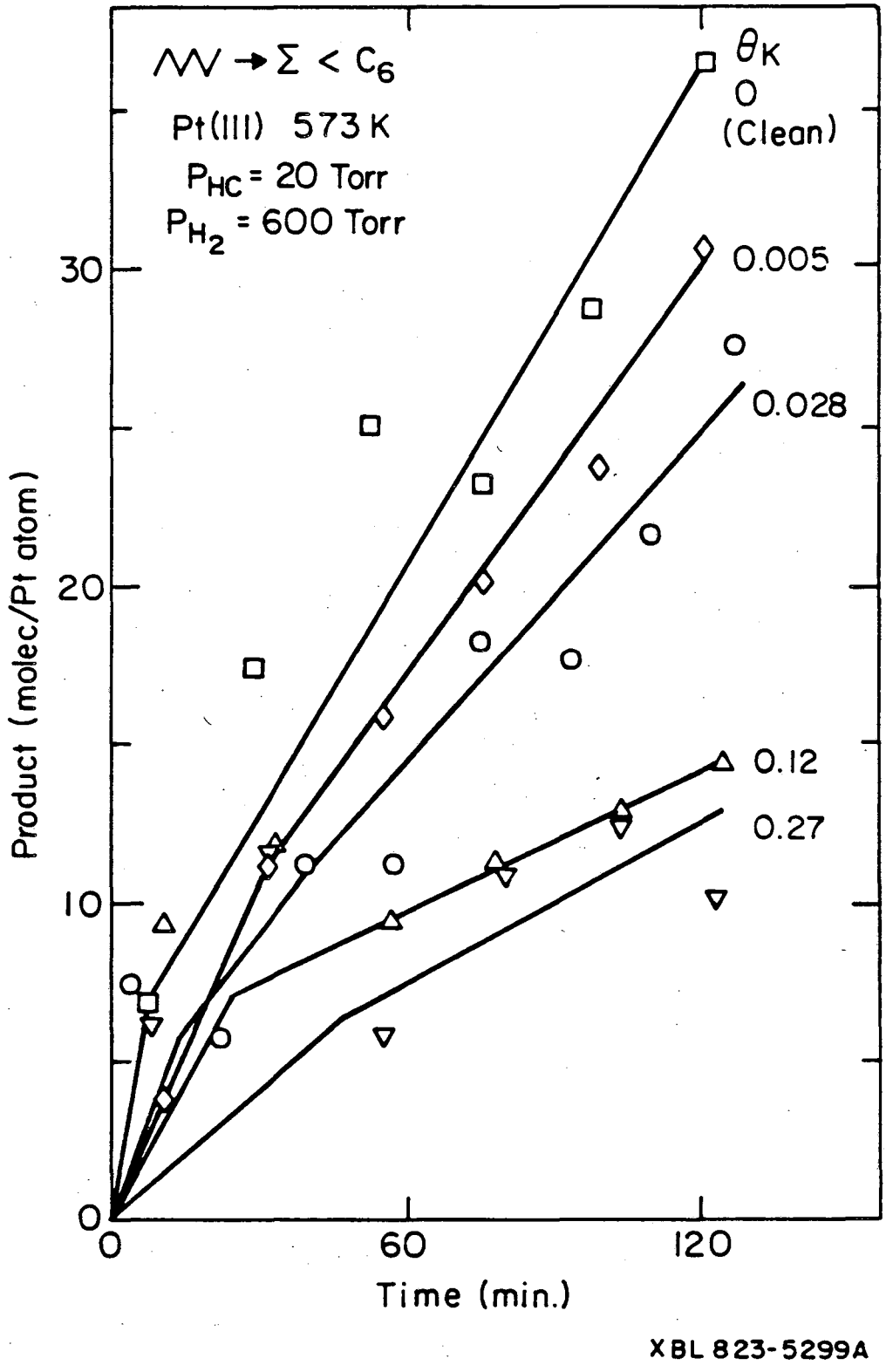
∧∨ → Σ < C6
Pt(111) 573 K
PHC = 20 Torr
PH2 = 600 Torr
θK
0
(Clean)
0.005
0.028
0.12
0.27
Product (molec/Pt atom)
Time (min.)
0
10
20
30
0
60
120
XBL 823-5299A

fig. 5.1

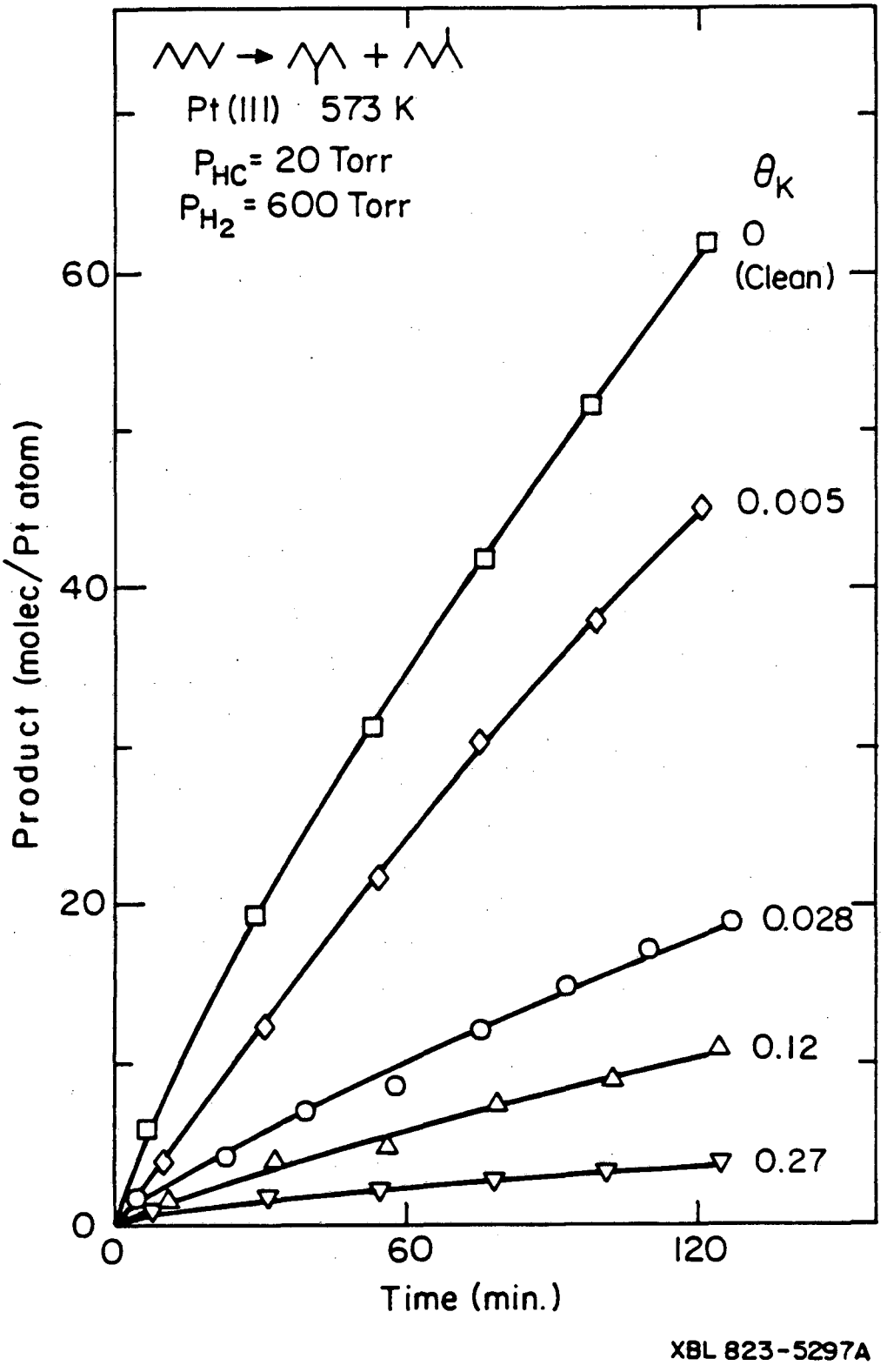
Pt (111) 573 K
P_{HC} = 20 Torr
P_{H_2} = 600 Torr
θ_K
0
(Clean)
0.005
0.028
0.12
0.27
Product (molec/Pt atom)
Time (min.)
0
20
40
60
0
60
120
XBL 823-5297A

fig. 5.2

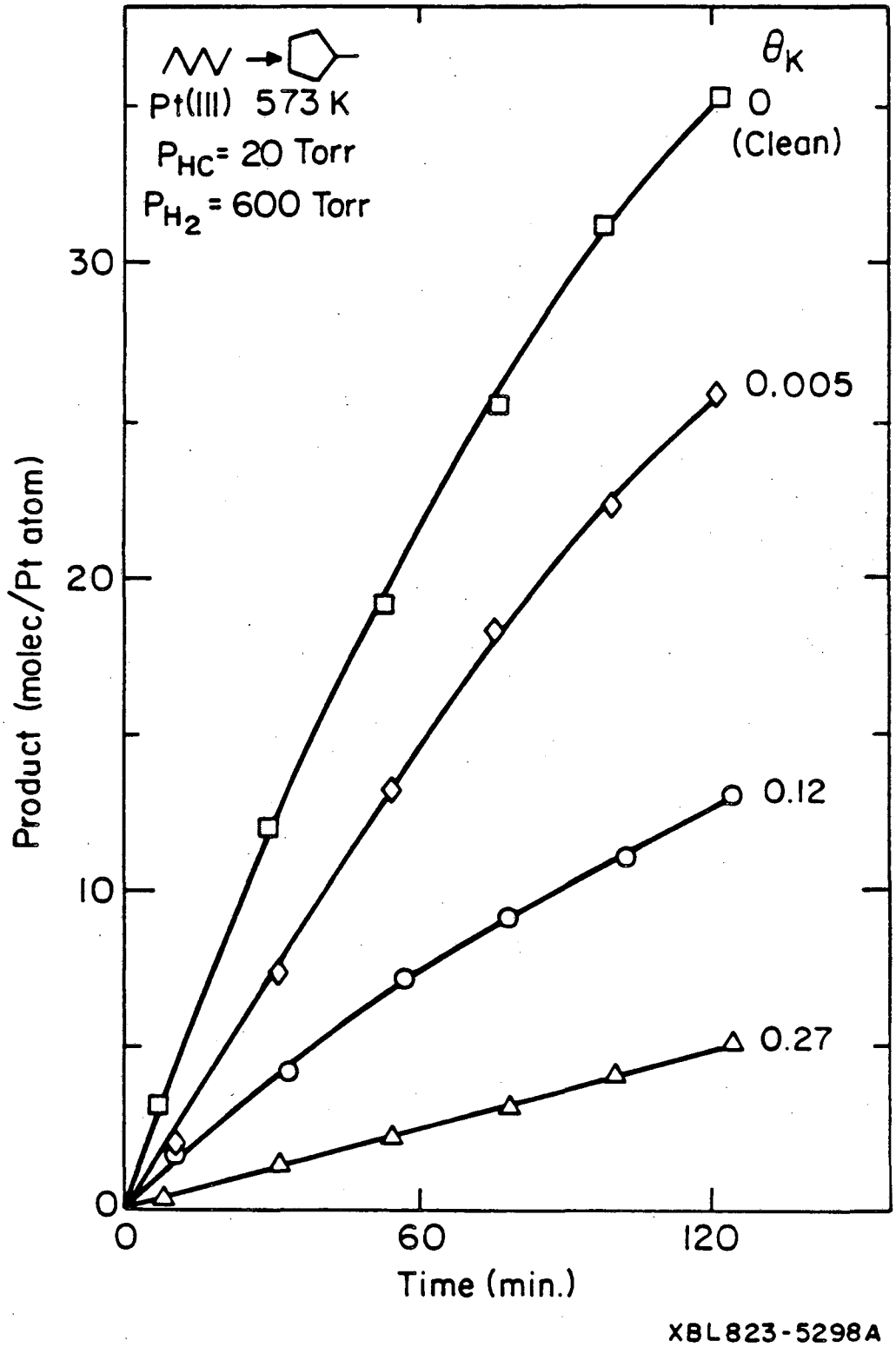
Pt(111) 573 K
P_{HC}= 20 Torr
P_{H_2} = 600 Torr
θ_K
0
(Clean)
0.005
0.12
0.27
Product (molec/Pt atom)
0
10
20
30
0
60
120
Time (min.)
XBL823-5298A

fig. 5.3

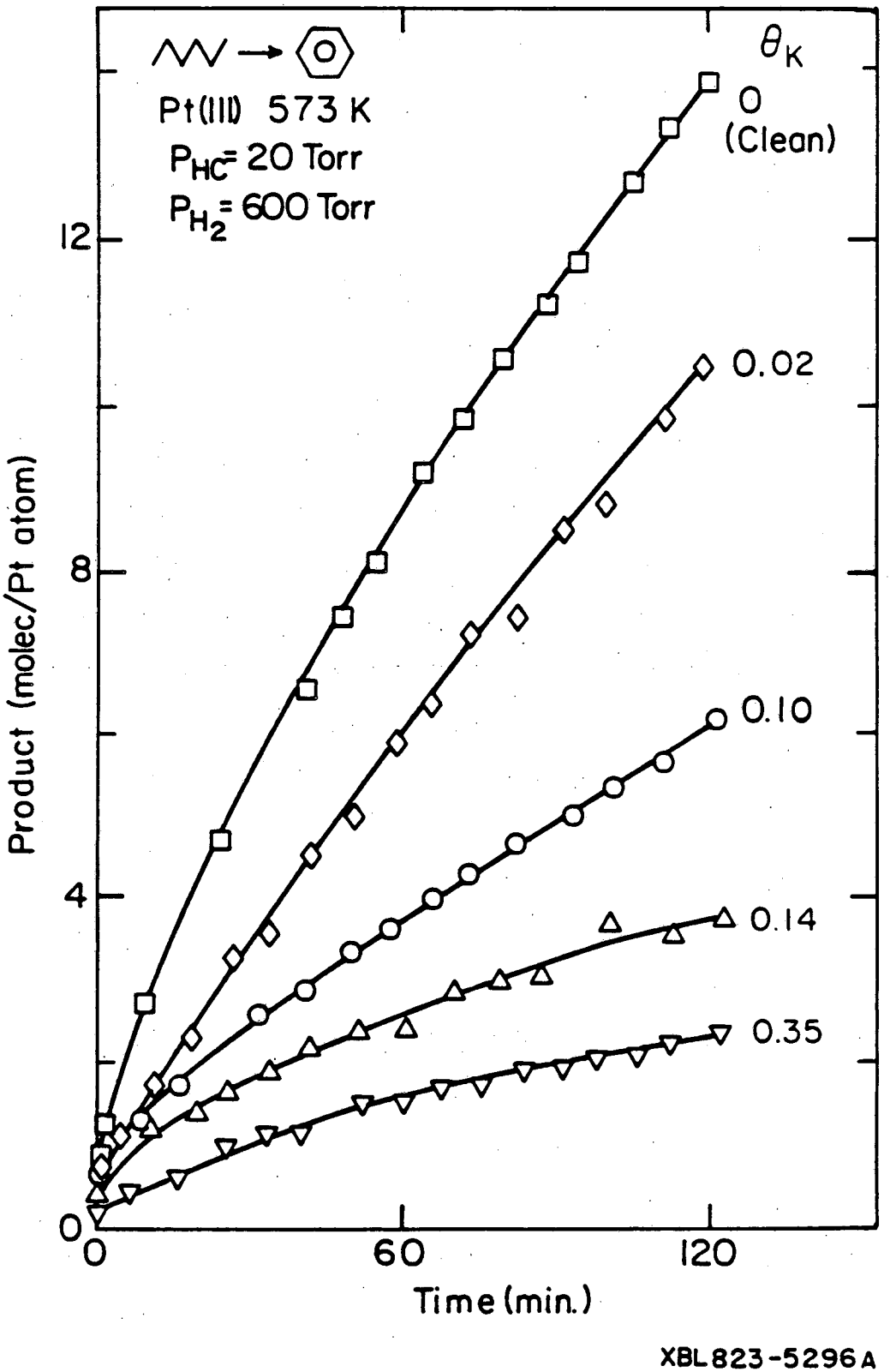
Pt(111) 573 K
P_{HC}= 20 Torr
P_{H_2}= 600 Torr
θ_K
0
(Clean)
0.02
0.10
0.14
0.35
Product (molec/Pt atom)
Time (min.)
0
4
8
12
0
60
120
XBL823-5296A

fig. 5.4

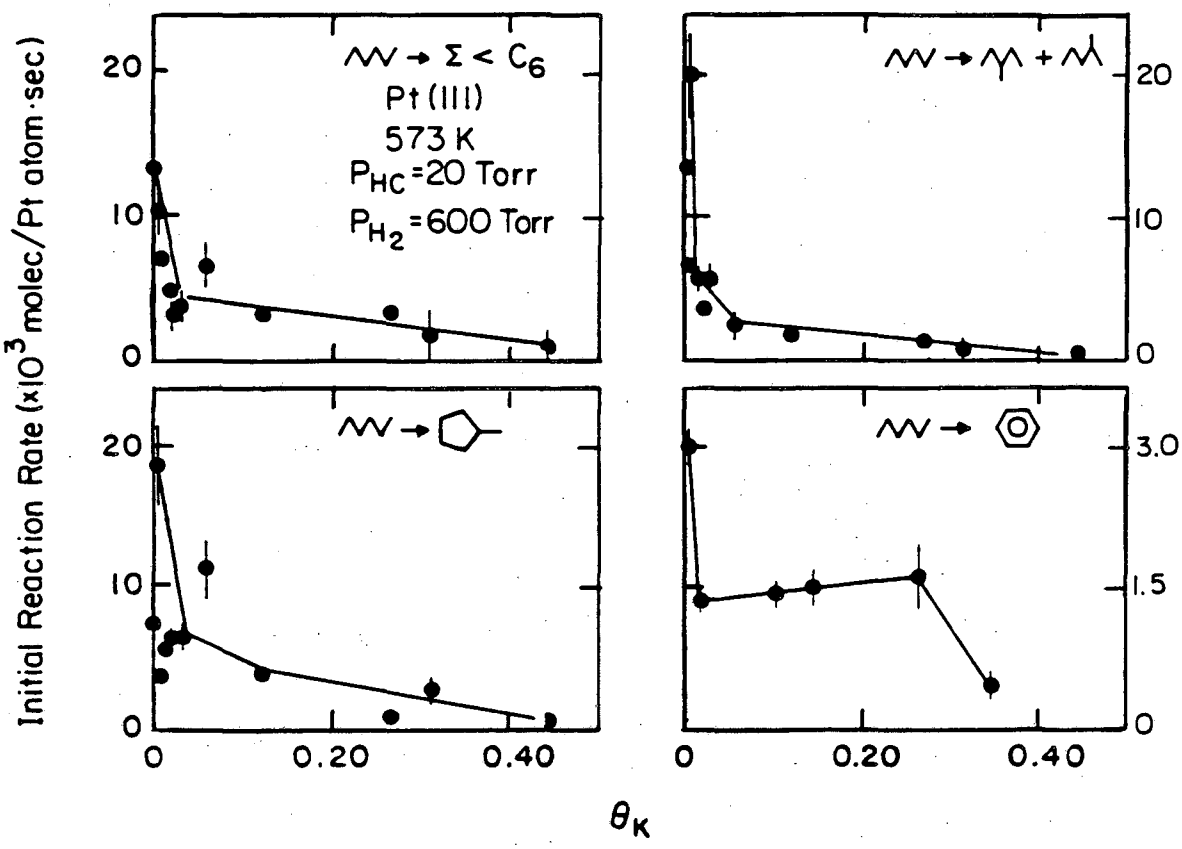

XBL 823-5289A

fig. 5.5

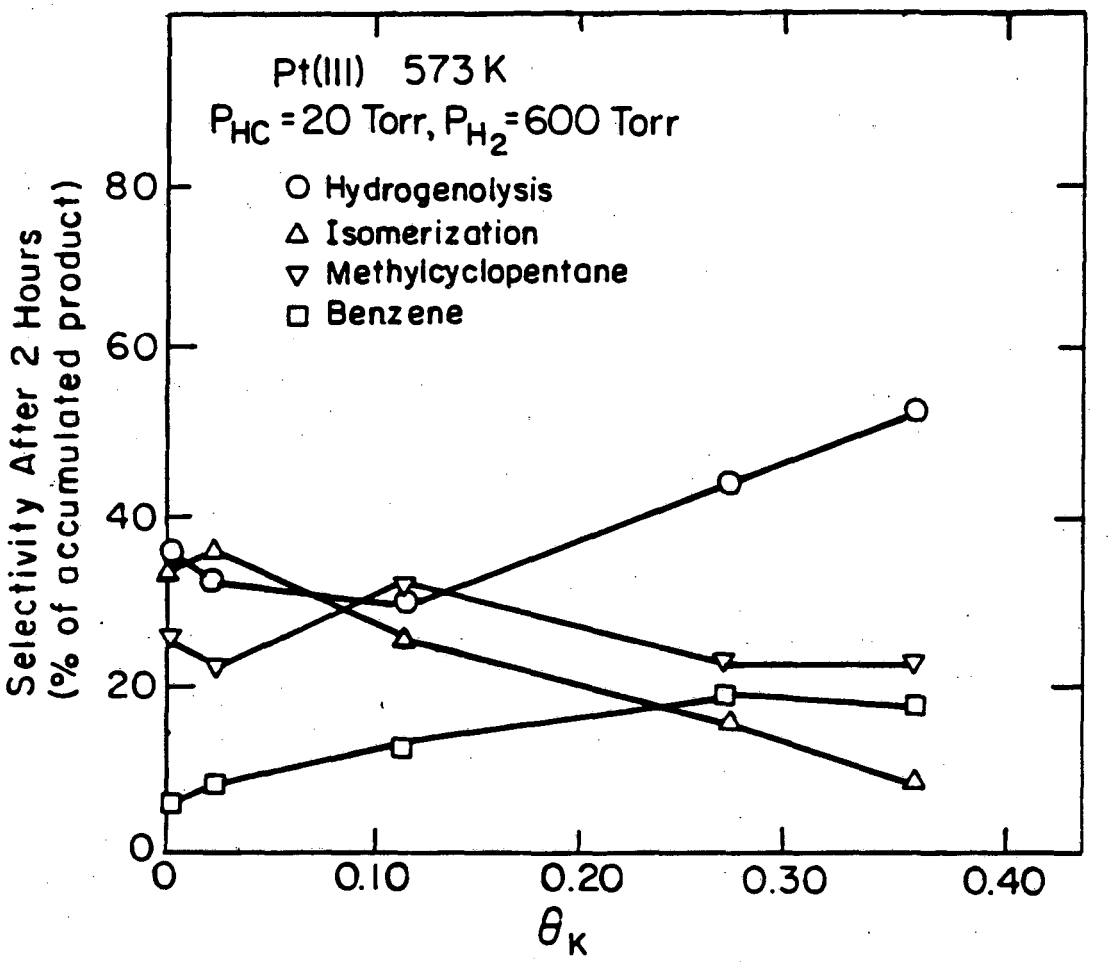
Pt(111) 573 K
P_{HC} = 20 Torr, P_{H_2} = 600 Torr
O Hydrogenolysis
Δ Isomerization
▽ Methylcyclopentane
□ Benzene
Selectivity After 2 Hours
(% of accumulated product)
80
60
40
20
0
0
0.10
0.20
0.30
0.40
θ_K
XBL 823-5291A

fig. 5.6

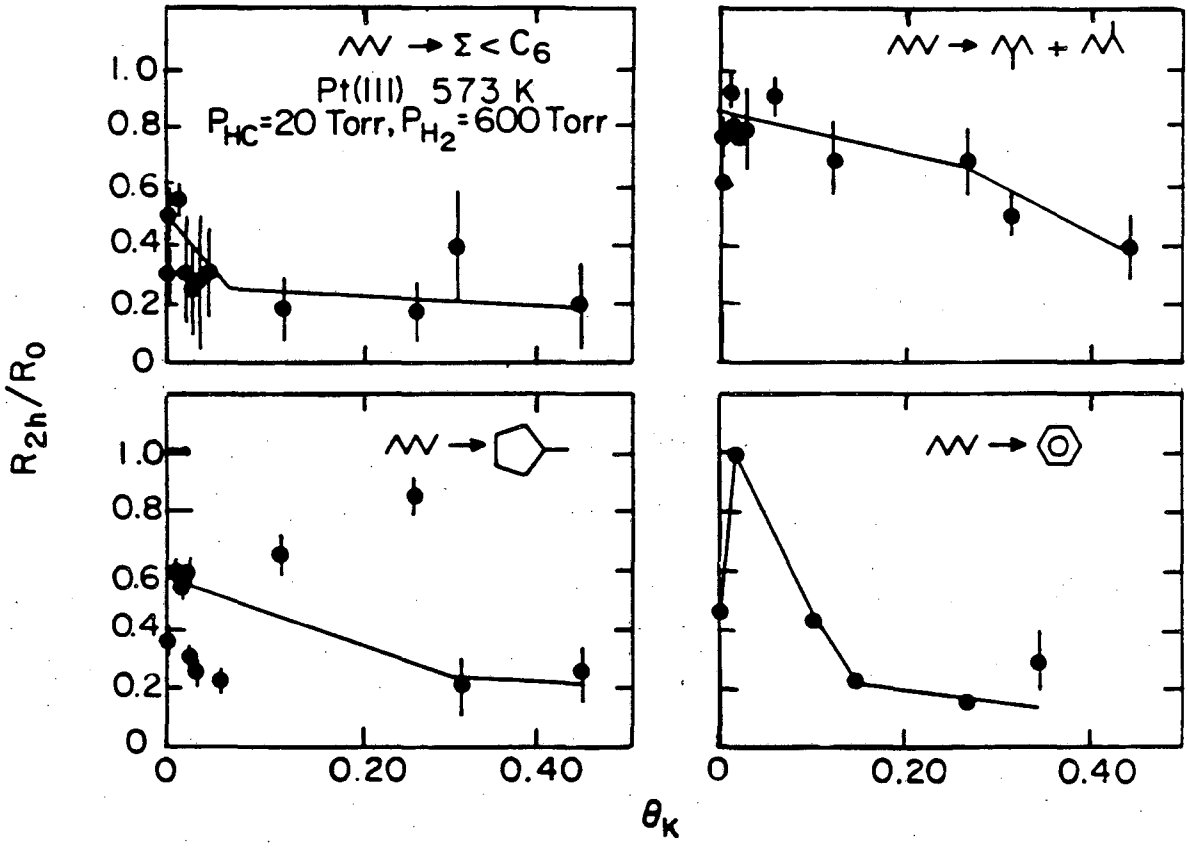

XBL 823-5292A

fig. 5.7

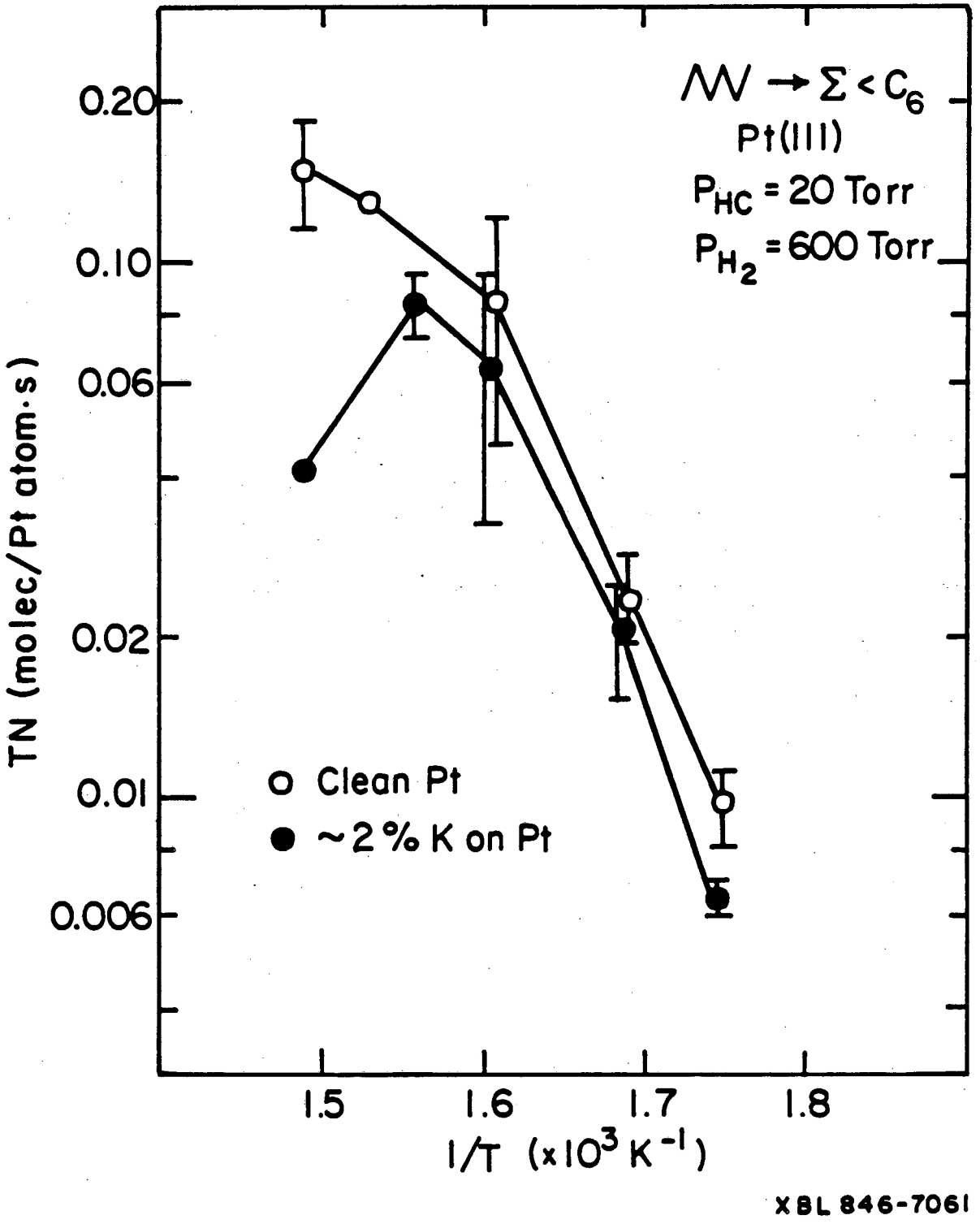
0.20
0.10
0.06
0.02
0.01
0.006
TN (molec/Pt atom·s)
1.5
1.6
1.7
1.8
1/T (x10³ K⁻¹)
Clean Pt
~2% K on Pt
Pt(111)
P_HC = 20 Torr
P_H2 = 600 Torr
XBL 846-7061

fig. 5.8

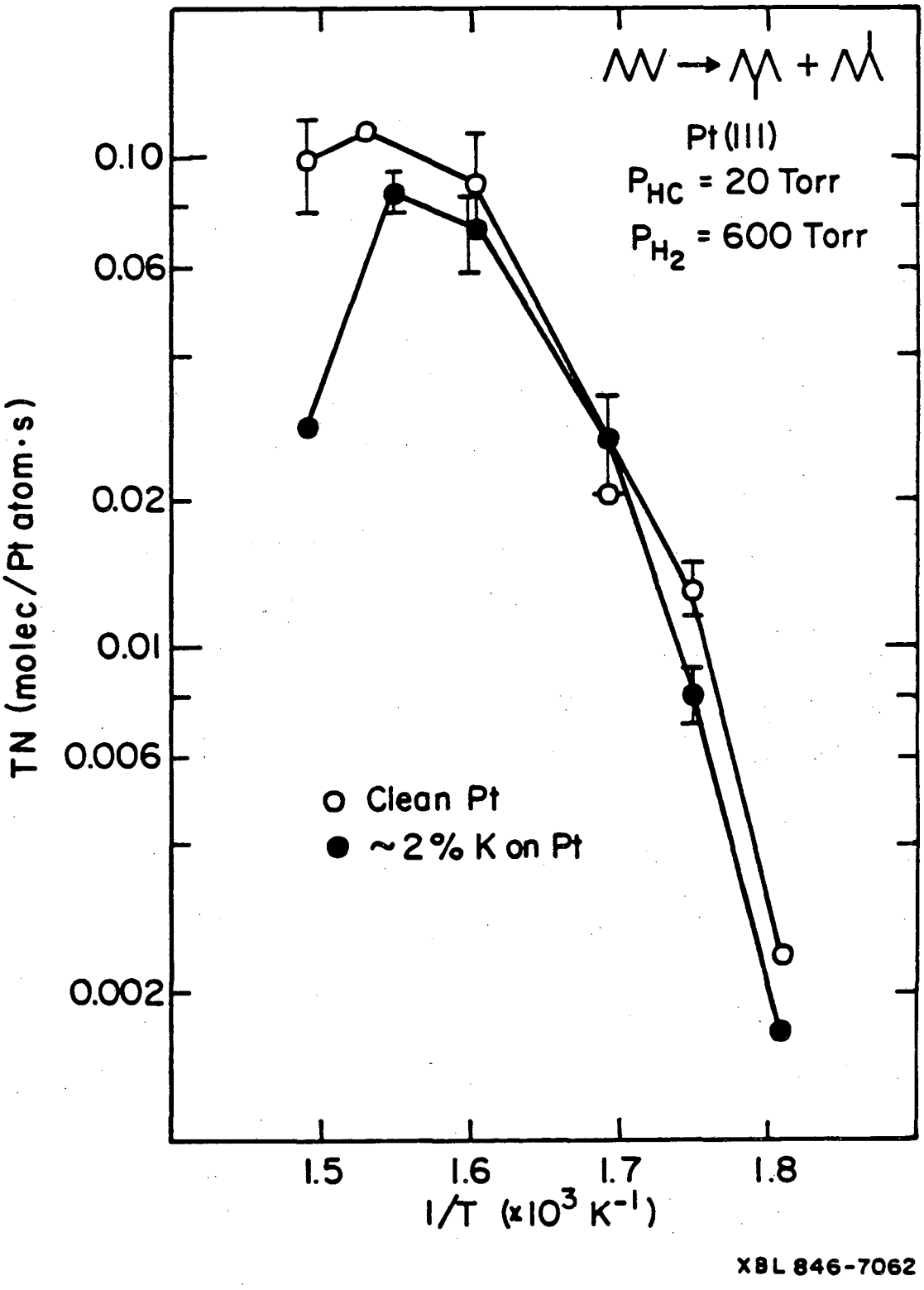
Pt(111)
P_{HC} = 20 Torr
P_{H_2} = 600 Torr
0.10
0.06
0.02
0.01
0.006
0.002
TN (molec/Pt atom·s)
O Clean Pt
● ~2% K on Pt
1.5
1.6
1.7
1.8
1/T (×10³ K⁻¹)
XBL 846-7062

fig. 5.9

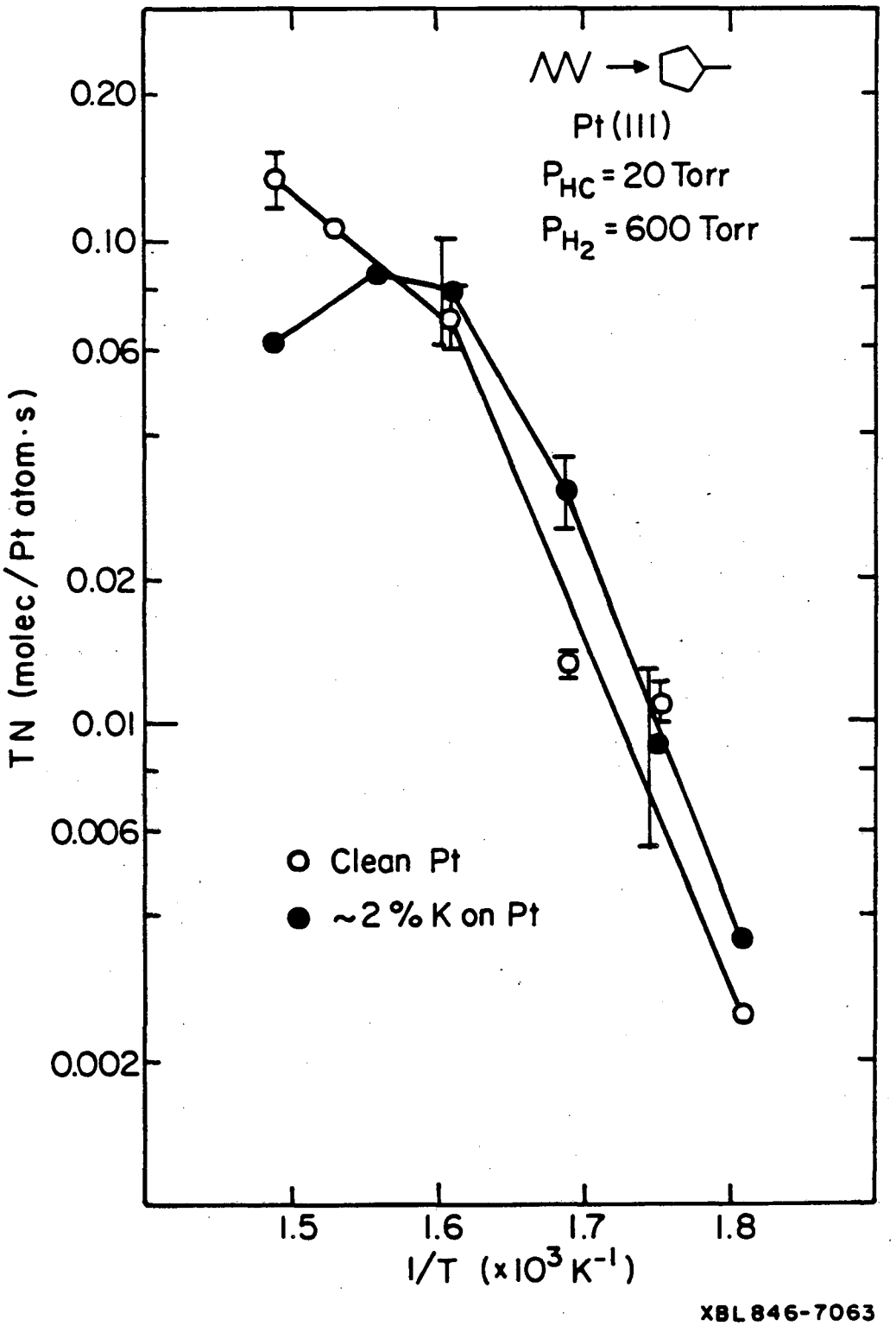
Pt (111)
P_{HC} = 20 Torr
P_{H_2} = 600 Torr
TN (molec/Pt atom·s)
0.20
0.10
0.06
0.02
0.01
0.006
0.002
O Clean Pt
● ~2 % K on Pt
1.5
1.6
1.7
1.8
1/T (×10³ K⁻¹)
XBL 846-7063

fig. 5.10

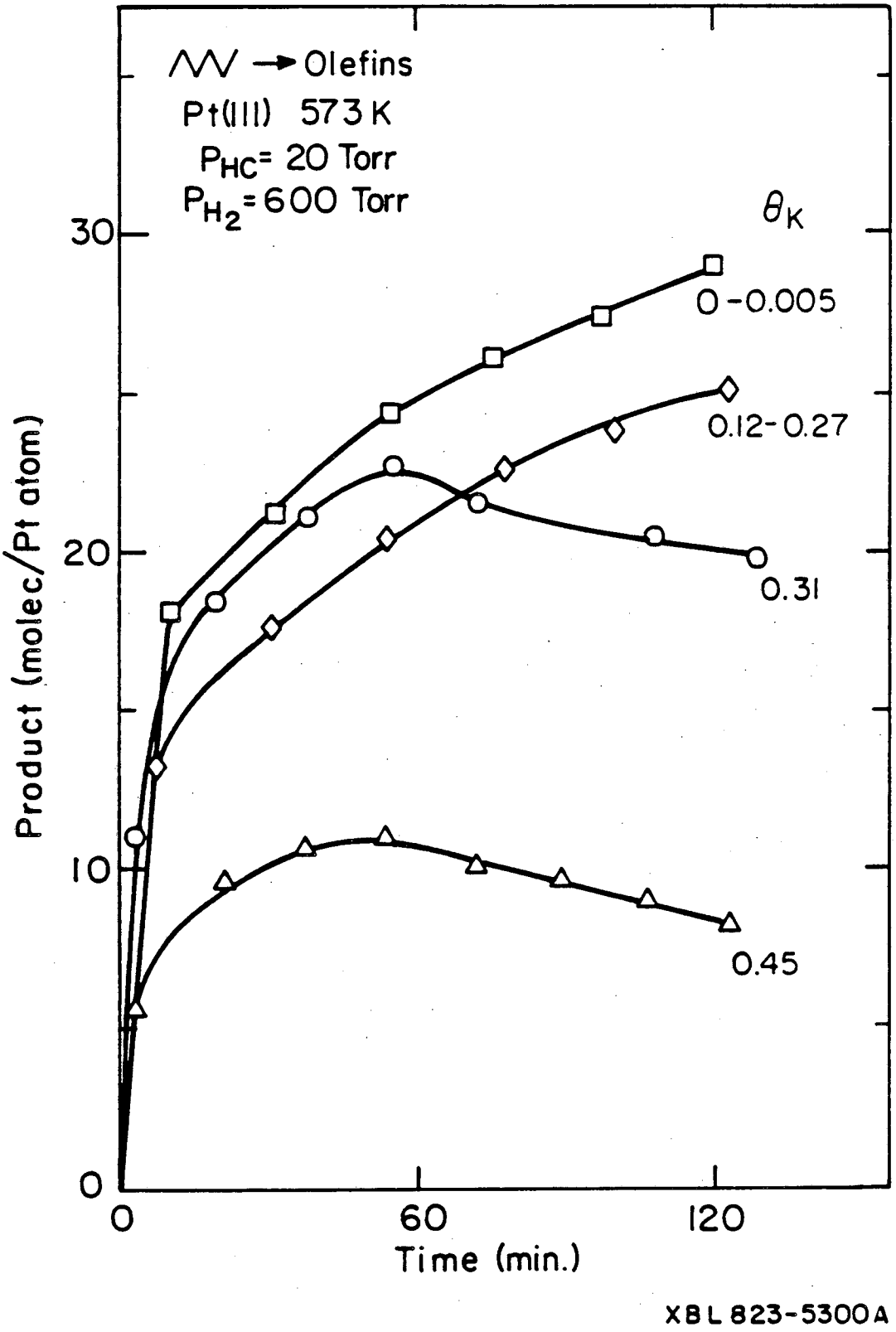
∧∨ → Olefins
Pt(111) 573 K
P_{HC}= 20 Torr
P_{H_2}= 600 Torr
θ_K
0-0.005
0.12-0.27
0.31
0.45
Product (molec/Pt atom)
Time (min.)
0
10
20
30
0
60
120
XBL 823-5300A

fig. 5.11

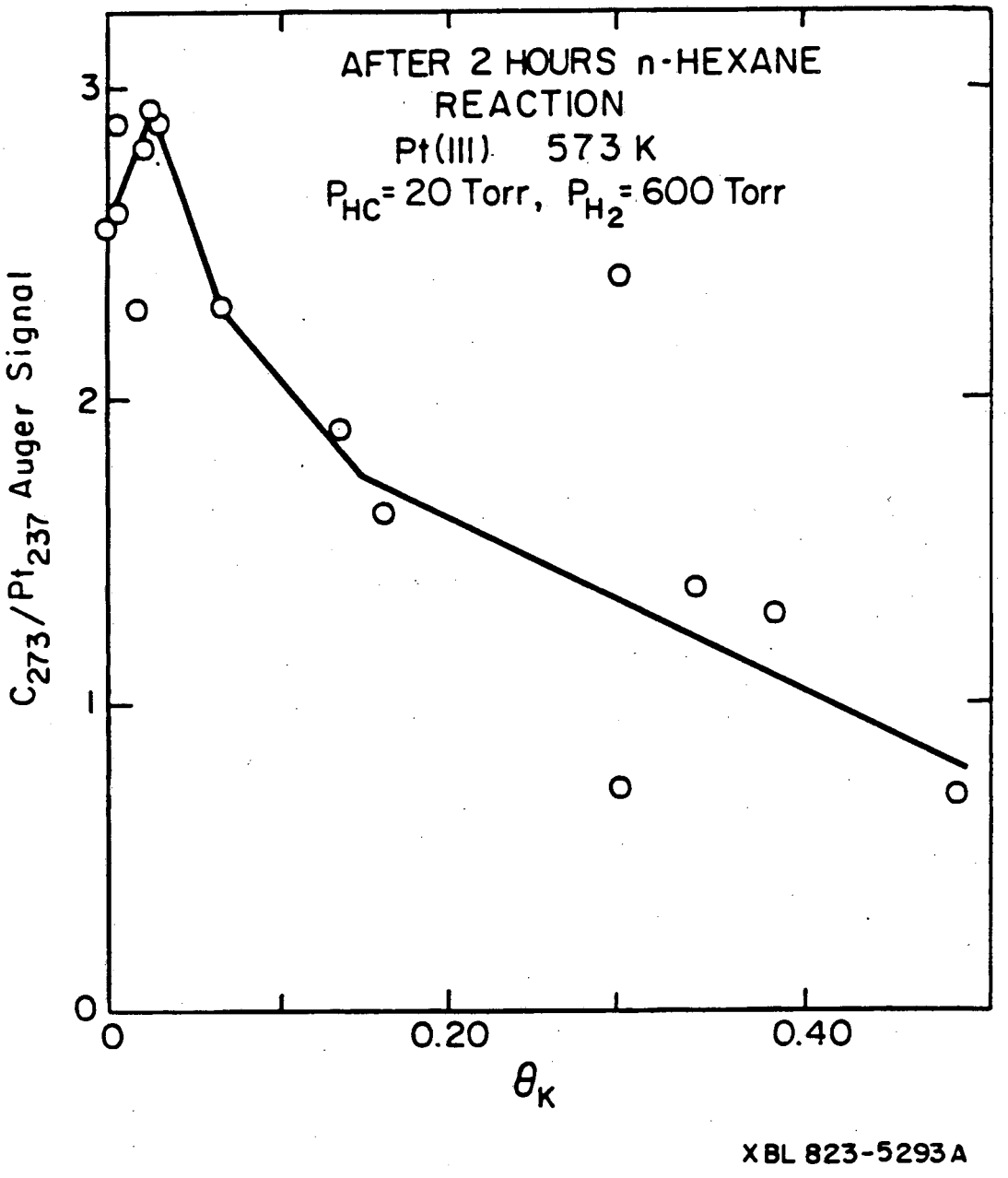
AFTER 2 HOURS n-HEXANE
REACTION
Pt(111) 573 K
P_{HC}= 20 Torr, P_{H_2}= 600 Torr
C_{273}/Pt_{237} Auger Signal
3
2
1
0
0
0.20
0.40
θ_K
XBL 823-5293A

fig. 5.12

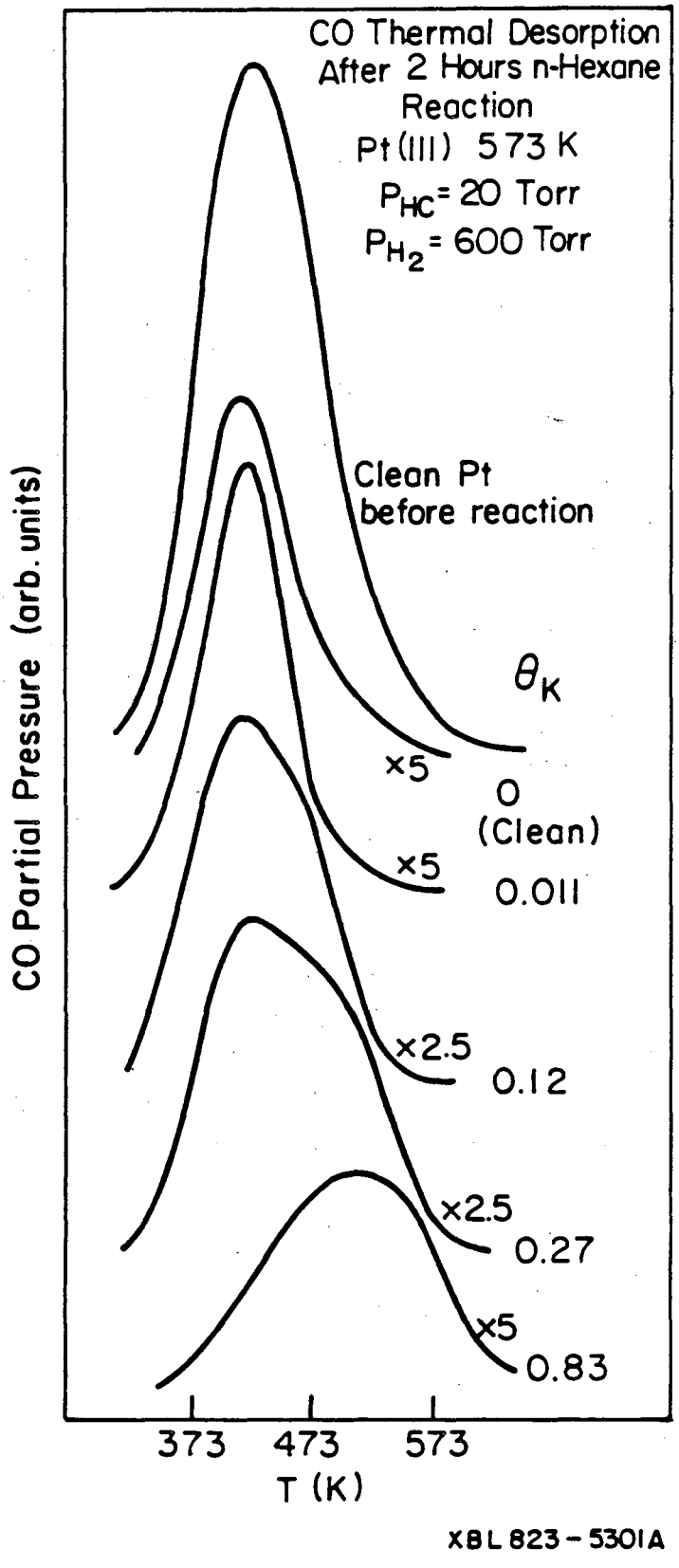
CO Thermal Desorption
After 2 Hours n-Hexane
Reaction
Pt(111) 573 K
P_{HC} = 20 Torr
P_{H_2} = 600 Torr
Clean Pt
before reaction
θ_K
×5
0
(Clean)
×5
0.011
×2.5
0.12
×2.5
0.27
×5
0.83
CO Partial Pressure (arb. units)
373
473
573
T (K)
XBL 823-5301A

fig. 5.13

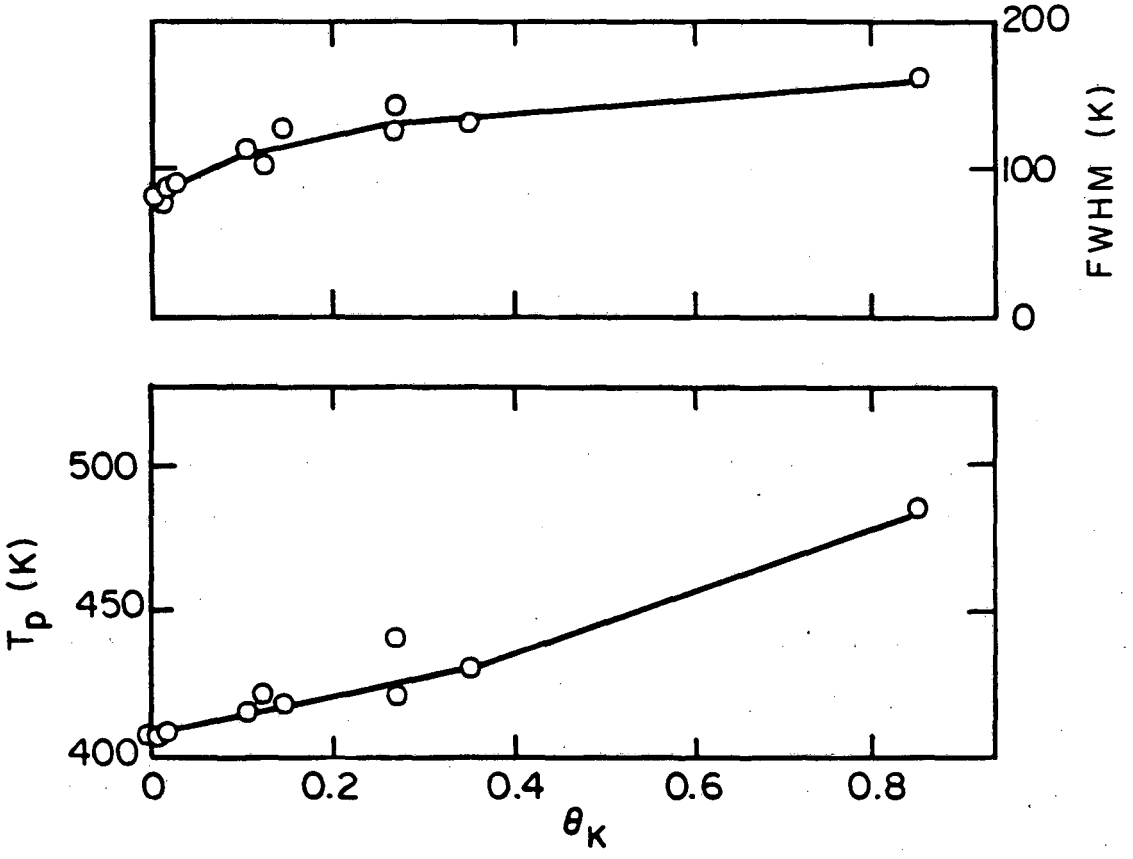

XBL 846-7064

fig. 5.14

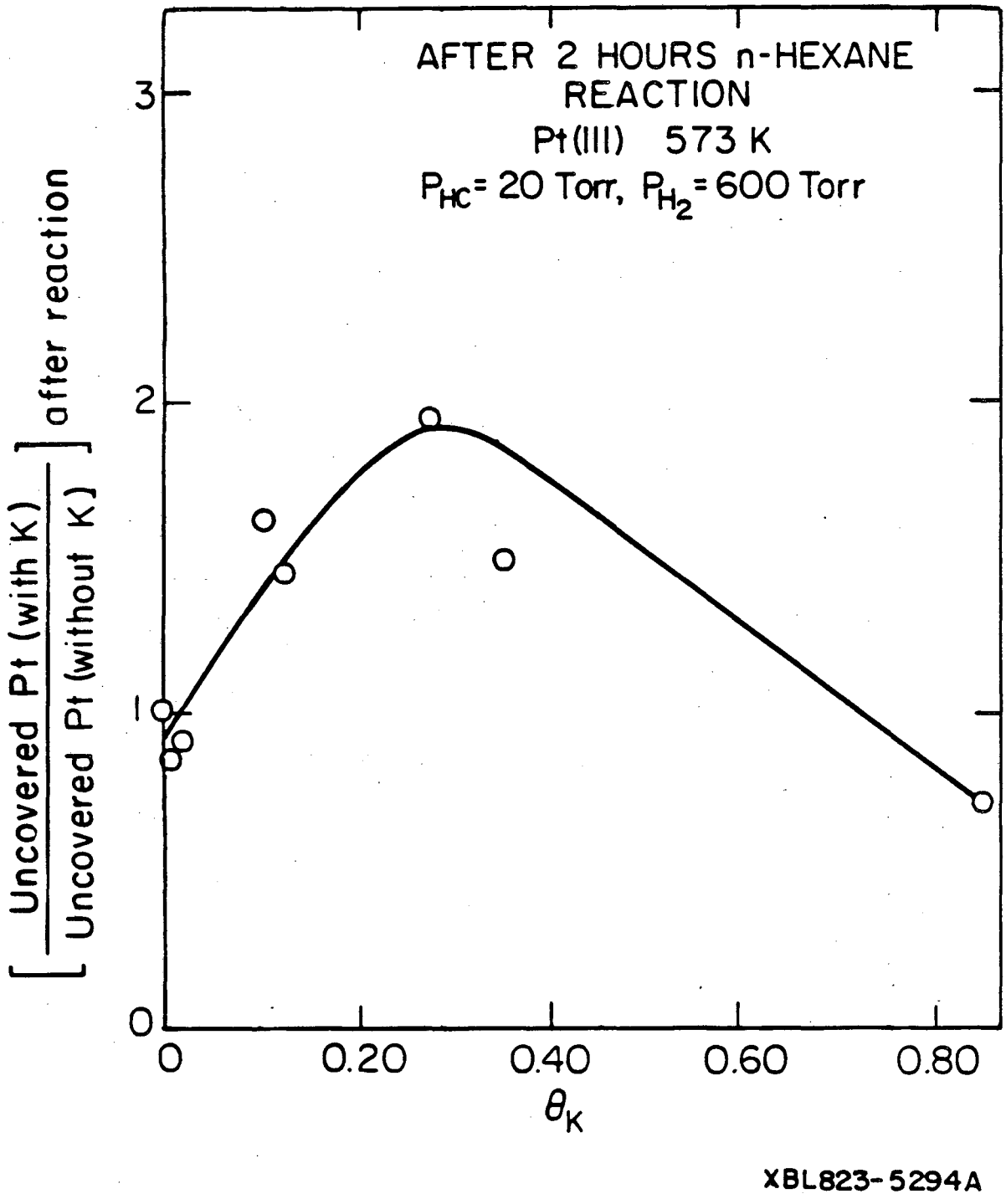
AFTER 2 HOURS n-HEXANE
REACTION
Pt(111) 573 K
P_{HC}= 20 Torr, P_{H_2}= 600 Torr
$\left[\frac{\text{Uncovered Pt (with K)}}{\text{Uncovered Pt (without K)}}\right]$ after reaction
0
1
2
3
0
0.20
0.40
0.60
0.80
θ_K
XBL823-5294A

fig. 5.15

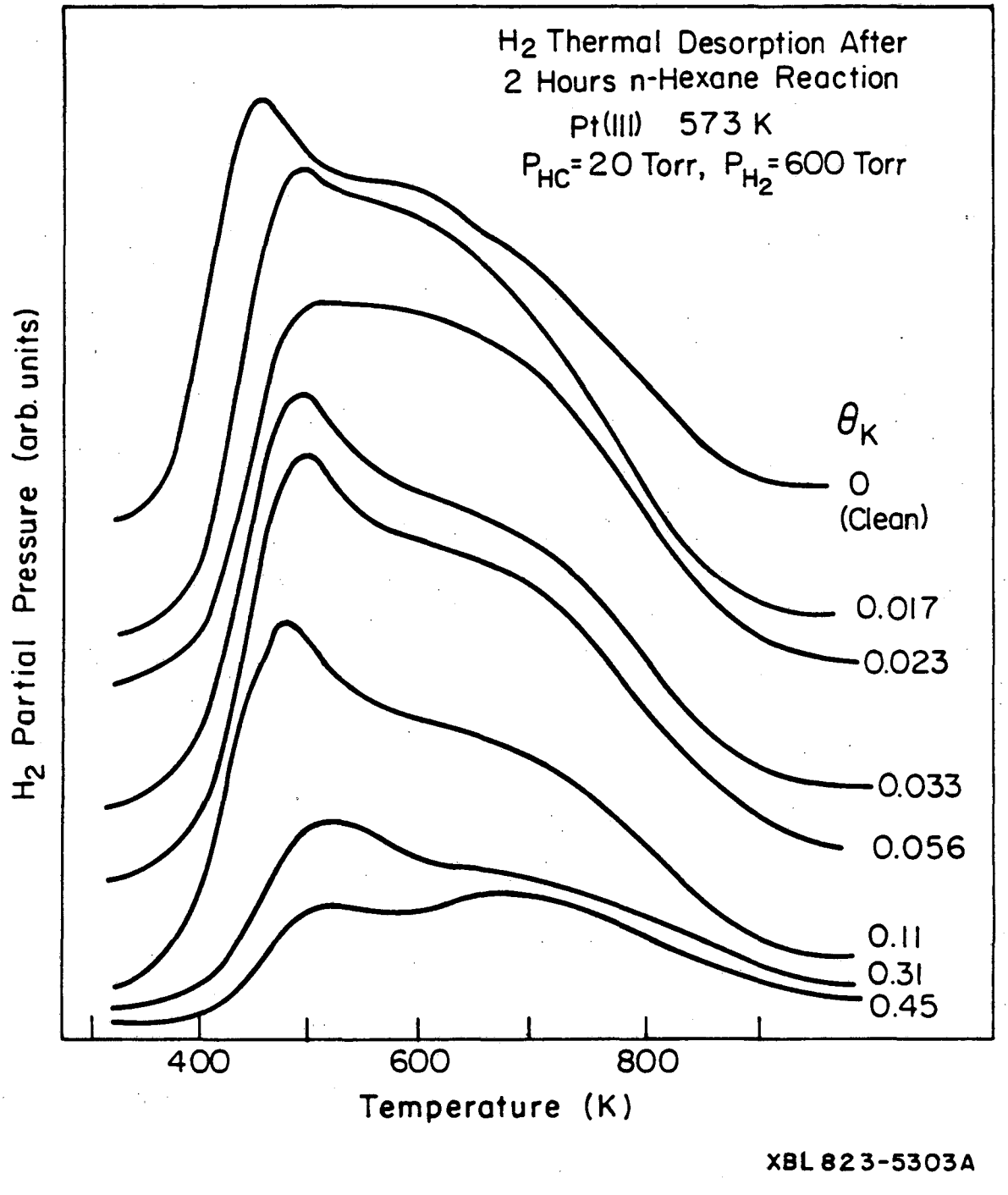
H2 Thermal Desorption After
2 Hours n-Hexane Reaction
Pt(111) 573 K
PHC = 20 Torr, PH2 = 600 Torr
θK
0
(Clean)
0.017
0.023
0.033
0.056
0.11
0.31
0.45
H2 Partial Pressure (arb. units)
400
600
800
Temperature (K)
XBL 823-5303A

fig. 5.16

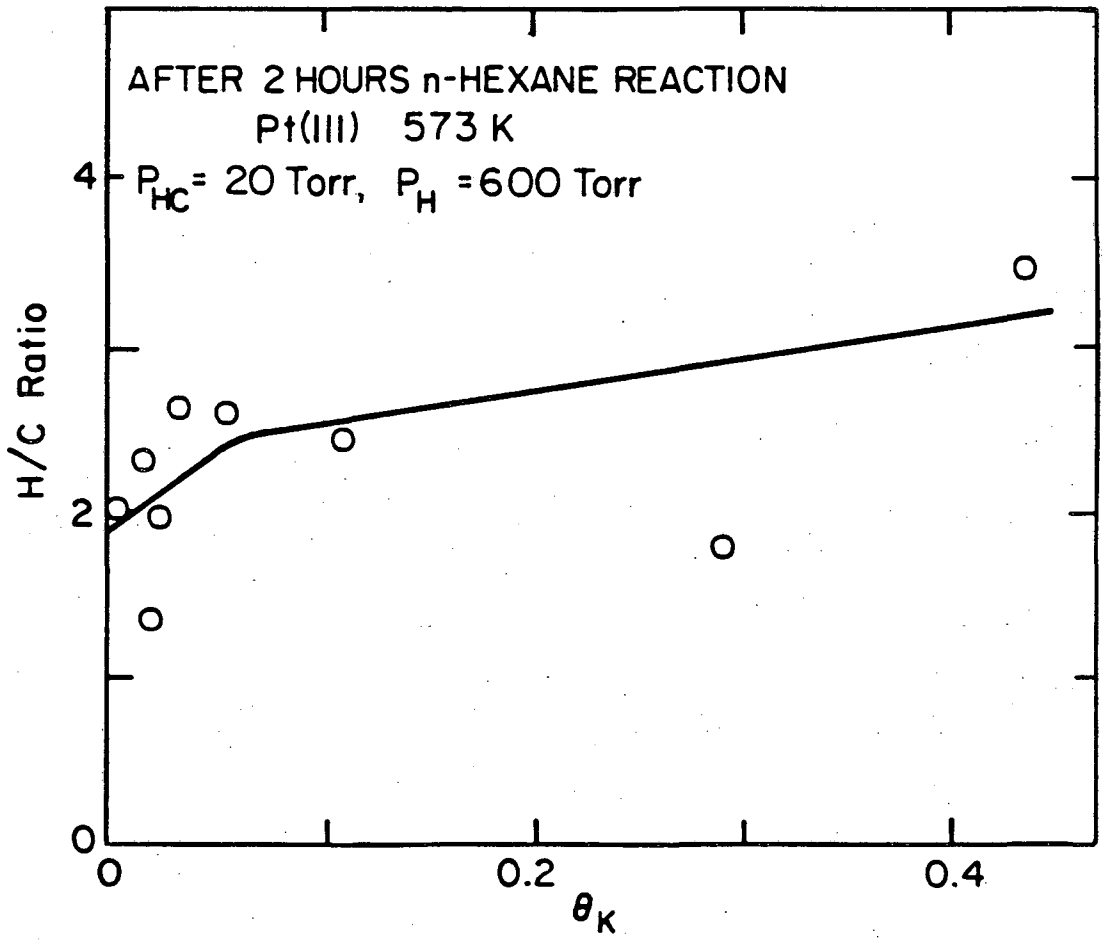

XBL846-7065

fig. 5.17

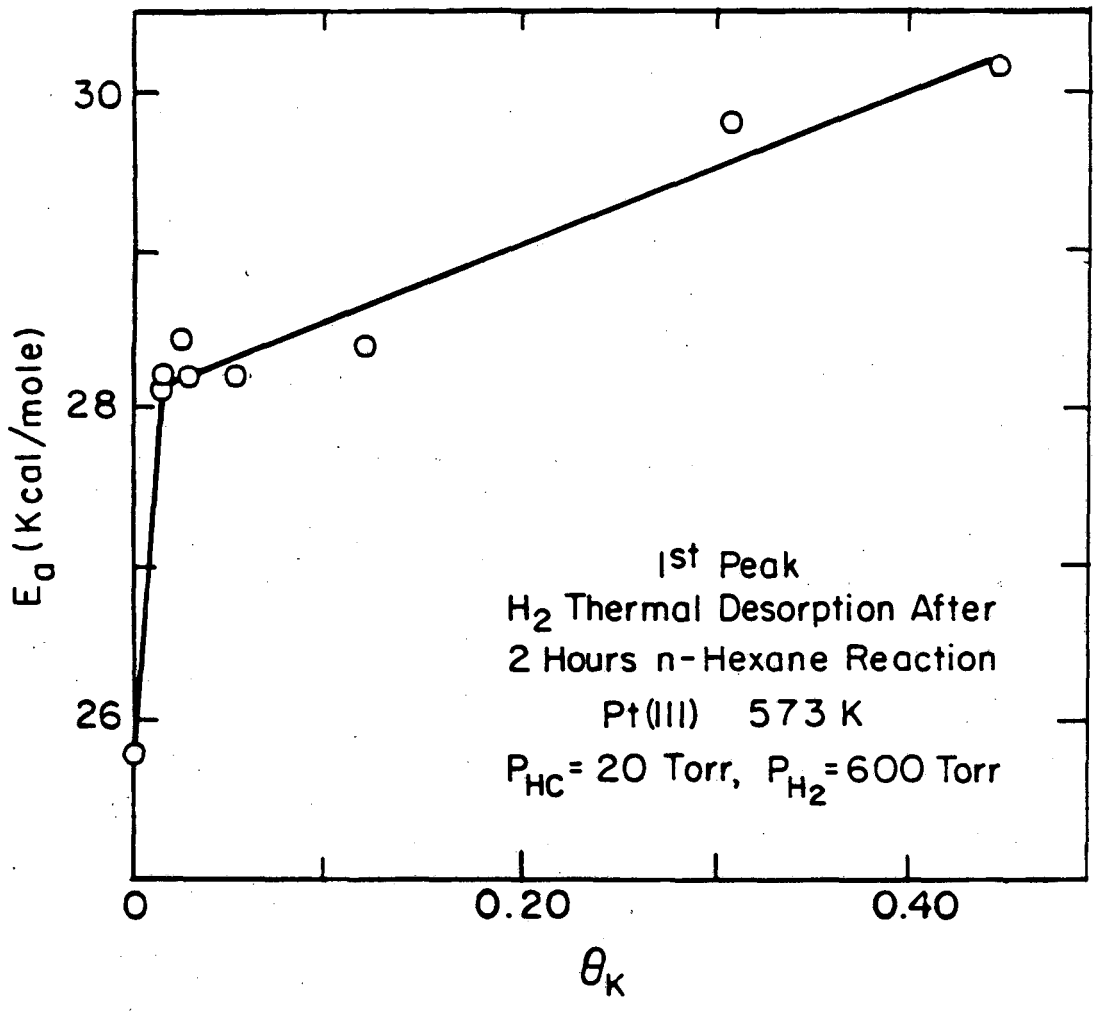

XBL 823-5304 A

fig. 5.18

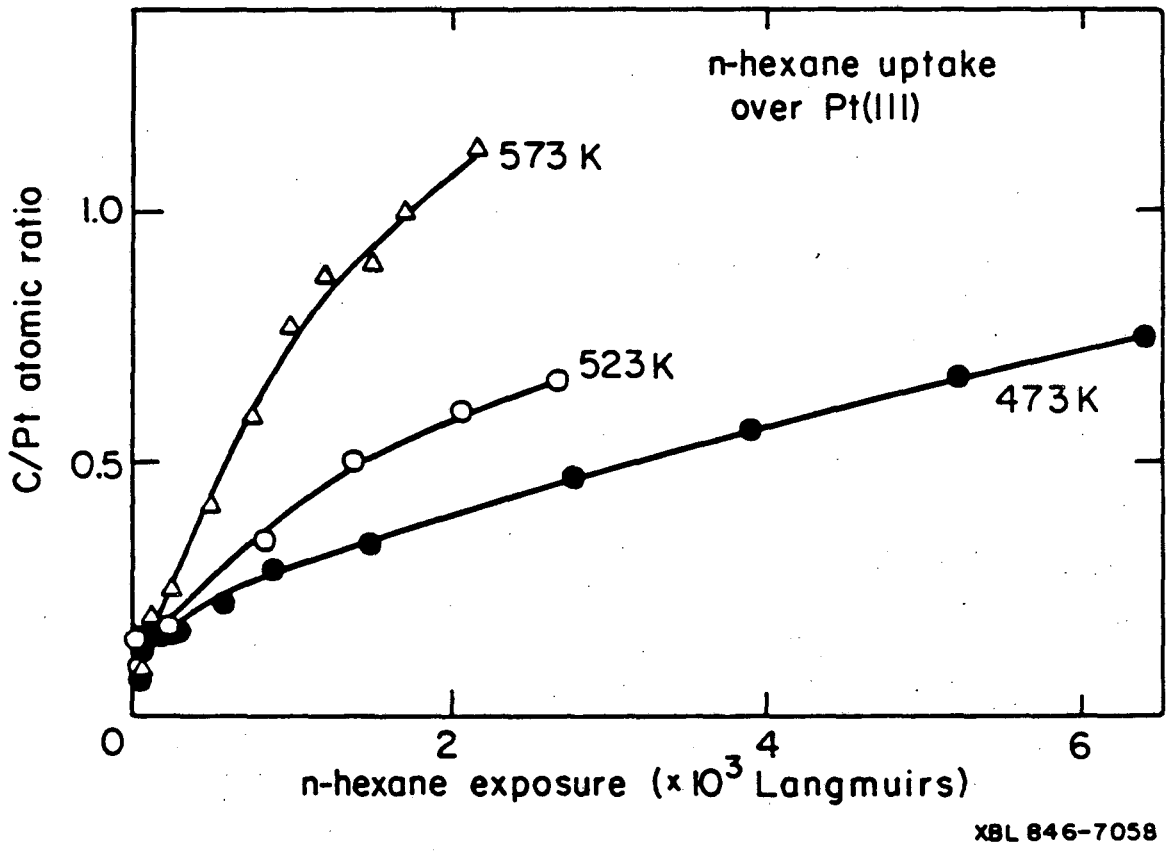
n-hexane uptake
over Pt(111)
573 K
523K
473K
C/Pt atomic ratio
1.0
0.5
0
2
4
6
n-hexane exposure (x 10³ Langmuirs)
XBL 846-7058

fig. 5.19

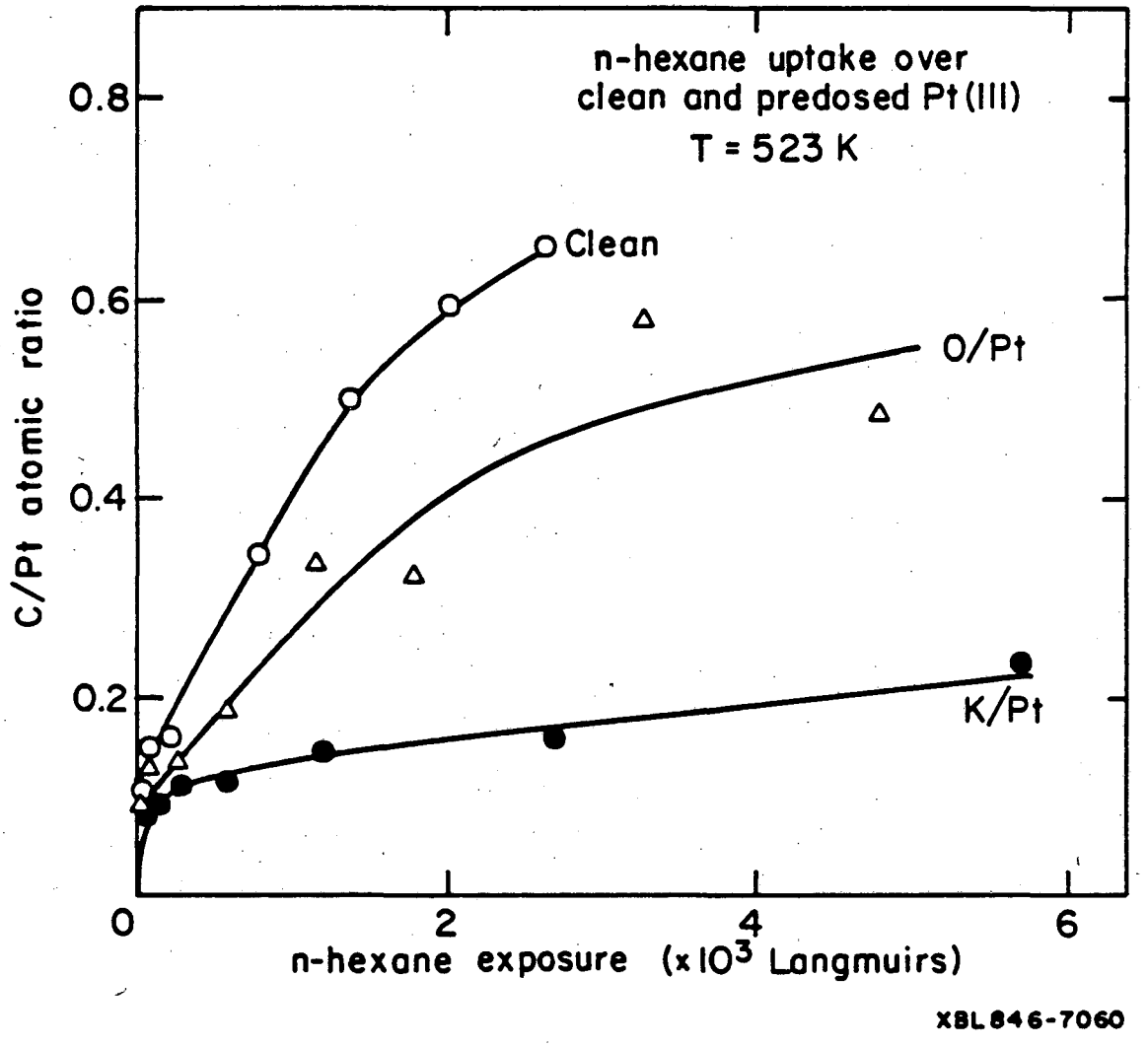
n-hexane uptake over
clean and predosed Pt(111)
T = 523 K
Clean
O/Pt
K/Pt
C/Pt atomic ratio
0.8
0.6
0.4
0.2
0
2
4
6
n-hexane exposure (x10³ Langmuirs)
XBL846-7060

fig. 5.20

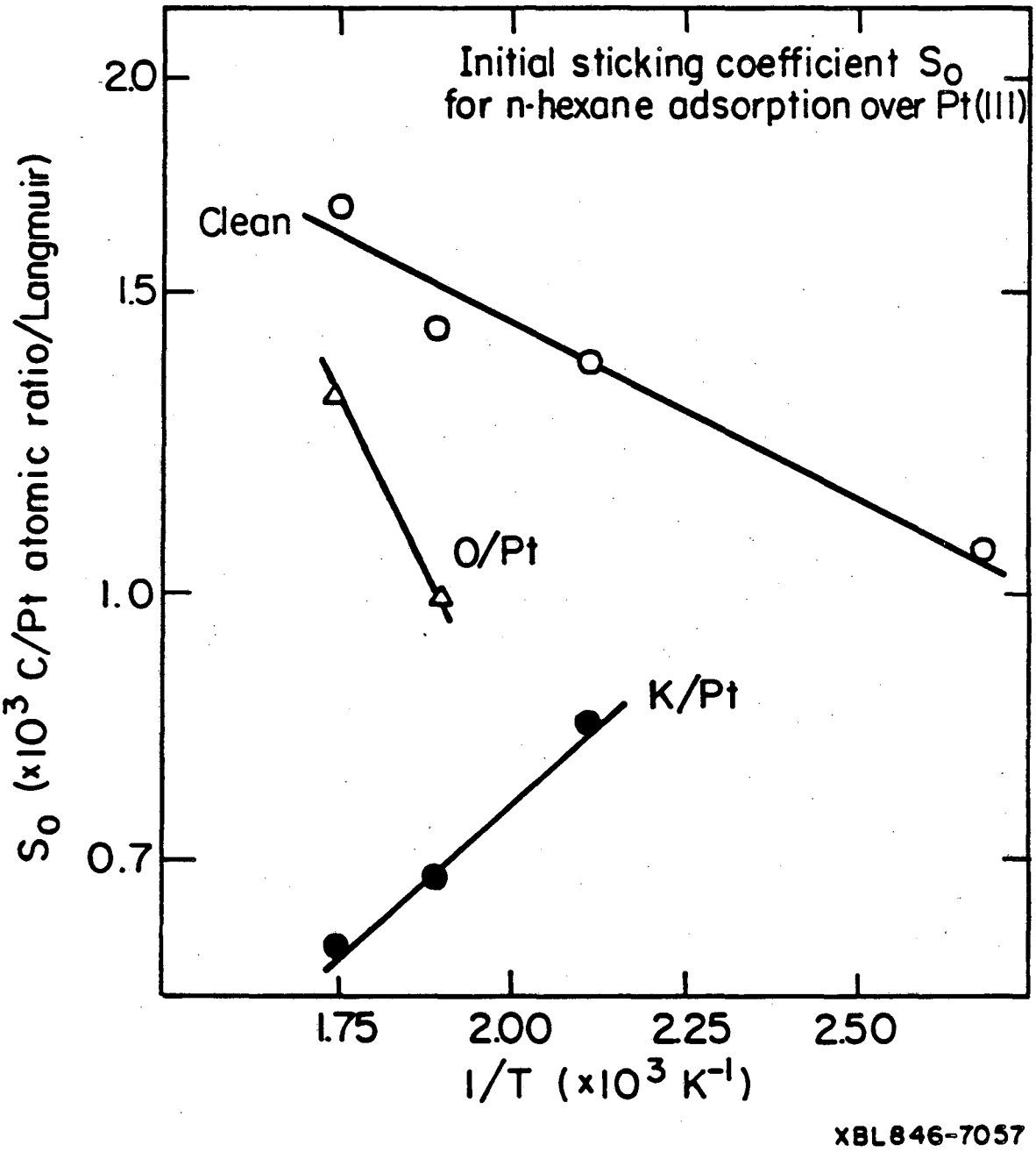
Initial sticking coefficient S_0
for n-hexane adsorption over Pt(111)
Clean
O/Pt
K/Pt
2.0
1.5
1.0
0.7
S_0 ($\times 10^3$ C/Pt atomic ratio/Langmuir)
1.75
2.00
2.25
2.50
1/T ($\times 10^3$ K^{-1})
XBL846-7057

fig. 5.21

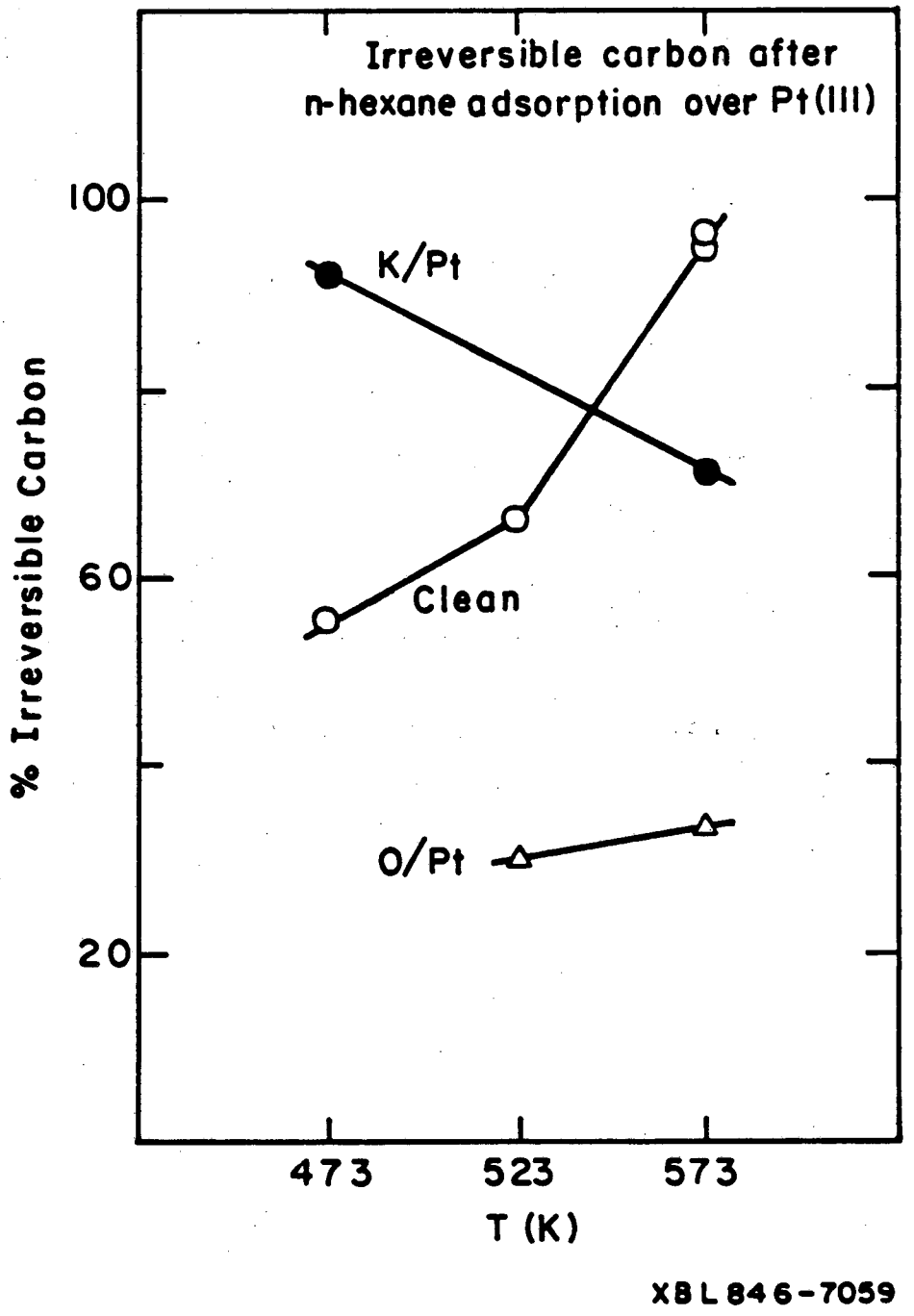
Irreversible carbon after
n-hexane adsorption over Pt(111)
100
60
20
% Irreversible Carbon
K/Pt
Clean
O/Pt
473
523
573
T (K)
XBL846-7059

fig. 5.22

5.2. Rhenium as a second metal in reforming.

5.2.1. Introduction.

Since platinum on alumina was introduced as a catalyst for reforming in 1949 [23], no major changes in the process have occurred until the discovery that a significant improvement in catalyst performance could be achieved by mixing platinum with a second metal. A bimetallic platinum-rhenium reforming catalyst was first introduced in 1968 by Chevron [24], and since then it has become the most used catalyst by the oil industry nowdays. Other alloys have also been reported to be useful for this process, including Pt-Ir [25] and Pt-Sn [26].

The main effects that the second metal has on the performance of reforming catalysts are to reduce the rate of poisoning due to coke formation and to improve the selectivity towards skeletal rearrangement rather than cracking to form gas products [27]. The reasons why this happens, however, are far from clear. Extensive work has been done on these catalysts since their discovery (see refs. 27-31 for the Pt-Re system), but very fundamental questions still remain unanswered:

- What exactly is the role of the second metal?
- What are the oxidation states of the metals?
- How important is the interaction between the second metal and the support for the catalyst performance?
- Are the metals alloyed?
- Is sulfur an important component in the catalyst?

In the present chapter some preliminary work done in order to isolate and try to answer some of these questions is described. In sec-

tion 5.2.2 the chemisorption of small molecules over rhenium films is explored to obtain and obtain some information concerning rhenium reactivity. The following section directly addresses the question of the oxidation state of rhenium under catalytic conditions. Finally, in section 5.2.4 some reactions were performed on platinum and rhenium based systems in an attempt to isolate the contribution of each individual component to the industrial catalyst.

5.2.2. Chemisorption of small molecules over rhenium films.

The chemisorptive properties of rhenium have been studied under ultra-high vacuum conditions by several autors. O_2, CO, NO, H_2O, H_2, C_2H_4 and C_2H_2 adsorption over Re (0001) single crystal surfaces have been characterized using different techniques [32-34]. Results on stepped surfaces [35-37] and foils [38-40] have also been reported. In the present section we investigate the chemisorption of small molecules over crystalline rhenium films grown on Pt (111) single crystals. The results are similar to those reported for Re (0001). Oxygen chemisorbs dissociatevily at low temperatures, forming a (2x2) or (2x1) overlayer, and does not desorb up to 1000 K. CO adsorbs molecularly and also orders on the surface, but between 5 and 10 % dissociates above 700 K (the rest desorbing at lower temperatures). the dissociated carbon and oxygen then recombine and desorb at around 800 K. The adsorption of CO can be modified by preadsorption of dissociated CO or O_2. Deuterium desorbs in three main temperature regimes, starting as low as 150 K. Ethylene partially decomposes, leaving carbon on the surfaces.

The Clean Surface. Rhenium was deposited on a Pt (111) single crystal substrate by evaporation from a Re filament, as mentioned in the experimental section. Other methods of deposition were tried, including the use of a planar magnetron sputtering gun and the decomposition of dirhenium decacarbonyl deposited under UHV, but these metals were not as reliable as the evaporation technique (for details see section 2.3.3). The films grow in a layer by layer mode, as indicated by distinctive breaks in the plots of Auger signal intensities versus time of deposition (fig.2.21). Thick enough films were grown, so that no platinum peaks were detected by AES. This corresponded to at a least 10 Å thick layer (about 3 layers), but much thicker layers were generally deposited to avoid possible changes in the surface properties due to the presence of the platinum underneath. The resulting surface, after cleaning and annealing to 1000 K, displayed a hexagonal LEED pattern characteristic of the rhenium basal plane, indicating epitaxial growth of the film. Since the interatomic distances for both metals are similar, the dimensions of the LEED pattern did not change while covering the platinum surface with rhenium (The atomic radii are 1.39 Å for Pt and 1.37 Å for Re). The films were stable upon heating up to about 1100 K, but at higher temperatures Re diffused into the Pt crystal bulk.

Auger peak ratios. An attempt was made to use Auger spectroscopy for quantitative measurements of coverages of various adsorbates. As mentioned earlier, a retarding field analyzer was used and the second derivative of the collected current was recorded. The primary electron beam had an energy of 1700 eV and the incident angle was 60^{o} from the surface normal.

The spectra for clean Pt and Re, recorded with these settings, are shown in fig. 5.23. Due to the low resolution, the 161 and 167 eV Re peaks are unresolved, and only one peak at 168 eV is obtained [41]. Other Re peaks are at 178, 217 and 227 eV. The intensity of the peaks, measured as the peak to peak heights, were compared to the Pt ones before the Re deposition. The signal ratio obtained was Re(217eV)/Pt(237eV)=0.46 (fig. 5.23). From this calibration, the relative cross sections for carbon and rhenium can be estimated. These values are available for platinum since the ^{14}C radiotracer technique was recently used in our laboratory to obtain the signal ratio C(273eV)/Pt(237eV)= 1.61 (±15%) [10].

Finally, a value for the relative cross section of oxygen was estimated in different ways, all based on the carbon to oxygen ratio. Auger spectra of CO saturated rhenium and platinum surfaces were recorded. Also, during the rhenium cleaning process, AES before and after high temperature flashing provided the difference value for the C and O signals, due to desorbing carbon monoxide from recombination. The average over many of these measurements gave a value for the ratio of C(273eV)/O(515eV)=1.60. A list of cross sections obtained for the different Auger peaks, referred to Re(168eV), is presented in table 5.5. These numbers are only reliable to whithin 20-30%. They will be used later to estimate absolute coverages.

Oxygen adsorption. Oxygen adsorbs at temperatures as low as 150 K. Once adsorbed, no desorption was observed up to 1100 K. An apparent (2x2) LEED pattern was observed at all temperatures above 150 K, and it

becomes sharper with increasing exposure of the surface to the electron beam. The O(515eV)/Re(217eV) Auger ratio was 1.2, suggesting a saturation coverage value between one half and one. As a result of this high coverage, the LEED pattern could be reinterpreted as due to the superposition of three (2x1) domains, as has been proposed previously [34]. This interpretation yields a saturation coverage of 0.5, to be compared with the literature value θ_{sat}=0.4 [42].

There is evidence suggesting that oxygen dissociates upon adsorption on rhenium. X-ray (XPS) and ultraviolet (UPS) photoelectron spectroscopy [34,39,43] clearly indicate the presence of atomic oxygen on the surface. We have used XPS to corroborate the previously reported results (next section). Beside an oxygen 1s peak characteristic of atomic oxygen, we have also observed a shift in the Re 4f peaks of about a volt towards higher binding energies when exposed to high pressures of oxygen. This shift is assigned to an oxidation state below Re^{+4}. In any case, this chemisorbed layer is very stable not only towards heating in vacuum, but also when exposed to high pressures of hydrogen. The oxygen covered surface remains unaltered even after a 1 atm H_2 treatment for several minutes, while heating up to 700 K. Finally, further chemisorption of other molecules on the oxygen saturated rhenium surface was almost totally inhibited.

CO adsorption. Carbon monoxide adsorption was studied using LEED, AES and TDS. The thermal desorption of CO from the rhenium film is very similar to the one reported in the literature for Re (0001) [34,35, 37,44] (fig 5.24a). Two α states are seen at low temperatures, with

maxima at 335 and 415 K, and one β state at high temperature, with maximum at 810 K. Desorption maxima of these peaks correspond to activation energies of 19, 24 and 44 Kcal/mole respectively, as calculated using Redhead equations (assuming first order desorption for the α states, $\nu_1=10^{13}$ s^{-1}, and second order for the β state, $\nu_2=10^{-2}$ cm^2/s, and $\theta_o=10^{14}$ molec/cm^2). The β state peak at temperatures identical to where carbon and oxygen recombine during the cleaning process, and it is believed to correspond to desorption of dissociated carbon monoxide. Since the heating rate in these experiments was 30 K/sec, the α states could not be well resolved. However, changes in thermal desorption peak shape could be brought about in several ways. The spectrum shown in fig. 5.24a was obtained after exposing the surface to 30 L CO. Much higher doses (more than 1000 L) increased the relative amount of CO in the low temperature desorption peak (335 K). Also, if the surface was saturated with CO, flashed up to about 700 K, and then cooled and resaturated with CO, a spectrum like that shown in fig. 5.24b was obtained. Finally, if the experiment was performed on a surface exposed to oxygen (half saturation coverage) prior to before the CO exposure, a TDS like the one in fig. 5.24c was seen. In this later case a little CO_2 was also detected as a desortion product (fig. 5.24d).

A diffuse LEED pattern was obtained when CO the surface was saturated with CO at low temperatures (<150K). This pattern, represented schematically in fig. 5.25, is similar to the ones reported for Re(0001) [44], and Ru(001) [45]. It is unstable, and dissapears after prolonged exposure to the electron beam. When the surface is heated to 700 K, the CO from the α state desorbs, leaving only dissociated

carbon monoxide on the surface [46]. At this stage, an apparent (2x2) LEED structure is present, similar to the one reported for oxygen adsorption. Further adsorption of CO on this surface yields a combination of both patterns.

The CO saturation coverage is not well known. The LEED structure mentioned previously has been assigned to either $(5\sqrt{3}x5\sqrt{3})R30^{o}$ (θ_{sat}=0.65) or three domains of ($\sqrt{3}x4$) (θ_{sat}=0.75). Other studies report coverages between 0.45 and 0.5 [35,44]. Our Auger measurements using a defocussed beam to avoid electron stimulated desorption, gave ratios of C(273eV)/Re(217eV)=0.4 and O(515eV)/Re(217eV)=0.25, corresponding to a saturation coverage of about 0.3. Further work is needed to obtain a more reliable value for this quantity.

Deuterium adsorption. Deuterium adsorbs onto rhenium at temperatures below 150 K. The thermal desorption of D_2 after saturation is shown in fig. 5.26. The peak at 335 K corresponds to a previously reported state observed after H_2 adsorption over Re(0001) at room temperature [37]. There is also a shoulder in the high temperature side of the main peak that was also seen in previous work. Finally, a third low temperature state starts to populate below the lowest temperatures we can obtain with our present experimental conditions. The corresponding activation energies for the second order desorption processes are <14, 19 and 20 Kcal/mole ($\nu=10^{-2}$ cm^2/s, $\theta_o=1.5x10^{15}$ $molec/cm^2$).

Ethylene adsorption. After low temperature saturation of the rhenium surface with ethylene, sometimes a $(\sqrt{3}x\sqrt{3})R30^{o}$ LEED pattern

would appear. However, this result was not reproducible, and most often no ordered structure would form. Thermal desorption after saturation exhibit partial decomposition of the ethylene. Hydrogen (m/e=2) and ethylene (m/e=27) desorption were followed, and the spectra are shown in fig. 5.27. Some intact ethylene desorbs giving a peak with maximum at 250 K (Ea<14 Kcal/mole), while the rest decomposes, giving hydrogen peaks at 357, 460 and 650 K (Ea= 21, 27 and 38 Kcal/mole respectively, assuming 1^{st} order desorption). The high temperature region of the H_2 TDS resembles spectra reported earlier on Re(0001) [33,39], but due to the lower adsorption temperatures used in our work, desorption of molecular ethylene could be detected, and an additional low temperature peak is present in the H_2 TDS. The results reported by Ducros et. al., on the other hand, were performed at room temperature, and some hydrogen evolution was detected during adsorption.

The saturation coverage was estimated using AES. A ratio C(273eV)/Re(217eV)=0.5 implies a saturation coverage value of about 0.2, instead of θ_{sat}=0.13, as reported by the French workers [33].

5.2.3. Oxidation state of rhenium.

The final oxidation state of rhenium in the industrial platinum-rhenium catalyst has been a matter of great controversy in the literature. While Johnson and LeRoy claim that rhenium is present as Re^{+4} in the final catalyst [47]. Webb reports the presence of rhenium in a metallic form [48].

During catalyst preparation, it is clear that rhenium is pre-

sent as an oxide (Re_2O_7) after co-impregnation of the support with the platinum and rhenium salts and subsequent calcination [49]. Although this oxide is volatile, it seems that the interaction with the alumina support prevents it from disappearing from the catalyst [49,50]. The major problem is in determining the final state after reduction. Re_2O_7 is easy to reduce at 575-625 K [51,52], but lower oxidation states of rhenium are more stable, and difficult to convert into metallic form when water is present [53,54]. However, platinum is known to catalyze the reduction by hydrogen of a number of metal oxides, including rhenium [55]. The calcination temperature is a crucial parameter in the subsequent response of the oxide to reduction [56].

One problem with most studies related to this research topic is that the techniques used for oxidation state determinations are based on titrations, chemisorption or reactivity experiments, and the results are therefore not reliable [57-59]. Few experiments have been performed using more direct tools like x-ray adsorption [60] and XPS [61], but no final conclusions were reached. In the present section the oxidation and reduction of rhenium deposited over or alloyed with platinum have been studied using XPS. The Re 4f electron binding energies are compared to those of reference rhenium oxide compounds. We found that rhenium can be easily oxidized to +4 and +7 oxidation states in an oxygen atmosphere, but it can be equally easily reduced, mostly to the metallic form, once treated under high pressures of hydrogen.

XPS of rhenium oxides. XPS were obtained for ReO_2, ReO_3 and Re_2O_7, they are displayed in figs. 5.28 to 5.30. The regions around

the Re 4f and O 1s electrons were studied in more detail. Several oxidation states were present on the surface of most of the samples. ReO_2 is mostly in the Re^{+4} state, but a little ReO_3 is present on its surface. The peaks in the 40-50 eV region are assigned to the $4f_{7/2}$ (binding energy, BE, of 42.6 eV) and $4f_{5/2}$ (BE=45.1 eV; the separation between them being 2.5 eV, close to the value reported in the literature [62]. The spectrum for ReO_3 shows three peaks at 42.4, 45.1 and 47.4 eV. The presence of a peak at 42.4 eV indicates the existance of some Re^{+4} on the surface, which also contributes to the intensity of the 45.1 eV peak. Re^{+6} is the responsible for both the 47.4 eV shoulder ($4f_{5/2}$ electrons) and a peak around 44.9 eV (estimated using the 2.5 eV splitting for $4f_{5/2}$-$4f_{7/2}$) that overlaps with the signal from the +4 oxidation state. Finally, in the case of Re_2O_7, Re^{+7} is indicated by peaks at 49.5 and 46.9 eV. The presence of some Re^{+6} can be inferred from a third peak at 44.1 eV. Most of these mixtures of oxides on the surface have been observed previously [63,64]. The binding energies obtained for all these compounds are summarized in table 5.6 and fig. 5.31.

The O 1s spectra are more complicated to interpret. Although the absolute values for the binding energy of these peaks seems to shift for the different compounds studied, the difference between the O is and the Re $4p_{1/2}$ maxima remains almost constant (table 5.6). Since the $4p_{1/2}$ peak of rhenium is not expected to shift appreciably with oxidation state, the values for O 1s binding energies obtained could have been affected by charging or reproducibility problems in the spectrometer. However, there are at least two oxygen peaks convoluted in the spectra for both ReO_2 and ReO_3, with a separation between them of

about 1 eV. The peak at lower binding energy could be associated with ReO_2, while the other would be originated by oxygen atoms bonded to either Re^{+6} or Re^{+7}. Using that assigment, the presence of some ReO_2 can be seen in the ReO_3 spectrum, and little ReO_3 is observed in the ReO_2 spectrum as well, consistent with the results from the Re 4f spectra. Rough estimations of the contributions of each oxide to the total spectrum have been made by deconvolution of the different peaks (table 5.7). The different values obtained in the calculations from the Re 4f spectra and those from the O 1s data can be explained in terms of the penetration depth of the electrons, because the contaminant oxides are only present on the surface.

An attempt was also made to obtain relative cross sections for the O 1s and Re $4p_{1/2}$ transitions, and the former was found to be about twice the later. The values obtained are summarized in table 5.7.

Oxidation and reduction of rhenium in the presence of platinum. Rhenium films were obtained by deposition from a Re filament onto a platinum foil, as described in detail in the experimental section. Changes in these films when exposed to an atmosphere of either oxygen or hydrogen were followed using XPS. Spectra for the Pt and Re 4f electrons at different stages of the treatment are shown in fig 5.32. The rhenium film was first exposed to 1 atm O_2 and heated to various temperatures. Some oxygen chemisorption can be seen immediatly after room temperature exposure, consistent with results reported in the previous section. No further changes are then observed until the sample temperature is raised

to about 475 K, when new features due to Re^{+6} become visible in the spectrum. Still higher temperatures increases the formation of oxidized species, until Re_2O_7 formes and evaporates at 600 K. The Re^{+7} oxide formation is then responsible for the decrease in rhenium signal observed in fig. 5.32 d and e. This loss requires sufficiently high temperatures and the presence of an oxidizing atmosphere. Treatment at similar temperatures under a H_2 environment do not causes further loss of rhenium from the surface (fig. 5.32 f). A more detailed study of the rhenium oxidation states was done by carefully looking at the Re 4f signal (fig. 5.33). Already at 475 K, the presence of some features at around 47 eV binding energy in the spectrum indicate the formation of ReO_3. At higher temperatures additional peaks grow, including signals at around one eV higher binding energies as compared to the metallic Re, due to an oxidation state below +4. Above 600 K a small signal at around 50 eV indicates the presence some Re_2O_7, which is responsible for the loss of rhenium. When the oxidized sample is treated with 1 atm H_2 at 575 K, most of the surface oxides disappear, indicating almost complete reduction to the metallic form. However, the peaks which are shifted 1 eV from the metal signal persist, indicating that this low oxidation state (perhaps ReO) is stable towards further reduction. The oxygen XP spectra corroborates the conclusions obtained from the Re 4f signal (fig. 5.34).

The previous results were obtained from rhenium films grown on top of a platinum foil. Similar experiments were performed on a Pt-Re surface alloy, prepared by depositing rhenium over the platinum surface and annealing to about 900 K for few seconds. The formation of the alloy

becomes evident by the change in the relative Pt and Re signals, as measured by both XPS and AES. XPS of the 4f region of both metals indicates no significant changes in binding energy: the Pt $4f_{7/2}$ maxima was at 71.1 eV (Pt $4f_{7/2}$ BE for the metal is 71.0 ev), and the Re $4f_{7/2}$ was at 40.0 eV, the same value obtained for the Re film. These results are in contradiction with those reported by Alnot et. al. [65], where shifts of 0.9 and 0.4 eV were reported for Pt and Re respectively.

When the alloy was heated in oxygen at 575 K all the rhenium present was oxidized, and predominantly formed ReO_2 and ReO_3. The changes in the Re 4f XPS signal are shown in fig. 5.35. The spectrum after oxidition resembles that obtained for the ReO_2 sample. Complete reduction was obtained after exposing the oxidized alloy to an hydrogen atmosphere (700 Torr H_2 at 575 K). In this case the low oxidation state, if formed, was also converted to the zero valence state.

The data reported here agrees well with results reported previously by other research groups. Rhenium oxidizes easily under an oxygen atmosphere, and even more easily when alloyed with platinum. There is little doubt that Re is highly oxidized in the reforming catalyst after calcination [49]. Reduction of the higher oxidation states occurs easily under mild conditions [51,52,55], but oxidation states below +4 are harder to convert to the metallic form [47,48,53,54]. Also, platinum is known to catalyze the reduction of such oxides [55]. In our case full reduction was only achived for the alloy, in which platinum was in intimate contact with the rhenium. For the rhenium film, the reduction was almost complete, except for the ReO that appeared to re-

main. Therefore, if the support has no effect on these reactions, it must be concluded that the final oxidation state of rhenium in reforming catalysts depend on the degree of mixing with the platinum. The formation and high volatility of Re_2O_7 during calcination suggest the possibility of mixing of both metals in the final catalyst, in which case they would be metallic after reduction. This simple interpretation does not, however, take into consideration the effect of the presence of water during the treatment [47,48,56,59], the support [47,56], and sulfur added before the oil feedstock is introduced [66]. More model studies are required to unequivocaly establish the importance of each of these factors.

5.2.4. Reactions over rhenium and platinum-rhenium systems.

Although most of the research concerning the bimetallic catalyst has been concentrated in its characterization, few catalytic studies have been reported in the literature [57,59-70]. The major improvement in the performance as compared to the original platforming system has been in the increased lifetime without significant self-poisoning from coke formation [24]. A historic review has been published by Ciapetta and Wallace [71] regarding the incorporation of the new process into the industrial plants and the modifications made afterwards in order to further improve the overall results. In this section we report studies done over model catalysts with hydrocarbon compounds in order to detect changes in selectivities and/or activities.

It was found that ethane-deuterium exchange reactions have comparable rates over platinum and rhenium surfaces. Hydrogenolysis, in contrast, is several orders of magnitude faster on rhenium as com-

pared to platinum. Similarly, the selectivity for n-hexane conversion changes drastically when going from platinum to rhenium, and methane production, an undesirable side reaction, becomes predominant on Re catalysts. The changes occur gradually as the amount of rhenium on the surface increases. The addition of sulfur to either metal reduces all activity for n-hexane conversion, but especially decreases hydrogenolysis reaction rates, improving therefore the reforming selectivity.

Ethane deuterium exchange and hydrogenolysis. Preliminary work was done on the reaction of ethane with deuterium over rhenium films prepared as described before. A reaction mixture of 100 Torr C_2H_6 and 1000 Torr D_2 was used, and the reaction was studied at temperatures of 520 and 570 K. The kinetic parameters obtained for deuterium exchange and hydrogenolysis are summarized in table 5.8 and fig. 5.36, together with the corresponding data obtained for Pt (111) (section 3.3). Rhenium displayed rates for exchange comparable to platinum, but hydrogenolysis was 2-3 orders of magnitude faster over Re. The activation energy for deuterium exchange was about 12 Kcal/mole, 7 Kcal/mole lower than for Pt, but the preexponential factor was equally reduced so that the final turnover frequencies were only 2-4 times bigger for Re over the temperature range studied. This compensation effect has been observed previously for the same reaction over several other metals [72]. The deuterium distribution peaks at d_1 and d_6, as with platinum, suggesting the presence of two pathways in a competitive mechanism to account for such results.

Ethane hydrogenolysis (producing methane) was much faster over

Re than over Pt. Although hydrogenolysis and deuterium exchange activities were comparable in the Re case, the main product of hydrogenolysis was fully deuterated methane. Re has been reported to be about five orders of magnitude more effective for carbon-carbon bond breaking in ethane than Pt [73]. The same hydrogenolysis enhancement is observed for other hydrocarbons, such as n-hexane, presented below.

n-Hexane conversion. n-Hexane conversion over Re films and foils was briefly studied. Initial rates and rates after two hours of reaction for experiments under similar conditions to those conducted over platinum (chapter 4) are reported in table 5.9. The main product in all cases was methane, from multiple carbon-carbon bond breaking of the reactant. Little benzene formation and isomerization were also observed, but no dehydrocyclization to methylcyclopentane was detected. Similar results were reported by Clarke and Taylor [74] over rhenium films, although isomerization and aromatization selectivities changed after the films were sintered. Hydrogenolysis also accounted for more than 99% of the products in isobutane conversion, as measured by Kemball and co-workers [68]. Activities for platinum surfaces partially covered with rhenium had values in between those for clean Pt and clean Re surfaces. No maxima in reaction rates or selectivities were observed, as opposed to results reported in the literature [52,68].

Hydrogen thermal desorption and AES measurements were made after reactions in order to characterize the carbonaceous deposites formed (fig. 5.37). Larger amounts of carbon per metal atom were observed after reactions over Re as compared to Pt; atomic ratios up to 3 C/Re were

obtained (as opposed to 1.5 for Pt). This result tends to rule out the possibility that rhenium acts as an agent for reducing the formation of coke during the reforming process [75]. Also from fig. 5.37 it can be concluded that the carbonaceous deposits formed over Re are more dehydrogenated, and that the remaining hydrogen atoms are much more strongly bonded than in the case of Pt.

The effect of sulfur. Sulfur is believed to play a key role in the performance of the Pt-Re reforming catalyst [66,76,77]. A few experiments were performed using n-hexane over sulfur cevered Re (0001) single crystal surfaces. The conditions used were the same used for the foil, and sulfur coverages were in the range θ_S=0.2-0.5. The results are presented in table 5.9. The total activity dropped drastically with the addition of sulfur, but hydrogenolysis rates were still considerably higher than those for platinum. No isomerization or methylcyclopentane formation were detected within the limits of the experiments. One noticible difference from clean rhenium was the modification in hydrogenolysis product distribution, where methane production was suppresed by a factor several times higher than ethane formation. The dehydrogenation rate to form hexenes was also measured, giving values around 0.10 molec/Re atom·sec, much higher than all other reactions. Since no isomerization could be detected, no selectivity improvments can be claimed. In the case of Pt (111) addition of sulfur decreases the total activity of the catalyst, but this poisoning was accompanied by a decrease in hydrogenolysis selectivity (fig. 5.38) [7]. More work is under way in our laboratory to obtain more accurate results.

Table 5.5

Auger relative cross sections.

V_{pp} = 10 V, E_p = 1700 eV.

Peak	Relative cross section
Re (168eV)	1.00 (reference)
Re (217eV)	0.34±0.04
Pt (237eV)	0.7 ±0.2
C (273eV)	0.4 ±0.1
O (515eV)	0.25±0.07

Table 5.6

Binding energies, in eV, for O 1s and Re 4f electrons in several rhenium oxides.

Compound	O 1s - Re $4p_{1/2}$	Re $4f_{5/2}$	Re $4f_{7/2}$
Re (metal)	-	42.5	40.0
ReO_2	9.8	45.1	42.6
ReO_3	9.7	47.4	44.9
Re_2O_7	9.8	49.5	46.9

Table 5.7

Deconvolution of XPS spectra for rhenium oxides.

Peak	Compound	Signal contribution (%) ReO_2	ReO_3	Re_2O_7	λ^a
Re $4f_{7/2}$	ReO_2	83	17	-	20
	ReO_3	45	55	-	
	Re_2O_7	-	41	59	
O 1s	ReO_2	68	32	-	10
	ReO_3	53	47	-	

Relative cross sections.

Ratio[b]	Compound ReO_2	ReO_3	Re_2O_7
Signal areas	4.0	6.7	8.0
Atomic	2.0	3.0	3.5
Cross section	2.0	2.2	2.3

a) Penetration depth of the electrons at that kinetic energy, in Å.

b) all expresed as O/Re ratios.

Table 5.8

Kinetic parameters for ethane-D_2 reactions over rhenium and platinum catalysts.

Reaction	Parameter	Re	Pt
D_2 exchange	TF[a] (525 K)	8.8	2.2
	(575 K)	24.5	15.0
	E_a (Kcal/mole)	12	19
	Log A[a]	5.9	8.4
	$\bar{M}$	3.0	4.0
Hydrogenolysis	TF[a] (575 K)	4.5	0.012

a) in molec/metal atom·sec.

Table 5.9

Reaction rates for n-hexane over rhenium catalysts[a].

Catalyst[c]	Time (min)	TF[b] Hyd	Iso	MCP	Bz
Re foil	0	300	0.8	0	3.3
	120	62	0.3	0	1.9
Re film	0	51	5.3	0	12
	120	5.3	0.1	0	2.5
Re (0001)/S	0	4-20	0	0	-

Hydrogenolysis product distribution (%).

Catalyst[c]	C_1	C_2	C_3	C_4	C_5
Re foil	91	4	3	1	1
Re film	45	20	19	9	7
Re (0001)/S	25	55	12	6	2

a) P_{HC}=20 Torr, T=573 K.

b) Turnover frecuency, $x10^{-3}$ molec/Re atom·sec. Hyd=hydrogenolysys, Iso=isomerization, MCP=methylcyclopentane formation, Bz=aromatization.

c) P_{H_2}=600 Torr for foil and single crystal, 200 Torr for film.

FIGURE CAPTIONS

Fig. 5.23. Auger electron spectra of a clean Pt(111) single crystal and a rhenium film, using a retarding field analyzer. The incident electron beam energy was 1700 eV, at an incident angle of 60°. The field was modulated with a 10 V peak to peak ac voltage (2 V for energies under 110 eV).

Fig. 5.24. CO thermal desorption spectra from rhenium film surfaces. a) After CO saturation at 150 K. b) After CO saturation at 150 K, heating to 700 K and CO saturation again at 150 K. c) After O_2 adsorption to half saturation and subsequent CO saturation at 150 K. d) CO_2 trace for the same experiment as c). Heating rate ~ 30 K/sec.

Fig. 5.25. Schematic LEED pattern obtained after CO saturation of a Re film at 150 K. The dark dots represent the rhenium surface, while the open circles are due to the CO overlayer. Heating rate ~ 30 K/sec.

Fig. 5.26. D_2 thermal desorption spectrum from a rhenium film after saturation at 150 K. Heating rate ~ 30 K/sec.

Fig. 5.27. Ethylene and H_2 thermal desorption spectra from a rhenium surface saturated with ethylene at 150K. Heating rate ~ 30 K/sec.

Fig. 5.28. XPS spectra of ReO_2: wide scan (top), Re 4f (middle) and O 1s and Re $4p_{1/2}$ (bottom).

Fig. 5.29. XPS spectra of ReO_3: wide scan (top), Re 4f (middle) and O 1s and Re $4p_{1/2}$ (bottom).

Fig. 5.30. XPS spectra of Re_2O_7: wide scan (top), Re 4f (middle) and O is and Re $4p_{1/2}$ (bottom).

Fig. 5.31. Binding energy for Re $4f_{7/2}$ electrons as a function of formal oxidation state. Our data is compared to literature values: refs. 61 (Δ), 63 (o) and 64 (#).

Fig. 5.32. Rhenium and platinum 4f XPS spectra for rhenium film deposited over a platinum foil, after subsequent oxidation and reduction.

Fig. 5.33. Re 4f XPS spectra for rhenium films deposited on top of a platinum foil, after subsequent oxidation and reduction.

Fig. 5.34. O 1s and Re $4p_{1/2}$ XPS spectra for rhenium films deposited on top of a platinum foil, after subsequent oxidation and reduction.

Fig. 5.35. Re 4f XPS spectra for a surface Pt-Re alloy, after subsequent oxidation and reduction.

Fig. 5.36. Deuterium atom distribution in the resulting ethane from exchange with D_2 over a rhenium film (at two different conversions).

Fig. 5.37. H_2 TDS after n-hexane reactions over Pt (111), clean and partially covered with Re, and over a Re film. Also shown is the total amount of carbon on the surface, as measured by AES.

Fig. 5.38. Catalytic behavior of a sulfur pretreated Pt (111) surface for n-hexane reactions. In the lower frame the reaction rates

for the precovered surface have been divided by those over clean Pt (111), and plotted against sulfur coverage (AES signal ratio). In the upper frame the product distributions for clean and sulfur covered surfaces are compared.

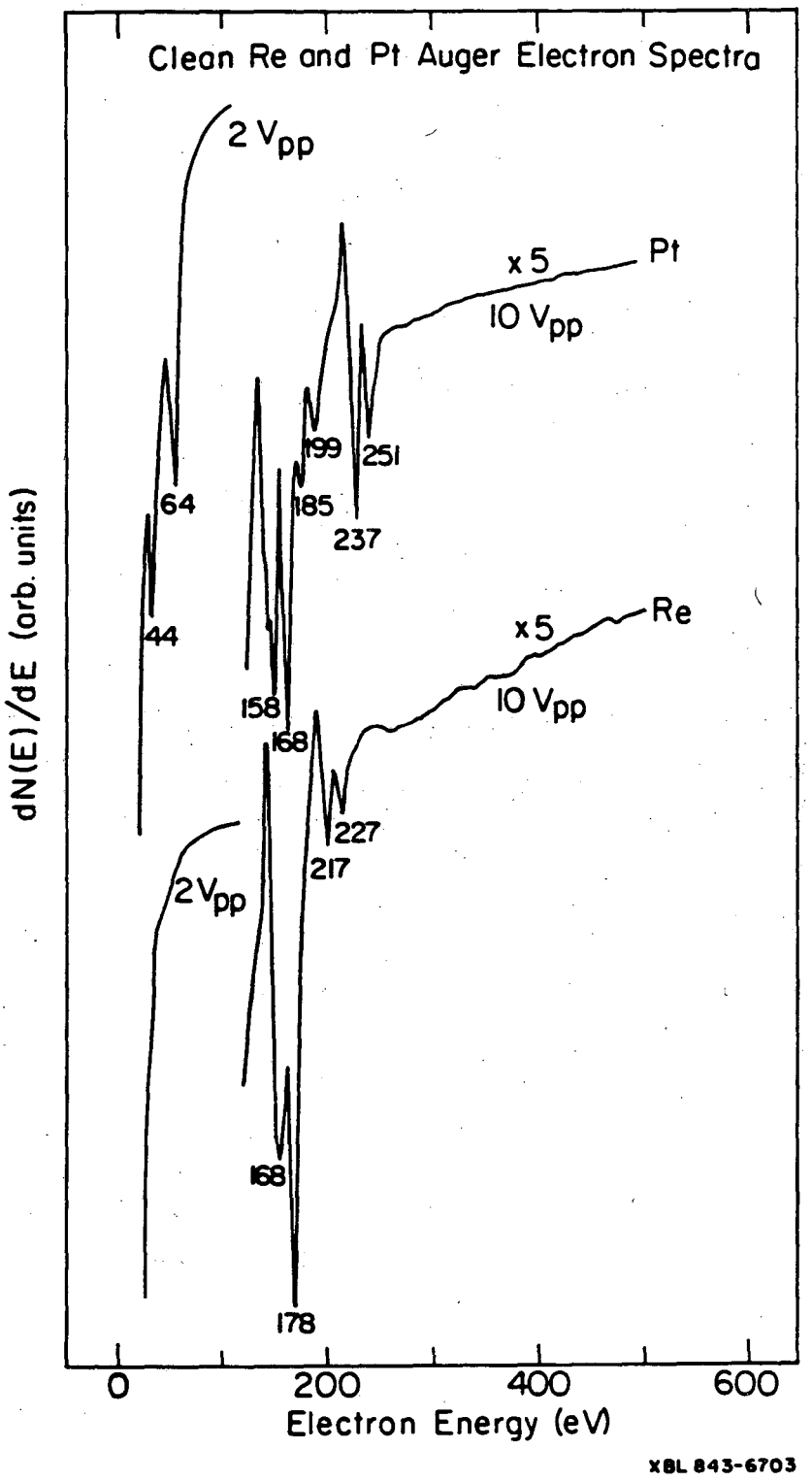
Clean Re and Pt Auger Electron Spectra
2 Vpp
x 5
Pt
10 Vpp
64
44
199
251
185
237
158
168
x 5
Re
10 Vpp
227
217
2 Vpp
168
178
dN(E)/dE (arb. units)
0
200
400
600
Electron Energy (eV)
XBL 843-6703

fig. 5.23

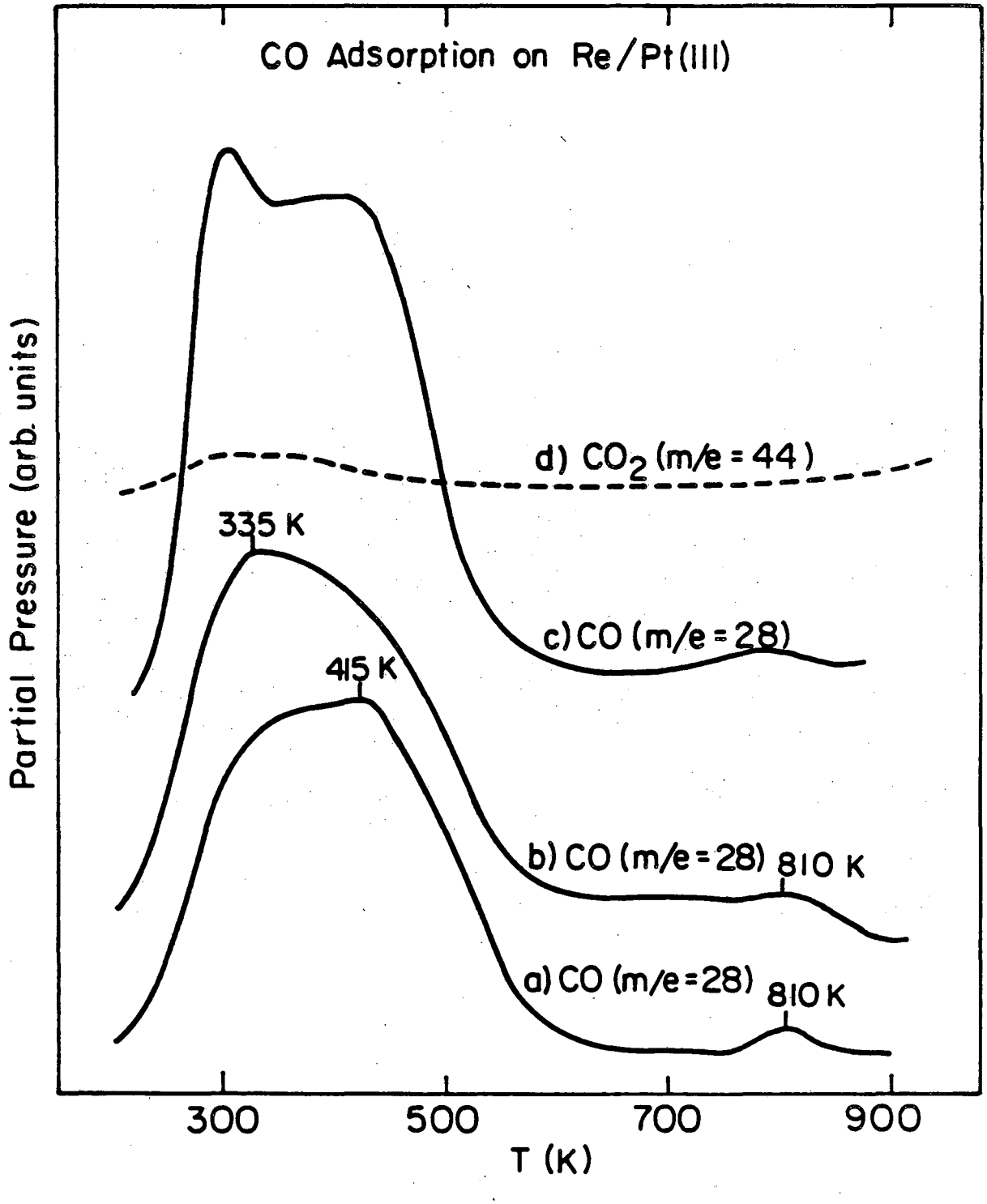
CO Adsorption on Re/Pt(111)
Partial Pressure (arb. units)
d) CO_2 (m/e = 44)
335 K
c) CO (m/e = 28)
415 K
b) CO (m/e = 28)
810 K
a) CO (m/e = 28)
810 K
300
500
700
900
T (K)
XBL 843-6704

fig. 5.24

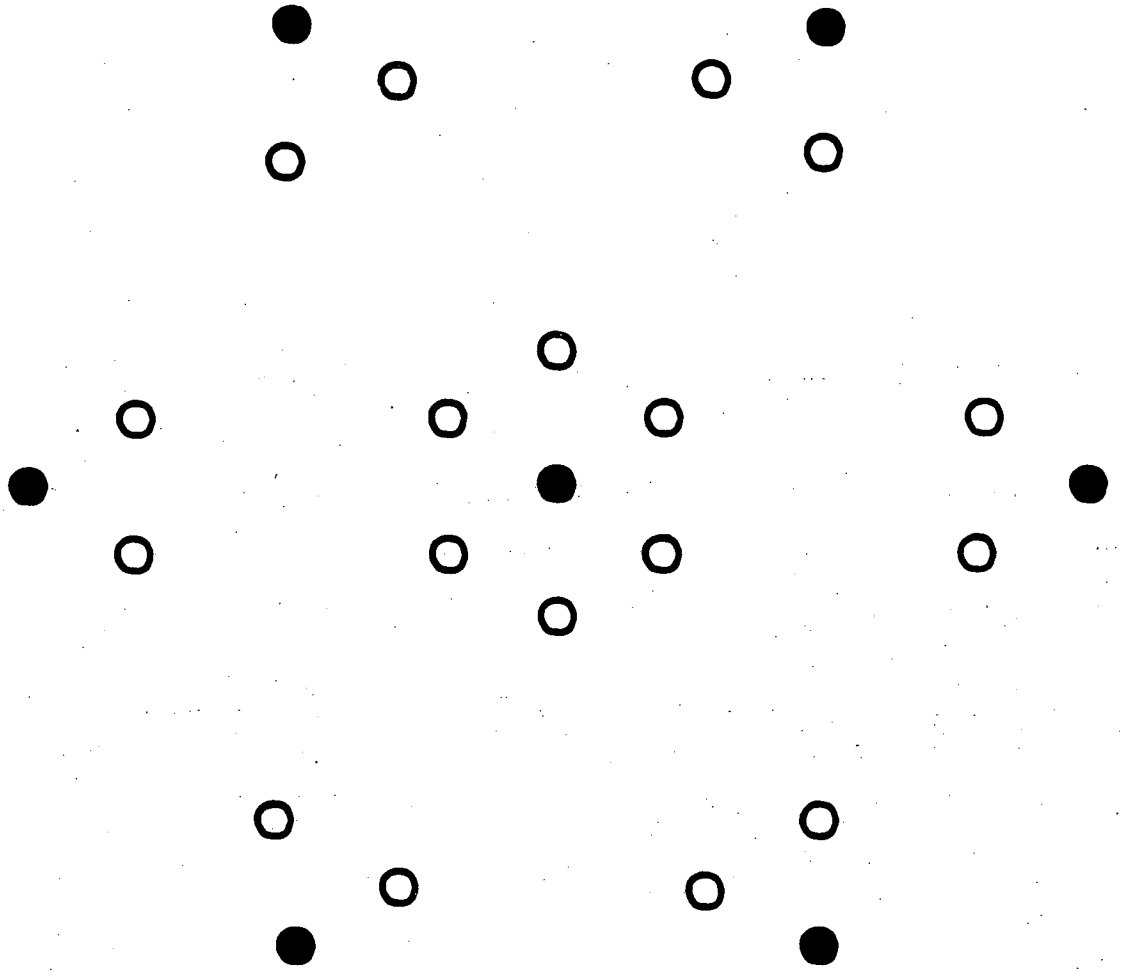

XBL 843-6707

fig. 5.25

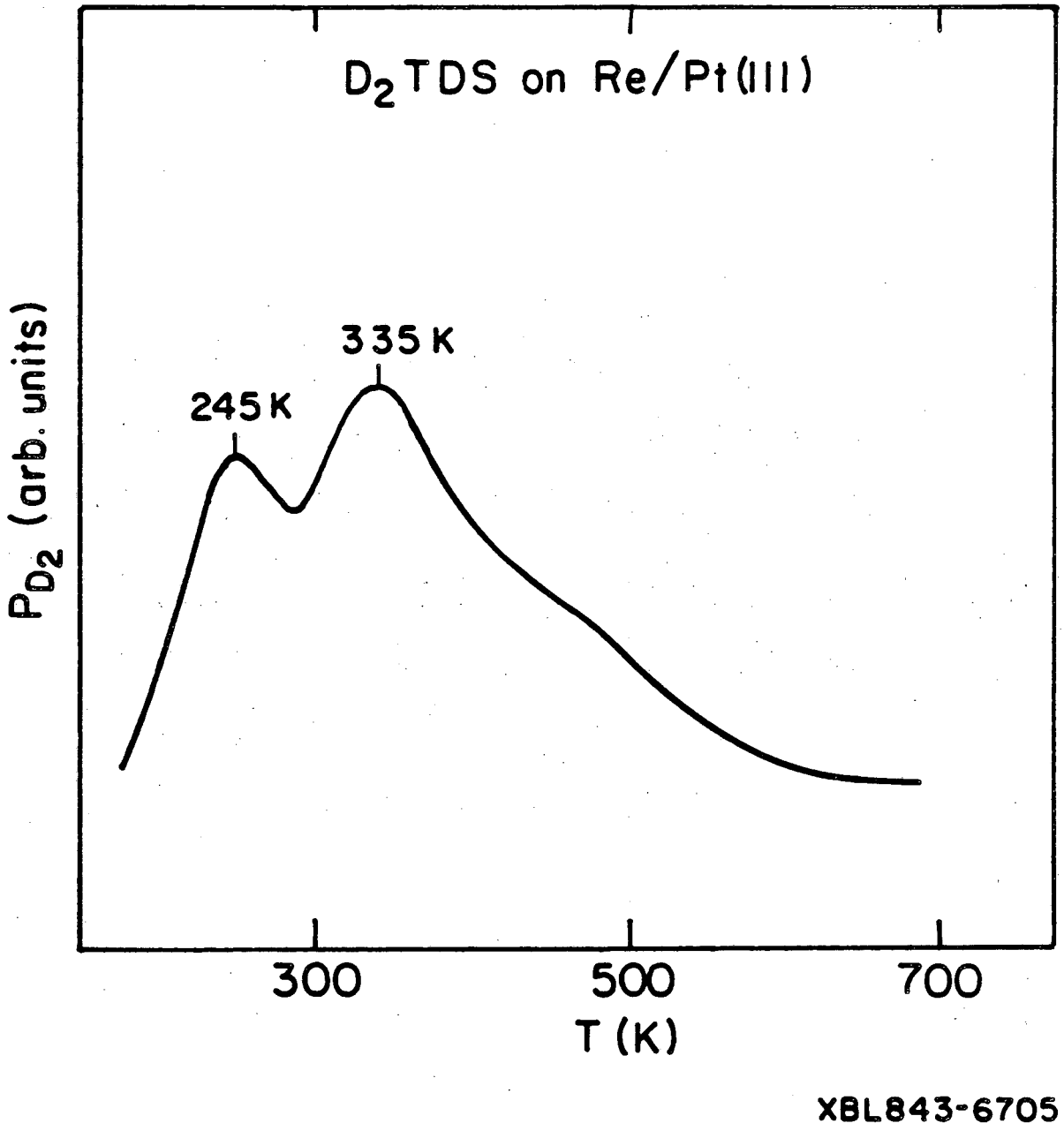
D2 TDS on Re/Pt(111)
335 K
245 K
PD2 (arb. units)
300
500
700
T (K)
XBL843-6705

fig. 5.26

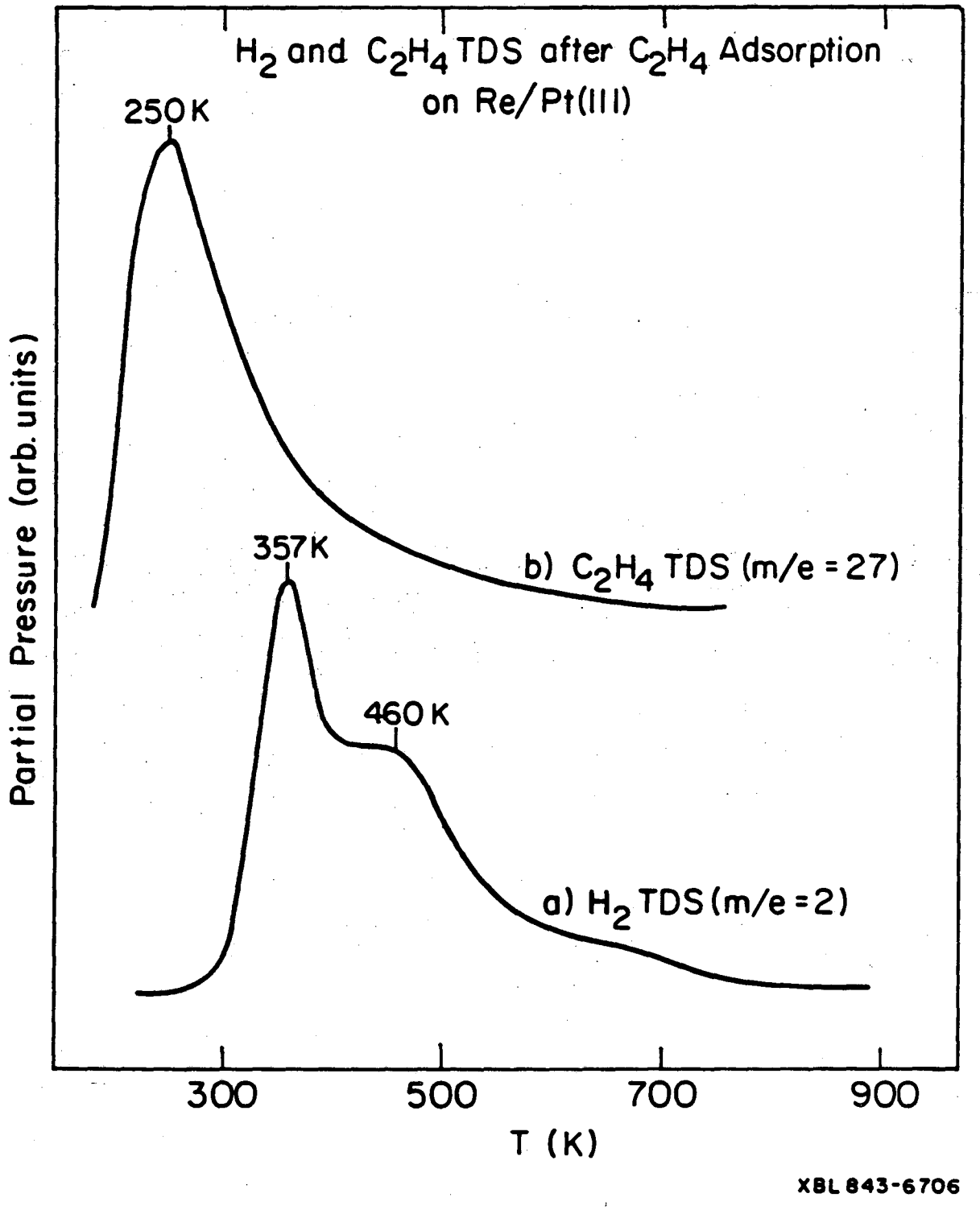
H2 and C2H4 TDS after C2H4 Adsorption
on Re/Pt(111)
250K
357K
460K
b) C2H4 TDS (m/e = 27)
a) H2 TDS (m/e = 2)
Partial Pressure (arb. units)
300
500
700
900
T (K)
XBL 843-6706

fig. 5.27

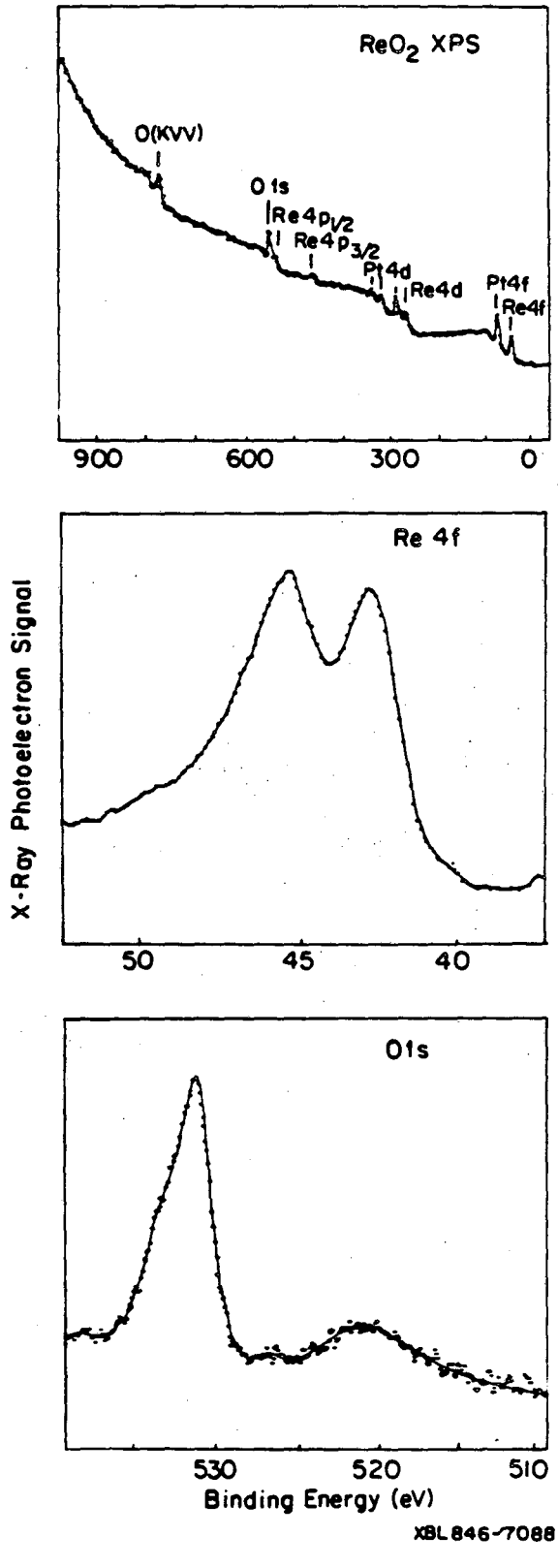
ReO_2 XPS
O(KVV)
O 1s
Re 4p1/2
Re 4p3/2
Pt 4d
Re 4d
Pt 4f
Re 4f
900
600
300
0
Re 4f
X-Ray Photoelectron Signal
50
45
40
O 1s
530
520
510
Binding Energy (eV)
XBL 846-7088

fig. 5.28

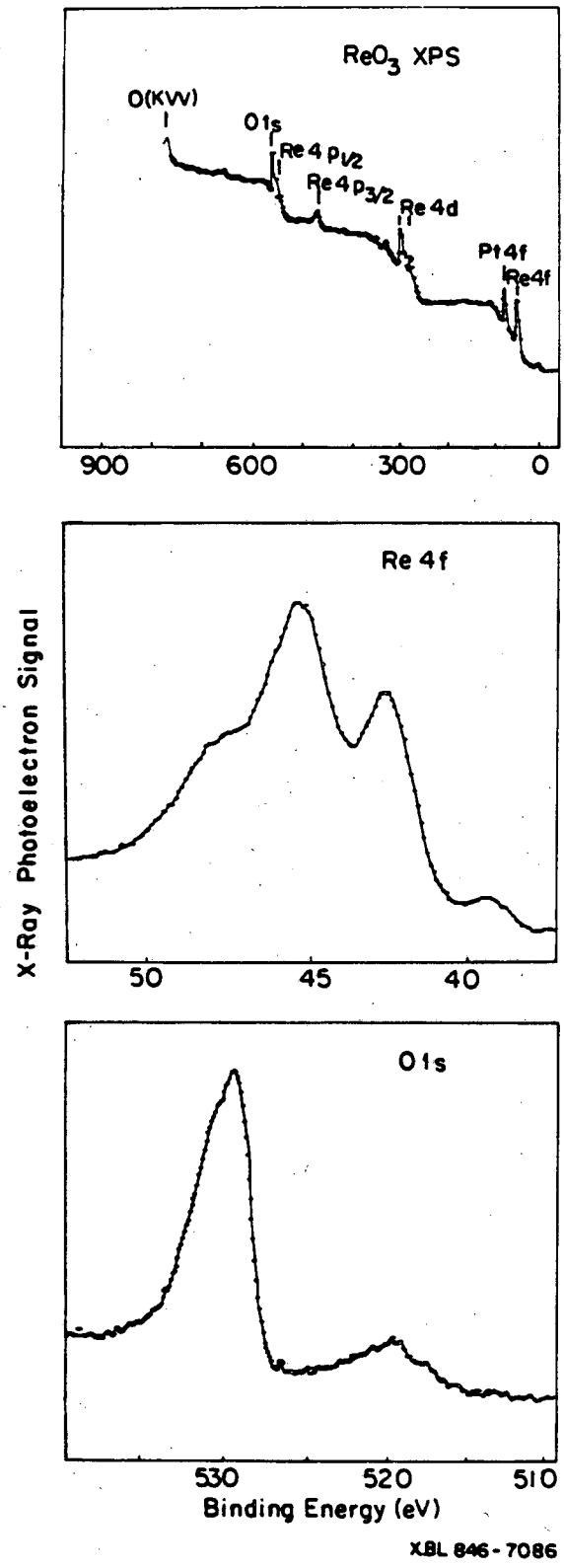
ReO_3 XPS
O(KVV)
O1s
Re 4 $p_{1/2}$
Re 4 $p_{3/2}$
Re 4d
Pt 4f
Re 4f
900
600
300
0
Re 4f
50
45
40
O1s
530
520
510
X-Ray Photoelectron Signal
Binding Energy (eV)
XBL 846-7086

fig. 5.29

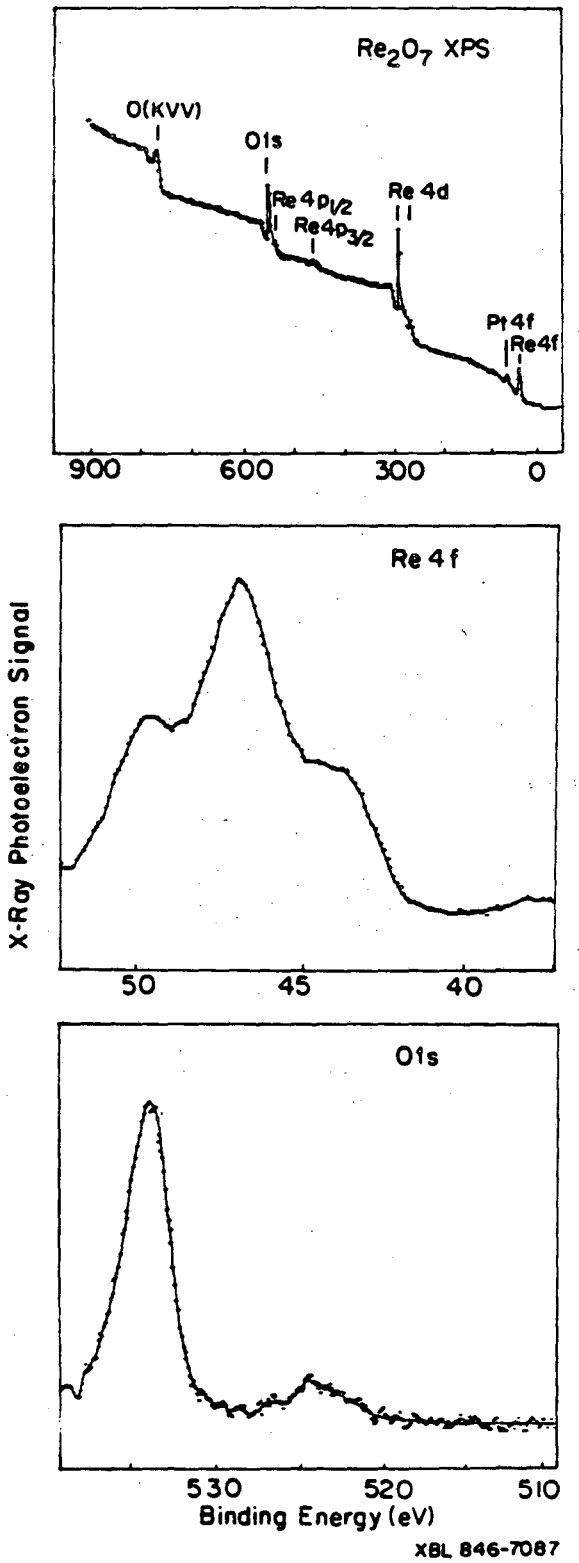
Re_2O_7 XPS
O(KVV)
O1s
Re 4p1/2
Re 4p3/2
Re 4d
Pt 4f
Re 4f
900
600
300
0
Re 4f
X-Ray Photoelectron Signal
50
45
40
O1s
530
520
510
Binding Energy (eV)
XBL 846-7087

fig. 5.30

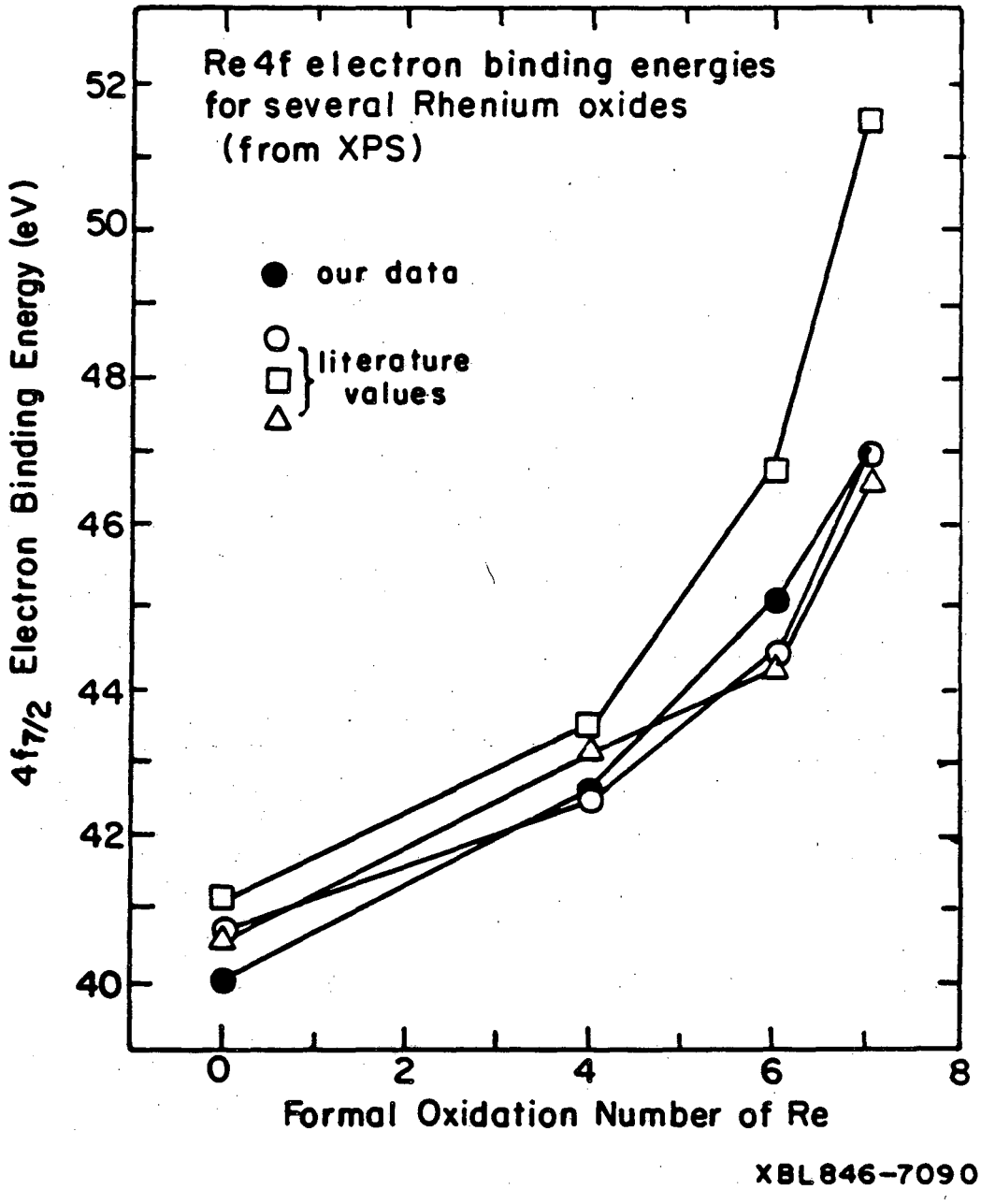
Re 4f electron binding energies
for several Rhenium oxides
(from XPS)
our data
literature values
$4f_{7/2}$ Electron Binding Energy (eV)
52
50
48
46
44
42
40
0
2
4
6
8
Formal Oxidation Number of Re
XBL846-7090

fig. 5.31

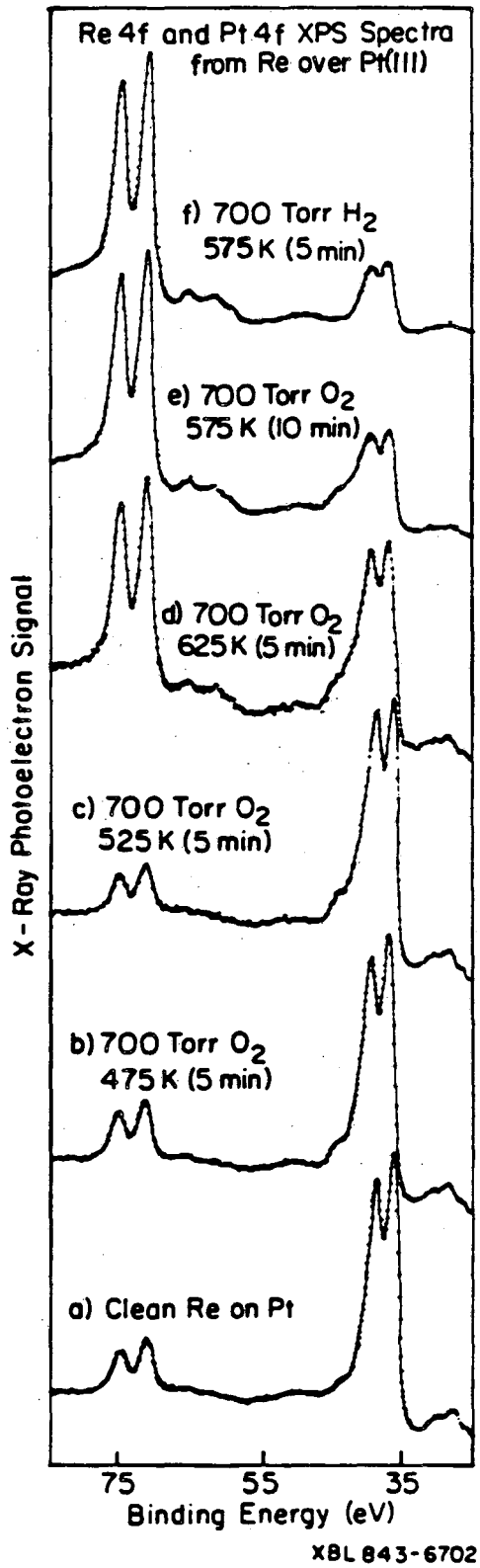
Re 4f and Pt 4f XPS Spectra
from Re over Pt(111)
f) 700 Torr H_2
575 K (5 min)
e) 700 Torr O_2
575 K (10 min)
d) 700 Torr O_2
625 K (5 min)
c) 700 Torr O_2
525 K (5 min)
b) 700 Torr O_2
475 K (5 min)
a) Clean Re on Pt
X-Ray Photoelectron Signal
75
55
35
Binding Energy (eV)
XBL 843-6702

fig. 5.32

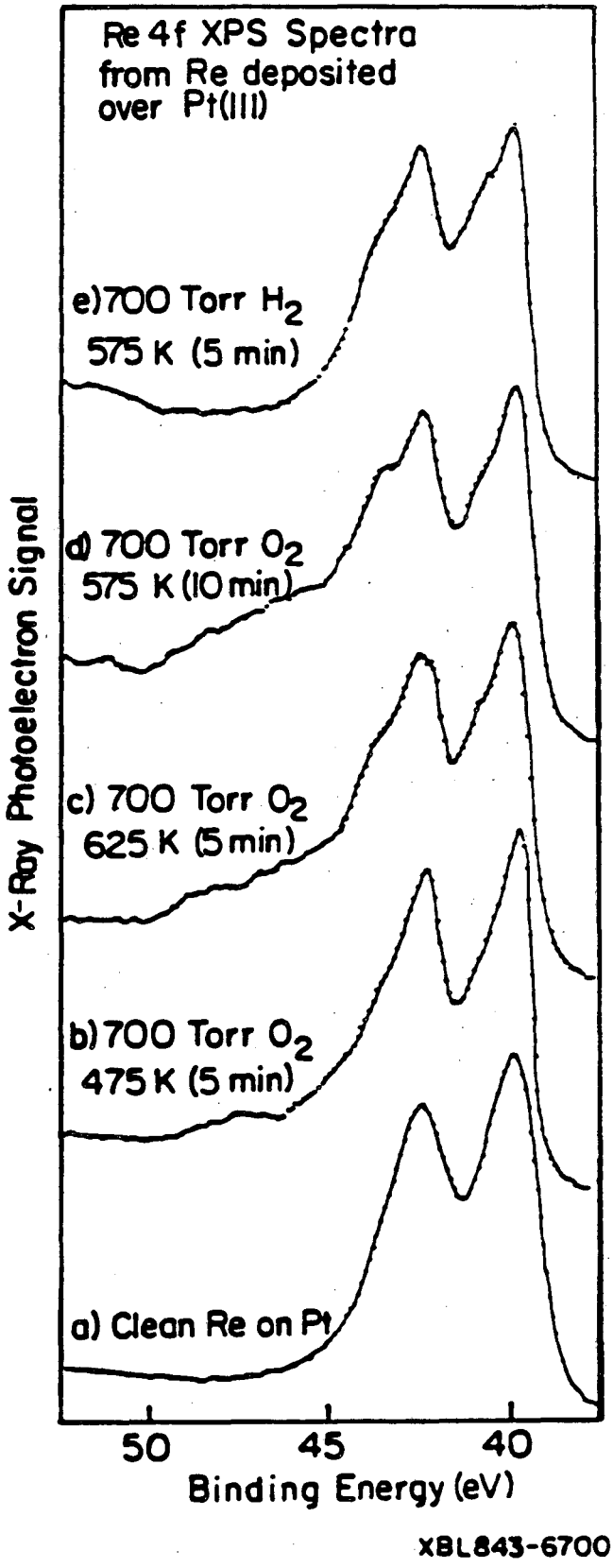
Re 4f XPS Spectra
from Re deposited
over Pt(111)
e) 700 Torr H_2
575 K (5 min)
d) 700 Torr O_2
575 K (10 min)
c) 700 Torr O_2
625 K (5 min)
b) 700 Torr O_2
475 K (5 min)
a) Clean Re on Pt
X-Ray Photoelectron Signal
50
45
40
Binding Energy (eV)
XBL843-6700

fig. 5.33

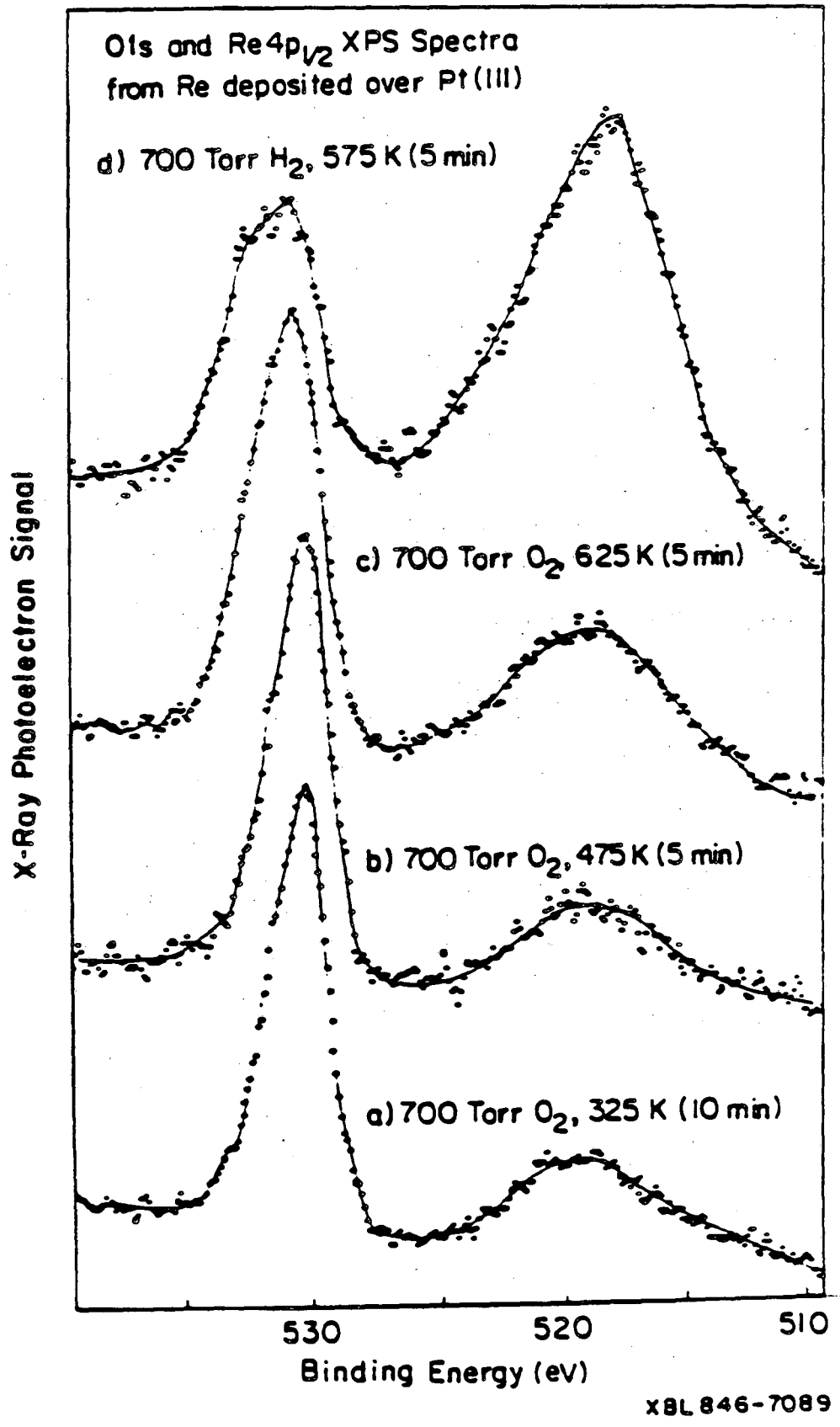
O1s and Re4p1/2 XPS Spectra
from Re deposited over Pt(111)
d) 700 Torr H2, 575 K (5 min)
c) 700 Torr O2, 625 K (5 min)
b) 700 Torr O2, 475 K (5 min)
a) 700 Torr O2, 325 K (10 min)
X-Ray Photoelectron Signal
530
520
510
Binding Energy (eV)
XBL 846-7089

fig. 5.34

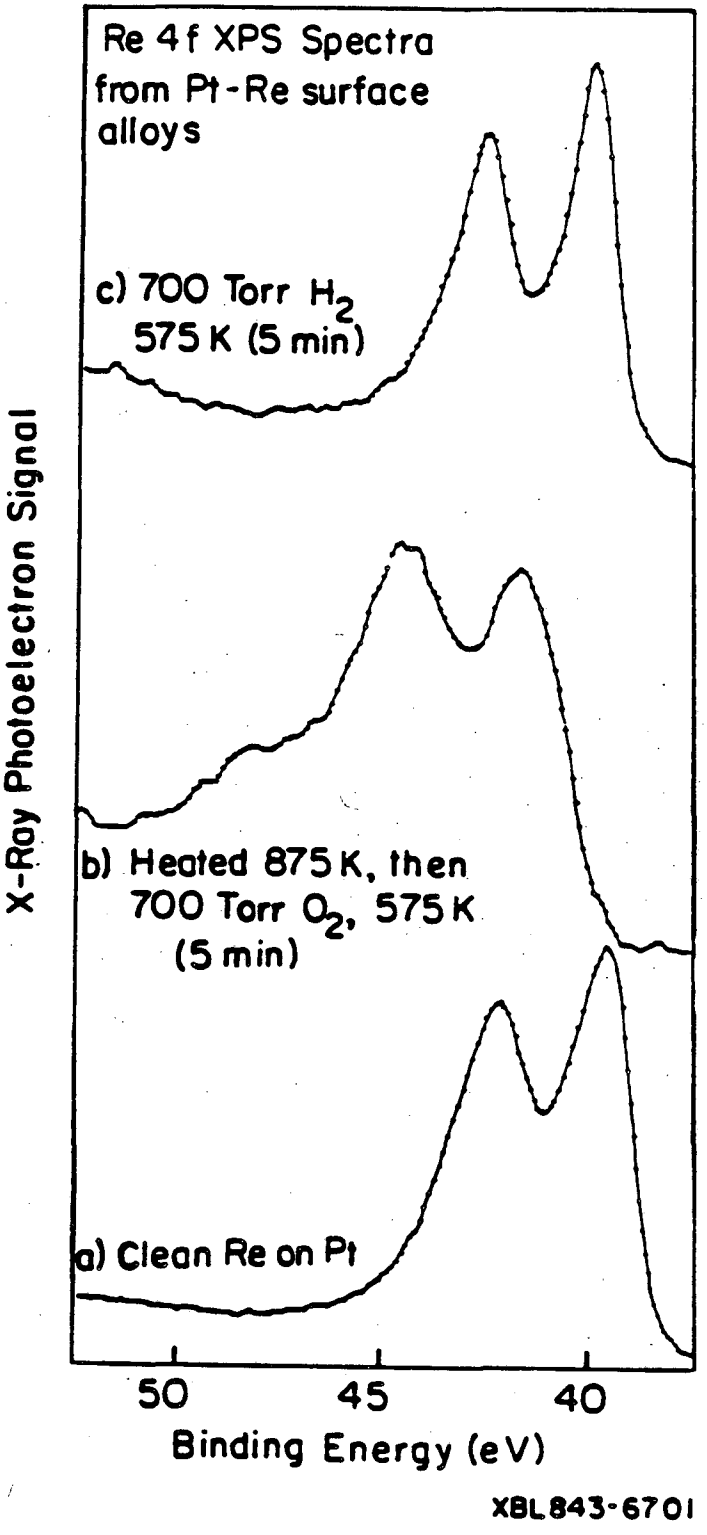
Re 4f XPS Spectra
from Pt-Re surface
alloys
c) 700 Torr H_2
575 K (5 min)
b) Heated 875 K, then
700 Torr O_2, 575 K
(5 min)
a) Clean Re on Pt
X-Ray Photoelectron Signal
50
45
40
Binding Energy (eV)
XBL843-6701

fig. 5.35

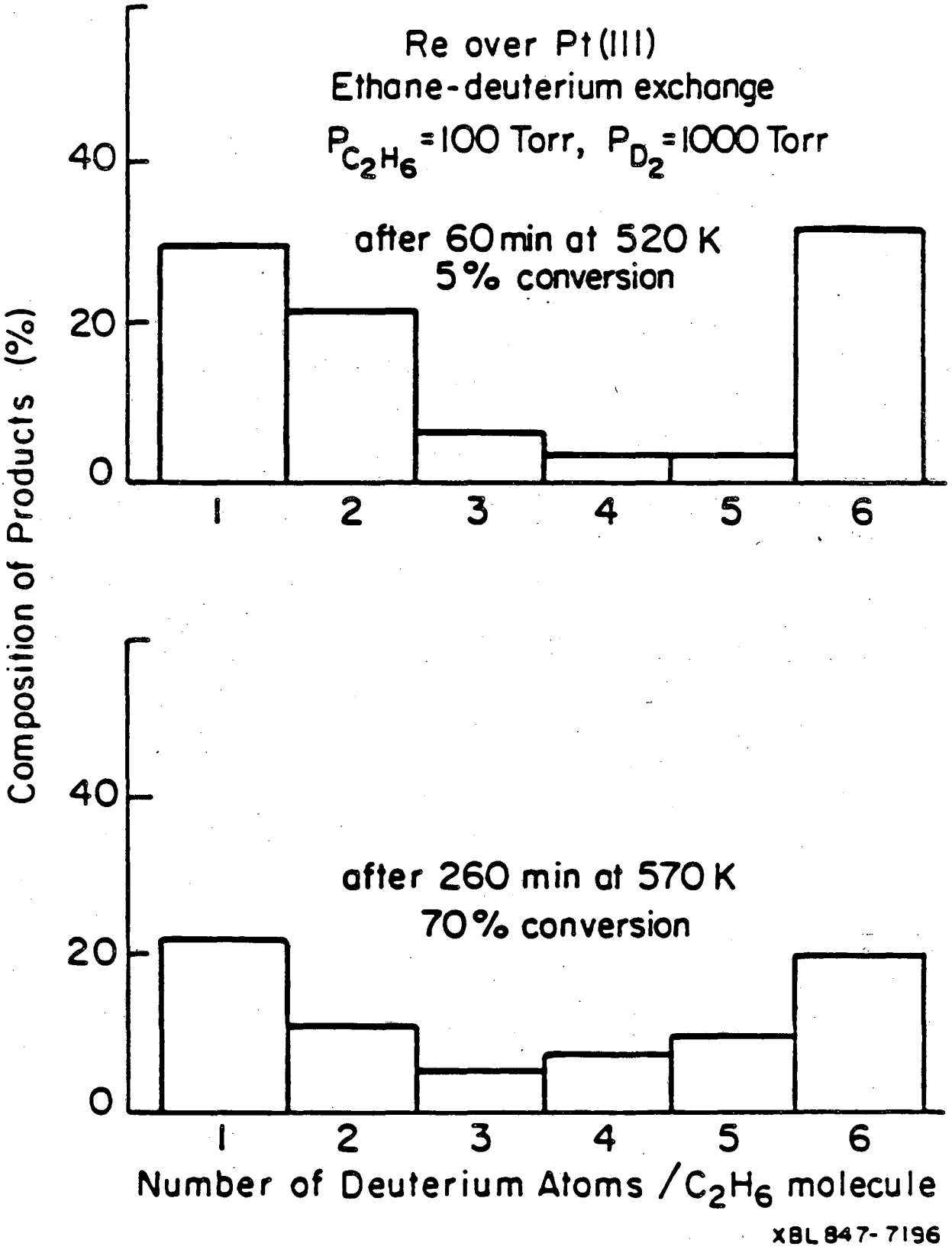
Re over Pt(111)
Ethane-deuterium exchange
$P_{C_2H_6}$ = 100 Torr, P_{D_2} = 1000 Torr
after 60 min at 520 K
5% conversion
after 260 min at 570 K
70% conversion
Composition of Products (%)
0
20
40
1
2
3
4
5
6
Number of Deuterium Atoms / C_2H_6 molecule
XBL 847-7196

fig. 5.36

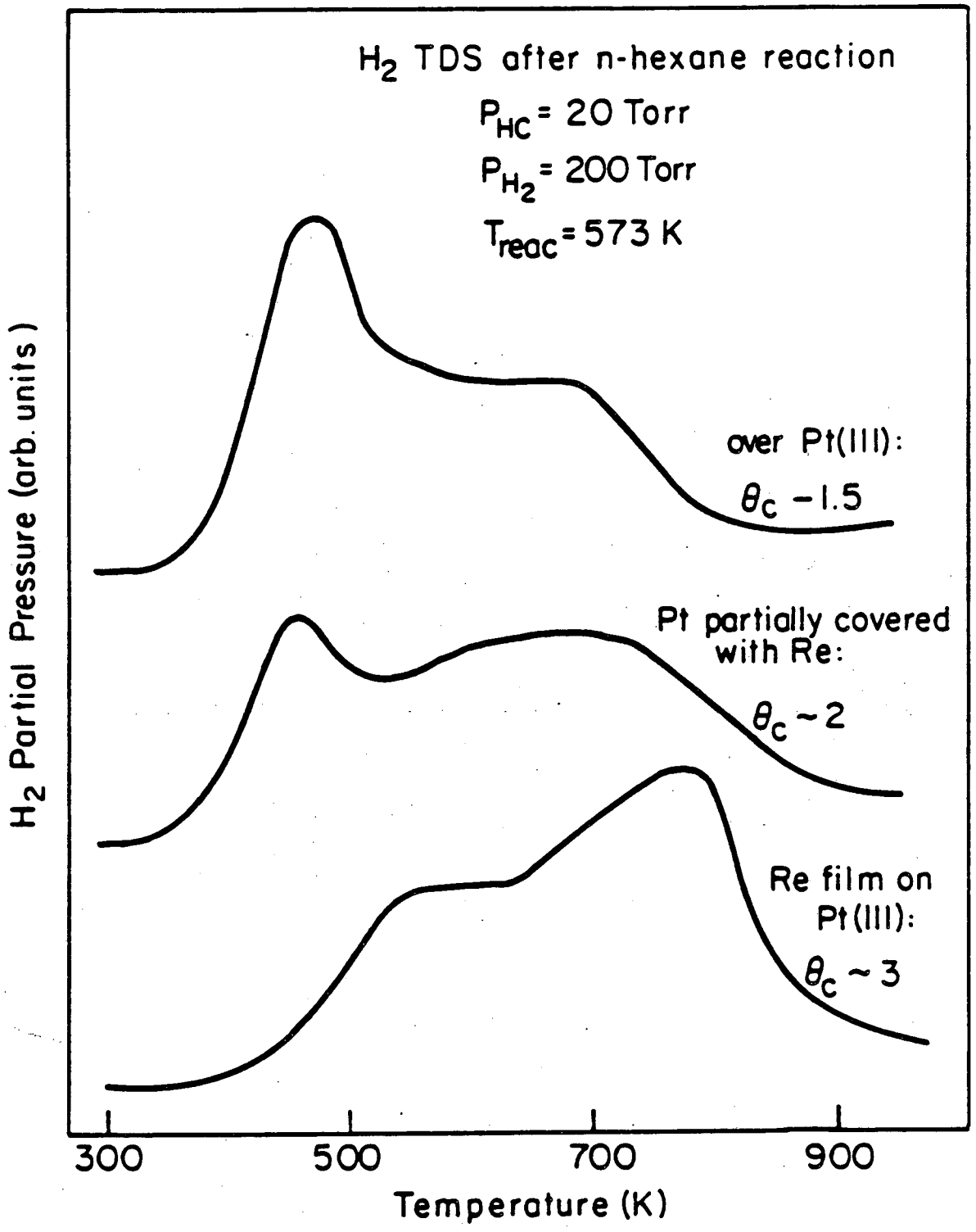
H2 TDS after n-hexane reaction
PHC = 20 Torr
PH2 = 200 Torr
Treac = 573 K
over Pt(111):
θc ~1.5
Pt partially covered with Re:
θc ~2
Re film on Pt(111):
θc ~3
H2 Partial Pressure (arb. units)
300
500
700
900
Temperature (K)
XBL 847-7197

fig. 5.37

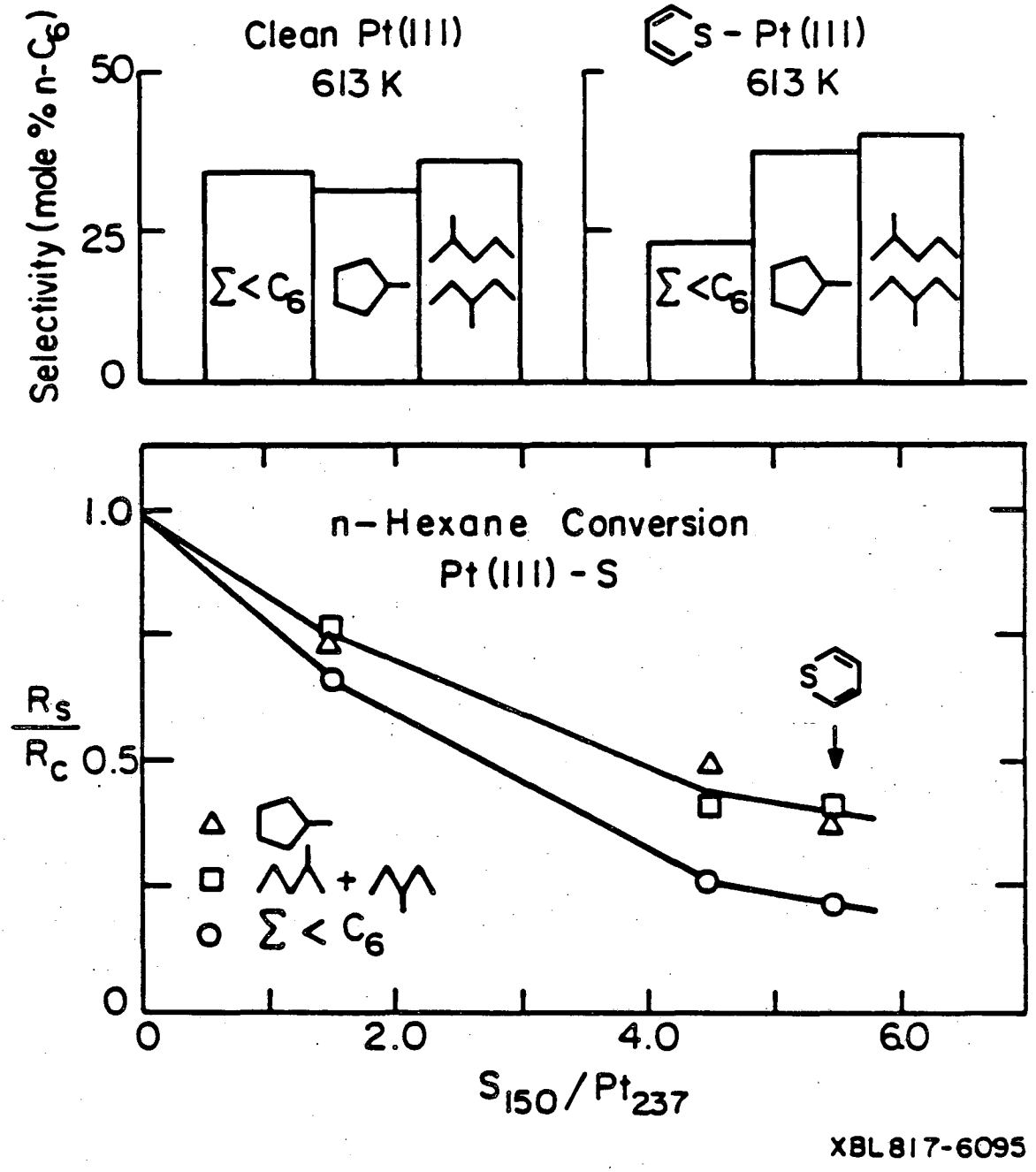
Clean Pt(111)
613 K
S - Pt(111)
613 K
Selectivity (mole % n-C6)
50
25
0
Σ<C6
Σ<C6
n-Hexane Conversion
Pt(111) - S
1.0
0.5
0
Rs/Rc
S
Σ < C6
0
2.0
4.0
6.0
S150/Pt237
XBL817-6095

fig. 5.38

5.3. References.

1) P.H. Emmet, "The Physical Basis for Heterogeneous Catalysis", Plenum, New York 1975.

2) G. Ertl, Catal. Rev.- Sci. Eng., 21, 201 (1980).

3) H.H. Storch, in "Advances in Catalysis", Vol. 1, D.D. Eley, H. Pines and P.B. Weisz, eds., Academic Press, New York, 1948, p. 1.

4) G.A. Somorjai, Surf. Sci., 89, 496 (1979).

5) N.R. Bussian, S.B. Kogan and P.P. Bol'shakov, Kinet. and Catal. (USSR), 17, 1329 (1977).

6) D.A. Dowden, in "Catalysis", Vol. 2, C. Kemball and D.A. Dowen, eds., The Chemical Society Burlington House, London 1978, pp. 1-27 (1978).

7) S.M. Davis, Ph.D. Thesis, University of California, Berkeley 1981.

8) German patent 2,339,840, from J.J. McCarroll, Surf. Sci., 53, 297 (1975).

9) W.D. Gillespie, Ph.D. Thesis, University of California, Berkeley 1979.

10) S.M. Davis, B.E. Gordon, M. Press and G.A. Somorjai, J. Vac. Sci. Technol., 19, 231 (1981).

11) S.M. Davis, F. Zaera and G.A. Somorjai, J. Catal., 77, 439 (1982).

12) J.E. Crowell, E.L. Garfunkel and G.A. Somorjai, Surf. Sci., 121, 303 (1982).

13) S.M. Davis, F. Zaera, B.E. Gordon and G.A. Somorjai, Submitted to J. Catal.

14) See, for instance, H. Mayer, Z. Physik, 115, 729 (1940).

15) A. Cimino, M. Boudart and H.S. Taylor, J. Phys. Chem., 58, 796 (1954).

16) J.K.A. Clarke and J.J. Rooney, in "Advances in Catalysis", Vol. 25, D.D. Eley, H. Pines and P.B. Weisz, eds., Academic Press, New York, 1976, p. 125.

17) J.R. Anderson and N.R. Avery, J. Catal., 7, 315 (1967).

18) See, for instance, J.E. Demuth and D.E. Eastman, Phys. Rev. Lett., 32, 1123 (1974).

19) J.L. Gland, Ph.D. Thesis, University of California, Berkeley 1973.

20) P.E.C. Franken and V. Ponec, Surf. Sci., 53, 341 (1975).

21) K. Foger and J.R. Anderson, J. Catal., 54, 318 (1978).

22) D. Loebich, Jr. and C.J. Raub, Plat. Met. Rev., 25, 113 (1981).

23) V. Haensel, U.S. patent 2,479,109 (1949).

24) H.E. Kluksdahl, U.S. patent 3,415,737 (1968).

25) J.H. Sinfelt, U.S. patent 3,953,368 (1976).

26) F.M. Dautzenberg, German patent 2,121,765 (1971).

27) J.H. Sinfelt, in "Catalysis: Science & Technology", Vol. 1, J.R. Anderson and M. Boudart, eds., Springer-Verlag, Berlin 1981, pp. 257-300.

28) R.L. Moss, in "Catalysis", Vol. 1, C. Kemball, ed., The Chemical Society Burlington House, London 1977, pp. 37-86.

29) D.A. Dowden, in "Catalysis", Vol. 2, C. Kemball and D.A. Dowden, eds., The Chemical Society Burlington House, London 1978, pp. 1-7.

30) J.H. Sinfelt and J.A. Cusumano, in "Advanced Materials in Catalysis", J.J. Burton and R.L. Garten, eds., Academic Press, New York 1977, pp. 1-31.

31) J.J. Burton and R.L. Garten, in "Advanced Materials in Catalysis", J.J. Burton and R.L. Garten, eds., Academic Press, New York 1977, pp. 33-65.

32) G.J. Dooley III and T.W. Haas, Surf. Sci., 19, 1 (1970).

33) R. Ducros, M. Housley, M. Alnot and A. Cassuto, Surf. Sci., 71, 433 (1978).

34) R. Ducros, M. Alnot, J.J. Ehrhardt, M. Housley, G. Piquard and A. Cassuto, Surf. Sci., 94, 154 (1980).

35) M. Housley, R. Ducros, G. Piquard and A. Cassuto, Surf. Sci., 68, 277 (1977).

36) R. Pantel, M. Bujor and J. Bardolle, Surf. Sci., 83, 228 (1979).

37) R, Ducros, M. Housley, G. Piquard and M. Alnot, Surf. Sci., 109, 235 (1981).

38) M.D. Scheer and J.D. McKinley, Surf. Sci., 5, 332 (1966).

39) Y. Fukuda, F. Honda and J.W. Rabalais, Surf. Sci., 93, 338 (1980).

40) Y. Fukuda, F. Honda and J.W. Rabalais, Surf. Sci., 99, 289 (1980).

41) P.W. Palmberg, G.E. Riach, R.E. Weber and N.C. MacDonald, "Handbook of Auger Electron Spectroscopy", Physical Electronics Industries, Inc., Minnesota, 1972.

42) R. Ducros, M. Housley and G. Piquard, Phys. Status Solidi (a), 56, 187 (1979).

43) S. Tatarenko, P. Dolle, R. Morancho, M. Alnot, J.J. Ehrhardt and R. Ducros, Surf. Sci., 134, L505, (1983).

44) S. Tatarenko, R. Ducros and M. Alnot, Surf. Sci., 126, 422 (1983).

45) E.D. Williams and W.H. Weinberg, Surf. Sci., 82, 93 (1979).

46) R. Ducros, B. Tardy and J.C. Bertolini, Surf. Sci., 128, L219 (1983).

47) M.F.L. Johnson and V.M. LeRoy, J. Catal., 35, 434 (1974).

48) A.N. Webb, J. Catal., 39, 485 (1975).

49) H.C. Yao anf M. Shelef, J. Catal., 44, 392 (1976).

50) W.H. Davenport, V. Kollonitsch and C.H. Kline, Ind. Eng. Chem., 60, 10 (1968).

51) C. Bolivar, H. Charcosset, R. Frety, M. Primet, L. Tournayon, C. Betizeau, G. Leclerq and R. Maurel, J. Catal., 45, 163 (1976).

52) C. Betizeau, G. Leclerq, R. Maurel, C. Bolivar, H. Charcosset, R. Frety and L. Tournayon, J. Catal., 45, 179 (1976).

53) B.D. McNicol, J. Catal., 46, 438 (1977).

54) M.F.L. Johnson, J. Catal., 39, 487 (1975).

55) C. Bolivar, H. Charcosset, R. Frety, M. Primet, L. Tournayon, C. Betizeau, G. Leclerq and R. Maurel, J. Catal., 39, 249 (1975).

56) R. Busch, Plat. Met. Rev., 22, 57 (1976).

57) H. Charcosset, R, Frety, G, Leclerq, E. Mendes, M. Primet and L. Tournayon, J. Catal., 56, 468 (1979).

58) N. Wagstaff and R. Prins, J. Catal., 59, 434 (1979).

59) B. Isaacs and E.E. Petersen, J. Catal., 77, 43 (1982)

60) Y.I. Yermakov, B.N. Kuznetzov, I.A. Ovsyannikova, A.N. Startsev, S.B. Erenburg, M.A. Sheromov and L.A. Mironenko, React. Kinet. & Catal. Lett., 7, 309 (1977).

61) E.S. Shpiro, V.I. Avaev, G.V. Antoshin, M.A. Ryashentseva and Kh.M. Minachev, J. Catal., 55, 402 (1978).

62) C.D. Wagner, W.M. Riggs, L.E. Davis, J.F. Moulder and G.E. Muilenberg, "Handbook of X-Ray Photoelectron Spectroscopy", Perkin-Elmer Corp., Physical Electronic Div., Minnesota 1978.

63) A. Cimino, B.A. De Angelis, D. Gazzoli and M. Valigi, Z. Anorg. Allg. Chem., 460, 86 (1980).

64) E. Broclawik, J. Haber and L. Ungier, J. Phys. Chem. Solids, 42, 203 (1981).

65) M. Alnot, A. Cassuto, R. Ducros, J.J. Ehrhardt and B. Weber, Surf.

Sci., 114, L48 (1982).

66) P. Biloen, J.N. Helle, H. Verbeek, F.M. Dautzenberg and W.M.H. Sachtler, J. Catal., 63, 112 (1980).

67) B.H. Davis, J. Catal., 46, 348 (1977).

68) I.H.B. Haining, C. Kemball and D.A. Whan, J. Chem. Research (s), 1977, 170 (1977).

69) L.W. Jossens and E.E. Petersen, J. Catal., 76, 265 (1982).

70) J.L. Carter, G.B. McVicker, W. Weissman, W.S. Kmak and J.H. Sinfelt, Appl. Catal., 3, 327 (1982).

71) F.G. Ciapetta and D.N. Wallace, Catal. Rev., 5, 67 (1971).

72) J.R. Anderson and C. Kemball, Proc. Royal Soc., Serie A, 223, 361 (1954).

73) J.H. Sinfelt, in "Advancees in Catalysis", Vol. 23, D.D. Eley, H. Pines and P.B. Wisz, Eds., Academic Press, New York 1980, pp. 91-119.

74) J.K.A. Clarke and J.F. Taylor, J. Chem. Soc. Faraday Trans. I, 71, 2063 (1975).

75) R.J. Bertolacini and R.J. Pellet, in "Catalyst Deactivation", B. Delmon and G.F. Froment, eds., Elsevier, Amsterdam 1980, pp. 73-77.

76) P.G. Menon and J. Prasad, in "Proc. 6th Int. Cong. Catal., London 1976", G.C. Bond, P.B. Wells and F.C. Tompkins, eds., The Chemical Society Burlington House, London 1977, pp. 1061-1070.

77) C.R. Apesteguía and J. Barbier, J. Catal., 78, 352 (1982).

78) J. Crowell, W.T. Tysoe and G.A. Somorjai, to be published.

This report was done with support from the Department of Energy. Any conclusions or opinions expressed in this report represent solely those of the author(s) and not necessarily those of The Regents of the University of California, the Lawrence Berkeley Laboratory or the Department of Energy.

Reference to a company or product name does not imply approval or recommendation of the product by the University of California or the U.S. Department of Energy to the exclusion of others that may be suitable.

TECHNICAL INFORMATION DEPARTMENT
LAWRENCE BERKELEY LABORATORY
UNIVERSITY OF CALIFORNIA
BERKELEY, CALIFORNIA 94720